2015-01-01

A Heterogeneous Multiscale Method for Poroelasticity

Paul M. Delgado
University of Texas at El Paso, pmdelgado2@utep.edu

A HETEROGENEOUS MULTISCALE METHOD FOR POROELASTICITY

PAUL M. DELGADO

Computational Science Program

APPROVED:

Vinod Kumar, Chair, Ph.D.

Son Young Yi, Ph.D.

Aaron Velasco, Ph.D.

Reza Ashtiani, PhD.

Charles Ambler, Ph.D.
Dean of the Graduate School

to my

WIFE, SON, MOTHER, FATHER, and SISTER

with love.

A HETEROGENEOUS MULTISCALE METHOD FOR POROELASTICITY

by

PAUL M. DELGADO, B.S., M.S.

DISSERTATION

Presented to the Faculty of the Graduate School of

The University of Texas at El Paso

in Partial Fulfillment

of the Requirements

for the Degree of

DOCTOR OF PHILOSOPHY

Computational Science Program

THE UNIVERSITY OF TEXAS AT EL PASO

May 2015

Table of Contents

List of Tables

List of Figures

Chapter 1

Introduction

1.1 Overview

Poroelasticity is the study of the transitory interactions between solid deformation and fluid flow within a porous medium. It is characterized by a time dependent, two-way coupling where changes in the state variables of one phase alter those of the other. As illustrated by the poroelastic medium in figure 1.1, applying external load to a saturated porous medium causes changes in the fluid pressures which induces a flow. Likewise, a change in fluid pressures induces stresses that deform the solid skeleton. Karl Terzaghi, a founding father of modern soil mechanics, was the first to observe and characterize the coupling phenomenon in a single dimension[28, 70]. The equations governing poroelasticity matured into a full multi-dimensional theory with the groundbreaking work of Maurice Biot [16, 17, 18]. Biot's equations were initially derived phenomenologically[61] and later validated rigorously by analytical means[23, 21] and experimental observation[46].

Central to the success of Biot's model is its predictive nature in a wide range of applications. Petroleum engineers extract oil by injection of fluids and are vitally interested in issues such as injectivity maintenance surface subsidence[61]. Studies on carbon sequestration and storage technology model the risks of leakage and fracture formation associated with carbon storage using poroelasticity theory[59]. Geotechnical engineers employ Biot's models to characterize soil properties and design appropriate foundations for various structures[67]. Seismologists use Biot's equations in conjunction with Mohr-Coulomb theory for fault activation and interaction studies[29, 30]. Soil scientists also develop irrigation and crop management strategies under the theory of poroelasticity. Hydrologists

Figure 1.1: Conceptually, one can observe poroelasticity through the time dependent effects of external loads applied to a wet, saturated sponge. As it is squeezed, it both deforms the solid material and induces fluid flow.

manage aquifers, water wells, and dams with the guidance of poroelasticity equations[22]. Biological applications include bone deformation[31] and soft tissue modeling[6].

Despite the existence of a number of *analytical* solutions[12, 11, 20, 16, 53, 10] for specific cases, Biot's poroelasticity equations have no closed form analytical solution in the general case. Philips[61] specifies three specific cases of particular importance which have analytical solutions:

- *Terzaghi's Problem*[28]: A one dimensional consolidation problem closely validated against experimental results and whose analytical series solution was obtained by Biot[16]

- *Mandel's Problem*[53]: A two dimensional problem involving a saturated porous media squeezed between two rigid plates. Its solution illustrates a temporary increase in pore pressures above those produced by the initial loading. This is known as the "Mandel-Creyer" effect and its existence demonstrates the importance of time dependent coupling between flow and deformation.

- *Barry & Mercer's Problem*[10]: A problem involving an oscillating point source/sink term which artificially mimics an injection/production process common in petroleum reservoir simulation. Boundary conditions are specifically chosen to produce an analytical solution.

In contrast, a number of numerical methods have been developed. Zenisek[75] and Showalter [69] characterized the existence and uniqueness of weak and strong solutions of Biot's equations, respectively. Showalter [69] further demonstrated that the partial differential equations in biot's equations essentially form a parabolic system[61]. Finite Element Methods [74, 62, 63, 64, 49, 78, 77] are by far the most commonly used approach to solving these equations, with mixed finite element methods being the most ubiquitous among them. Extensive analysis of various one dimensional finite difference methods [43, 41, 44, 42, 2] shows that the use of staggered grids for displacement and pressure leads to greater numerical stability. The recent work of Naumovich[58] extends the Marker & Cell grid method of Gaspar [42] into a generalized 3D finite volume method with staggered control volumes. More recent efforts emphasize operator splitting methods[49, 39] to enable legacy code reuse.

1.2 The Problem

One key phenomenon not addressed by conventional numerical methods for poroelasticity is the existence of heterogeneous material properties in natural porous media. The standard Biot model of poroelasticity assumes relatively homogenous material properties such that elastic moduli and permeabilities are either constant or slowly varying. In various applications[48, 8, 68, 5], spatial distributions of permeability and elastic moduli vary significantly at scales significantly smaller than the typical modeling domain of interest. For example, oil reservoirs require simulations on domains on the order of kilometers while the fundamental scale of heterogeneity in permeability may be millimeters or less[45]. Soils mixtures comprised of organic and inorganic solids and varying grain sizes also oscillate

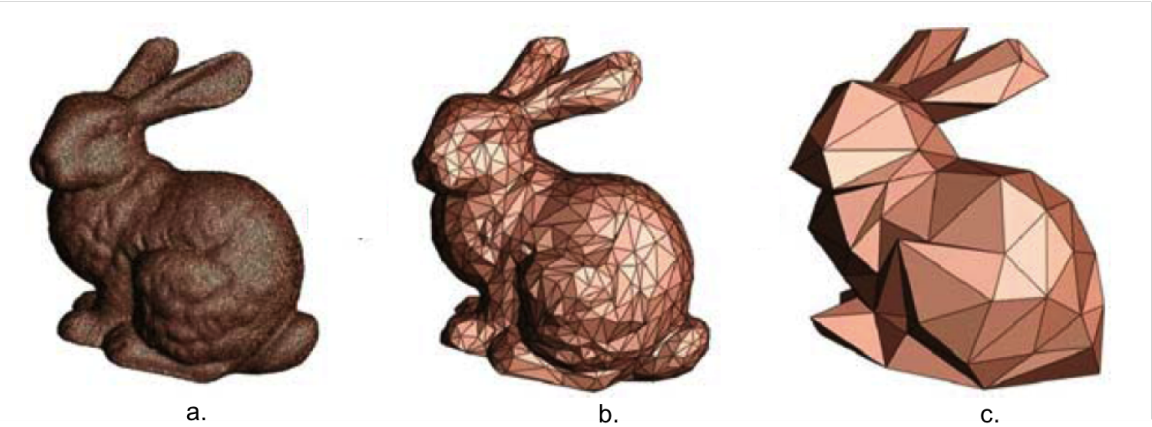

Figure 1.2: Modeling highly heterogeneous materials using continuum scale discretization produces a trade-off between efficiency and accuracy. (a) Highly accurate models are too detailed to yield computationally tractable solutions. (c) Tractable, efficient solutions are highly inaccurate. (b) Multiscale models balance the need for accuracy and efficiency

tremendously in terms of elastic modulus and permeability. The ubiquitious presence of natural fractures further complicates the distribution of stiffnesses in subsurface formations[9].

The distribution of large contrasts in both permeability and stiffness over small spatial scales complicated numerical simulation result in large relative errors when numerical discretization h in space is larger than the scale of heterogeneity ϵ [4]. Consequently, highly accurate poroelasticity simulation results are computationally expensive or intractable by conventional discretization methods.

Multiscale methods emerged from the need to address heterogeneity while balancing the competing needs for accuracy and efficiency. They can be broadly classified in one of two strategies: Upscaling and Divide & Conquer. Upscaling methods attempt to replace the fine scale problem with an effective coarse scale description by means of an averaging process[60]; typically either volume averaging or asymptotic homogenization. Divide & Conquer methods aim to decompose the fine scale problem into many small subproblems; each of whose solution is easily computed.

Both multiscale approaches have advantages and disadvantages. Upscaling methods are

widely applicable to many various partial differential equation models, including poroelasticity[14]. They are highly accurate under certain assumptions such as periodicity or isotropy. For general heterogeneous materials, these assumptions may not be valid and upscaling can lead to high relative errors. On the other hand, Divide & Conquer methods handle general heterogeneity with more accuracy but must be tailored to a specific problem or model in question.

A brief survey on multiscale literature reveals that a large body multiscale methods apply to elliptic PDE's with a single dependent variable[25]. Multiscale methods for coupled problems is an active area of contemporary research. As far as the current author is aware, no known Divide & Conquer methods directly address heterogeneity in Biot's poroelasticity equations.

1.3 The Proposed Solution

Motivated by Kim[49]'s recent work on legacy code reuse in poroelasticity, the current thesis proposes a method which decomposes the multiscale poroelasticity equations into a sequence of elliptic partial differential equations sufficiently general to capitalize on the ample algorithms available for multiscale elliptic PDE's. This method is based on block operator splittings of the poroelasticity equations based on fixed point iterations. The resulting formulation is a pair of continuous elliptic PDE subproblems with multiscale coefficients. In this formulation, any applicable multiscale algorithm can be applied to solve the resulting flow and deformation equations separately. The current thesis also proposes an extension to an existing heterogeneous multiscale algorithm to solve both the deformation and flow under a common framework.

The current thesis proposes both the block operator splitting method and the multiscale method and presents preliminary analysis of both methods. We test the convergence of the operator splitting method under various material property contrasts and develop a heuristic convergence criterion. For the multiscale method, we first verify a method developed by

Chu et al. (2012)[27, 26] for fluid flow in porous media. Two extensions of this method to solve the the fluid flow and deformation problems in our operator splitting method are also proposed. Numerical experiments are conducted to assess its convergence.

Chapter 2

Literature Review

2.1 Poroelasticity

Central to Biot's formulation are three key assumptions: quasi-static deformation, Terzaghi's Principle, and Increment in Fluid Content η. The quasi-static deformation assumption refers to the idea that we typically neglect temporal derivative terms in the linear elasticity equations, but not in the fluid flow equations. This is because the solid phase of a porous medium usually deforms at significantly slower rates than the fluid flow such that at any one instant in time, the solid equation is in a steady state. Terzaghi's Principle and Increment in Fluid Content are constitutive assumptions made to modify the traditional solid and fluid mechanics equations to account for coupling between the separate physics.

In this section, we summarize the mathematical equations governing poroelastic deformation with careful attention to the relevant conservation laws and coupling parameters.

2.1.1 Solid Deformation

For any open subset V of a solid domain Ω, the total stress σ_{total} acting on the surface ∂V is in opposition to the body forces f internal to V in an equilibrium state. Mathematically, this is written as

$$-\int_{\partial V} \sigma_{total} \cdot \vec{n} dA = \int_V f dV$$

where $\vec{n}$ is the unit outward normal vector. By divergence theorem, we can rewrite this

equation as

$$-\int_{\partial V} \nabla \cdot \sigma_{total} dV = \int_V f dV. \tag{2.1}$$

Since 2.1 is true for any arbitrary volume $V \subseteq \Omega$, we can omit the integrals, leaving the momentum equation

$$-\nabla \cdot \sigma_{total} = f \tag{2.2}$$

In traditional solid mechanics, σ_{total} is a function of solid strain $\epsilon = \left(\nabla u + \nabla u^T\right)$ only, where the solid displacement u is independent of time. In deformable porous media, stress u is generally a function of both time and space, leading to temporal changes in σ_{total} given through fluid coupling.

More importantly, the constitutive relation for porous media must be modified to account for both solid strain ϵ and fluid effects. The appropriate constitutive relation is given by Terzaghi's Principle. Terzaghi [70] was the first to illustrate that fluids bear significant loads in porous media, rendering the traditional constitutive relation for solids invalid for porous media. In the one dimensional case, the total measurable stress σ_{total} in a porous medium decreases with increasing pore pressure P, resulting in the relation

$$\sigma_{total} = \sigma_{eff} - p$$

where the effective solid stress σ_{eff} is a function of the strain ϵ. Inspired by similar formulations in thermoelasticity, Biot & Willis [16, 19] extended Terzaghi's principle into multiple dimensions using a symmetric deviatoric stress tensor and by introducing a dimensionless factor $\alpha \in [0, 1]$ to account for the strength of the coupling between flow and deformation, yielding the relation

$$\sigma_{total} = \sigma_{eff} - \alpha p I. \tag{2.3}$$

where I is the identity tensor. The factor α effectively captures the limiting behavior for various media, with $\alpha \to 0$ for porous media with rigid solid skeletons and $\alpha \to 1$ for unconsolidated (easily deformable) porous media.

Rice & Cleary[66] reformulated the constitutive relation 2.3 to relate bulk moduli to characterize experimentally observed short and long term behaviors. The short term or *undrained* behavior is characterized by initial no flow conditions under applied loads. The long-term or *drained* behavior is characterized by release of fluid under constant pore pressure conditions. We note that Rice & Cleary's formulation is widely adopted in the geophysical community, while Biot-Willis's formulation is commonly used in the mathematical community.

In the current study, we use the Biot-Willis formulation of the constitutive relation with the standard linear stress-strain relation for effective solid stress. Following [62, 63, 64, 69] we assume the linear solid stress-strain relation

$$\sigma_{eff} = \lambda tr(\epsilon) + 2\mu\epsilon \tag{2.4}$$

with

$$\epsilon \equiv \left(\nabla u + \nabla u^T\right). \tag{2.5}$$

Substituting Eqs. 2.3, 2.4 and 2.5 into 2.2, we obtain the solid deformation equation

$$-\left(\lambda + \mu\right)\nabla(\nabla \cdot u) - \mu\nabla^2 u + \alpha\nabla p = f \text{ in } \Omega \tag{2.6}$$

As stated earlier, the solid displacement u must necessarily be a function of both space and time with temporal variation obtained from interaction with fluid flow. In the next section, we derive the coupled fluid flow equations.

2.1.2 Fluid Flow

For fluid flows at sufficiently low reynolds numbers, we can neglect momentum effects and use mass conservation alone to model the flow. For any arbitrary volume[1] $V \subseteq \Omega$, the total rate of change of density ρ is the sum of fluid sources g internal to volume V minus the

[1]In this case, V is an open subset of Ω.

total mass ejected through the boundary. Mathematically, we write

$$\frac{\partial}{\partial t}\int_V \rho = \int_V g - \int_{\partial V} (v\rho)\cdot n$$

where n is the unit normal to the surface ∂V. Applying divergence theorem, we obtain

$$\frac{\partial}{\partial t}\int_V \rho = \int_V g - \int_V (\nabla \cdot v\rho).$$

As with the deformation equation, since the equation above is true for any arbitrary $V \subseteq \Omega$, we can omit the integrals and write

$$\frac{\partial \rho}{\partial t} = g - (\nabla \cdot (v\rho)).$$

Under the appropriate assumptions [2], fluid discharge velocity v in porous media is linearly proportional to head h, yielding the so-called Darcy's Law[32]

$$v = \frac{k}{\mu_f}\nabla h$$

where μ_f is the fluid viscosity, and k is the permeability tensor. The term $h = \nabla p + \rho g z$, where p is the fluid pressure, and $\rho g z$ denotes the gravitational flow potential at height z above some given datum. Neglecting gravitational effects, it is henceforth assumed $h = \nabla p$. Substituting Darcy's law into the mass conservation law, we obtain the fluid flow equation

$$\frac{\partial \rho}{\partial t} = -\nabla \cdot \left(\frac{\rho k}{\mu}\nabla p\right) = g \tag{2.7}$$

We note that Darcy's law is only valid under the assumption of negligible deformation of the solid skeleton in porous media. When consolidation processes deform significant volume fractions in porous media, Darcy's law alone is not enough to characterize fluid flow. Terzaghi [70] observed that after initial loading, fluid pressure obeys parabolic diffusion in the one dimensional case. He proposed the consolidation law

$$c_0 \frac{\partial P}{dt} = k\frac{\partial^2 P}{\partial z^2}$$

[2] Steady state, incompressible, single phase laminar, newtonian flow at low reynolds numbers $Re < 10$ in rigid porous media.

where k is positive and c_0 is the non-negative specific constrained storage coefficient. Note that Terzagi's equation only accounts for fluid effects and does not account for solid-fluid interaction effects.

While Biot [16] was not the first to extend Terzaghi's equation to higher dimensions, he was the first to successfully derive equations for the dynamic interaction fluid pressure and solid deformation. We follow the mixed stiffness formulation[71] of Biot's equations which implicitly assumes that the fluid density ρ in continuity equation 2.7 is scaled by the dimensionless *increment in fluid content* η. Thus, we obtain

$$\frac{\partial(\rho\eta)}{\partial t} = -\nabla \cdot \left(\frac{\rho k}{\mu}\nabla p\right) = g \tag{2.8}$$

We note that η is conceptually similar to *strain* in solid mechanics [37]. Where strain ϵ quantifies changes in length per unit length, increment in fluid content η quantifies the change in fluid volume (from a reference volume) per unit bulk volume[16]. Like strain, the variable η can take on both positive and negative values denoting expansion and contraction conditions, respectively. For incompressible fluids, ρ is a constant and thus can be factored out of all derivative terms in 2.8. In this setting, η can also be interpreted as the increment in porosity per bulk volume. Dividing from both sides of 2.8 by ρ, we obtain

$$\frac{\partial(\eta)}{\partial t} = -\nabla \cdot \left(\frac{k}{\mu}\nabla p\right) = \tilde{g} \tag{2.9}$$

where $\tilde{g}$ is now interpreted as a volumetric source term.

The fundamental assumption in Biot theory[71] is that increment in fluid content η can be modeled as a linear combination of both fluid pressure and volumetric strain $\epsilon_v \equiv \nabla \cdot u$; i.e.

$$\eta = a_1 p + a_2 \epsilon_v. \tag{2.10}$$

The parameters a_1 and a_2 capture the limiting behavior in porous media. Coefficient a_1 is the rate of change in fluid content η per unit pressure under constant strain conditions, i.e. the specific constrained storage coefficient c_0. The other coefficient $a_2 \equiv \alpha$ is the rate of change in fluid content η per unit strain under constant pressure conditions. Under the

assumption of reciprocity[71, 16], it can be shown that the volume of fluid ejected by an increase in compressive stress under constant pressure conditions is equal to the volumetric expansion due to fluid pressure increase. Hence, the coefficient a_2 must necessarily be equivalent to the Biot-Willis coefficient α found in equation 2.3. Defining $\epsilon_v \equiv \nabla \cdot u$, we can write equation 2.10

$$\eta = c_0 p + \alpha \nabla \cdot u. \tag{2.11}$$

Substituting 2.11 into the modified continuity equation 2.9, we obtain the fluid equation

$$\frac{\partial}{\partial t}\left(c_0 p + \alpha \nabla \cdot u\right) = -\nabla \cdot \left(\frac{k}{\mu}\nabla p\right) = \tilde{g} \tag{2.12}$$

Paring Eqs 2.12 and 2.6, we arrive at the coupled partial differential equations

$$-\left(\lambda + \mu\right)\nabla(\nabla \cdot u) - \mu\nabla^2 u + \alpha\nabla p = f \text{ in } \Omega \tag{2.13}$$

$$\frac{d}{dt}\left(c_0 p + \alpha \nabla \cdot u\right) - \frac{1}{\mu_f}\nabla \cdot (K\nabla p) = h \text{ in } \Omega \tag{2.14}$$

with mixed boundary conditions

$$\begin{aligned} p &= p^*(x) \quad \text{on } \partial\Omega_p \\ \frac{1}{\mu_f}\nabla \cdot (K(x)\nabla p) \cdot n &= q \text{ on } \partial\Omega_f \\ u &= u^*(x) \quad \text{on } \partial\Omega_d \\ \sigma \cdot n &= t_N \text{ on } \partial\Omega_t. \end{aligned}$$

Here, the boundaries $\partial\Omega_p$, $\partial\Omega_f$, $\partial\Omega_d$, $\partial\Omega_t$ refer to the portions of the boundary with fixed pressure, flux, displacement, and traction conditions. Note that Eqs 2.13- 2.14 are fully coupled in pore pressure p and displacement u through the time derivative of fluid content $(c_0 p + \alpha \nabla \cdot u)$.

Since 2.13- 2.14 are time dependent, the system also requires an initial condition $[u(0, x), p(0, x)]^T$. According to [37], the initial condition cannot be chosen arbitrarily and must satisfy certain constraints. In [43], the initial condition is chosen such that the initial increment in fluid content η is zero so that the fluid phase is ejected with finite velocity. Hence, we impose the condition

$$c_0 p + \alpha \nabla \cdot u = 0.$$

at $t = 0$. According to [61], this condition is usually combined with the static equilibrium condition in solid equation 2.13 to produce a unique initial condition.

In the asymptotic limit $t \to \infty$, the rate of change in fluid content is zero; yielding the *steady state* poroelasticity equations

$$-(\lambda + \mu)\nabla(\nabla \cdot u) - \mu \nabla^2 u + \alpha \nabla p = f \text{ in } \Omega \tag{2.15}$$

$$-\frac{1}{\mu_f} \nabla \cdot k(x)(\nabla p - \rho_f g) = h \text{ in } \Omega \tag{2.16}$$

Since 2.16 is independent of displacement u, the steady state case is a *one way* coupled system of elliptic partial differential equations. This formulation has been successfully applied to estimate heterogeneities in permeabilities over large scale basins in California[3].

2.2 Multiscale Modeling

Classical continuum scale models, such as Biot's Poroelasticity Model, implicitly assume homogeneous material properties such that macroscopic constitutive laws are sufficient to predict the overall behavior of the system. When materials properties are highly heterogeneous, macroscopic constitutive relations are often unknown explicitly or require discretization at scales much smaller than is computationally expedient. The most obvious approach to treat heterogeneity is through Direct Numerical Simulation (DNS); whereby the resolution of the spatial discretization h must necessarily be smaller than the scale of the heterogeneity ϵ. Generally, the domain of interest is many orders of magnitudes larger than the scale of heterogeneity. Of course, this results in time consuming simulations which even the fastest supercomputers on earth cannot handle.

Multiscale modeling emerges from the necessity to balance the two mutually opposing modeling needs that neither macroscopic simulation or direct numerical simulation

can address: detail and efficiency. Multiscale methods can be broadly classified into two categories: Upscaling and Divide & Conquer methods[4]

2.2.1 Upscaling Methods

Upscaling methods replace the heterogeneous material properties in the system by effective macroscopic parameters. Thus, the system is resolved only on the macroscopic grid. Volume Averaging and Asymptotic Homogenization are classical examples of upscaling methods.

In Volume Averaging, the heterogeneous, spatially varying material property $\psi(x)$ at a discrete point x_i of the macroscopic grid is replaced by

$$\bar{\psi}(x_i) = \frac{1}{||V_{x_i}||} \int_{V_{x_i}} \psi(x) dV$$

where V_{x_i} is a window encompassing the point x_i with volume $||V_{x_i}||$. The locally average quantities $\bar{\psi}(x_i)$ can be reduced to a scalar quantity by arithmetic or harmonic average as necessary. Volume Averaging is both intuitive to understand and easy to implement but is insufficient to treat anisotropy or nonlinearities [4].

Homogenization methods treat heterogeneous material properties a_ϵ as a locally periodic quantity that varies in both a slow (x) and fast (y) variable. In the limit as the scale $\epsilon \to 0$, the oscillations are removed but their coarse scale effects remain. Asymptotic homogenization is based upon the power series expansion

$$u_\epsilon(x) = u_0(x, y) + \epsilon u_1(x, y) + \epsilon^2 u_2(x, y) + ...$$

where $u_i(x, y)$ are unknown periodic functions in $y = \frac{x}{y}$. It is expected that $u_\epsilon \to u_0$ as $\epsilon \to 0$. For elliptic partial differential equations of the form

$$-\nabla \cdot (a_\epsilon(x, y) \nabla u(x, y)) = f,$$

we substitute the scaled gradient

$$\nabla \equiv \nabla_x + \frac{1}{\epsilon} \nabla y$$

and the ansatz $u_\epsilon(x)$ into the partial differential equations of the system. Equating like coefficients of ϵ on both sides of the resulting equation, we observe the following:

1. $u_0(x, y)$ is necessarily only a function of the slow variable x. Thus, we write $u_0(x, y) = u_0(x)$.

2. $u_1 = \sum_j \omega_j(x, y)\partial_j u_0(x)$ where ω_j solve locally defined cell problems of the form

$$\nabla_y \cdot [a_\epsilon(x, y)\nabla_y \omega_j(x, y)] = \nabla_y \cdot [a(x, y)e_j] \text{ in } \Omega$$

   where ω_j is periodic in y.

3. The original PDE is replaced by the equation

$$\nabla \cdot [a_0 \nabla u_0] = f$$

   where the coefficients of the effective tensor a_0 are given as

$$(a_0)_{ij} = \frac{1}{||Y||} \int_Y a(x, y) \left(\partial_i^y \omega_j(x, y) + \delta_{ij}\right) dy$$

   where Y and $||Y||$ are the local cell domain and volume, respectively.

Asymptotic Homogenization is mathematically rigorous in terms of convergence theory and accuracy, but also has drawbacks. Though the effective coefficient a_0 is obtained from microstructure, the u_0 alone lacks microstructure. $u_0 \not\approx u_\epsilon$. Intuition suggests that since term u_1 contains microstucture information, it could be combined with u_0 to provide a more accurate solution. However, the introduction of u_1 can fail to satisfy local conservation principles[4]. More importantly, it is very difficult to derive a periodic $a(x, y)$ from a general heterogeneous material property $a_\epsilon(x)$. Where heterogeneity is randomly distributed throughout the medium, the periodicity assumption is invalid.

A recent survey of multiscale methods [14] suggests that heterogeneity in poroelasticity is generally resolved by upscaling, with volume averaging being the most common approach due to its relative simplicity in comparison to homogenization. The aforementioned limitations of upscaling approaches motivate the need to develop efficient numerical methods for

heterogeneous poroleastic media. Divide & Conquer type multiscale methods, in general, lend themselves more easily to adapt not only to heterogeneity, but anisotropy as well. For this reason, we focus the remainder of the current thesis on developing a framework for a Divide & Conquer type multiscale method for heterogeneous poroelastic media.

2.2.2 Divide & Conquer Methods

Divide & Conquer methods decompose the macroscopic problem into many small coarse scale subproblems. Within each subproblem, a local solution is obtained by treating the the small scale heterogeneity directly. The local solutions are then coupled to the macroscopic problem and resolved at larger scales. The objective of these methods is to solve a coarse scale problem at a resolution h larger than the scale of heterogeneity ϵ by solving individual subproblems at subresolutions h_{sub} smaller than the scale of heterogeneity ϵ. Multiscale Finite Element/Variational Methods (MSFEM, MSVM), Mortar Methods (MMM) and the Heterogeneous Multiscale Method (HMM) are all examples of the Divide & Conquer strategy and all share a common framework:

1. **Localization**: Decomposition of the domain into coarse elements of scale h such that $h > \epsilon$.

2. **Solution of Subproblems**: Local subproblems are assigned appropriate boundary conditions and solved at a scale h_{sub} such that $h_{sub} < \epsilon$

3. **Coarse-Grid Coupling**: Solutions of local subproblems are used to assemble and solve the problem on the coarse grid of scale h.

One important component of multiscale methods which distinguish it from traditional domain decomposition methods is the notion of *subsampling*. That is, an *efficient* multiscale method never fully coupled to all the scale details, but rather samples the fine scale details in such a way to reduce degrees of freedom while preserving accuracy. Thus, not only

should the coarse grid problem be efficiently solved, but each subproblem must be easily solved with fewer details than traditional domain decomposition methods.

A survey of divide & conquer multiscale methods [72] indicates that a vast majority of multiscale methods apply to single physics simulations (i.e. fluid flow only, solid deformation only, etc.). In the case of poroelasticity, upscaling is the predominant method[14, 54, 36, 24, 51]. Azevedo et al.[7] used statistical scaling relations coupled to a macroscale finite element discretization within a monte carlo algorithm to extract probable effects of fluid injection and extraction. Ladeveze & Nouy[51] employ spatiotemporal homogenization within the so-called LATIN framework. As far as the current author is aware, no domain decomposition methods have been devised specifically for coupled flow and deformation processes in porous media.

The current work follows the Divide & Conquer strategy known as the Heterogeneous Multiscale Framework, which we briefly summarize below.

2.2.3 Heterogeneous Multiscale Method

As described by Weinan E[72], the Heterogeneous Multiscale method is a framework of different methods consisting of an incomplete macroscopic description of the systems behavior whose missing data is supplemented by microscopic simulation. The general methodology consists of four main components:

1. Macroscopic solver - an effective macroscopic description of the systems behavior, often consisting of an incomplete conservation equation and boundary/initial conditions.

2. Restriction operator - a method which projects state variables from the macroscopic domain to local microscopic subdomains, often in the form of boundary and/or initial conditions

3. Microscopic solver - an effective microscopic description of the system behavior, often

consisting of conservation and micro-constitutive relations whose boundary conditions are obtained by the restriction operator.

4. Data Estimator - an effective equation which predicts the data needed to complete the macroscopic conservation equation from local microscopic simulation

2.2.4 Chu et. al.'s Model

The current work is based on a heterogeneous multiscale method for flow in porous media based on Chu et al.[27, 26] with the following components:

1. Macroscopic solver: Finite Volume Method
2. Restriction operator: Linear interpolation
3. Microscopic solver: Direct Stiffness method (pore network models)
4. Data Estimator: Cross-sectional Flux summation

In the following sections, we describe their method in detail.

Microscale Model

The microscale model is a discretization of the void space within a porous medium into a network of cylindrical pipes (throats) and spherical chambers (pores) [38]. In this context, the network forms a discrete graph of nodes and edges, known as a Pore Network (PN) Model. The topology of the network can be structured or unstructured, as needed to model a particular porous medium. Figure 1 illustrates a structured network with constant throat lengths.

For incompressible fluids, imposing mass conservation at each pore i results in conser-

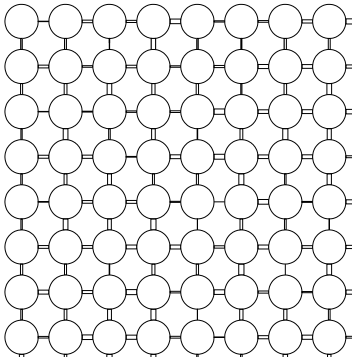

Figure 2.1: A structured 8x8 microscale network model with constant pore size and random throat radii.

vation of volumetric flux given by

$$\sum_{j \in K_i} q_{ij} = s_i \tag{2.17}$$

$$q_{ij} = g_{ij}(\Delta P_{ij}) \tag{2.18}$$

where q_{ij} represents the volumetric flow rate from pore i to pore j, K_i denotes the set of all pores connected to pore i, and g_{ij} is the hydraulic conductance, which is a function of the pressure difference ΔP_{ij} between pores i and j, and s_i is an internal volumetric source term. In the laminar newtonian flow case, the function g_{ij} is given by the linear Hagen-Poisseuille relation:

$$g_{ij}(\nabla P_{ij}) = \frac{\pi r_{ij}^4}{8\mu L_{ij}} \nabla P_{ij} \tag{2.19}$$

where r_{ij}, L_{ij}, and μ are the throat radii, throat lengths, and fluid viscosity, respectively. Though g_{ij} is presented as a linear function here, it may be a non-linear for other fluids or flow regimes.

The equations given by (1), (2), and (3) result in the linear system:

$$[C]p = b \tag{2.20}$$

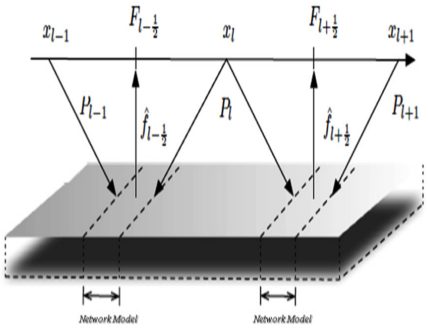

Figure 2.2: Macroscale-microscale model coupling, adapted from [27, 26]

where C is the conductance matrix, p is the pressure, and b represents the vector containing boundary conditions. Typically, two opposite faces of the network model are defined as the axial boundaries with dirichlet conditions. The remaining boundary faces in the network model are defined as the transverse boundaries. Periodic conditions are imposed on the transverse boundaries for strongly isotropic materials, but alternative boundary conditions have been developed for anisotropic conditions[27, 26].

Macroscopic Model

At the continuum scale, the mass conservation principle for incompressible fluids is governed by

$$\nabla \cdot v = S(x) \tag{2.21}$$

where v is the bulk flow velocity and S represents source/sink terms. The standard Darcy model of fluid flow assumes $v = \kappa \nabla P$, where P and κ are the macroscopic pressure and permeability, respectively. The current study follows [27, 26] by assuming no explicit form of v. Instead, v is implicitly assumed as a function of position, pressure and pressure gradient. That is, $v = v(x, P, \nabla P)$.

The Finite Volume (FV) discretization of (4) results in dual grids representing the macroscopic pressures and fluxes of representative control volumes as seen in Figure 2.

The divergence theorem[3] applied to the one dimensional discretization of (3) results in:

$$F_{i+\frac{1}{2}} - F_{i-\frac{1}{2}} = S(x_i)\Delta x \tag{2.22}$$

where $F_{i+\frac{1}{2}}$ represents the volumetric flux through the boundaries of the control volumes.

Iterative Coupling Algorithm

The key to coupling the two models above is a reformulation of the macroscopic flux in terms of both microscopic flux *and* macroscopic pressure. In [27, 26] , the coupling is achieved primarily through the assumption that $F = 0$ when ∇P=0. In the one dimensional case where ∇P is a scalar quantity, the mean value theorem implies that there exists ξ such that

$$\frac{F(x, P, \xi)}{d\nabla P} = \frac{F(x, P, \nabla P) - F(x, P, 0)}{\nabla P - 0} \tag{2.23}$$

or equivalently

$$F(x, P, \nabla P) = \frac{F(x, P, \xi)}{d\nabla P}\nabla P \tag{2.24}$$

where ξ is between 0 and ∇P. We note that the macroscopic model requires the evaluation of the flux F at the point $x_{i+\frac{1}{2}}$. Thus, the quantity $\frac{dF(x_{i+\frac{1}{2}}, P, \xi)}{d\nabla P}$ is estimated as

$$\frac{dF(x_{i+\frac{1}{2}}, P, \xi)}{d\nabla P} \approx \frac{F_{i+\frac{1}{2}}(x_{i+\frac{1}{2}}, P, \nabla P) - F_{i+\frac{1}{2}}(x_{i+\frac{1}{2}}, P, 0)}{\nabla P - 0} = \frac{F_{i+\frac{1}{2}}(x_{i+\frac{1}{2}}, P, \nabla P)}{\nabla P} \tag{2.25}$$

with $\nabla P \approx \frac{P^R_{i+\frac{1}{2}} - P^L_{i+\frac{1}{2}}}{\delta}$, where $P^R_{i+\frac{1}{2}}$ and $P^L_{i+\frac{1}{2}}$ are the interpolated dirichlet boundary conditions on the network model centered at $x_{i+\frac{1}{2}}$ with length δ. Assuming linear interpolation of the boundary conditions from the macroscopic pressure values, we replace $\nabla P \approx \frac{P^R_{i+\frac{1}{2}} - P^L_{i+\frac{1}{2}}}{\delta}$ by the discrete forward difference operator $D^+[P_i] \equiv \frac{P_{i+1} - P_i}{\Delta x}$. Hence, we can define an effective macroscopic coefficient $K_{i+\frac{1}{2}}$ as

$$-K_{i+\frac{1}{2}}(P_i, P_{i+1}) \equiv \frac{F_{i+\frac{1}{2}}(x_{i+\frac{1}{2}}, P, \nabla P)}{D^+[P_i]}$$

[3]See [27, 26] for higher dimensional schemes.

and

$$F_{i+\frac{1}{2}}(x_{i+\frac{1}{2}}, P_i, P_{i+1}) = -K_{i+\frac{1}{2}}(P_i, P_{i+1})D[P_i] \tag{2.26}$$

where $D[\cdot]$ is a difference operator and $K_{i+\frac{1}{2}}$.

Substituting $F_{i+\frac{1}{2}}$ into the macroscopic equation 2.22, we obtain

$$D\left[\frac{f_{i+\frac{1}{2}}(P_i, P_{i+1})}{D^+[P_i]}D[P_i]\right] = S_i \tag{2.27}$$

We note that the formulation 2.27 is sufficiently general enough to handle both linear and non-linear fluxes. Hence, 2.27 is, in general a system of non-linear equations which can be solved by fixed point iteration[4] or by quasi-newton methods [27, 26]. Hence, the iteratively coupled multiscale model is linearized as:

$$D^-\left[\frac{f\left(P_i^{(n)}, P_{i+1}^{(n)}\right)}{D^+[P_i^{(n)}]}D^+[P_i^{(n+1)}]\right] = S_i \tag{2.28}$$

$$[C_{i+\frac{1}{2}}]p_{i+\frac{1}{2}} = b_{i+\frac{1}{2}} \text{ for } i = 0, ..., n. \tag{2.29}$$

The algorithm iterates between micro and macro scale models until some convergence criteria is satisfied. In [27, 26], Chu et. al. prove this multiscale system has analogous convergence rates as multiscale homogenization in the linear case. We note that the formulation presented is independent of the linearity assumptions on the velocity. Chu et al. proceed to demonstrate this model's applicability to non-linear constitutive relations at the microscale in [27, 26].

2.3 Operator Splitting

Poroelasticity falls into the broader category of coupled multiphysics problems defined by systems of partial differential equations describing the interaction between two or more field variables. Multiphysics problems differ from general mixed PDE formulations in that

[4]Convergence of the fixed point iteration from any starting value is established in [27, 26]

"neither domain can be solved separately from each other [and] neither set of dependent variables can be explicitly eliminated" [76]. Coupled problems are further classified into two categories based on the degree of domain overlap where the state variables are defined[78].

Type I problems (also known as Interfacial Problems) are characterized by systems of equations whose dependent variables lie on separate, non-overlapping domains and with interaction occurring solely through domain interfaces. Fluid-structure interaction is a typical Type I problem where the interface divides the regions where the distinct media and their governing partial differential equations are valid. As they are dynamic problems, interfacial displacement is tracked through additional time dependent mesh variables and equations into Type I systems. Kumar [50] characterized discretized systems of equations for fluid-structure interaction in terms of dynamic structure u_s, mesh u_m, and fluid u_f variables. The system of equations is summarized as

$$\begin{cases} \vec{N_s}(u_s, u_m, u_f) = 0 \\ \vec{N_m}(u_s, u_m, u_f) = 0 \\ \vec{N_f}(u_s, u_m, u_f) = 0 \end{cases} \tag{2.30}$$

where $\vec{N_s}$, $\vec{N_m}$, and $\vec{N_f}$ are the (typically non-linear) equations governing the structure u_s, mesh u_m, and fluid u_f variables, respectively.

Type II problems (also known as Overlapping Problems) are those systems whose dependent variables lie on partially or totally overlapping domains. Thermo-structure interaction is a typical Type II problem where the state variables of temperature, stress, and strain interact within the same medium. In contrast to Type I problems, Type II problems do not require additional terms to account for dynamic mesh displacement, even when the coupling is strong. In the context of fluid-solid coupling, equations 2.30 reduce to the simplified form:

$$\begin{cases} \vec{N_s}(u_s, u_f) = 0 \\ \vec{N_f}(u_s, u_m, u_f) = 0 \end{cases}$$

After temporal and spatial discretization, Biot's poroelasticity equations 2.13-2.14 form a saddle point system of the form:

$$\begin{bmatrix} A & B^T \\ B & -C \end{bmatrix} \begin{bmatrix} u \\ p \end{bmatrix}^{t+1} = \begin{bmatrix} f \\ g \end{bmatrix}^{t+1} \tag{2.31}$$

at each timestep t, where A, B, C are symmetric positive definite. Matrix systems of this form are saddle point problems whose spectrum contains both positive and negative eigenvalue[13].

2.3.1 Fractional Step Methods

The rationale behind operator splitting methods is that fully coupled time dependent dynamics can be decomposed into the superposition of the individual operators corresponding to separate physical processes, such as diffusion, advection, reaction, etc. Fractional splitting methods apply easily to hyperbolic differential equations of the form

$$y_t = (A + B)y \tag{2.32}$$

where A and B are differential operators. The various splitting methods resolve this ODE by solving a sequence of subproblems composed of each individual operator over a fixed number of iterations with or without predictor-corrector adjustments between each iteration. For example, Lie-Trotter Splitting is a first order accurate method requiring the solution of two subproblems alternately applying each operator within a single timestep:

$$\frac{y^* - y_t}{\Delta t} = Ay^t \tag{2.33}$$

$$\frac{y_{t+1} - y^*}{\Delta t} = By^* \tag{2.34}$$

Other methods, such as Strang Splitting, achieve higher order accuracy by advancing over partial timesteps between t and $t + 1$ while alternating between operators. In general, fractional step methods are not guaranteed to converge in a fixed number of iterations despite stable time-stepping discretization[49].

Poroelasticity equations cannot be converted into the form 2.32 except in the particular case where $c_0 \equiv 0$. In this case, Gaspar et al[40] showed that it can be transformed into

an alternative form which was amenable to a specialized fractional step method. The key to their work was the application of additional differential operators to the flow and deformation equations to eliminate certain terms in the equations. Introducing new variables for the pressure laplacian $q = -\Delta p$ and deformation velocity $v = \frac{du}{dt}$, they resolved the poroelasticity equations by solving a sequence of subproblems[5] within each timestep in the following order:

$$\frac{q^{t+1} - q^t}{\Delta t} - (\lambda + 2\mu)k\nabla^2 q^{t+1} = -(\lambda + 2\mu)\nabla^2 f^{t+1} \tag{2.35}$$

$$-\nabla^2 p^{t+1} = q^{t+1} \tag{2.36}$$

$$-\mu\nabla^2(\nabla \cdot v^{t+1}) + \nabla\left(\frac{p^{t+1} - p^t}{\Delta t}\right) + (\lambda + 2\mu)k\nabla q^{t+1} = (\lambda + \mu)\nabla f^{t+1} \tag{2.37}$$

In the general case where $c_0 \neq 0$ is not easily amenable to the above approach. The general quasi-static poroelasticity problem is denoted by

$$Au = 0 \text{ for deformation} \tag{2.38}$$

$$Bu_t + Cu = 0 \text{ for flow} \tag{2.39}$$

In this form, the problem cannot transformed into the canonical form established by 2.32. Consequently, alternative splitting methodologies have been developed.

2.3.2 Kim et al's work

Motivated by an industrial need to enable highly optimized legacy codes and solvers for individual flow and deformation equations, Kim[49] analyzed four operator splitting strategies for a non-linear formulation of the poroelasticity equations for multiphase flow & deformation. His approach decomposes the coupled system into solutions of single set of equations for flow or deformation at a time. When necessary, he used pressure and displacement predictor/corrector methods which impose the respective conservation principles.

[5]With appropriately adjusted boundary conditions and additional stabilization techniques.

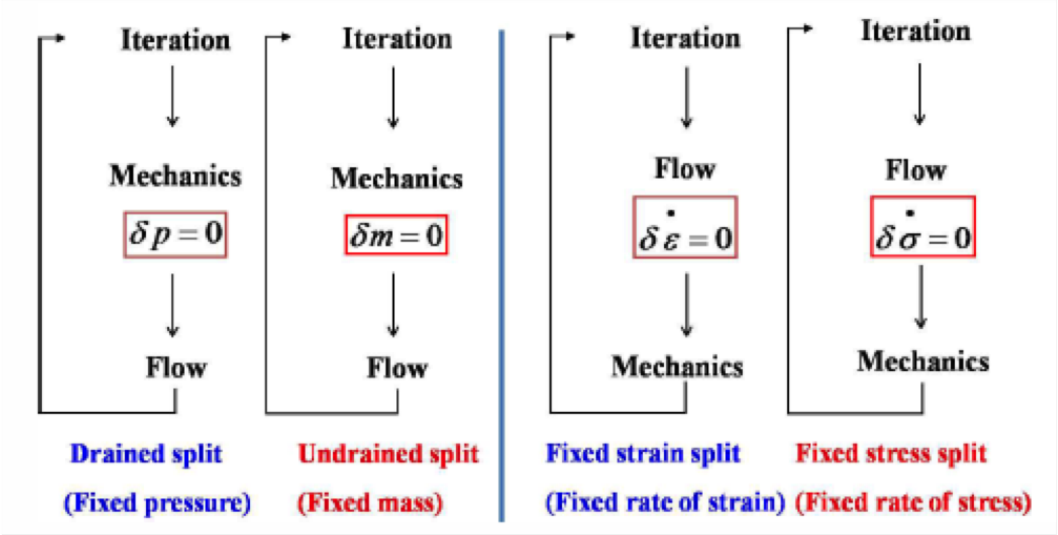

Figure 2.3: Visualization of the four operator splitting methods developed by Kim[49].

The Drained Splitting method solves the deformation problem first by holding the pressure constant and consequently solving fluid flow using the updated deformations. The Undrained Splitting method imposes constant fluid mass while the deformation equation is resolved, requiring an additional pressure correction. Fixed Strain Splitting method solves the flow equation first, holding the volumetric strain constant. The updated pressures are then used to resolve the deformation equation. Like the drained splitting method, no additional predictor/corrector is used to update the pressures. Finally, the fixed stress splitting method also resolves the fluid equation first, but holds the total mean rate of stress constant such that the volumetric stress is automatically computed.

Kim[49] derived stability criteria for the drained, undrained, fixed strain and fixed stress splittings as well as the fully coupled problem by Von Neumann Analysis. They noted that drained and fixed strain splittings (i.e. the methods which did not employ predictor-corrector adjustments) have a stability criterion related to the ratio of the bulk stiffnesses of the fluid and solid skeleton. On the other hand, the undrained, fixed stress, and fully coupled methods were unconditionally stable.

He further tested and verified their applications to four specific test cases including

Terzaghi's and Mandel's problem as mentioned in chapter 1. Furthermore, he observed that drained and fixed strain splittings were inconsistent if limited to a fixed number of iterations. That is, if not permitted to iterate until convergence, these two methods become inconsistent over time. Though both undrained and fixed stress splitting are unconditionally stable, fixed stress splitting required fewer iterations than undrained splittings for the cases tested. Furthermore, we note that Kim's stability work assumed constant parameter values which are not necessarily applicable to the variable coefficient case.

2.4 Previous Work

The current author proposed a one-dimensional model of quasi-static poroelasticity[35] based on an operator decomposition of the coupled PDE's and a generalized heterogeneous multiscale method using an incomplete macroscopic Finite Volume method supplemented by a microscopic direct stiffness network model. The method is summarized below

2.4.1 Iterative Splitting

We apply Rothe Semi-Discretization to equations 3.1-3.2 using Backward Euler time integration while leaving the spatial variable x as a continuous variable. This results in the implicit semi-discrete equations

$$-\frac{d}{dx}\left(\gamma(x)\frac{du^t}{dx}\right)+\alpha\frac{dp^t}{dx}=0, \tag{2.40}$$

$$\left(c_0\frac{p^t-p^{t-1}}{\Delta t}+\alpha\frac{\frac{du^t}{dx}-\frac{du^{t-1}}{dx}}{\Delta t}\right)-\frac{d}{dx}\left(K(x)\frac{dp^t}{dx}\right)=0, \tag{2.41}$$

where t is the discrete time step and Δt is the temporal increment. Note that all terms $t-1$ are known quantities in the tth timestep and thus can be treated as source terms.

Hence, we rewrite equations 3.10- 3.11 as

$$-\frac{d}{dx}\left(\gamma(x)\frac{du^t}{dx}\right)+\alpha\frac{dp^t}{dx}=0, \tag{2.42}$$

$$\left(c_0p^t+\alpha\frac{du^t}{dx}\right)-\frac{d}{dx}\left(\Delta tK(x)\frac{dp^t}{dx}\right)=R^{t-1}, \tag{2.43}$$

where

$$R^{t-1}=c_0p^{t-1}+\alpha\frac{du^{t-1}}{dx}.$$

Introducing new notation, we define four continuous linear operators A,G,D, and B as follows:

$$Au \equiv -\frac{d}{dx}\left(\gamma(x)\frac{du}{dx}\right) \tag{2.44}$$

$$Gp \equiv \alpha\frac{dp}{dx} \tag{2.45}$$

$$Du \equiv \alpha\frac{du}{dx} \tag{2.46}$$

$$Bp \equiv -\frac{d}{dx}\left(K(x)\frac{dp}{dx}\right)+c_0p \tag{2.47}$$

Then, we can rewrite equations 3.12- 3.13 in terms of a single linear system

$$Lv^t=b,$$

where

$$L\equiv\begin{bmatrix}A & G\\ D & B\end{bmatrix},\quad v^t\equiv\begin{bmatrix}u^t\\ p^t\end{bmatrix},\quad b\equiv\begin{bmatrix}0\\ R^{t-1}\end{bmatrix} \tag{2.48}$$

To uncouple these equations, we apply a method of successive approximations which resolve the current iterate $u^{t,n},p^{t,n}$ in terms of the previous iterate $u^{t,n-1},p^{t,n-1}$. In [35], we illustrate two such methods by decomposing L as the sum of two separate operators $L=M+N$. Substituting for L and applying fixed point iteration, we obtain a sequence of equations of the form

$$Mv^{t,n}+Nv^{t,n-1} = b. \tag{2.49}$$

The key to our approach is to determine a suitable choice of M that is invertible and leads to a contraction mapping[6]. In our case, the convergence strongly depends on the choice of the operator M. We introduce two such choices of M which we shall refer to as the **Block Jacobi** and **Block Gauss-Seidel** approaches. The Block Jacobi approach selects M as the block-diagonal operators of L with

$$M \equiv \begin{bmatrix} A & 0 \\ 0 & B \end{bmatrix}, \quad N \equiv \begin{bmatrix} 0 & G \\ D & 0 \end{bmatrix}. \tag{2.50}$$

This leads to the sequence of PDE's

$$-\frac{d}{dx}\left(\gamma(x)\frac{du^{t,n}}{dx}\right) = S_p^{t,n-1}, \tag{2.51}$$

$$-\frac{d}{dx}\left(\Delta t K(x)\frac{dp^{t,n}}{dx}\right) + c_0 p^{t,n} = S_u^{t,n-1} + R^{t-1}, \tag{2.52}$$

where

$$S_p^{t,n-1} \equiv \alpha\frac{dp^{t,n-1}}{dx} \text{ and } S_u^{t,n-1} \equiv \alpha\frac{du^{t,n-1}}{dx}.$$

Likewise, the Block Gauss-Seidel approach utilizes the block lower or upper triangular operators of L in M. The lower triangular case results in the sequence of PDE's

$$-\frac{d}{dx}\left(\gamma(x)\frac{du^{t,n}}{dx}\right) + \alpha\frac{dp^{t,n-1}}{dx} = 0, \tag{2.53}$$

$$\left(\frac{c_0}{\Delta t}p^{t,n} + \frac{\alpha}{\Delta t}\frac{du^{t,n}}{dx}\right) - \frac{d}{dx}\left(K(x)\frac{dp^{t,n}}{dx}\right) = R^{t-1}, \tag{2.54}$$

while the upper triangular case results in

$$-\frac{d}{dx}\left(\gamma(x)\frac{du^{t,n}}{dx}\right) + \alpha\frac{dp^{t,n}}{dx} = 0, \tag{2.55}$$

$$\left(\frac{c_0}{\Delta t}p^{t,n} + \frac{\alpha}{\Delta t}\frac{du^{t,n-1}}{dx}\right) - \frac{d}{dx}\left(K(x)\frac{dp^{t,n}}{dx}\right) = R^{t-1}. \tag{2.56}$$

[6]This is consequence of the Banach Fixed Point Theorem

Observe that Block Jacobi and both Block Gauss-Seidel methods result in a sequence of decoupled elliptic PDE's of the form

$$-\frac{d}{dx}\left(\gamma(x)\frac{du}{dx}\right) = f, \tag{2.57}$$

$$-\frac{d}{dx}\left(K(x)\frac{dp}{dx}\right) + \frac{c_0}{\Delta t}p = g \tag{2.58}$$

Note that the solid equation 3.31 is a pure diffusion equation while the fluid equation 3.32 is a reaction diffusion equation. Both of these equations contain a multiscale coefficient and require numerical methods to capture the heterogeneous material behavior in a computationally efficient manner. Next, we present a common methodology to resolve both sequences efficiently.

2.4.2 Heterogeneous Multiscale Method

We present a heterogeneous multiscale method[72] based on a macroscopic finite volume discretization and a microscopic direct stiffness method. We extend the approach pioneered in[27, 26] to handle the presence of the reaction term in equation3.32. We introduce the generalized problem

$$\nabla \cdot \Phi(x, \Psi, \nabla\Psi) + h(\Psi) = S(x) \tag{2.59}$$

where Φ denotes a unspecified function of a state variable Ψ[7]& its gradient $\nabla\Psi$, $S(x)$ denotes a source term, and $h(\Psi)$ is a linear function of the state variable. Note that the case with $h \equiv 0$ corresponds directly to the solid equation 3.31 and $h \equiv c_0 P$ corresponds to the fluid equation 3.32.

We subdivide the domain Ω into finitely many equispaced control volumes $B_i = [x_{i-\frac{1}{2}}, x_{i+\frac{1}{2}}]$ with discrete values of Ψ defined at the cell center x_i. Integrating equation 3.42 over each control volume B_i and applying the divergence theorem, we obtain an expression of the form

$$\hat{\Phi}_{i+\frac{1}{2}} - \hat{\Phi}_{i+\frac{1}{2}} + h(\Psi_i)\Delta x = \hat{F}_i \Delta x. \tag{2.60}$$

[7]The variable Ψ represents *displacement* in the solid equation 3.31 and *pressure* in the fluid equation 3.32.

where $\hat{\Phi}_{i+\frac{1}{2}} \equiv \Phi_{i+\frac{1}{2}} \Delta A$, with ΔA denoting the cross-sectional area of the control volume.

In its current form, equation 3.43 is incomplete because no explicit macroscopic constitutive relation is known or assumed for Φ. The missing information is therefore supplemented by estimates derived from microscopic simulations. At the microscopic scale, the fluids and solids occupy non-overlapping spaces and are modeled by a network of connected elements which obey a discrete conservation law. In the case of fluid flow, we use the analogy of a network of conductive pipes and chambers with flux conservation imposed at any given node[8]. In the case of solid deformation, we conceptualize a network of interconnected beam elements with equilibrium force balance imposed at all nodal points. In either, conservation is expressed as superposition of microscopic conserved quantities ϕ in terms of its corresponding microscopic state variable ψ. Assuming a microscopic spatial step size L, we write the microscopic conservation law as

$$\sum_{j \in K_l} \phi_{lj} + h(\psi_l) L = s_l L \tag{2.61}$$

$$\tag{2.62}$$

To complete the model, we require a relation between the microscopic conserved quantity ϕ and its corresponding state variable ψ. In our case, we choose the relation

$$\phi_{ij} = \frac{EA}{L} (\psi_i - \psi_j)$$

for the solid model and

$$\phi_{ij} = \frac{\pi r^4}{8 \mu L} (\psi_i - \psi_j)$$

for the fluid model.

The key to coupling the macro and micro models is a linearized flux assumption[27, 26] where

$$\hat{\Phi}(x, \Psi, \nabla \Psi) = 0 \text{ when } \nabla \Psi = 0.$$

[8] Under the assumption of incompressible fluids

. We use the taylor expansion of $\Phi(x, \Psi, \nabla\Psi)$ in terms of the third argument $\nabla\Psi$ and apply the mean value theorem to obtain

$$\hat{\Phi}(x, \Psi, \nabla\Psi) = \hat{\Phi}(x, \Psi, 0) + \frac{d\hat{\Phi}(x, \Psi, \xi)}{d\nabla\Psi} (\nabla\Psi - 0). \tag{2.63}$$

for some $\xi \in (0, \nabla\Psi)$. Applying the linearized flux assumption, the first term on the right hand side is eliminated, yielding

$$\hat{\Phi}(x, \Psi, \nabla\Psi) = \frac{d\hat{\Phi}(x, \Psi, \xi)}{d\nabla\Psi}\nabla\Psi. \tag{2.64}$$

Since the quantity $\frac{d\hat{\Phi}(x_i, \Psi, \xi)}{d\nabla\Psi}$ must be evaluated at the boundary of the control volume, it is approximated as

$$\begin{aligned} \frac{d\hat{\Phi}(x, \Psi, \xi)}{d\nabla\Psi} &= \frac{\hat{\Phi}_{i+\frac{1}{2}}(x, \Psi, \nabla\Psi)}{\nabla\Psi} \\ &\equiv -K_{i+\frac{1}{2}}(\Psi_i, \Psi_{i+1}). \end{aligned} \tag{2.65}$$

Substituting 3.46 into equation 3.45 and approximating $\nabla\Psi$ by the forward finite difference $D^+[\Psi_i] \approx \frac{\Psi_{i+1} - \Psi_i}{\Delta x}$, we obtain the expression

$$\hat{\Phi}_{i+\frac{1}{2}}(x, \Psi_i, \Psi_{i+1}) = -K_{i+\frac{1}{2}}(\Psi_i, \Psi_{i+1})D^+[\Psi_i] \tag{2.66}$$

Deriving an analogous expression for $\Phi_{i-\frac{1}{2}}$ and substituting it and equation 3.47 into equation 3.43, we obtain

$$-\left[K_{i+\frac{1}{2}}(\Psi_i, \Psi_{i+1})D^+[\Psi_i] - K_{i-\frac{1}{2}}(\Psi_{i-1}, \Psi_i)D^+[\Psi_{i-1}]\right] + h(\Psi_i)\Delta x = \hat{F}_i\Delta x \tag{2.67}$$

Regardless of whether $K_{i\pm\frac{1}{2}}$ is a constant function, equation 3.48 can be resolved by successive approximations Ψ_i^{n+1} (i.e. fixed point iteration) for all i as

$$-\left[K_{i+\frac{1}{2}}(\Psi_i^n, \Psi_{i+1}^n)D^+[\Psi_i^{n+1}] - K_{i-\frac{1}{2}}(\Psi_{i-1}^n, \Psi_i^n)D^+[\Psi_{i-1}^{n+1}]\right] + h(\Psi_i^{n+1})\Delta x = \hat{F}_i\Delta x \tag{2.68}$$

2.4.3 Results

In [35], we investigated the stability of the operator splitting method and convergence of the multiscale method under simplified conditions.

Operator Splitting

Exploiting Banach Fixed Point Theory, we realized a numerical investigation of the operator splitting stability for the non-dimensionalized poroelasticity equations under homogeneous and linearly heterogeneous conditions. Since we found no qualitative difference between Block Jacobi and Block Gauss-Seidel approaches, we address the results of both approaches in tandem.

In the homogeneous material property case, non-dimensionalization revealed that the product between the constrained specific storage coefficient and the elastic moduli $\beta = c_0\nu$ adequately characterizes the convergence behavior for constant Biot-Willis Coefficient α. We define a threshold surface β^* for each α which separates the parameter space into problems guaranteed to converge or diverge for each choice of Δt and Δx. As $\alpha \to 0$, the surface uniformly decreases to the plane $\beta = 0$. This corresponds both to a larger range of parameter values which converge and faster convergence rates. The physical interpretation of this limit is a characterization of a weakened coupling between the fluid flow and deformation processes. Moreover, the threshold surface β^* always approaches a limiting plane parallel to the Δx-Δt plane, above which convergence is assured. In the strongly-coupled case with $\alpha = 1$, the limiting plane is given by $\beta = 1$. This result indicates that problems with $\beta > 1$ are guaranteed to converge with a rate of convergence that increases as β increases.

We use the characterization of the homogeneous case to guide our tests of the linearly variable coefficient case with $\nu(x) = k(x) = mx + b$. We find that the increases in slope m shift the threshold surfaces toward the origin, enabling the convergence of the operator splitting for a larger set of problems. However, the slope does not lower the value of the limiting plane which the threshold surface does not cross. This limiting plane is strongly affected by variations in c_0 and α. Again as $\alpha \to 0$, the strength of the coupling decreases and the limiting plane also decreases with it.

More importantly, large material property gradients result in a wider range of convergent problems for larger values of Δt and Δx. This suggests that larger heterogeneity results in improved convergence of the operator splitting method. In the context of multiscale

poroelasticity, this is significant because we wish to approximate the solution on a coarse mesh corresponding to Δx larger than the scale of the heterogeneity. Further testing is needed to determine if this trend holds true for highly oscillatory material coefficients with large amplitudes.

The numerical experiments give evidence that the threshold surface separating convergent and divergent problems for our operator splitting method approaches an asymptotic limit as Δt and Δx approach zero. This is, by no means, an analytical proof of the limit. Given the complexity of determining the analytical form of the spectral radius of the stationary operator $M^{-1}N$, this is our best attempt to characterize the parameter space which guarantees convergence.

These results only apply to the case linear heterogeneity and with $\nu(x) = k(x)$ only. Because of the infinitely many possible choices of functions $\nu(x)$ and $k(x)$, it is impossible to characterize all possible variations and permutations. One particular case of interest not addressed by this thesis is the case with highly oscillatory $\nu(x)$ and $k(x)$. This is an important benchmark case for a multiscale method for poroelasticity and we seek to test this case in the future for various amplitudes and frequencies.

Number of iterations needed to achieve convergence within a given error tolerance is a significant drawback to the proposed operator splitting method. As the material parameter values approach the threshold surface, more iterations are required for the operator splitting method to converge. The computational cost of multiple iterations using the operator splitting method can supersede the cost of a single solve of the fully coupled equations.

The proposed operator splitting methods are pure decompositions of the coupled operator at a specific time t. In the block gauss-seidel splitting methods, the unmodified solution from one equation is used as a source term in the remaining equation without projective corrections. In the framework of fixed point iterations, various acceleration methods can be employed to improve the rate of convergence. Most notably, successive overrelaxation, Aitken, Chebyshev, and various krylov methods can be used to accelerate its convergence. An ideal method enables convergence in a fixed number of iterations independent of pa-

rameter values and spatiotemporal discretization. Use of Kim[49]'s projective corrections may significantly improve the convergence rates, but it remains unclear if these methods can be extended to the variable coefficient case.

Multiscale Convergence

In the course of attempting to replicate the results of Chu et al.'s multiscale algorithm, we implemented and tested their algorithm for diffusion in porous media in three benchmark cases; two of which were not addressed in their original paper: Homogeneous and Linearly Variant conductances. In addition to replicating the results for the heterogeneous (random) conductance case, we discovered two important facts about the algorithm. Firstly, in the case of the Hagen-Poiseuille conductance model, Chu et al. (2012) claimed that convergence is theoretically attained in a single iteration within machine precision. Our results indicate that residual error decreases significantly in the first iteration, but not necessarily to within machine precision even in the homogeneous conductance case. This indicates that the we cannot impose excessively small error tolerances between the multiscale and fully microscopic solutions, even in the most idealized circumstances.

Secondly, while convergence is achieved in the linearly variant conductance case, significant relative errors exist when subsampling is used. In this case, relative errors are only small when fully micro sampling is used. The only case in which subsampling proved efficient is in the heterogeneous (random) conductance case. In the heterogeneous case, we confirm that convergence is achieved when the number of sampling subdomains μ is held constant and the length of the samples δ increases but not vice-versa. Constant δ and increasing μ results in increasing relative errors both in pressure and flux. Similar trends were also reported in Chu et al. (2012).

We proposed a method for multiscale solid deformation in 1D based on coupling finite volume method at the macroscopic level with direct stiffness methods at the microscopic level. We achieved analogous convergence behavior for the homogeneous, linearly variant, and heterogeneous cases in comparison to the aforementioned replication tests. Our results

indicate a similar lack of convergence in the heterogeneous case with constant sample length δ and increasing the number of sampling subdomains μ. Chu et al. (2012) claimed this behavior to be the result of the imposition of uniform dirichlet boundary conditions along cross-sections of the fully microscopic model with non-uniform conductances. Since our micromodel is 1D, this behavior cannot be attributed to this phenomenon. It is clear that the use of purely dirichlet boundary conditions in the micromodel contains within it inherent errors that amplify with increasing sampling subdomains. The exact source of these errors is unknown and requires further testing.

We also proposed a method to solve the multiscale reaction-diffusion problem resulting from the decoupled flow problem. Our method proposed an alternative network model which accounts for the reaction term in the macroscopic equation. The characteristics of the test problem produce a boundary layer which is difficult to capture even in the constant coefficient case with finite difference method. Our preliminary results indicate that our multiscale algorithm produces more accurate results than the standard finite difference method for the constant and linearly varying coefficient cases. The heterogeneous (random) case produced inconsistent convergence results related to negative fluxes generated in the reaction-diffusion micromodels. Despite the use of purely dirichlet boundary conditions in the axial directions and periodic boundary conditions along the transverse boundaries, monotonicity was not preserved in the micromodel. Further investigation is required to determine the exact cause of the negative fluxes.

The constant coefficient cases of solid deformation and Chu et al.'s method reveals that the multiscale method does not achieve accuracy to approximately machine precision. We note that Chu et al. never disclosed results in the constant coefficient or linearly increasing case. Furthermore, the micromodels in our method utilized a distinct topological structure in comparison to Chu et al.'s work. In our models, we use connectivity number 4 and 2 in the replication study and the solid deformation model, respectively while Chu et al. (2012) used connectivity 6 arranged in a triangular mesh structure. We hypothesize the difference in performance results may partially be attributed to this difference.

Except for the constant coefficient cases, significant sampling area is always required to achieve small relative errors in Chu et al.'s model and the multiscale solid deformation model. Particularly in the linearly variant case, relative errors do not diminish significantly except in the case of full sampling of the microscopic model. While this appears to be a significant limitation of the method, one must keep in mind that it is inherently unrealistic to expect large accuracy using extremely small sampling subdomains in a multiscale method. The fact remains that convergence is achieved in the limit as the total sampling area approaches the size of the full computational domain. For many engineering applications, relative error less than 5% may be adequate. It remains unclear, however, how significant the impact of the relative error in the multiscale method is on the convergence of the operator splitting method. Further testing is required to determine the scope of this impact.

Extensions of the multiscale method to higher dimensions is more complicated in the case of solid deformation. Static determinacy limitations and lack of shearing effects severely reduce the use of truss-elements to the one dimensional case only. Moreover, the discrete nature of the fully microscopic model necessitates that the sample length δ cannot be chosen smaller than the length of the elements of the micromodels (e.g. the length of the throat in a pore network model). The assumption is that the underlying microstructure is known exactly and can be represented as a discrete graph. If the material properties $\nu(x)$ and $k(x)$ are given as smooth functions, we may substitute the discrete network models for other continuous representations. Our heterogeneous multiscale framework enables us to use any suitable microscale model which approximates the flux locally within each sampling subdomain. Alternative continuum approaches may be suitable replacements for the discrete microscopic network models at the micro-scale.

2.5 Summary of Current Investigation

This dissertation continues the work proposed in [35] by improving and extending our method in several directions not addressed by Chu et al [27, 26].

First, we develop a hybrid strategy which combines our previous iterative splitting method with the well-established fixed-stress splitting approach. We show consistency and stability of our method in the case of constant material coefficients. We further illustrate that this method works even for cases with random heterogeneity.

We previously developed a one dimensional model for purely dirichlet boundary conditions and no source terms. In this work, we extend our method to account for multidimensional problems, mixed boundary conditions and source terms. We further obtain an error estimate for our multiscale method for the reaction diffusion and solid deformation problems in the case of highly oscillatory periodic material coefficients.

In our previous work, we only tested operator splitting and multiscale methods separately. In our current work, we combine both methods together in the case of steady state poroelasticity with one-way coupling. We also analyze the algorithmic performance of our method in 1D for both sequential and parallel implementations. We test two parallelization strategy for efficient implementation on high performance computers.

We outline a summary of our operator splitting and multiscale methodology for basic 1D case the next chapter.

Chapter 3

Methodology

3.1 Assumptions

To begin the process of developing a multiscale method for Biot's equations, we make several assumptions to the standard quasi-static formulation of the linear poroelasticity equations[69]. For simplicity, we consider the 1D formulation of Biot's equations 2.13- 2.14 in the spatial domain $\Omega \equiv [0, L]$ with no source terms:

$$-\frac{d}{dx}\left((\lambda + 2\mu)\frac{du}{dx}\right) + \alpha\frac{dp}{dx} = 0, \ x \in \Omega \tag{3.1}$$

$$\frac{d}{dt}\left(c_0 p + \alpha\frac{du}{dx}\right) - \frac{1}{\mu_f}\frac{d}{dx}\left(k\frac{dp}{dx}\right) = 0, \ x \in \Omega. \tag{3.2}$$

The boundary conditions are imposed as fixed values

$$p = p_L \quad \text{at } x = 0 \tag{3.3}$$

$$(\lambda + 2\mu)\frac{du}{dx} = -T_L \text{ at } x = 0 \tag{3.4}$$

$$u = u_R \quad \text{at } x = L \tag{3.5}$$

$$\frac{1}{\mu_f}k\frac{dp}{dx} = F_R \text{ at } x = L \tag{3.6}$$

where and $p_L, t_L, u_R, f_R \geq 0$. We also impose a finite the initial condition satisfying

$$c_0 p + \alpha\frac{du}{dx} = 0 \text{ at } t = 0. \tag{3.7}$$

Note in the situation where $p_L = u_R = f_R = 0$ and $\lambda, \mu, c_0, \alpha, \mu_f$ & k are constant, equations 3.1- 3.7 are equivalent to the classic Terzaghi Problem where a constant (compressive) load t_L is suddenly applied to the top ($x = 0$) of a column of fluid-saturated

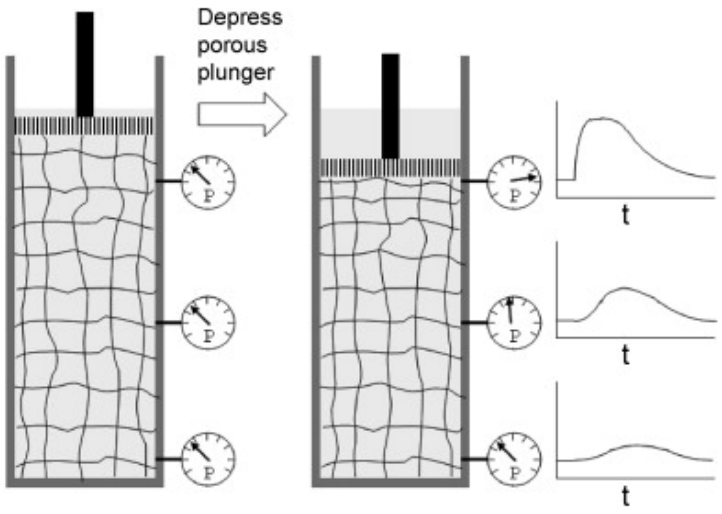

Figure 3.1: Depiction of the 1D Terzaghi Problem, adapted from Mitchison et. al.[57]

porous medium of finite length. The load is induced by a permeable plunger or piston such that fluid drains through the top boundary as shown in figure **??**. Due to draining conditions, the top of the medium is also subject to zero excess pore pressure conditions. The dirichlet and neumann conditions at $x = 1$ model the situation that the bottom of the medium is both rigid and impermeable, respectively. The medium is constrained in the transversal directions by a rigid container such that it is subject only to uniaxial strain[71]. The initial condition captures the fact that there is no increment in fluid content upon initial loading.

Next, we assume the lame parameters λ, μ and permeability k in equations 3.1- 3.2 vary in space but not in time. We further assume that these variable material parameters are highly heterogeneous, but not necessarily periodic. More precisely, we assume $\lambda(x)$, $\mu(x)$ and $k(x)$ are continuous functions with sharp gradients of positive characteristic length $\epsilon << 1$ distributed randomly within the computational domain Ω. All other material parameters are assumed to be constant. Consequently, we model λ, μ, and k as functions

of x and rewrite equations 2.13- 2.14 as:

$$-\frac{d}{dx}\left(\nu(x)\frac{du}{dx}\right)+\alpha\frac{dp}{dx}=0,\ x\in\Omega \tag{3.8}$$

$$\frac{d}{dt}\left(c_0p+\alpha\frac{du}{dx}\right)-\frac{d}{dx}\left(K(x)\frac{dp}{dx}\right)=0,\ x\in\Omega \tag{3.9}$$

with $\nu(x)=\lambda(x)+2\mu(x)$ and $K(x)=\frac{k(x)}{\mu_f}$.

Due to the heterogeneity encapsulated in ν and K, equations 3.8- 3.9 cannot be accurately resolved by conventional continuum methods without an extremely small spatial discretization $h<\epsilon$. To resolve this issue, we first propose an operator splitting strategy which resolves equations 3.8- 3.9 as a sequence of two uncoupled elliptic PDE's. Then, we propose a heterogeneous multiscale method which resolves both elliptic equations by a common framework.

3.2 Operator Splitting

To decouple equations 3.8- 3.9, we follow Rothe's semi-discretization methodology using a backward euler finite difference in time t while leaving the spatial variable x and its corresponding operators continuous. This results in the implicit semi-discrete equations

$$-\frac{d}{dx}\left(\nu(x)\frac{du^t}{dx}\right)+\alpha\frac{dp^t}{dx}=0,\ x\in\Omega \tag{3.10}$$

$$\left(c_0\frac{p^t-p^{t-1}}{\Delta t}+\alpha\frac{\frac{du^t}{dx}-\frac{du^{t-1}}{dx}}{\Delta t}\right)-\frac{d}{dx}\left(K(x)\frac{dp^t}{dx}\right)=0,\ x\in\Omega \tag{3.11}$$

where t is the discrete time step and Δt is the temporal increment. Note that all terms $t-1$ are known quantities in the tth timestep and thus can be treated as source terms. Hence, we rewrite equations 3.10- 3.11 as

$$-\frac{d}{dx}\left(\nu(x)\frac{du^t}{dx}\right)+\alpha\frac{dp^t}{dx}=0,\ x\in\Omega \tag{3.12}$$

$$\left(\frac{c_0}{\Delta t}p^t+\frac{\alpha}{\Delta t}\frac{du^t}{dx}\right)-\frac{d}{dx}\left(K(x)\frac{dp^t}{dx}\right)=R^{t-1},\ x\in\Omega \tag{3.13}$$

where $R^{t-1} = \frac{c_0}{\Delta t} p^{t-1} + \frac{\alpha}{\Delta t} \frac{du^{t-1}}{dx}$.

Introducing new notation, we define four continuous linear operators A,G,D, and B as follows:

$$Au \equiv -\frac{d}{dx}\left(\nu(x)\frac{du}{dx}\right) \tag{3.14}$$

$$Gp \equiv \alpha\frac{dp}{dx} \tag{3.15}$$

$$Du \equiv \frac{\alpha}{\Delta t}\frac{du}{dx} \tag{3.16}$$

$$Bp \equiv \frac{c_0}{\Delta t}p - \frac{d}{dx}\left(K(x)\frac{dp}{dx}\right) \tag{3.17}$$

Then, we can rewrite equations 3.12- 3.13 in terms of a single linear system $Lv^t = b$, where

$$L \equiv \begin{bmatrix} A & G \\ D & B \end{bmatrix}, \quad v^t \equiv \begin{bmatrix} u^t \\ p^t \end{bmatrix}, \quad b \equiv \begin{bmatrix} 0 \\ R^{t-1} \end{bmatrix} \tag{3.18}$$

We shall refer to system 3.18 as the fully coupled semi-discrete equations. Note that in this formulation, u and p are continuous variables coupled to each other only at the current timestep. To uncouple these equations, we apply the method of successive approximations[1] by formulating a sequence of approximations which resolve the current iterate $u^{t,n}, p^{t,n}$ in terms of the previous iterate $u^{t,n-1}, p^{t,n-1}$. We propose two different decoupling methods motivated by block operator decompositions of L.

3.2.1 Block Jacobi Splitting

In the Block Jacobi Splitting method, we formulate a sequence of approximations $v^{t,n} \equiv [u^{t,n}, p^{t,n}]^T$ by decomposing the operator L as a sum of the its diagonal and off-diagonal components. That is, we write $L = M + N$ where

$$M \equiv \begin{bmatrix} A & 0 \\ 0 & B \end{bmatrix}, \quad N \equiv \begin{bmatrix} 0 & G \\ D & 0 \end{bmatrix} \tag{3.19}$$

[1] Also known as Fixed Point Iteration or Picard Iteration.

Hence, system 3.18 is rewritten as

$$Mv^t + Nv^t = b. \tag{3.20}$$

Next, we apply a fixed point iteration such that all instances of u^t in equation 3.12 and all instances of p^t in equation 3.13 use the current iterate n. All other (off-diagonal) terms use the previous iterate $n-1$. Consequently, the solution at each timestep t is resolved by the system

$$Mv^{t,n} + Nv^{t,n-1} = b. \tag{3.21}$$

or equivalently

$$-\frac{d}{dx}\left(\nu(x)\frac{du^{t,n}}{dx}\right) = S_p^{t,n-1},\ x \in \Omega \tag{3.22}$$

$$\frac{c_0}{\Delta t}p^{t,n} - \frac{d}{dx}\left(K(x)\frac{dp^{t,n}}{dx}\right) = S_u^{t,n-1} + R^{t-1},\ x \in \Omega. \tag{3.23}$$

where $S_p^{t,n-1} \equiv \alpha\frac{dp^{t,n-1}}{dx}$ and $S_u^{t,n-1} \equiv \frac{\alpha}{\Delta t}\frac{du^{t,n-1}}{dx}$.

3.2.2 Block Gauss-Seidel Splittings

The Block Gauss-Seidel Splitting method uses a block operator decomposition of the form $L = M + N$ where M is either the block lower or upper triangular portions of L while N contains the remaining blocks of L. When M is the block lower triangular, we obtain a splitting similar in scope to Kim's Drained Splitting method[49], where

$$M \equiv \begin{bmatrix} A & 0 \\ D & B \end{bmatrix}, \quad N \equiv \begin{bmatrix} 0 & G \\ 0 & 0 \end{bmatrix} \tag{3.24}$$

Alternatively for M upper triangular, the resulting Block Gauss-Seidel method is similar to Kim's Fixed Strain splitting method[49], where

$$M \equiv \begin{bmatrix} A & G \\ 0 & B \end{bmatrix}, \quad N \equiv \begin{bmatrix} 0 & 0 \\ D & 0 \end{bmatrix} \tag{3.25}$$

Substituting for L and applying fixed point iteration, we again arrive at the system

$$Mv^{t,n} + Nv^{t,n-1} \quad = \quad b. \tag{3.26}$$

In the upper triangular case, all instances of u^t and p^t in equation 3.13 and all instances of u^t in equation 3.13 use the current iterate. The remaining term p^t in equation 3.12 uses the previous iterate. The block lower Gauss-Seidel splitting can alternatively be formulated as

$$-\frac{d}{dx}\left(\nu(x)\frac{du^{t,n}}{dx}\right) + \alpha\frac{dp^{t,n-1}}{dx} = 0,\ x \in \Omega \tag{3.27}$$

$$\left(\frac{c_0}{\Delta t}p^{t,n} + \frac{\alpha}{\Delta t}\frac{du^{t,n}}{dx}\right) - \frac{d}{dx}\left(K(x)\frac{dp^{t,n}}{dx}\right) = R^{t-1},\ x \in \Omega. \tag{3.28}$$

Analogously, the block upper Gauss-Seidel splitting can be written as

$$-\frac{d}{dx}\left(\nu(x)\frac{du^{t,n}}{dx}\right) + \alpha\frac{dp^{t,n}}{dx} = 0,\ x \in \Omega \tag{3.29}$$

$$\left(\frac{c_0}{\Delta t}p^{t,n} + \frac{\alpha}{\Delta t}\frac{du^{t,n-1}}{dx}\right) - \frac{d}{dx}\left(K(x)\frac{dp^{t,n}}{dx}\right) = R^{t-1},\ x \in \Omega. \tag{3.30}$$

Although both block Gauss-Seidel splittings are not entirely decoupled, one of the two resulting equations at each iteration is always independent of a state variable. Thus for each iteration n, one equation is solved for one variable and its solution is incorporated as a source term in the other equation.

3.2.3 Convergence

Clearly, both Block Jacobi and Gauss-Seidel strategies compute the solution at each timestep $[u^t, p^t]^T$ coupled semi-discrete system as a sequence of two PDE's of the form

$$-\frac{d}{dx}\left(\nu(x)\frac{du}{dx}\right) = f, \tag{3.31}$$

$$\frac{c_0}{\Delta t}p - \frac{d}{dx}\left(K(x)\frac{dp}{dx}\right) = g \tag{3.32}$$

In the Block Jacobi case, f and g are independent of u and p. In the Block Gauss-Seidel case, f is independent of u and p, but g is a function[2] of u. Note that equation 3.31 is

[2]In particular, g is a function of $\frac{du}{dx}$

an elliptic diffusion equation whie 3.32 is an elliptic reaction-diffusion equation. Since our decomposition method does not yet assume a particular spatial discretization, we conjecture that any numerical method can be applied to 3.31- 3.32. However, the numerical method must satisfy certain criteria in order to ensure convergence. In particular, Banach's fixed point theorem suggests that if the mapping $v^{t,k-1} \rightarrow v^{t,k}$ is a contraction, then the sequence of iterations converges.

For a given splitting $L = M + N$, we can write the split system as $Mv^t = -Nv^t + b$ and denote the functional $F(v) \equiv M^{-1}(-Nv + b)$. The functional iteration is expressed in the form $v^n = F(v^{n-1})$. According to Banach's fixed point theorem, the iteration converges if for any v_1 and v_2 in the domain of F,

$$||F(v_1) - F(v_2)|| \leq q||v_1 - v_2|| \tag{3.33}$$

for some $0 < q < 1$. Note that 3.33 is sufficiently generalizable to continuous and discrete operators. If equations 3.31- 3.32 are discretized on a macroscopic equispaced grid of interval length Δx, then operators M and N are linear matrices and theorem 3.33 is automatically satisfied if $||M^{-1}N|| < 1$. In this case, the sequence of iterates v^k approaches the exact solution v^* at a rate closely related to the spectral radius ρ of $M^{-1}N$. Furthermore, the fixed point iteration converges faster as $\rho \rightarrow 0$ and slower as $\rho \rightarrow 1$.

Note that convergence is not guaranteed for all combinations of material parameters and spatiotemporal discretizations. Also, convergence is not guaranteed for a fixed number of iterations as described by Kim[49]. The principal advantage of the proposed method is that the solution to the coupled poroelasticity equations at each timestep is decomposed into the solution of a sequence of elliptic diffusion and elliptic reaction diffusion equations with multiscale coefficients for which many multiscale algorithms are readily available. Moreover, as many of these methods are iterative in scope, they can be more readily implemented in this particular form.

3.2.4 Fixed Stress Splitting

The fixed stress operator splitting strategy for poroelasticity is a well studied method with good convergence properties. It is based on imposing a constraint upon the volumetric stress in the flow equation. Recall that the flow equation can be discretized by a backward finite difference in time as

$$c_0 \frac{p^{t+1} - p^t}{\Delta t} + \alpha \frac{\epsilon_v^{t+1} - \epsilon_v^t}{\Delta t} - \frac{d}{dx} \cdot (k(x) \frac{dp^{t+1}}{dx}) = g \tag{3.34}$$

where $\epsilon_v^t \equiv \nabla \cdot u^t$ and u^t are the volumetric strain and displacement at time t.

The traditional approach is more appropriately interpeted not as fixed stress, but as **fixed rate of stress** since it constrains the variation in the *time derivative* of the volumetric stress as

$$\delta \dot{\sigma}_v = 0, \tag{3.35}$$

which in discrete form becomes

$$\frac{\sigma_v^{t+1} - \sigma_v^t}{\Delta t} - \frac{\sigma_v^t - \sigma_v^{t-1}}{\Delta t} = 0 \tag{3.36}$$

To convert (3.36) in terms of the primary variable u (displacement), we exploit the relation between volumetric stress, volumetric strain, and pore pressure given by

$$\sigma_v - \sigma_{v,0} = K_{dr}(x)\epsilon_v - \alpha\,(p - p_0) \tag{3.37}$$

whose derivative is

$$\frac{d\sigma_v}{dt} = K_{dr}(x)\frac{d\epsilon_v}{dt} - c_0 \frac{dp}{dt}. \tag{3.38}$$

The backward and forward finite difference approximations of (3.38) with respect to timestep t are

$$\frac{\sigma_v^{t+1} - \sigma_v^t}{\Delta t} = K_{dr}(x)\frac{\epsilon_v^{t+1} - \epsilon_v^t}{\Delta t} - c_0 \frac{p^{t+1} - p^t}{\Delta t} \tag{3.39}$$

and

$$\frac{\sigma_v^t - \sigma_v^{t-1}}{\Delta t} = K_{dr}(x)\frac{\epsilon_v^t - \epsilon_v^{t+1}}{\Delta t} - c_0 \frac{p^t - p^{t+1}}{\Delta t} \tag{3.40}$$

respectively. By substituting these discrete derivatives into (3.36) and solving for ϵ_v^{t+1}, we obtain

$$\epsilon_v^{t+1} = 2\epsilon_v^t - \epsilon_v^{t-1} + \frac{\alpha}{K_{dr}(x)}\left(p^{t+1} - 2p^t + p^{t-1}\right) \tag{3.41}$$

By simply substituting (3.41) into (3.34), we eliminate the flow equation's dependence on ϵ_v^{t+1} and can solve directly in terms of p^{t+1} alone. Note that the form of (3.41) suggests that We note that this spliitng strategy only requires a single solve of the flow equation and requires information from two previous timesteps t and $t-1$.

3.3 Generalization of Chu et al.'s Multiscale Method

Regardless of the splitting strategy employed, the two resulting elliptic PDE's can be generalized into the one dimensional form

$$\frac{d}{dx}\left[\Phi(x, \Psi, \Psi_x)\right] + h(\Psi) = S(x) \tag{3.42}$$

where Φ denotes a function of a scalar state variable Ψ & its gradient Ψ_x, $S(x)$ denotes a source term, and $h(\Psi)$ is a linear function of the state variable. When $h(\Psi)$ is identically zero, we obtain the elliptic diffusion equation which describes the solid deformation equation. The flow equation is obtained by setting $h(\Psi) = c^* P$ where c^* is a constant which depends on given material parameters and the chosen time stepsize Δt.

In a recent paper[34], the current author established that the fundamental assumptions inherent to Chu et al.'s multiscale algorithm are applicable not only to steady state fluid flow in porous media, but also solid deformation and steady state heat transfer as well. More importantly, the microscale pore network model used in Chu et al.'s algorithm belongs to a much more general class of finite element methods known as Direct Stiffness Methods. In the solid deformation case, [34, 33], direct stiffness methods can be incorporated into the Chu et al.'s multiscale framework both in the single[34] and higher dimensional cases.

In the context of the operator splitting method as outlined in the previous section, we note two main observations about Chu et al.'s original algorithm. While it was verified as

a tool for fluid flow in porous media, it has never been verified as a tool to model solid deformation. Also, while it was developed under the assumption of an elliptic diffusion equation as in the solid deformation equation 3.31, it is has not been tested on an elliptic reaction-diffusion equation. Specifically, it has never been applied to solve the fluid flow equation described by the 3.32.

Hence, this thesis also addresses both the verification of Chu et al.'s multiscale method in the context of solid deformation in the form 3.31 and proposes an extension of this method to handle the fluid flow equation 3.32. Both proposed methods are based on coupling the Finite Volume Method at the continuum scale with a Direct Stiffness Finite Element [52, 15] at the microscale. Details of these two models are summarized in the same macroscopic framework described in the next section, with the two separate cases of fluid flow and solid deformation handled by distinct microscopic models.

3.3.1 Macroscopic Model

Using equation 3.42, we apply the finite volume method by discretizing the domain Ω into finitely many equispaced cells $B_i = [x_{i-\frac{1}{2}}, x_{i+\frac{1}{2}}]$ with discrete values of Ψ defined at the cell center x_i as in figure 3.2. Integrating this equation over each control volume B_i and applying the divergence theorem, we obtain an expression of the form

$$\hat{\Phi}_{i+\frac{1}{2}} - \hat{\Phi}_{i+\frac{1}{2}} + h(\Psi_i)\Delta x = \hat{F}_i \Delta x. \tag{3.43}$$

where $\hat{\Phi}_{i+\frac{1}{2}} \equiv \Phi_{i+\frac{1}{2}} \Delta A$, with ΔA denoting the cross-sectional area of the control volume. The variables Ψ and Φ have different interpretations corresponding to the flow and deformation problems. For fluid flow, the variable Ψ and Φ represent the macroscopic pressure P and flux F. For solid deformation, displacement U and total boundary force $\tilde{F}$ are represented by Ψ and Φ, respectively. The fractional indices in 3.43 indicate that conserved quantities are defined on the boundary of control volume, while integer indices denote cell centered values. In its current form, equation 3.43 is incomplete because no explicit macroscopic constitutive relation is known or assumed.

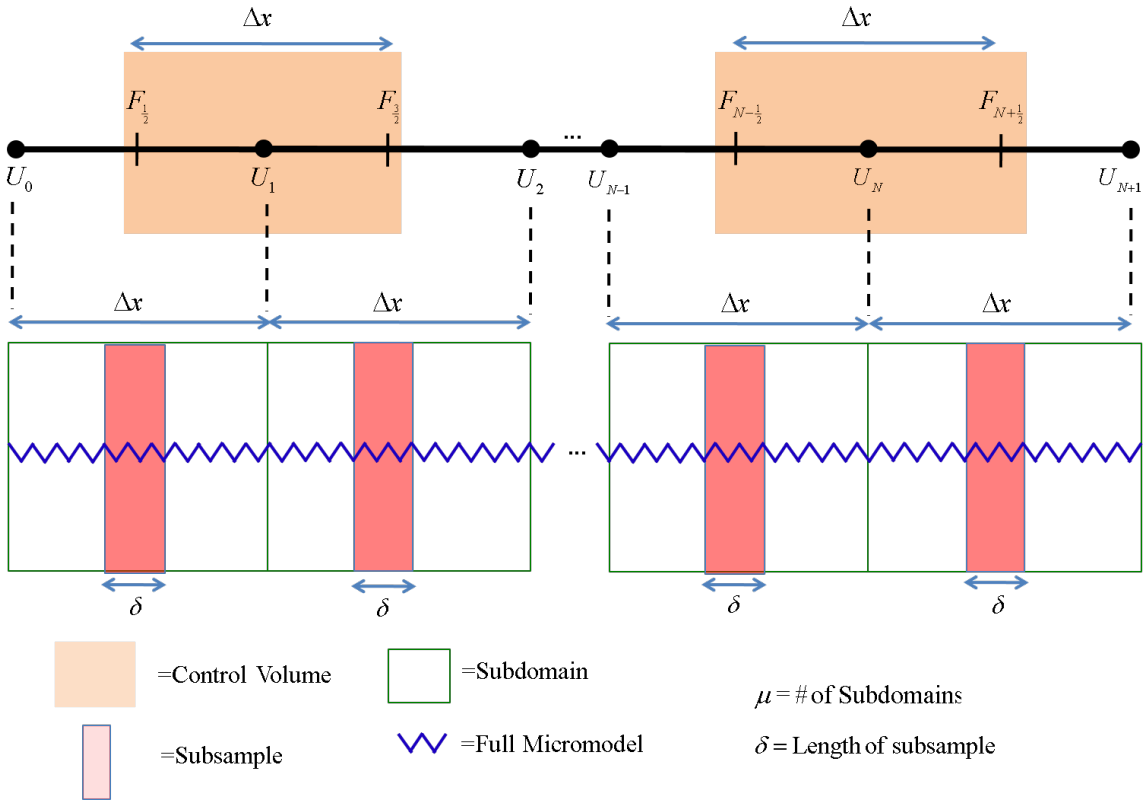

Figure 3.2: Visualization of the heterogeneous multiscale model sampling the fully microscopic model. In the fluid flow case, the fully microscopic model is a network model of pores and throats. In the solid deformation case, it is an assemblage of spring elements using in a direct stiffness model.

The key assumption to couple macro and micro spatial scales in [27, 26] is that the volumetric flux is zero when the pressure gradient is zero. In [34], the current author observed that this assumption extends from a linear potential flow assumption that can be extended into other physical phenomena. In heat transfer contexts, for example, we can assume a zero heat flux when there is no temperature gradient. In solid deformation contexts, this assumption can be interpreted as a zero strain inducing a zero stress. Hence, we make the fundamental assumption that

$$\hat{\Phi}(x, \Psi, \Psi_x) = 0 \text{ when } \Psi_x = 0.$$

To establish the coupling between scales, we apply the mean value theorem to the first order taylor expansion of $\Phi(x, \Psi, \Psi_x)$ in terms of the third argument Ψ_x and use our fundamental assumption. Here we assume the one dimensional case where Ψ_x is a scalar quantity. Consequently, there exists $\xi \in (0, \Psi_x)$ such that

$$\hat{\Phi}(x, \Psi, \Psi_x) = \hat{\Phi}(x, \Psi, 0) + \frac{d\hat{\Phi}(x, \Psi, \xi)}{d\Psi_x} (\Psi_x - 0). \tag{3.44}$$

Note that in one dimension, the gradient Ψ_x is also a scalar quantity. In higher dimesions, the gradient is a vector, but can be expanded in terms of its scalar components. We shall demonstrate this process in chapter 7.

Applying our fundamental assumption, the first term on the right hand side is eliminated, yielding

$$\hat{\Phi}(x, \Psi, \Psi_x) = \frac{d\hat{\Phi}(x, \Psi, \xi)}{d\Psi_x} \Psi_x. \tag{3.45}$$

Since the quantity $\frac{d\hat{\Phi}(x_i, \Psi, \xi)}{d\Psi_x}$ must be evaluated at the boundary of the control volume, it is approximated as

$$\begin{aligned} \frac{d\hat{\Phi}(x, \Psi, \xi)}{d\Psi_x} &\approx \frac{\hat{\Phi}_{i+\frac{1}{2}}(x, \Psi, \Psi_x) - \hat{\Phi}_{i+\frac{1}{2}}(x, \Psi, 0)}{\Psi_x - 0} \\ &= \frac{\hat{\Phi}_{i+\frac{1}{2}}(x, \Psi, \Psi_x)}{\Psi_x} \\ &\equiv -K_{i+\frac{1}{2}}(\Psi_i, \Psi_{i+1}). \end{aligned} \tag{3.46}$$

Substituting 3.46 into equation 3.45 and approximating Ψ_x by the forward finite difference $D^+[\Psi_i] \approx \frac{\Psi_{i+1}-\Psi_i}{\Delta x}$, we obtain the expression

$$\hat{\Phi}_{i+\frac{1}{2}}(x, \Psi_i, \Psi_{i+1}) = -K_{i+\frac{1}{2}}(\Psi_i, \Psi_{i+1})D^+[\Psi_i] \tag{3.47}$$

Deriving an analogous expression for $\Phi_{i-\frac{1}{2}}$ and substituting it and equation 3.47 into equation 3.43, we obtain

$$-\left[K_{i+\frac{1}{2}}(\Psi_i, \Psi_{i+1})D^+[\Psi_i] - K_{i-\frac{1}{2}}(\Psi_{i-1}, \Psi_i)D^+[\Psi_{i-1}]\right] + h(\Psi_i)\Delta x = \hat{F}_i\Delta x \tag{3.48}$$

Regardless of whether $K_{i\pm\frac{1}{2}}$ is a constant function, equation 3.48 can be resolved by successive approximations Ψ_i^{n+1} (i.e. fixed point iteration) for all i as

$$-\left[K_{i+\frac{1}{2}}(\Psi_i^n, \Psi_{i+1}^n)D^+[\Psi_i^{n+1}] - K_{i-\frac{1}{2}}(\Psi_{i-1}^n, \Psi_i^n)D^+[\Psi_{i-1}^{n+1}]\right] + h(\Psi_i^{n+1})\Delta x = \hat{F}_i\Delta x \tag{3.49}$$

So far, equation 3.49 still remains incomplete because no method has yet been specified to estimate $\hat{\Phi}_{i\pm\frac{1}{2}}$. The missing quantities are evaluated by a model which requires limited information at the microscopic scale. In the following section, we outline two separate methods to estimate the missing information based on direct stiffness methods as a microscopic model.

3.3.2 Microscopic Deformation Model

In the deformation case, the reaction term $h \equiv 0$ while the missing quantities $\hat{\Phi}_{i\pm\frac{1}{2}}$ in 3.43 describes the total forces acting at the boundaries of a control volume. We estimate this total force by simulation of a microscopic model defined on a small region $B_\delta(x_{i+\frac{1}{2}})$ centered at $x_{i+\frac{1}{2}}$ with total length δ. For a one dimensional medium, we can neglect shearing forces and assume only axial deformations.

At sufficiently small deformations, we can describe a one dimensional medium as an assemblage of springs of varying stiffnesses connected at discrete nodes. For a particular node i, the sum of all forces from the connected springs F_{ij} is balanced by the total internal forces s_i acting directly on the node itself. Mathematically, this relation is written as

$$\sum_{j \in C_l} F_{lj} = s_l \tag{3.50}$$

where C_l denotes the set of nodes which connected to node l.

For simplicity, we assume that internodal forces are linearly proportional to the displacement by the linear relation

$$F_{lj} = K_{lj} \left(u_l - u_j \right)$$

where u_i and u_j are respectively the displacements at nodes l and j, and

$$K_{lj} = \frac{E_{lj} A_{lj}}{L_{lj}}$$

where E_{lj} is the young's modulus, A_{lj} is the cross-sectional area, and L_{lj} is the length of the spring.

Given fixed displacement conditions or a mix of fixed traction and fixed displacement at the boundaries produces a unique solution. In the context of the heterogeneous multiscale framework, we require a restriction operator which produces suitable boundary conditions onto the locally defined microscopic models. For the deformation model, microscale boundary conditions are linearly interpolated from the macroscopic displacements U_i and U_{i+1} to the boundaries of each $B_\delta(x_{i+\frac{1}{2}})$. For purely dirichlet boundary conditions, we can denote the left and right boundaries of the microscopic model $B_\delta(x_{i+\frac{1}{2}})$ as $u^L_{i+\frac{1}{2}}$ and $u^R_{i+\frac{1}{2}}$. By linear interpolation, these two boundary values are given as

$$u^L_{i+\frac{1}{2}} = U_{i+\frac{1}{2}} - \frac{U_{i+1} - U_i}{\Delta x} \left(\frac{\delta}{2} \right) \tag{3.51}$$

$$u^R_{i+\frac{1}{2}} = U_{i+\frac{1}{2}} + \frac{U_{i+1} - U_i}{\Delta x} \left(\frac{\delta}{2} \right) \tag{3.52}$$

where $U_{i+\frac{1}{2}} = \frac{U_i + U_{i+1}}{2}$ is the average macroscopic displacement value.

The poroelasticity problem addressed in this thesis is of the form 3.8- 3.9, which include mixed dirichlet-neumann boundary conditions in both displacement and pressure.

After operator splitting, the multiscale solid equation 3.31– 3.32 also retain mixed boundary conditions. The use of mixed boundary conditions was not addressed by Chu et al. (2012)[27, 26]. For a one dimensional medium, we still use purely dirichlet boundary conditions on the microscopic model. The current thesis hypothesizes that the neumann boundary condition need only be applied at the macroscopic level. Thus, the initial guess of macroscopic displacements generates purely dirichlet boundary conditions at the microscopic level.

To complete our heterogeneous multiscale solid deformation model in 1D, we prescribe a data estimator which approximates the missing values $\hat{\Phi}_{i+\frac{1}{2}}$ in each $B_\delta(x_{i+\frac{1}{2}})$. Here, $\hat{\Phi}_{i+\frac{1}{2}}$ denotes the total force acting on the boundary of control volume i. Given the 1D nature of the microscopic model, this total force can be approximated by the force through any spring element in micro model i. For the current model, we choose

$$\hat{\Phi}_{i+\frac{1}{2}} \approx [K_{lj}(u_l - u_j)]_{i+\frac{1}{2}}$$

where the spring connecting nodes l and j lies on the left boundary of the local micro model defined in the region $B_\delta(x_{i+\frac{1}{2}})$.

3.3.3 Microscopic Flow Model

The pore network model described in 2.17 is a suitable surrogate for the elliptic diffusion equation 2.21 because it is a localized discrete analogy of the volumetric, macroscopic scale conservation law. In the context of the flow equation derived from operator splitting 3.32, an additional term must be added to the microscale pore network model to account for the non-zero reaction term $h(\Psi) \equiv c^* P_i \Delta x$ appearing in the macroscopic equation. Hence, we

propose a modified network model

$$\sum_{j \in K_l} q_{lj} + c^* p_l \Delta x = s_l \tag{3.53}$$

$$q_{lj} = g_{lj}(\Delta P_{lj}) \tag{3.54}$$

$$g_{lj}(\nabla P_{lj}) = \frac{\pi r_{lj}^4}{8\mu L_{lj}} \tag{3.55}$$

We shall refer to this model as the ***Reaction-Diffusion Network Model (RDNM)***. Clearly, equation 3.53 is a discrete analogy of the macroscopic equation 3.32 and retains the essence of the macroscopic model. The flux term 3.54 and micro constitutive relation 3.55 are analogous to the pore network model using the Hagen-Poiseuille law.

As with Chu et al.'s original algorithm dirichlet boundary conditions are imposed onto opposite boundaries of the network model. Our proposed multiscale method uses the same restriction operator and data estimators as in Chu et al. (2012)[27, 26]. That is, we use linear interpolation formula analogous to 3.51 to obtain fixed pressure boundary conditions on opposite sides of the RDNM in the axial direction and impose periodic boundary conditions on the transverse boundaries. Given initial guess of macroscopic pressures P_i and P_{i+1}, linear interpolation produces left and right dirichlet boundary conditions $P^L_{i+\frac{1}{2}}$ and $P^R_{i+\frac{1}{2}}$ given as

$$p^L_{i+\frac{1}{2}} = P_{i+\frac{1}{2}} - \frac{P_{i+1} - P_i}{\Delta x}\left(\frac{\delta}{2}\right) \tag{3.56}$$

$$p^R_{i+\frac{1}{2}} = P_{i+\frac{1}{2}} + \frac{P_{i+1} - P_i}{\Delta x}\left(\frac{\delta}{2}\right) \tag{3.57}$$

We also approximate the flux through the RDNM by taking the sum of the fluxes along a cross-section perpendicular to the axis of flow. The presence of a reaction term in the micromodel suggests that flux is non-constant throughout the micromodel. The primary flux of interest is through the boundary of the macroscopic control volumes, which correspond to the center of the micromodels. Hence, instead of using the flux through throats connected at the boundary, we use the sum of fluxes through throats connected to the center of $B_\delta(x_{i+\frac{1}{2}})$. In the case of a micromodel with an even number of throats, we use

the average of the two cross-sectional fluxes through connected to the nodes corresponding to $x_{i+\frac{1}{2}}$. Denote $I^L_{i+\frac{1}{2}}$ and $I^R_{i+\frac{1}{2}}$ as the sets of all horizontal throats connected to a pore at $x_{i+\frac{1}{2}}$ from the left and right, respectively. Then, each $\hat{\Phi}_{i+\frac{1}{2}}$ is estimated as

$$\hat{\Phi}_{i+\frac{1}{2}} \approx \frac{f_1 + f_2}{2}$$

where $f_1 = \sum_{lj \in I^L_{i+\frac{1}{2}}} q_{lj}$ and $f_2 = \sum_{lj \in I^R_{i+\frac{1}{2}}} q_{lj}$ are the fluxes through the center-left and center-right cross-sections, respectively. The case with an odd number of horizontal throats only requires a single flux evaluation at the center throat.

3.4 Research Questions

The primary hypothesis of the current thesis is that the operator splitting method proposed above is sufficiently general that any suitable elliptic diffusion and ellitpic reaction-diffusion PDE may be utilized. In particular, this approach enables the use of iterative multiscale methods such as those of the divide & conquer strategy. Banach Fixed Point Theorem suggests that the proposed operator splitting method is convergent at each time step under sufficient conditions which depend on not only on the choice of temporal and spatial stepsizes, but also the material parameters.

Hence, this thesis focuses on the convergence of both the operator splitting scheme and the multiscale approximations. The objectives of this thesis are to:

- Characterize of the material parameter constraints which enable convergence of the operator splitting method.
- Develop an improved iterative operator splitting method for faster convergence for linear poroelasticity with heterogeneous material coefficients.
- Analyze the convergence of the proposed multiscale algorithms to resolve the two elliptic problems obtained from the operator splitting
- Extend the 1D multiscale methods to higher dimensions

- Evaluate the scalability of our multiscale algorithms for high performance computing applications.

In Chapter 4, we analyze the convergence of our iterative operator splitting methods via eigenvalue analysis. In chapter 5, we verify the convergence of the proposed multiscale methods for the solid and fluid equations derived from operator splitting in 1D. Chapters 6 introduces an improved iterative splitting method which blends fixed point iteration with fixed stress iteration into a hybrid method. Chapters 7 & 8 discuss the presence of source terms and mixed boundary conditions for the one dimensional models. We extend our current multiscale methods to 2D in chapter 9 and obtain error estimates in chapter 9. In chapter 11, we briefly explore the efficiency of our multiscale method in terms of computational complexity and parallelization strategies.

Chapter 4

Iterative Splitting Experiments

In this chapter, we test both our fixed point iteration splitting and fixed stress splitting approach for the linear elasticity problem with heterogeneous material coefficeints. To our knowledge, this is the first attempt to utilize the fixed stress splitting under the assumptions outlined in chapter 3 with heterogeneous material coefficients.

4.1 Fixed Point Iteration Splitting

The stability of our proposed operator splitting method in chapter 3 depends on the spectral radius ρ of the product of $M^{-1}N$, where M & N are block operators. The eigenvalues of $M^{-1}N$ depend on the chosen spatiotemporal discretization and the material properties $\nu(x)$, $K(x)$, α and c_0. The exact nature of this relation is unknown and this thesis seeks to estimate this relation numerically. We analyze three particular cases of poroelasticity problems distinguished by the degree of heterogeneity.

4.1.1 Case I

In Case I, we assume homogeneous material properties in equations 3.8- 3.9. That is, the parameters K, ν, α, and c_0 are all constant in space and time. To simplify our analysis, we nondimensionalize equations 3.8- 3.9 by introducing new spatial, temporal, and state variables. Here, we follow an analogous approach to [43]; nondimensionalizing with respect to the domain length L and traction boundary condition T_L. We select

$$\hat{x} \equiv \frac{x}{L} \text{ (dimensionaless space)}, \tag{4.1}$$

$$\hat{t} \equiv \frac{\nu k t}{L^2} \text{ (dimesionless time)}, \tag{4.2}$$

$$\hat{p} \equiv \frac{p}{T_L} \text{ (dimesionless pressure)}, \tag{4.3}$$

$$\hat{u} \equiv \frac{\nu u}{T_L L} \text{(dimensionless displacement)}. \tag{4.4}$$

Substituting the new variables into equations 3.8- 3.9, we obtain

$$-\frac{d^2\hat{u}}{d\hat{x}^2} + \alpha\frac{d\hat{p}}{d\hat{x}} = 0, \tag{4.5}$$

$$\frac{d}{d\hat{t}}\left(\beta\hat{p} + \alpha\frac{d\hat{u}}{d\hat{x}}\right) - \frac{d^2\hat{p}}{d\hat{x}^2} = 0, \tag{4.6}$$

where $\beta \equiv c_0\nu$. By these choices, the nondimensional domain becomes $\Omega_{nondimensional} \equiv [0, 1]$. The initial condition also becomes non-dimensionalized as

$$\beta p + \alpha\frac{d\hat{u}}{d\hat{x}} = 0.$$

By definition, $\alpha \in [0, 1]$ is a dimensionless parameter which characterizes the strength of the coupling between the flow and deformation equations. In the simplest case with $\alpha = 0$, the two equations are completely decoupled from each other. In contrast, the case with $\alpha = 1$ characterizes the strongest possible coupling between the two processes. We predict that as $\alpha \to 0$, a wider range of β values will converge for a given spatiotemporal stepsize Δx & Δt. We also predict that as $\alpha \to 1$, the range of β values result in a convergent operator splitting becomes narrower for a given Δt and Δx. Thus, for a given Δt and Δx there exists some threshold value β^* which separates the range of problems which can and cannot be solved by the proposed operator splitting methods for a specific Δt and Δx. This threshold value is attained precisely at the value of β^* such that the corresponding spectral radius of $M^{-1}N = 1$.

In the absence of analytical methods to determine a closed form of the spectral radius of $M^{-1}N$ in terms of α, β, Δt and Δx, we determine its relation numerically by finding

the optimal threshold β^* value for various choices of δt and δx. For each choice of α, δt and δx, we apply a bisection search algorithm of the parameter space $\beta \in [0, \infty)$ to find β^* such that $\rho(M^{-1}N) = 1$.

Given parameter α and stepsizes Δt and Δx. Let the operator splitting method (block jacobi or block gauss-seidel) also be given. Let the matrix pairs (M_1, N_1) and (M_2, N_2) be the discretized split operator pairs generated from applying our chosen operator splitting method to equations 4.5- 4.6. That is, M_1 and N_1 are constructed using α, Δt, and β_1 and discretizing the split operators by some numerical scheme with spatial stepsize Δx. The matrix pair (M_2, N_2) are constructed analogously using β_2 in place of β_1. Let ρ_1 and ρ_2 denote the two spectral radii of (M_1, N_1) and (M_2, N_2). Assume that ρ_1 and ρ_2 lie on opposite sides of the desired value $\rho^* \equiv 1$; that is,

$$(\rho_1 - \rho^*)(\rho_2 - \rho^*) < 0.$$

The bisection search algorithm works moving the bounds β_1 and β_2 containing the root of the equation $\beta^* - 1 = 0$ closer to the true value of β^*. This is accomplished selecting the midpoint value $\beta_{mid} = \frac{\beta_1 + \beta_2}{2}$ and determining the spectral radius ρ_{mid} corresponding to the discrete matrices M_{mid}, N_{mid} constructed from β_{mid}. If the value $(\rho_{mid} - \rho^*)(\rho_1 - \rho^*) < 1$ then the interval between β_{mid} and β_1 contains the desired value ρ^* and the bound β_2 is reassigned to β_{mid}. Otherwise, the interval between rho_{mid} and ρ_2 contains the desired value ρ^* and the bound β_1 is reassigned to β_{mid}. This process repeats itself until the residual $|\rho_{mid} - \rho^*|$ is less than some given tolerance ϵ.

Due to memory limitations and time constraints, we limit our experiments to spatiotemporal steps in terms of powers of two. That is, we choose $\Delta x = 2^{-i}$ for $i = 2, 3, ..., 8$ and $\Delta t = 2^{-j}$ for $j = 2, 3, ..., 18$. The spectral radius is obtained by using MATLAB's $EIG()$ function and selecting the maximum eigenvalue in absolute value. We formulate the matrix $M^{-1}N$ by explicit calculation of M^{-1} and its multiplication to N. The resulting matrix is dense and requires a computationally expensive process to determine the eigenvalues. Due to time and memory limitations, we are unable to select $\Delta x > 2^8$.

Figure 4.1: Staggered grid for finite difference discretization. Open and closed circles represent displacement and pressure points, respectively.

We repeat our analysis for successively decreasing values of α as $\alpha \to 0$. We predict that as $\alpha \to 0$, the convergence constraint diminishes for all spatiotemporal discretization choices.

The matrices M and N are obtained by discretizing the split operators derived from equations 4.5- 4.6 by finite difference method. We use a backward difference in time and centered differences in space for both first and second derivative approximations using a staggered grid as illustrated in figure 4.1. As noted in [58, 41], application of the finite difference method to the poroelasticity equations on standard collocated grids leads to large, non-physical oscillations which hinder the accuracy of the solution. Staggered grids consisting of alternating pressure and displacement points reduce this effect[44] and lead to greater overall accuracy[1]. In this case, the quantity Δx represents the distance between two consecutive pressure points and two consecutive displacement points. The number of intervals for each state variable is defined by $N = \frac{1}{\Delta x}$, which is always guaranteed to be a positive integer by our aforementioned choices of Δx. This choice induces $N + 1$ pressure points and $N+1$ displacement points (including boundary points), which produces staggered grid containing a total of $2N + 2$ points.

Figures 4.2- 4.13 display the threshold β^* values at various choices of Δt and Δx. Figures 4.2- 4.5, 4.6- 4.9, and 4.10- 4.13 show the thresholds for the Block Jacobi, Block Upper Gauss-Seidel, and Block Lower Gauss-Seidel splitting methods, respectively. Each individual graph represents a different value of α.

The results indicate that there is no qualitative difference between the convergence be-

[1]It is also stated in[41] that a backward time difference is unconditionally stable for all values of β. Note that stability and consistency of the finite difference method are insufficient conditions to guarantee convergence of the proposed operator splitting methods.

havior of the Block Jacobi and Gauss-Seidel splittings. They are all, at best, *conditionally convergent*. The existence of a surface separating convergent and divergent indicates that for any given Δt and Δx, there exists some range of parameter values such that the splitting will not converge. Non-dimensionalization of the homogeneous constant coefficient case indicates that for a given $\alpha \in [0, 1]$, the product $\beta \equiv c_0 \nu$ is the primary quantity which characterizes the convergence or divergence of the operator splitting. The space of convergent and divergent coupled problems separated by the surface $\beta^*(\Delta t, \Delta x)$, corresponding to the values of β such that the spectral radius of the discrete operator $M^{-1}N$ is less than unity for each tested value α. It was determined that the half space $\beta \geq \beta^*(\Delta t, \Delta x)$ always corresponds to the set of parameters such that the operator splitting converges.

In all operator splitting methods and for a given α and constant Δx, the surface $\beta^*(\Delta t, \Delta x)$ decreases as Δt increases. A similar trend is observed for all other values of α. Due to the unconditionally stable implicit timestepping scheme, this indicates that the recommended strategy to ensure convergence for a given β is to *increase* the time stepsize, rather than decreasing it. While this strategy ensures convergence, it sacrifices accuracy in the process as larger Δt decreases the order of accuracy in the obtained solution.

In the case of strong fluid-solid coupling ($\alpha = 1$), it was also observed that for all proposed operator splitting methods with constant α and $(\Delta t, \Delta x \to (0, 0)$, the threshold surface $\beta^*(\Delta x, \Delta t)$ increases asymptotically to unity. We conjecture that the range of parameters values β which enable convergence of all proposed operator splitting methods can be conservatively estimated by the half-space above the threshold plane $\beta = 1$.

In the limit as $\alpha \to 0$, we observe that the threshold surface $\beta^*(\Delta t, \Delta x)$ decreases uniformly in value as does the threshold plane. This indicates that a greater range of parameter values converge as the coupling strength decreases. For a fixed Δt, Δx, and β, the spectral radius of $M^{-1}N$ also decreases as $\alpha \to 0$. This implies that if convergent, the operator splitting methods converge faster as the strength of the coupling decreases. Indeed, this is consistent with our previous assumptions.

Although any value of β above the threshold surface ensures convergence, the number

Table 4.1: Convergence Table for $\alpha = 1$, $\Delta t = 0.001$, and $\Delta x = 0.002$

β	$\rho(M^{-1}N)$	iterations
0.9	1.0528	Does not converge
1	0.99877	2510
2	0.70624	16
5	0.4466	8
10	0.31584	6
100	0.099877	2

of iterations required to converge within a given error tolerance ϵ varies for different β. The rate of convergence of fixed point iterations is known to be inversely proportional to the spectral radius of the discrete operator $M^{-1}N$. Thus, the expected number of iterations required to converge as increases as $\beta \to \beta^*(\Delta x, \Delta t)$ and decreases as $\beta \to \infty$. Due to the diffusive nature of the solutions to the poroelasticity equations for fixed boundary conditions[2], the maximum number of iterations required to converge at any timestep is bounded by the first timestep. We also test the convergence behavior for a constant Δt, Δx, and α. In these tests, the fixed point iteration uses the residual convergence criterion

$$||v^t_{coupled} - v^{t,k}_{split}|| \leq \epsilon$$

where $v^t_{coupled} = (u^t, p^t)^T$ and $v^{t,k}_{split} = (u^{t,k}, p^{t,k})^T$ are the numerical solutions from solving the fully coupled and the jacobi operator splitting methods, respectively. For experimentation, we chose $\epsilon = 10^{-5}$ in all tests. The data displayed in Table 4.1 is consistent with theoretical predictions.

4.1.2 Case II

In Case II, we assume the elastic moduli $\nu(x)$ and mobility $K(x)$ are linear functions of space and all other material parameters are constant. Characterization of all the infinite

[2]Boundary conditions that do not vary in time.

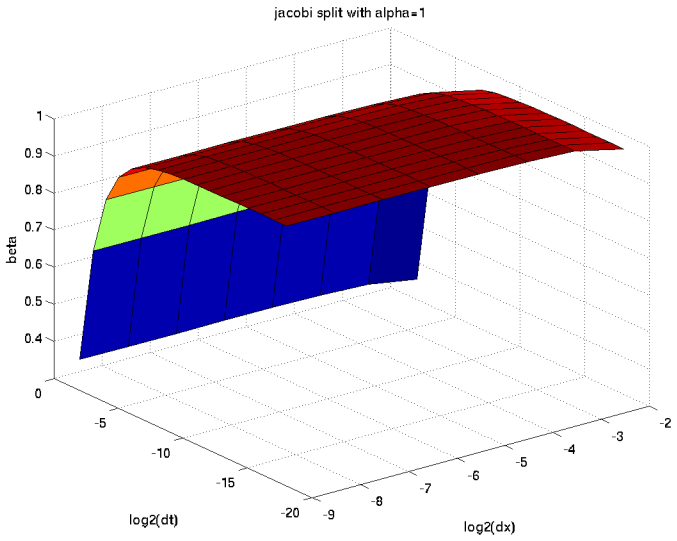

Figure 4.2: Threshold Surface β^* at various Δt and Δx values with $\alpha = 1$.

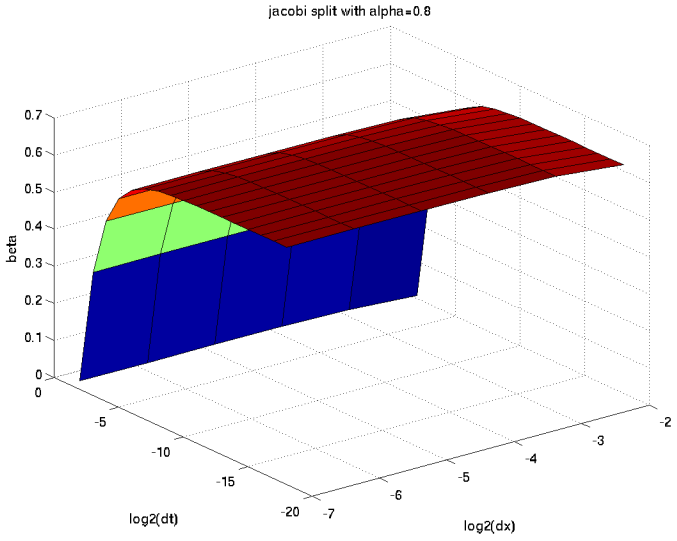

Figure 4.3: Threshold Surface β^* at various Δt and Δx values with $\alpha = 0.8$.

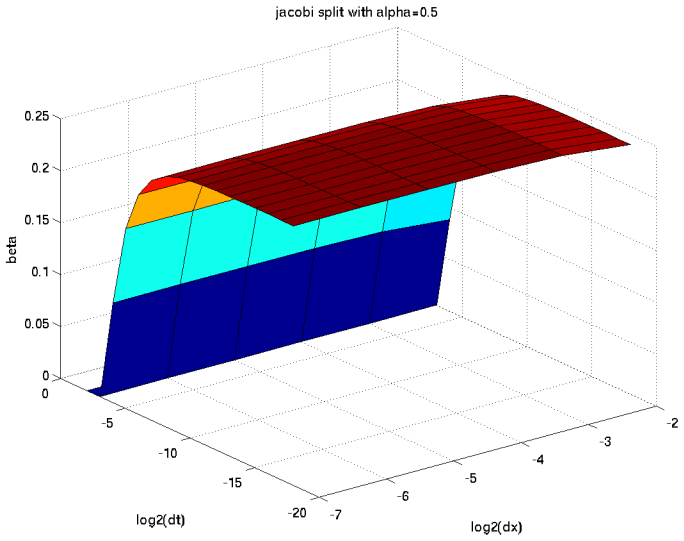

Figure 4.4: Threshold Surface β^* at various Δt and Δx values with $\alpha = 0.5$.

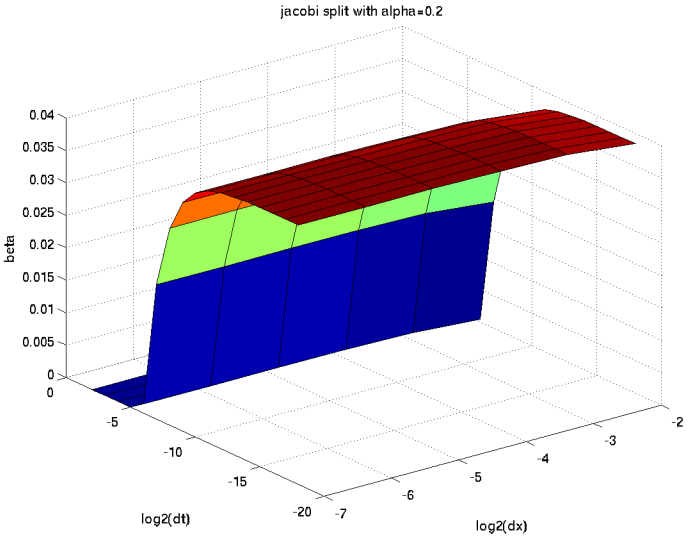

Figure 4.5: Threshold Surface β^* at various Δt and Δx values with $\alpha = 0.2$.

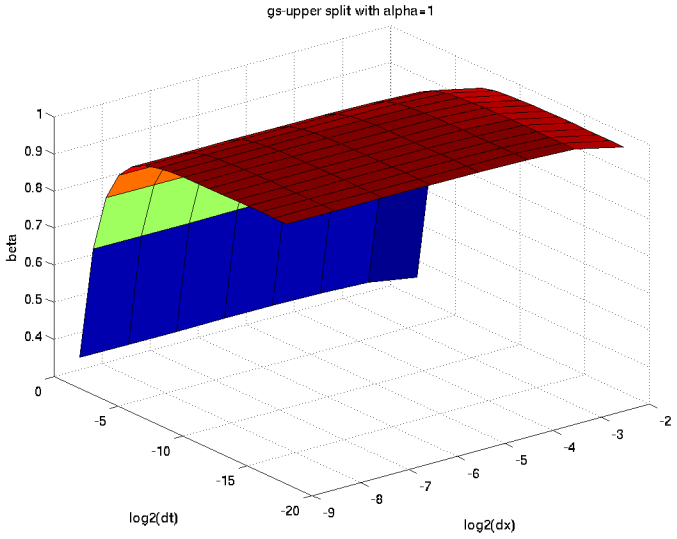

Figure 4.6: Threshold Surface β^* at various Δt and Δx values with $\alpha = 1$.

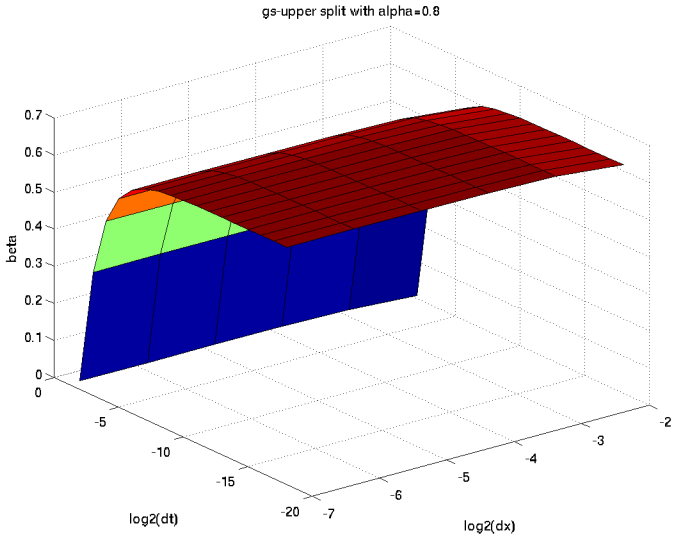

Figure 4.7: Threshold Surface β^* at various Δt and Δx values with $\alpha = 0.8$.

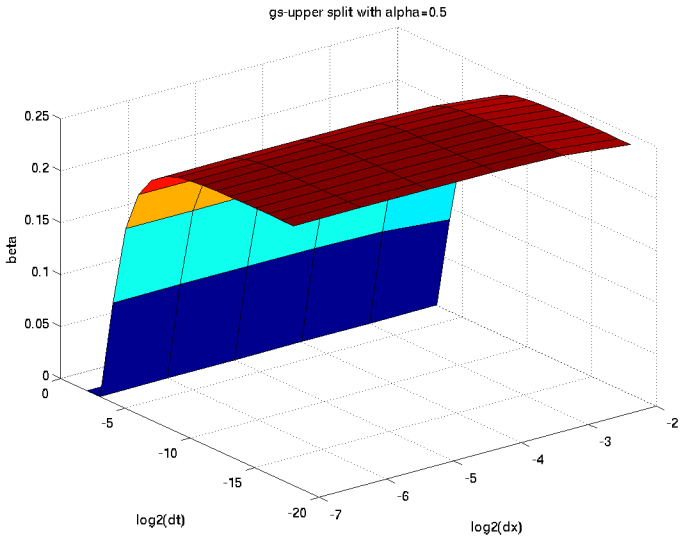

Figure 4.8: Threshold Surface β^* at various Δt and Δx values with $\alpha = 0.5$.

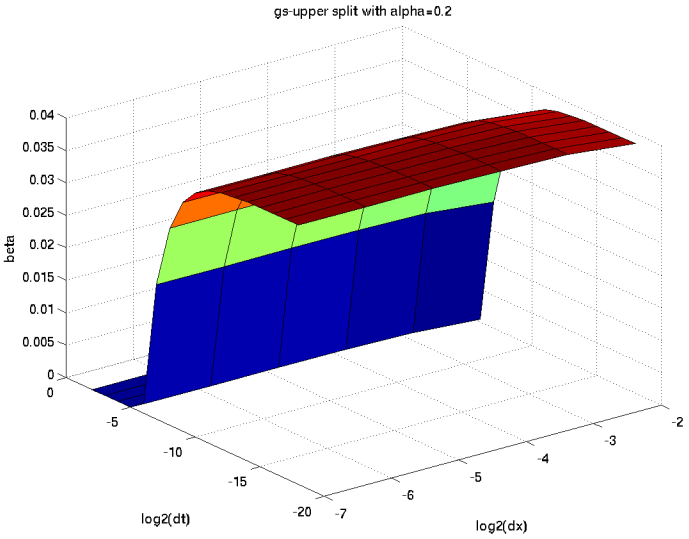

Figure 4.9: Threshold Surface β^* at various Δt and Δx values with $\alpha = 0.2$.

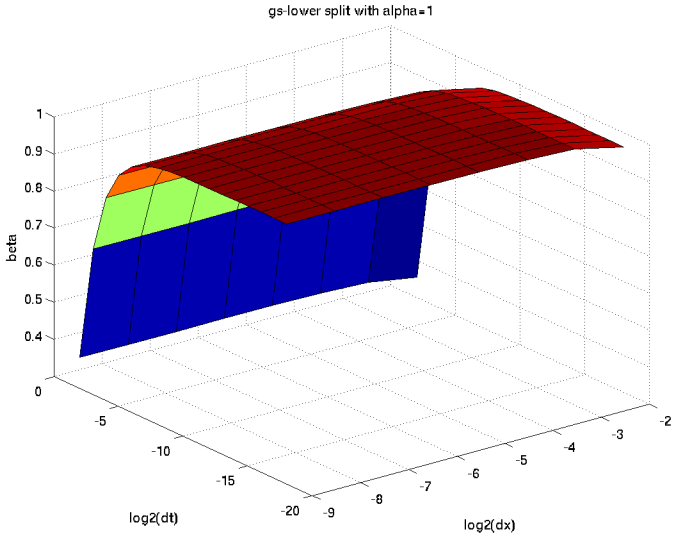

Figure 4.10: Threshold Surface β^* at various Δt and Δx values with $\alpha = 1$.

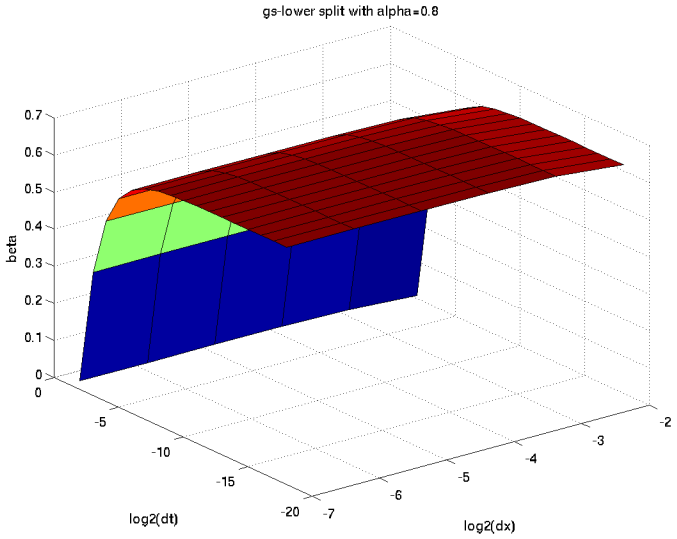

Figure 4.11: Threshold Surface β^* at various Δt and Δx values with $\alpha = 0.8$.

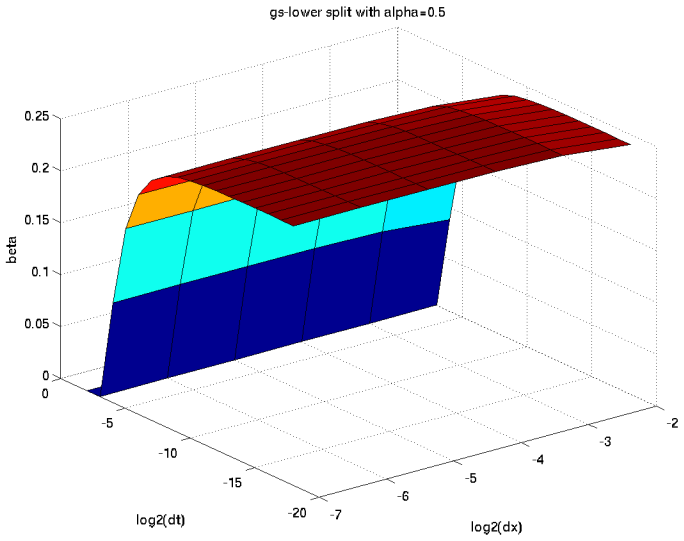

Figure 4.12: Threshold Surface β^* at various Δt and Δx values with $\alpha = 0.5$.

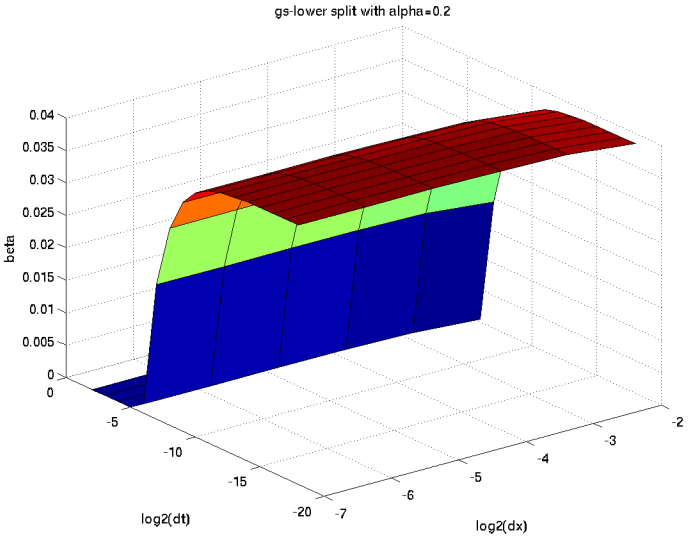

Figure 4.13: Threshold Surface β^* at various Δt and Δx values with $\alpha = 0.2$.

variations in possible choices $\nu(x)$ and $K(x)$ is beyond the scope of this thesis. We limit our current analysis to linear functions

$$\nu(x) = K(x) = mx + b > 0$$

with positive slope m. We also restrict our domain to the interval $[0, 1]$.

Motivated by the results of the non-dimensional constant coefficient case, we hypothesize that the values of $c_0\nu(x)$ play an essential role in the characterization of the convergence of the operator splitting methods. Without loss of generality, we restrict $c_0 = 1$ and $\alpha = 1$. In our tests, we also hold the slope m constant and determine the optimal threshold y-intercept b value which ensures convergence for each choice of Δt and Δx. Using the same framework as in Case I. We discretize the fully coupled and split equations by finite difference method on a staggered grid.

Based on the previous results, we predict that when $\nu(x) < 1$ for all $x \in [0, 1]$, the operator splitting diverges. Likewise, we expect the splitting method to converge when $\nu(x) \geq 1$ for all $x \in [0, 1]$. In this convergent case, we anticipate the rate of convergence to increase as as the $\min_{x\in[0,1]} \nu(x)$ increases. We also anticipate divergence if $\nu_{min} \leq \nu(x) \leq \nu_{max}$ for all $x \in [0, 1]$, with $0 < \nu_{min} < 1$ and $\nu_{max} > 1$.

Figures 4.14- 4.19 display the threshold y-intercept b surfaces at various Δt and Δx for constant $c_0 = \alpha = 1$. Each graph corresponds to a different value of the slope $m = 10^i$ for $i = -2, -1, ..., 3$ such that $\nu(x) = mx+b$. For the small positive slopes chosen in figures 4.14 and 4.15, the threshold surface b^* is bounded by the plane $b = 1$ over the range of Δt and Δx values tested. As before, the threshold surface is monotonically increasing as $\Delta t, \Delta x \to 0$ and $b^*(\Delta t, \Delta x) \to 0$ as Δt increases. This indicates that convergence can be ensured for fixed spatial discretization Δx by increasing the time step Δt. Further testing (not displayed) indicates that decreasing α also decreases in the asymptotic limiting plane which the threshold surface approaches, but never crosses.

As the slope m increases (figures 4.16- 4.19), the threshold surface b^* values decreases at all $(\Delta t, \Delta x)$. As shown in figure 4.16, the decrease in the threshold surface values

Table 4.2: Convergence for $c_0 = 1$

m	b	c_0	$\rho(M^{-1}N)$	iterations
0.2	0.9	1	1.01	Does not converge
0.2	1.0	1	0.96	162
0.2	1.1	1	0.92	16
0.2	2	1	0.68	8
0.2	5	1	0.44	6
0.2	20	1	0.2175	2

Table 4.3: Convergence for $c_0 = 0.5$

m	b	c_0	$\rho(M^{-1}N)$	iterations
0.2	1.8	0.5	1.02	Does not converge
0.2	1.9	0.5	0.98	522
0.2	2.0	0.5	0.96	168
0.2	5	0.5	0.61	14
0.2	20	0.5	0.2175	6

does not correspond to a vertical shift in the surface, but rather a lateral shift towards the origin in the Δx-Δt plane. In the case where $m = 100$ and $m = 1000$ (figures 4.18-4.19, respectively), the threshold surface reduces smaller than machine epsilon for double precision ($O(10^{-324})$. The plane $b = 1$ remains an asymptotic limit in these cases, despite not being visible in the range of $\Delta t, \Delta x$ displayed. This result indicates that the convergence of our operator splitting method is less restrictive for large Δx when material property gradient is large. In contrast, when the material property gradient is small, the threshold surface is nearly identical to the limit plane $b = 1$ over all Δt and Δx.

Tables 4.2-4.3 show the convergence behavior for various values of b and c_0 for $\alpha = 1$, $\Delta x = 0.002$ and $\Delta t = 0.001$. In the case with $c_0 = 0.5$, the optimal threshold y-intercept

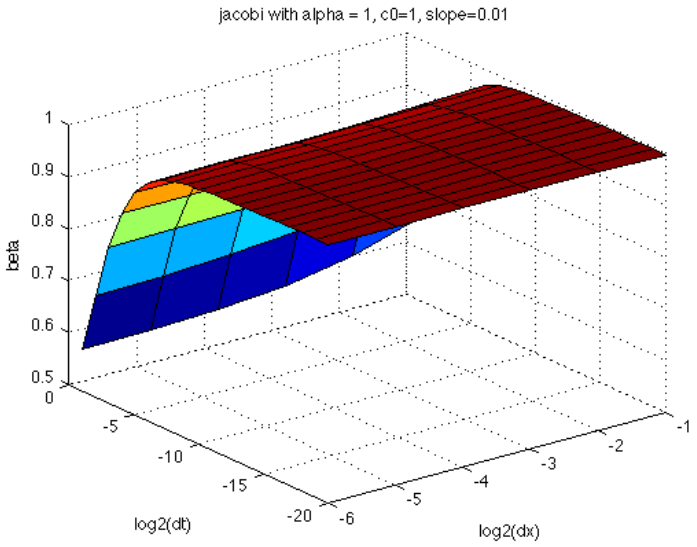

Figure 4.14: Threshold Surface of optimal y-intercept b^* values at various Δt and Δx values with $\alpha = c_0 = 1$ and $m = 0.01$.

b^* value is roughly double that of the case with $c_0 = 1$. This shift corresponds to a shift in the threshold surface upwards. Also, the optimal threshold b^* value shifts to slightly less than double the value with $c_0 = 1$. This is a byproduct of the variation encompassed by the slope $m = 0.2$. In this context, the value of the slope m shifts the threshold surface horizontally toward the origin in the Δx-Δt plane.

These findings contradict our initial assumption that the operator splitting method diverges when $\nu(x)$ obtains values less than and greater that unity in the domain $x \in [0, 1]$. It implies that the material property gradients play a significant role in characterizing the convergent problems for our proposed operator splitting methods. In the case of linear heterogeneity, our operator splitting method converges for a wider range of discretization choices Δt,Δx when a large gradient exists. However, the threshold surface increases as Δt, Δx decrease, approaching a limiting surface. This indicates that conditional stability holds for material properties under a limiting plane. The value of this plane strongly depends on the value of α and c_0.

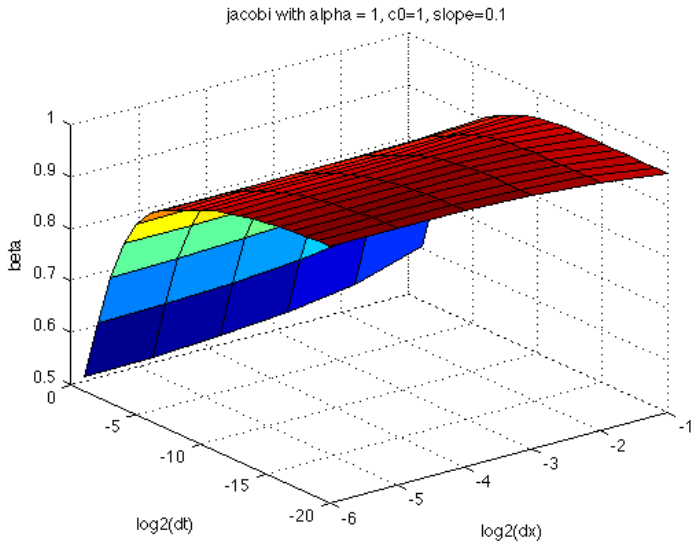

Figure 4.15: Threshold Surface of optimal y-intercept b^* values at various Δt and Δx values with $\alpha = c_0 = 1$ and $m = 0.1$.

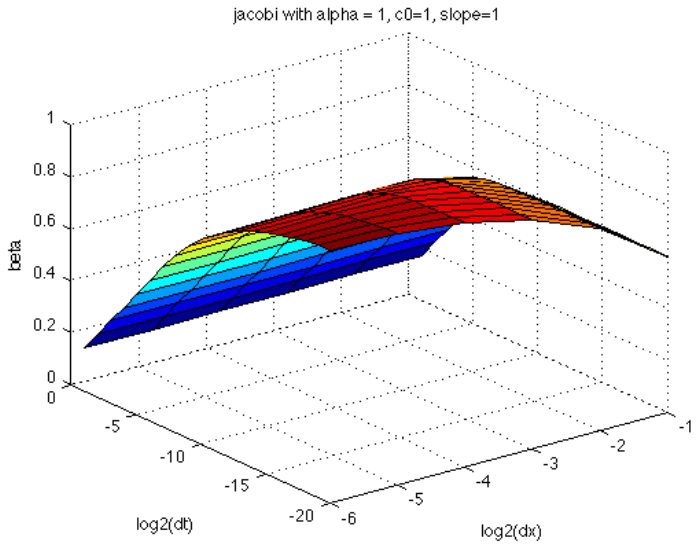

Figure 4.16: Threshold Surface of optimal y-intercept b^* values at various Δt and Δx values with $\alpha = c_0 = 1$ and $m = 1.0$.

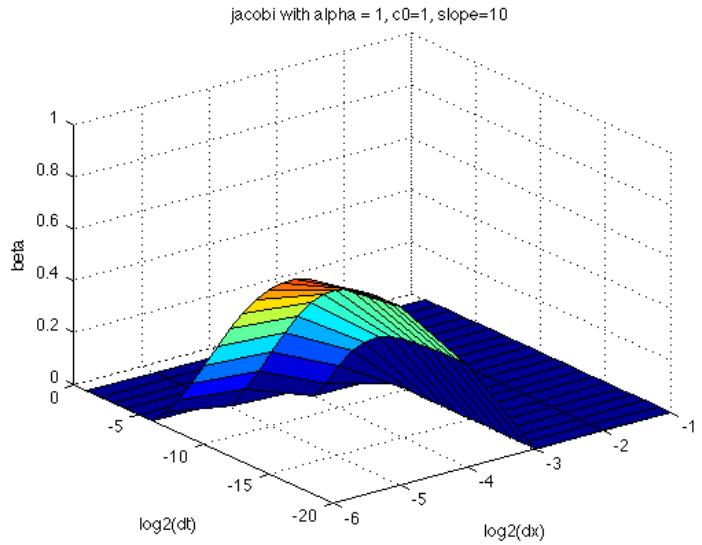

Figure 4.17: Threshold Surface of optimal y-intercept b^* values at various Δt and Δx values with $\alpha = c_0 = 1$ and $m = 10.0$.

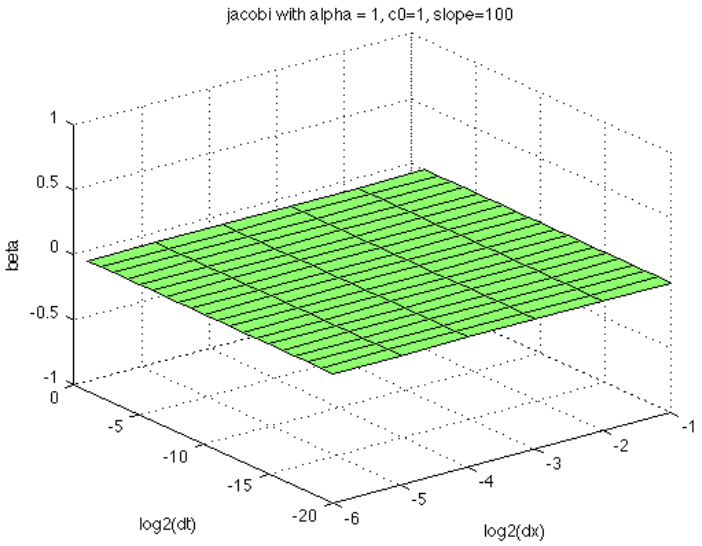

Figure 4.18: Threshold Surface of optimal y-intercept b^* values at various Δt and Δx values with $\alpha = c_0 = 1$ and $m = 100.0$.

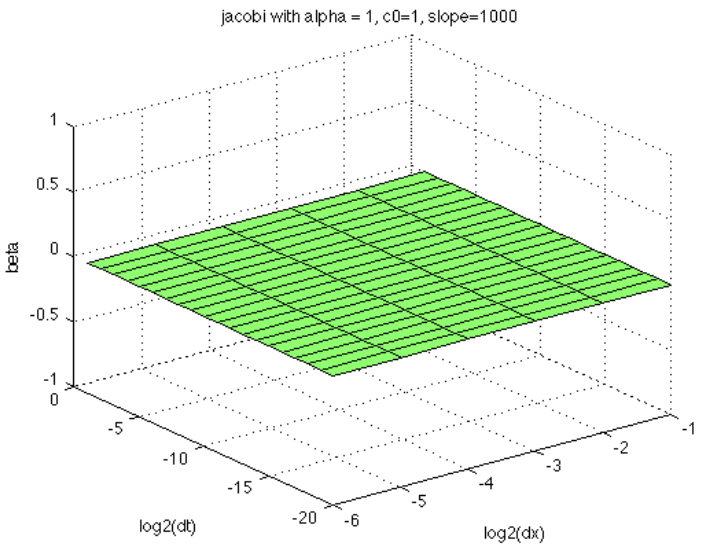

Figure 4.19: Threshold Surface of optimal y-intercept b^* values at various Δt and Δx values with $\alpha = c_0 = 1$ and $m = 1000.0$.

Chapter 5

1D Multiscale Experiments

In this chapter, we explore the convergence of the proposed multiscale method for fluid flow and solid deformation. We divide our analysis into three stages in which we verify the convergence of the following methods separately:

1. Chu et al.'s method for multiscale flow in porous media
2. Our multiscale solid deformation method
3. Our multiscale reaction-diffusion method

5.1 Verification of Chu et al.'s method

In our preliminary numerical verification experiments, we implemented Chu et al.'s method for fluid flow in porous media. We designed two dimensional medium consisting of a pore network of size 10×4096 throats of unit length L. Each interior pore is connected by four throats while boundary pores are connected by a single throat. The flux between flux is given as by the Hagen-Poisseuille Law. Additionally, a uniform pressure gradient was imposed with $p = 100$ on the left and $p = 0$ on the right axial boundaries (x-direction) and periodic conditions on the transverse boundaries (y-direction). For simplicity, a unit fluid viscosity was also used.

To confirm the convergence of the multiscale method, we vary the number of sampling subdomains μ and sample lengths δ to be positive integer powers of two such that $16 \leq \mu\delta \leq 4096 * L$. As illustrated in figure 5.1 samples of length δ are extracted from center of the subdomain $x_{l+\frac{1}{2}}$ of size Δx. Each sample pore network is of size $\delta \times 10$ throats.

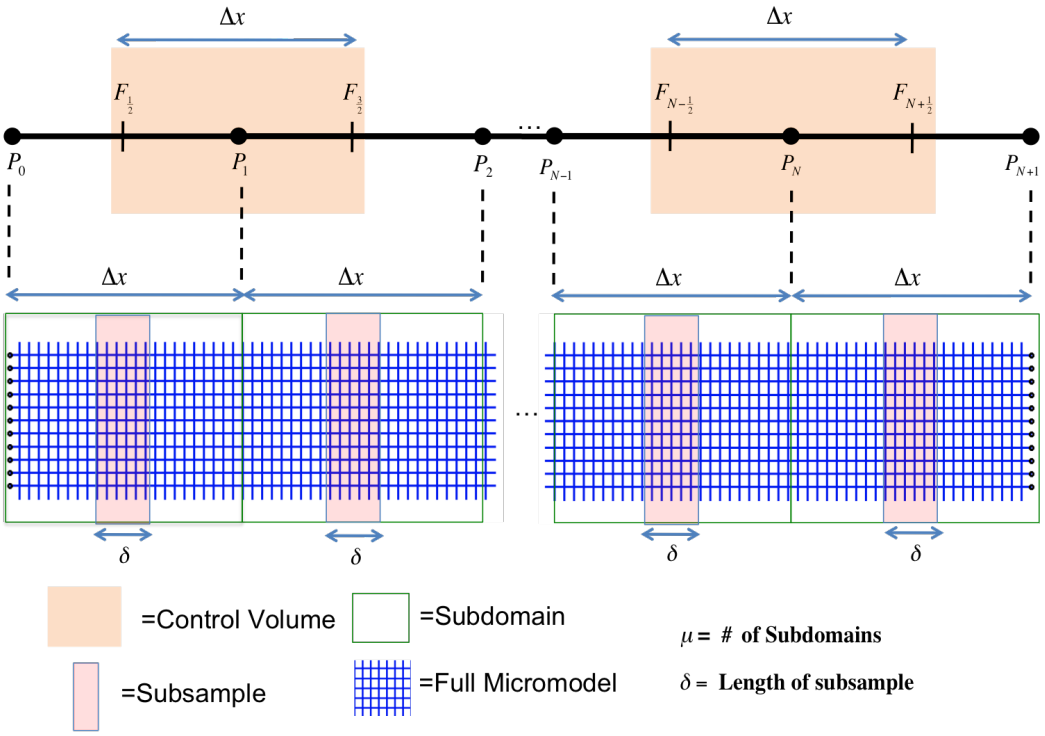

Figure 5.1: Illustration of a one dimensional multiscale flow model method sampling a two-dimensional pore network model

This ensures that the boundaries of all sampled pore networks correspond to nodes of the original network and no throats are artificially truncated.

To measure the error in the multiscale method, we compare the computed pressure and flux values to those of the fully microscopic pore network model consisting of 10×4096 throats. Note that the macroscopic pressure values computed in the multiscale method are in a one-dimensional domain, but the fully microscopic model is two dimensional. To compare, we average the pressure values along each vertical cross-section of the fully microscopic pore network model and compare only those pressure values at locations collocated in the macroscopic grid of the multiscale model. We define the relative ∞-norm metric in pressure and flux respectively as $e^p_\infty \equiv \frac{||P_m - P_d||_\infty}{||P_d||_\infty}$ and $e^F_\infty \equiv \frac{||F_m - F_d||_\infty}{||F_d||_\infty}$, where P_m and F_m are the pressure and flux values obtained from the multiscale method while P_d and F_d are the average pressure and flux values obtained from the fully microscopic model. In this

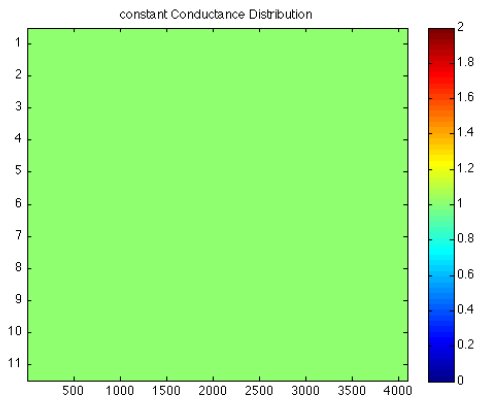

Figure 5.2: Conductance distribution for Fluid Flow Case I.

context, the infinity norm error produces the maximum error between the fully microscopic and multiscale models only at overlapping grid points. All other grid points of the fully microscopic model are ignored.

According to [27, 26], the multiscale method converges in a single iteration from any initial guess of the vector of macroscopic pressure values P satisfying the macroscopic boundary conditions assuming that the microscopic conductance is linear. In our experiments, we allow the multiscale method to iterate between micro and macroscale models until the maximum error in pressure between two consecutive iterations is less than $\epsilon \equiv 10^{-8}$. In all experiments, we chose the initial guess of macroscopic pressure to be linearly distributed between the (dirichlet) boundary conditions.

We conduct three classes of numerical experiments to verify the accuracy of the multiscale flow model. The three experiments correspond to different distributions of conductances within the fully microscopic model. Figures 5.3- 5.4 depict the conductances for the three cases tested.

In experiment I, we assume constant conductance values $g = 1$ at all locations in the fully microscopic grid. In this case, we hypothesize that all simulations, irrespective of sample size or number of sampling domains, converge to the same solution with the same accuracy.

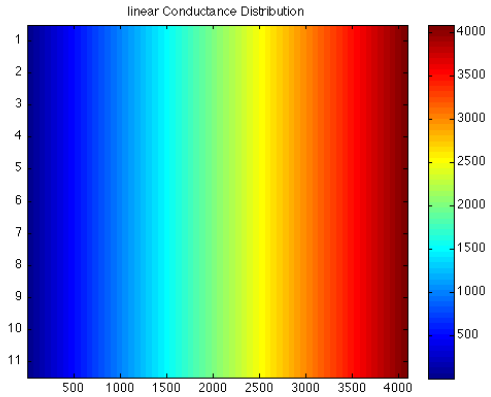

Figure 5.3: Conductance distribution for Fluid FLow Case II.

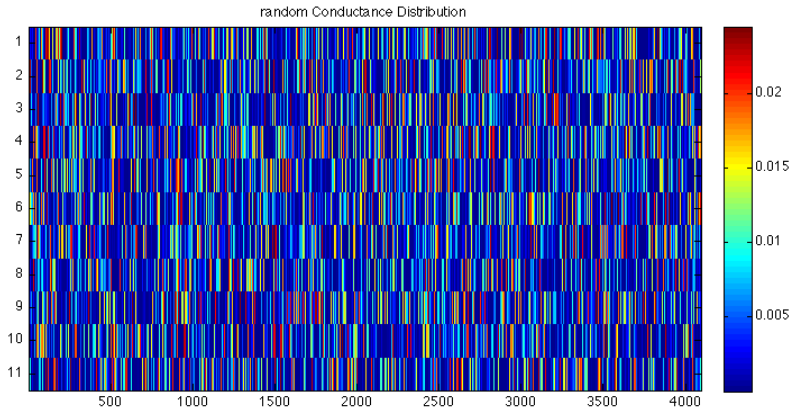

Figure 5.4: A random conductance distribution for Fluid Flow Case III.

In experiment II, we assume linearly increasing conductance values from the left to the right of the domain. $g(x) = x$ where x is the x-component of the coordinates center of the throat. As such, there is no variation in conductance values across any vertical cross-section in the fully microscopic model. All variations in conductances are in the horizontal direction. In this case, we hypothesize that the structured nature of the conductance values should lead to rapid convergence.

In experiment III, we assume the conductances are distributed randomly throughout the fully microscopic model. We generate the random conductances by randomly assigning

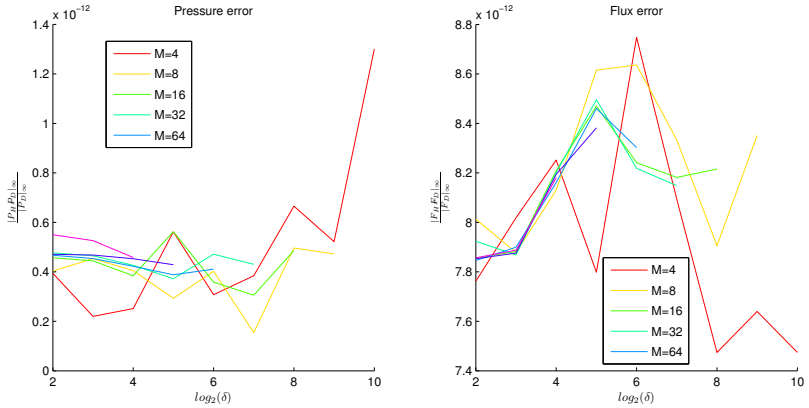

Figure 5.5: Experiment I Constant μ Analysis: Solid lines represent a constant number of sampling domains μ with relative errors displayed for pressure (left) and flux (right).

throat radii of the throats in the model. In our experiments, the throat radii are uniformily randomly assigned in a range $[r_{min}r_{max}]$, with $r_{min} = 0.005$ to $r_{max} = 0.5$. Since the Hagen-Poisseuille Law assigns conductance in quartic proportion with the radius of the throat connecting two pores this corresponds to a conductance range $[2.25 \times 10^{-10}, 2.25 \times 10^{-2}]$. To remove any bias in error calculation due to the distribution, we conduct 100 separate tests, each with its own separate initial distribution. Within each individual test, all subsequent error analysis varying the number of sampling domains μ and sample size δ is conducted on the same initial conductance distribution. Finally, all relative pressure and flux errors for each combination of μ and δ are averaged.

5.1.1 Experiment I

Recall that in Experiment I, we assume a constant conductance value distributed throughout the fully microscopic model. In this case, we previously assumed that the relative errors would be nearly zero in all cases. Clearly, Figures 5.5 and 5.6 illustrates that non-zero errors exist between the multiscale solution and the fully microscopic solution. Figure 5.5 illustrates the convergence of the multiscale method holding the number of sampling subdomains μ constant and varying the size of the sampling domain. Figure 5.8 illustrates

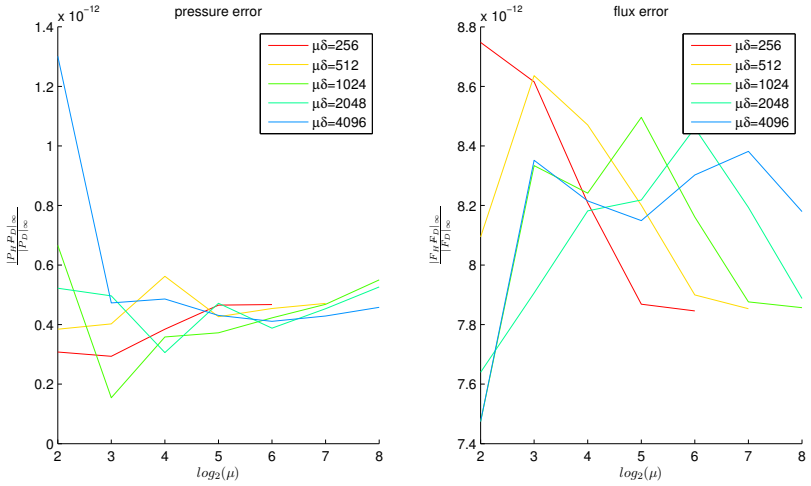

Figure 5.6: Experiment I Constant $\mu\delta$ Analysis: Solid lines represent a constant total sampling area $\mu\delta$ with relative errors displayed for pressure (left) and flux (right).

the convergence behavior as the total sampling area $\mu\delta$ is held constant and the number of sampling domains increases. The relative error is less than 1.4×10^{-12} for pressure and 8.6×10^{-8} in flux. Though the flux errors remained slightly larger in magnitude the flux errors, both were extremely small and nearly equal to the convergence criterion parameter ϵ.

Note that in all cases of Experiment I, the multiscale method converged in only two multiscale iterations, which is the minimum number possible under our constraints. Further experimentation with consecutive iteration error $\epsilon = 10^{-11}$ revealed higher accuracy, but required considerably more iterations. Further analysis of the absolute error in pressure $||P_m - P_d||_\infty$ shows the error oscillates at values between 10^{-10} and 10^{-11}. Using different suitable initial guesses, we observe that the multiscale method does in fact acheive considerable accuracy in the first iteration, but fails to improve this error significantly in subsequent iterations. This result indicates that the multiscale method gives a relatively accurate answer, but converges cannot achieve arbitrary accuracy even in the constant conductance case.

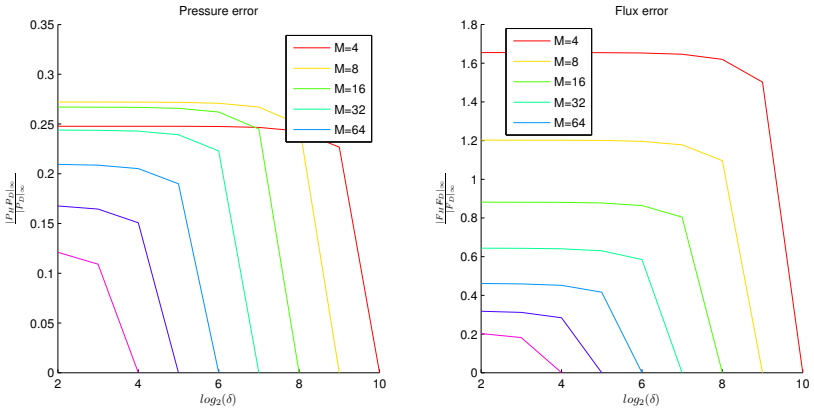

Figure 5.7: Experiment II Constant μ Analysis: Solid lines represent a constant number of sampling domains μ with relative errors displayed for pressure (left) and flux (right) in the linearly varying conductance case.

5.1.2 Experiment II

In experiment II, conductances remain constant along each vertical cross-section but vary linearly in the x-direction. We previously hypothesized that the structured nature of the conductance model would lead to fast convergence behaviors. Figures 5.7- 5.8 illustrate that the convergence behavior is much slower than expected. In Figure 5.7 shows the behavior as the number of sampling subdomains is held constant and the sample sizes successively double. It is easy to see that relative errors are high initially and do not decrease significantly until all possible information in the fully microscopic model is utilized.

Figure 5.8 illustrates the convergence behavior holding the total sampling area $\mu\delta$ constant and varying the number of sampling subdomains. We observe an interesting phenomenon: a slight initial increase in pressure errors when the number of sampling subdomains increases from $\mu = 2^2$ to $\mu = 2^3$. After this initial spike, the pressure errors decrease monotonically. The relative flux errors are significantly higher than the relative pressure errors in all cases except when $\mu\delta = 4096$. In other words, high accuracy is only achieved in the case when the total sampling area is equal to the total area of the domain. We interpret this case as a Domain Decomposition case because the sampling subdomains form

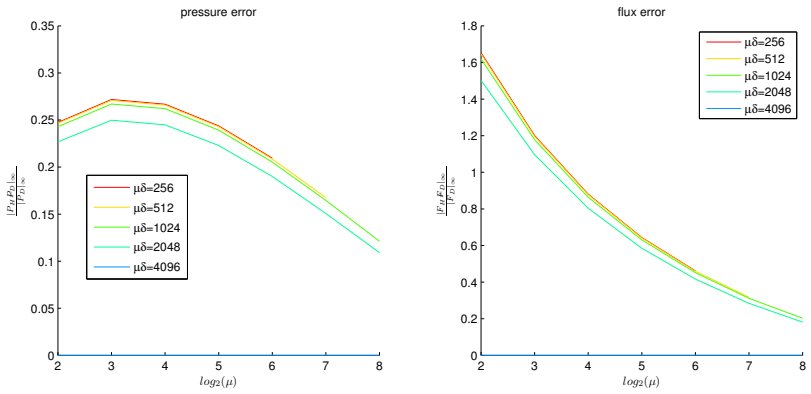

Figure 5.8: Experiment II Constant $\mu\delta$ Analysis: Solid lines represent a constant total sampling area $\mu\delta$ with relative errors displayed for pressure (left) and flux (right) in the linearly varying conductance case.

a complete, non-overlapping partition of the computational domain.

5.1.3 Experiment III

In experiment III, 100 tests were conducted using random conductances obtained from a uniformly random throat radii distribution. Each test consisted of fixing the conductance values initially and varying the number of sampling subdomains μ and sample size δ analogously as in Experiments I & II. After 100 tests, the results from each $\mu\delta$ combination are averaged and presented in figures 5.9- 5.10 with a logarithmic scale in the x-axis.

Figures 5.11- 5.14 compare a typical multiscale solutions to the solution of the fully microscopic model. The solid bold line represents the average pressures along each cross-section of the fully microscopic model at all points. The open circles at the end of each vertical line represents the approximated multiscale solution at the discrete point. Note that all error measures are the maximum difference between overlapping points between the macroscopic grid and the fully microscopic model. Observing these particular instances may lead the reader to believe that smaller sample sizes (e.g. $\delta = 4$in figure 5.11) lead to smaller errors than larger sample sizes (e.g. $\delta = 8$ in figure 5.12). However, the average

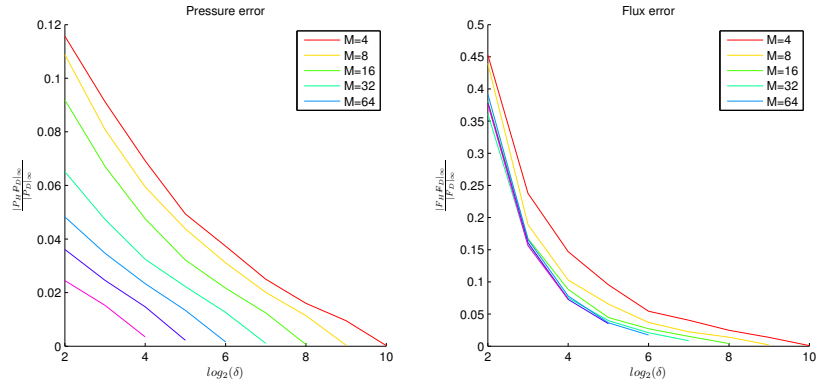

Figure 5.9: Experiment III Constant μ Analysis: Solid lines represent a constant number of sampling domains μ with relative errors displayed for pressure (left) and flux (right) in the random conductance case.

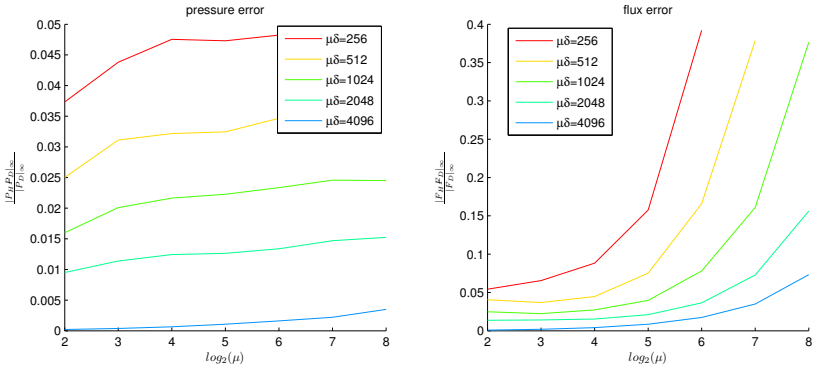

Figure 5.10: Experiment III Constant $\mu\delta$ Analysis: Solid lines represent a constant total sampling area $\mu\delta$ with relative errors displayed for pressure (left) and flux (right) in the random conductance case.

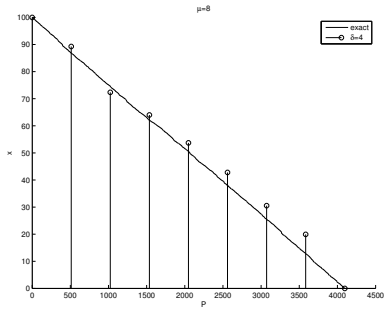

Figure 5.11: Comparison between the averaged fully microscopic solution and the multiscale solution with $\mu = 8$ subdomains and sample size $\delta = 4$.

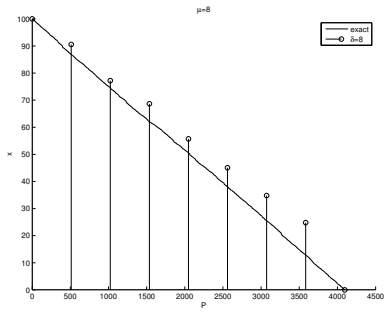

Figure 5.12: Comparison between the averaged fully microscopic solution and the multiscale solution with $\mu = 8$ subdomains and sample size $\delta = 8$.

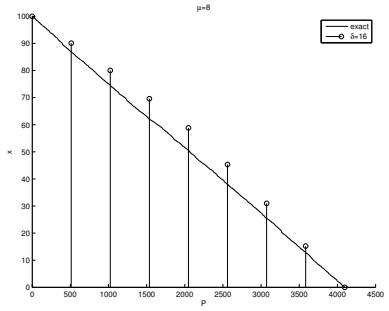

Figure 5.13: Comparison between the averaged fully microscopic solution and the multiscale solution with $\mu = 8$ subdomains and sample size $\delta = 16$.

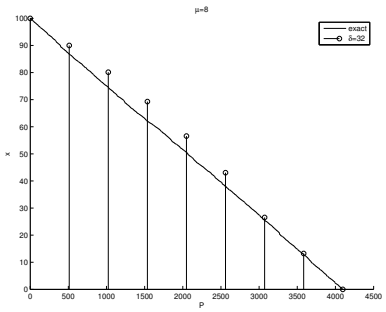

Figure 5.14: Comparison between the averaged fully microscopic solution and the multiscale solution with $\mu = 8$ subdomains and sample size $\delta = 32$.

trend as the sample size δ increases shows that the multiscale solution approaches the cross-section averaged solution of the fully microscopic model.

The results in figure 5.9 indicate that relative errors of both pressure and flux uniformily decrease when the number of sampling subdomains μ is held constant and the sample size δ increases. However, the results in figure 5.10 indicate that neither pressure nor flux achieve convergence when the total sampling area is constant and the number of sampling subdomains increases. In this case, the relative pressure error increases slightly, but the flux error increases dramatically.

Under analogous testing parameters, Chu et al.[27] encountered similar divergent tendencies. They reported that this lack of convergence is a byproduct of the constant boundary conditions imposed upon the local pore network models sampled from the fully microscopic model. The random distribution of conductances ensures that the true pressure across any vertical cross-section of the fully microscopic model is non-constant with probability 1. Hence, as more sampling subdomains are used, more vertical cross-sections are artificially held constant. This modeling error increases significantly and is in stark contrast to the convergence behavior observed in figure 5.9.

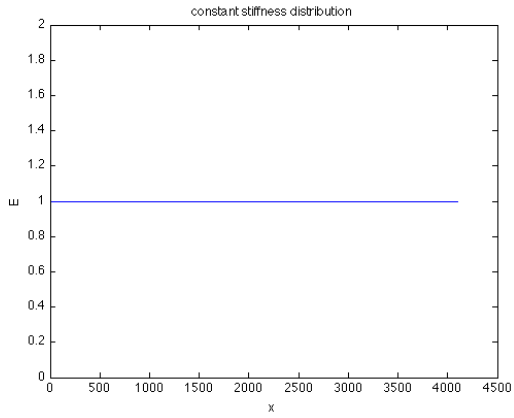

Figure 5.15: Stiffness distribution for Solid Deformation Case I.

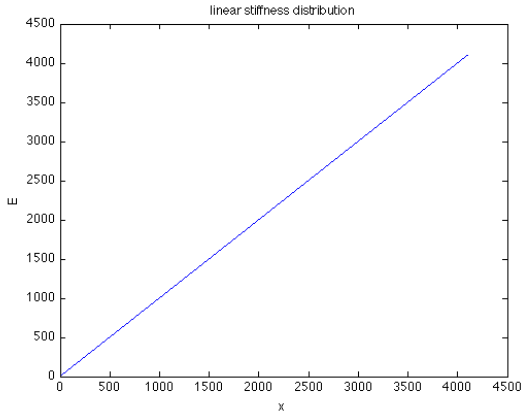

Figure 5.16: Stiffness distribution for Solid Deformation Case II.

5.2 Multiscale Solid Deformation

Like the multiscale flow experiments, we test the convergence of the multiscale deformation model with constant, linearly varying and random stiffnesses E_{ij}. Like the previous experiments, we use $E = 1$ for all springs in experiment I and $E(x) = x$ in experiment II. In experiment III, we choose stiffnesses from a uniformly random distribution in the interval $[1, 1000]$. Figures 5.15- 5.17 displays the stiffness distributions for the three experiments. Again, we choose the number of sampling subdomains μ and sample lengths δ as positive integer powers of two.

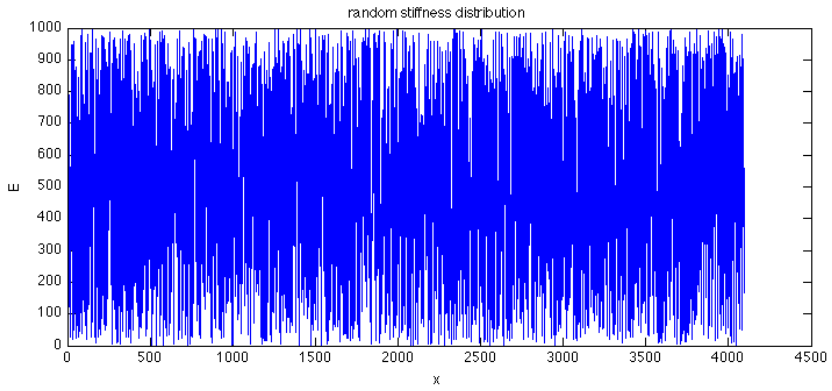

Figure 5.17: A random stiffness distribution for Solid Deformation Case III.

In all experiments, the fully microscopic model consists of $|\Omega| \equiv 2^8 = 4096$ spring elements with unit length and cross-sectional area. Consequently, we choose μ & δ as positive integer powers of two such that $\mu\delta \leq 4096$. We also impose purely dirichlet boundary conditions at the macroscopic level and compare the multiscale solutions to the solution of the fully microscopic model.

Based on the convergence behaviors observed in the multiscale flow algorithm, we predict that the multiscale deformation algorithm will have analogous behaviors. In Experiment I, we predict uniformly small relative errors in displacement and total force, regardless of the choice of μ and δ when all spring stiffnesses are constant. In Experiment II, we expect very small relative errors only when the multiscale model fully samples the underlying micro models; i.e. when $\mu\delta = 65,536$. In the case with μ constant and δ increases, we expect to see significant reduction in relative errors only when $\delta islarge$. In experiment III, we expect to observe convergence with μ constant and δ increasing, but not when $\mu\delta$ is constant and μ increasing.

5.2.1 Results

Figures 5.18- 5.23 show analogous convergence behaviors in displacement and total boundary force for the three cases considered as observed in the multiscale flow problem in the

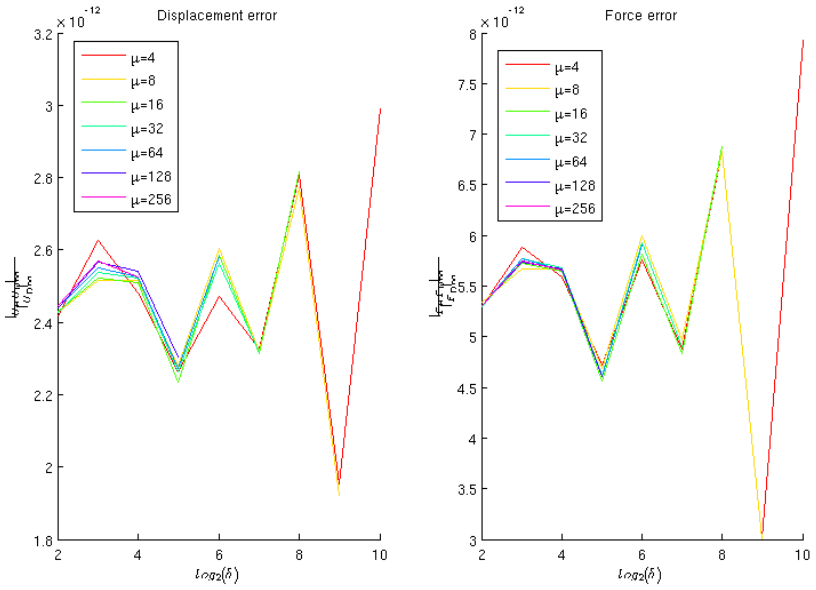

Figure 5.18: Multiscale deformation errors for constant stiffness and constant μ, varying sample size δ

previous section.

Small fluctuations in displacement and force errors exist when the stiffnesses are constant throughout the medium(figures 5.18- 5.19). The relative errors fluctuate within less than $10^{-}11$, indicating nearly constant accuracy 5.18. Analysis with constant sampling area (figure 5.19) shows that as the number of sampling subdomains μ increases, the relative errors in displacement and force fluctuate closer and closer to approximate asymptotes at 2.4×10^{-12} and 5.2×10^{-12}, respectively. The small relative errors across all simulations indicates that the multiscale algorithm converges with reasonable accuracy in the constant stiffness case.

Figures 5.20- 5.21 illustrate the convergence behavior for a medium with linearly increasing stiffness. An analogous phenomenon occurs as discovered in Experiment II of the multiscale flow problem in the previous section. Initial relative errors are large, but incrementally decreases as the sample size increases. In the simulations with full sampling $\mu\delta = |\Omega| = 4096$, relative errors are significantly smaller (relative error $< 10^{-10}$) than all

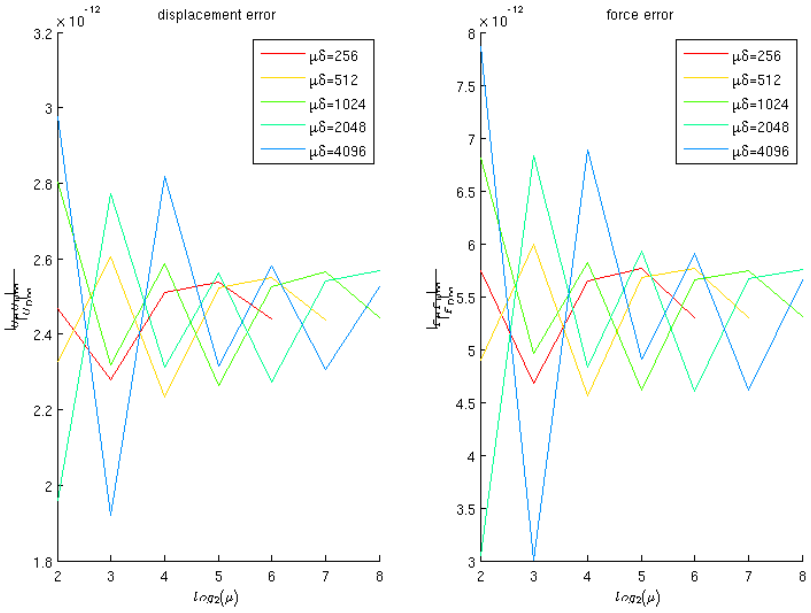

Figure 5.19: Multiscale deformation errors for constant stiffness and constant sampling area $\mu\delta$, varying number of sampling subdomains μ

other simulations. This indicates that the multiscale algorithm operates most effectively as a full domain decomposition method in this case. Holding μ constant, we observe uniform decrease in error as δ (figure 5.20) increases. Maintaining a constant sampling area $\mu\delta$, we observe a slight initial increase in relative error as μ increases from 2^2 to 2^3 sampling subdomains. After this initial increase, all other errors decay uniformly with increasing μ.

Figures 5.22- 5.23 illustrate the resulting averaged relative errors after 100 tests with uniformly random distributed stiffnesses $E \in [1, 1000]$. Figure 5.22 apparently illustrates that both displacement and force errors decrease uniformly with increasing μ and δ. However, Figure 5.22 clearly shows that the algorithm is divergent in displacement and force for constant $\mu\delta$ and increasing μ.

These results are consistent with the multiscale flow simulations in the previous chapters and with the results in [27, 26]. In [27, 26], they tested a fully two dimensional microscopic flow model with a one dimensional macroscopic model. They attributed lack of convergence

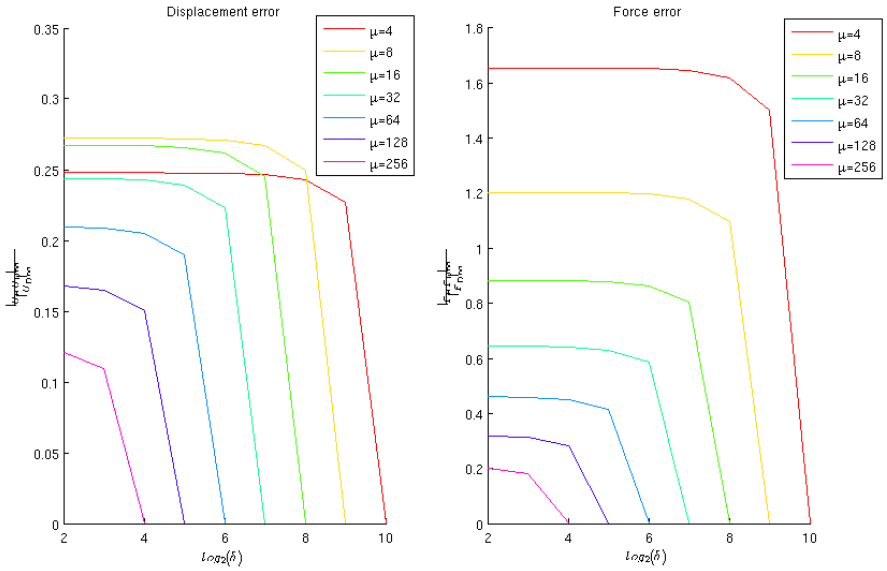

Figure 5.20: Multiscale deformation errors for linearly increasing and constant μ, varying sample size δ

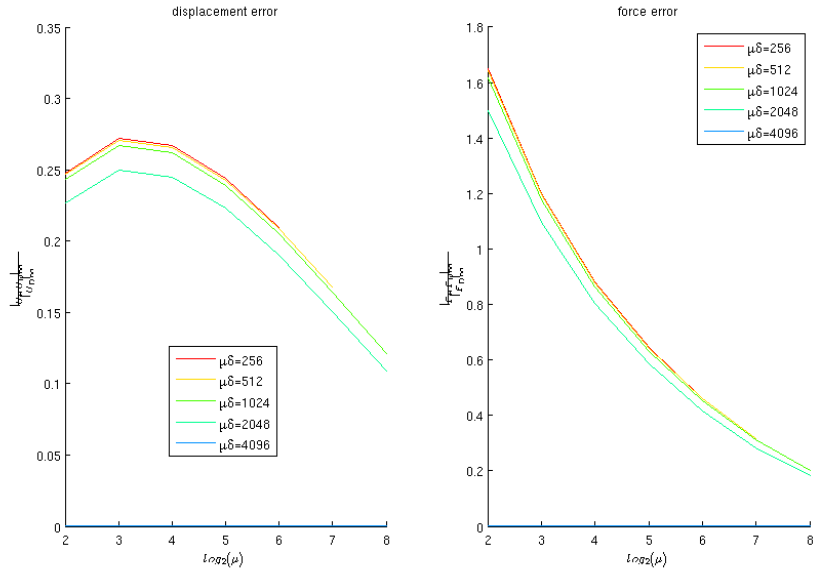

Figure 5.21: Multiscale deformation errors for linearly increasing stiffness and constant sampling area $\mu\delta$, varying number of sampling subdomains μ

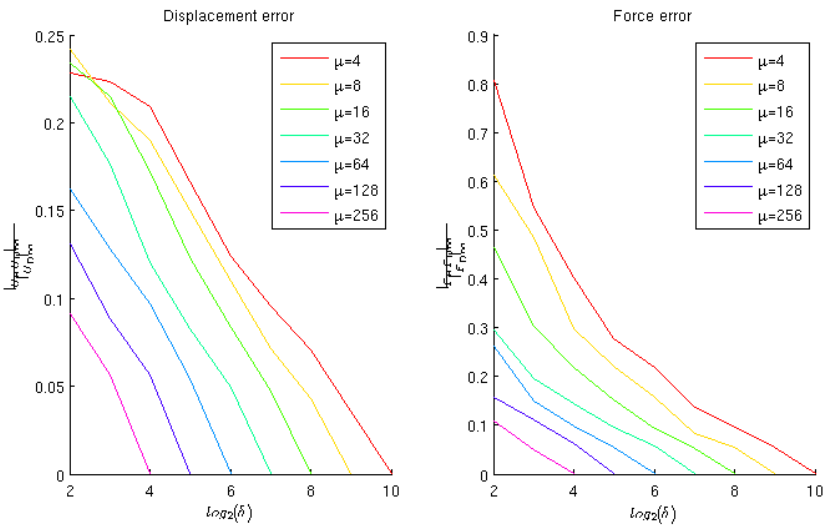

Figure 5.22: Average multiscale deformation errors for 100 random stiffness tests with constant μ, varying sample size δ

to the artificially constant dirichlet boundary condition imposed on vertical cross-sections of the two dimensional model despite non-constant (random) conductances along these cross-sections. It was argued that larger numbers of sampling subdomains μ result in more micro models with artificially constant dirichlet conditions and thus greater errors. Our results indicate that this may not be entirely accurate. Our model uses a one-dimensional fully microscopic and macroscopic model, but results in analogous divergent behavior as μ increases. We explore possible explanation of this phenomenon in the next chapter.

5.3 Multiscale Elliptic Reaction-Diffusion

We use the same testing framework as introduced in section 5.1 to test our multiscale elliptic reaction diffusion algorithm to solve

$$-\frac{d}{dx}\left(K(x)\frac{dp}{dx}\right) + c^*P = f.$$

The fully microscopic model is a two dimensional rectangular lattice network model with 4096×10 edges, each of unit length; yielding a one dimensional macroscopic domain

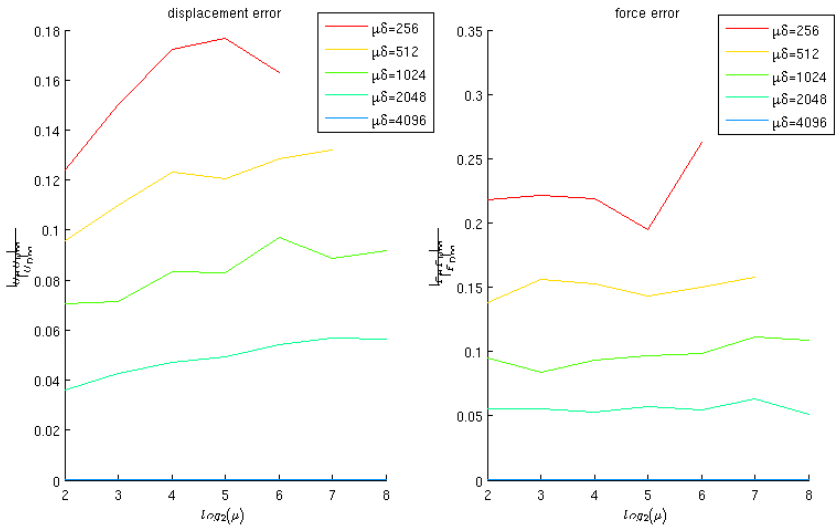

Figure 5.23: Average multiscale deformation errors for 100 random stiffness tests with constant sampling area $\mu\delta$, varying number of sampling subdomains μ

$\Omega \equiv [0, 4096]$. We impose purely dirichlet boundary conditions $P_L = 100$ and $P_R = 0$ at the left and right cross-sectional boundaries of model. We use its solution as the basis of comparison with the multiscale method. Again, we choose μ and δ as positive integer powers of two such that $\mu\delta \leq 4096$ and compare the multiscale solution to the fully microscopic solution.

In this case, we examine the convergence behavior of the constant coefficient case with $K(x) = 1$ and the the linear case with $K(x) = x$. Without loss of generality, we choose $c^* = 1$ in both cases. We only measure the relative pressure error measure in the L^∞ norm and do not consider the flux error. For additional comparison, we also compute errors in the finite difference solution on a mesh with $N = \mu$ equispaced intervals. The finite difference method uses a 2nd order centered spatial difference to approximate the second derivative term in the PDE. We hypothesize that the relative errors will be consistent with the behavior observed in the previous two sections. That is, we suspect relative errors on the order of 10^{-12} in all cases, with some fluctuations no greater than 10^{-11}. We also hypothesize no significant difference between the finite difference and multiscale solutions

for a given $\mu = N$.

5.3.1 Results

Figure 5.24 depicts the exact, finite difference, and multiscale solutions on a logarithmic y-axis for a given $N = \mu$ and sample length $\delta = 4$. Visually, it appears as though the non-linear nature of the fully microscopic solution is more easily captured by both the finite difference and our multiscale method when the number of macroscopic gridpoints increases. Examination of the relative errors in tables 5.1- 5.2, however, suggests a different story. As the macroscopic grid refines, larger errors are incurred in both the finite difference and multiscale methods. This apparent divergence is simply a by-product of the scale of heterogeneity in the true solution itself. At a very small length scale, the solutions sharply drop from the left boundary condition value $P_L = 100$ to nearly 0. Though the mesh is refined, the spatial stepsize is never completely refined to scales smaller than the finite interval containing this drop; neither for the finite difference nor for the multiscale model. Thus, the discrete solutions increase in absolute error as they approximate the large initial drop in values.

Figure pairs 5.26- 5.27 and 5.28- 5.29 show the convergence behavior for the constant and linearly varying conductance cases, respectively. In the constant case, our multiscale method converges to more accurate solutions than the finite difference solution as the sample lengths δ increase. As the number of sampling subdomains μ increases, errors apparently increase. However, as with the finite difference method, this is a byproduct of the inability of the macroscopic grid to capture the behavior in the heterogeneous region near the left boundary condition.

The linearly varying case exhibits dramatically distinct behavior in comparison to the analogous cases for solid deformation and Chu et al.'s model. Figure 5.25 shows that the non-constant conductance intensifies the decay in the solutions. This decay is illustrated by the smaller boundary layer near the x_0. The multiscale method's convergence more closely resembles the behavior of the constant case in the reaction diffusion problem. That

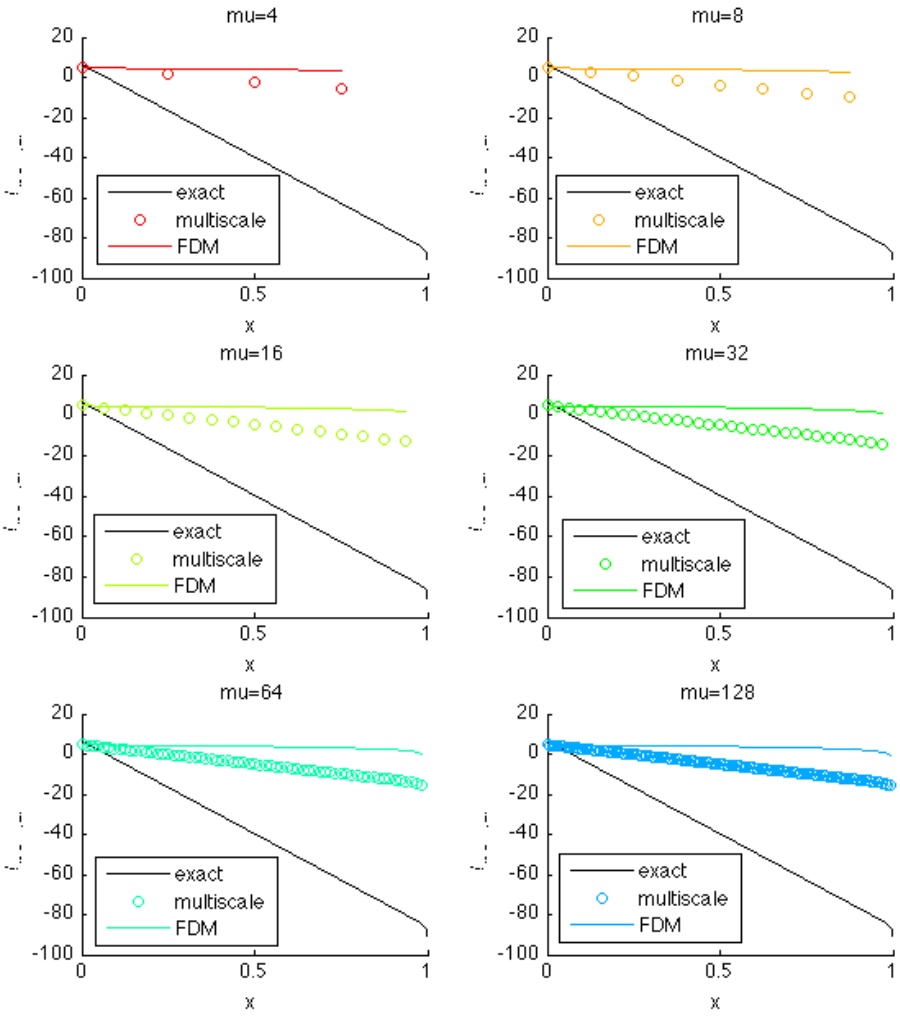

Figure 5.24: Exact, finite difference, and multiscale solutions to the reaction-diffusion equation with constant conductance $K(x) = 1$ and various number of sampling subdomains μ and $\delta = 4$. All graphs are plotted with a logarithmic scale on y-axis.

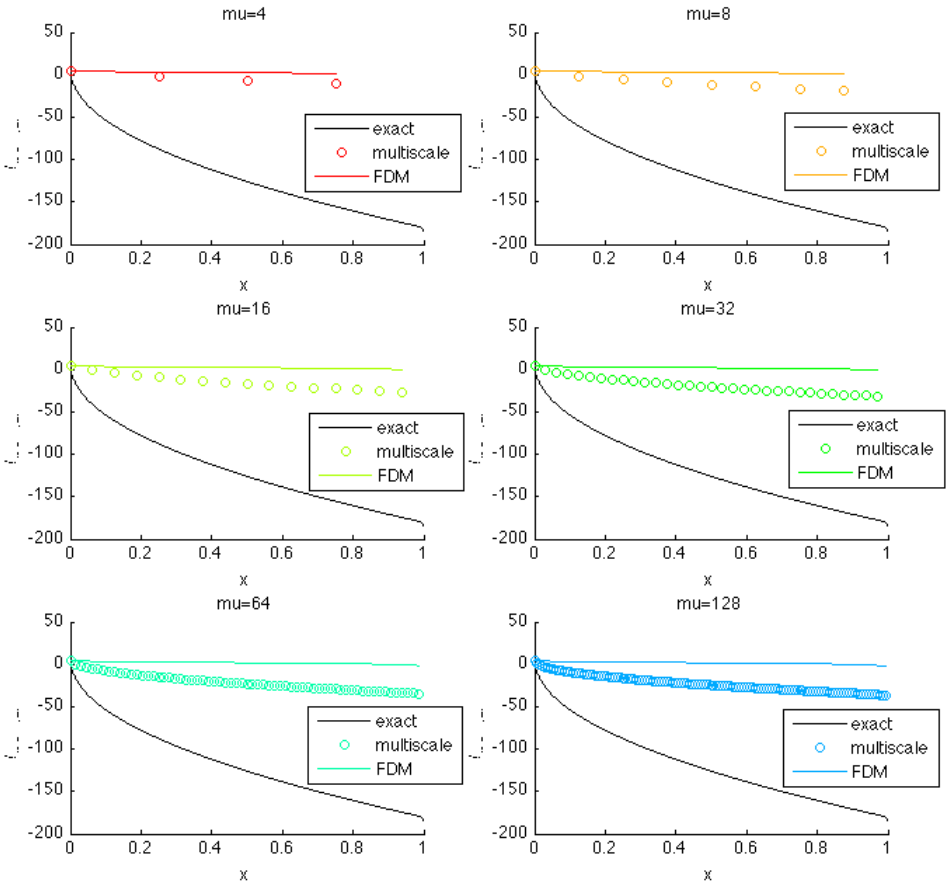

Figure 5.25: Exact, finite difference, and multiscale solutions to the reaction-diffusion equation with linearly increasing conductance $K(x) = x$ and various number of sampling subdomains μ and $\delta = 4$. All graphs are plotted with a logarithmic scale on y-axis.

Table 5.1: Relative Error in multiscale model solution w.r.t. fully microscopic model in the constant conductance case

		δ						
		4	**8**	**16**	**32**	**64**	**128**	**256**
μ	**4**	1.1154e-08	2.1192e-14	3.8248e-26	8.2631e-98	7.2690e-194	0	0
	8	8.9059e-08	6.7419e-13	1.9318e-23	7.9306e-45	6.6827e-88	2.3726e-174	9.9233e-215
	16	7.0971e-07	2.1325e-11	9.6264e-21	9.8081e-40	5.0910e-78	9.9616e-108	9.9616e-108
	32	5.6340e-06	6.6683e-10	4.6706e-18	1.1457e-34	3.1562e-54	3.1562e-54	
	64	4.4385e-05	2.0390e-08	2.1512e-15	1.7646e-27	1.7766e-27		
	128	3.4443e-04	5.9735e-07	8.5496e-13	4.2149e-14			
	256	2.5905e-03	1.5969e-05	2.0499e-07				

is, the relative errors decrease significantly as the number of sampling subdomains μ is held constant and the sample length increases. However, holding the total sampling area $\mu\delta$ constant and increasing μ, relative errors increase. This behavior is akin to the divergent behavior observed in the random heterogeneous cases for solid deformation and Chu et al.'s model. This increase in error is reflective of the macroscopic grid's inability to capture a steep, continuous gradient in a boundary layer near x_0.

The results above suggest that application to the heterogeneous (random) case would exhibit similar characteristics. At first glance, figure 5.30 seems to indicate positive results. Upon closer inspection, we observed two unexpected tendencies in our numerical results. First, the algorithm frequently generates ill-conditioned macroscopic matrix systems. The ill-conditioned systems are a consequence of the iterative algorithm approximating values less than machine precision and can be avoided by carefully choosing the convergence criterion. Secondly, and more problematically, the algorithm often generated negative pressure and flux values. Further investigation revealed that monotonicity was not preserved in the micromodels. Clearly, the lack of source terms in the elliptic PDE suggests that pres-

N	Relative Error
4	1.1154e-08
8	8.9059e-08
16	7.0971e-07
32	5.6340e-06
64	4.4385e-05
128	3.4443e-04
256	2.5905e-03

Table 5.2: Relative Error in finite difference solution w.r.t. fully microscopic model

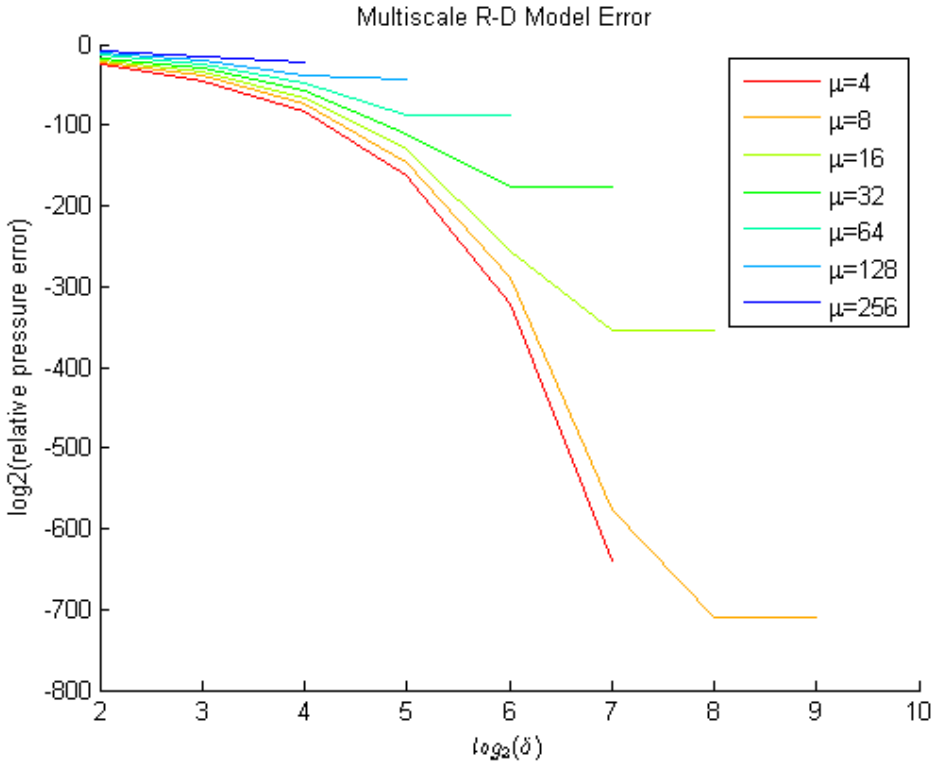

Figure 5.26: Logarithms of relative pressure error for Multiscale Reaction-Diffusion PDE with constant conductance; holding μ constant and increasing δ.

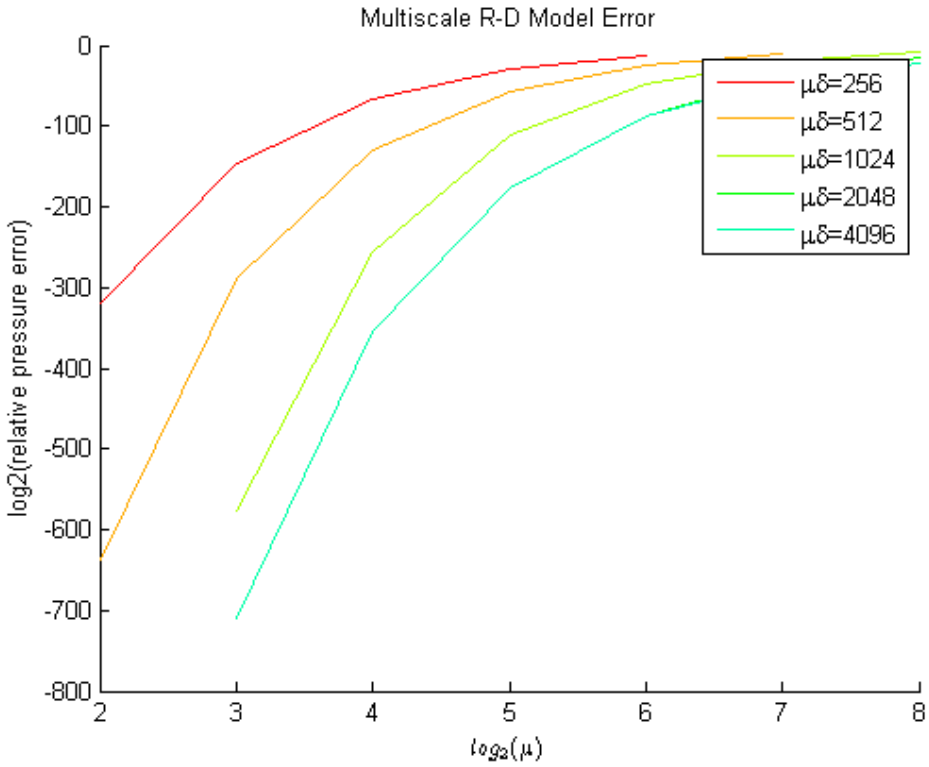

Figure 5.27: Logarithms of relative pressure error for Multiscale Reaction-Diffusion PDE with constant conductance, holding total sample area $\mu\delta$ constant and increasing μ

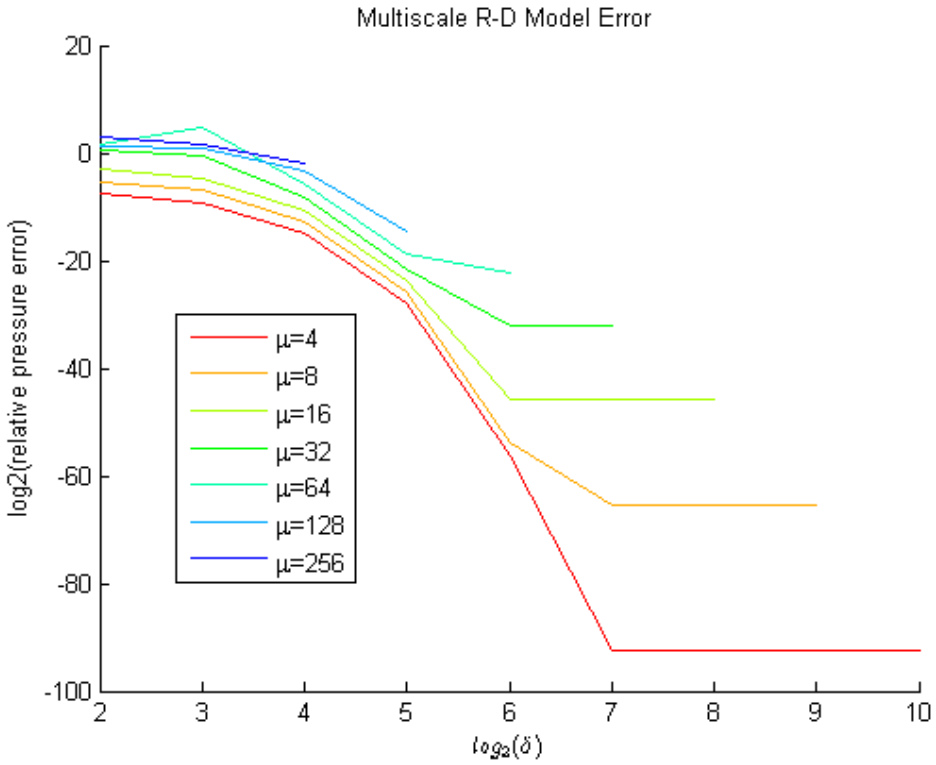

Figure 5.28: Logarithms of relative pressure error for Multiscale Reaction-Diffusion PDE with linearly varying conductance, holding μ constant and increasing δ.

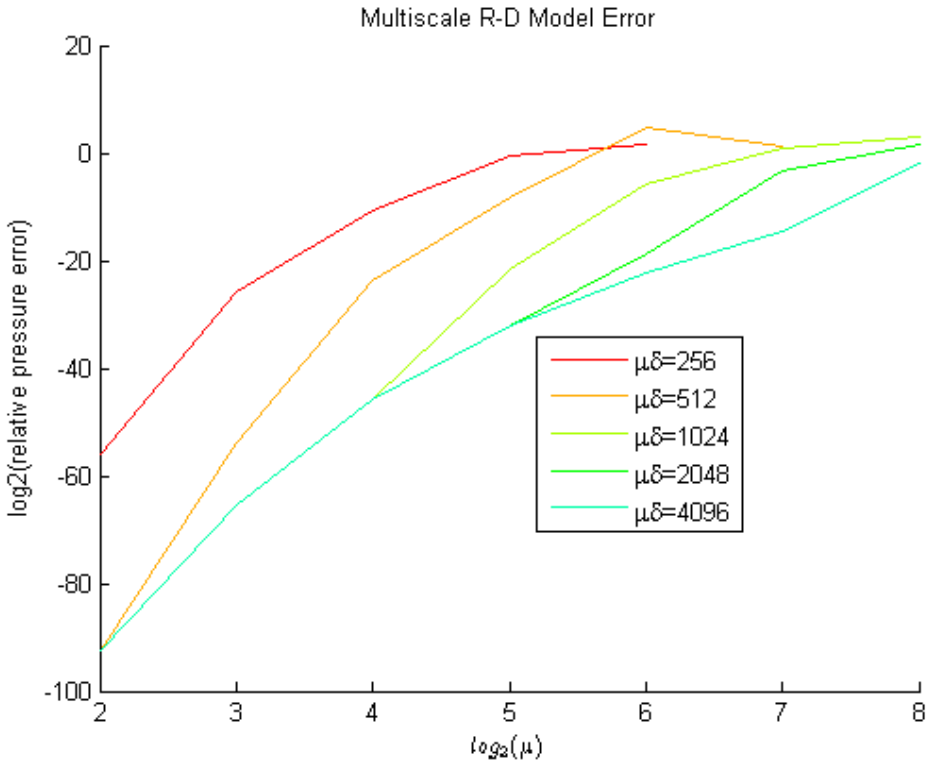

Figure 5.29: Logarithms of relative pressure error for Multiscale Reaction-Diffusion PDE with linearly varying conductance, holding total sample area constant $\mu\delta$ and increasing μ.

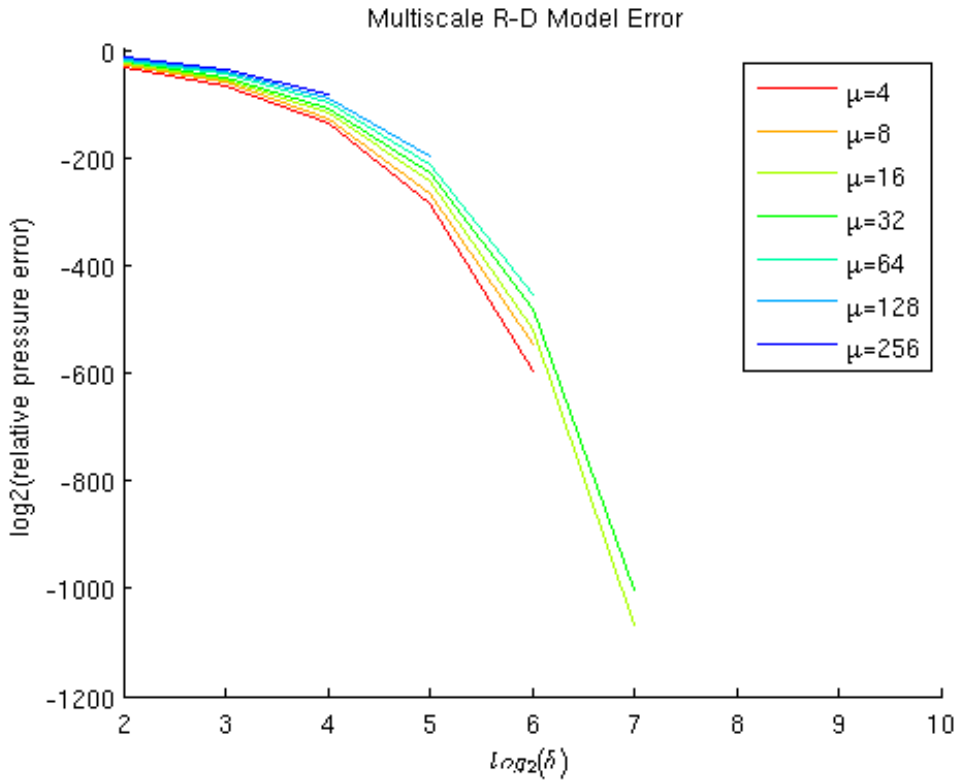

Figure 5.30: Logarithms of average relative pressure error for Multiscale Reaction-Diffusion PDE with random conductance, holding μ constant and increasing δ.

sure values be bounded by the boundary conditions. Monotonicity in the solution also suggests that flux values also be non-negative for a negative pressure gradient. Lack of these two properties suggests that the proposed microscale model may not approximate the heterogeneous case effectively.

5.4 Modified Reaction-Diffusion Model

To improve the accuracy of our 1D multiscale model, we modified the microscopic model so that it more closely reflects a finite volume discretization similar to the macroscopic model. Recall the microscopic equations 3.53- 3.55 given by

$$\sum_{j \in K_l} q_{lj} + c^* p_l \Delta x = s_l \tag{5.1}$$

$$q_{lj} = g_{lj}(\Delta P_{lj}) \tag{5.2}$$

$$g_{lj}(\nabla P_{lj}) = \frac{\pi r_{lj}^4}{8\mu L_{lj}} \tag{5.3}$$

Note that s_l is interpreted as a volumetric source term whose value was assumed to be contained implicitly. In reality, the volumetric source term can be defined as the integral of a source density function $f(x)$ over a fine scale control volume of size L centered at a given node x_l. This density function was also used to define the source term in the macroscopic equation. The finite volume discretization of the macroscopic source term also results in a mid-point integral approximation of the form $\int_{CV} f(x) \approx f(x_i)\Delta x$, which converts the right hand side of the PDE into a volumetric source term.

To ensure coherence between the scales, we must utilize an equivalent form of the source terms in our microscopic model. Thus, we need only modify the microscopic model (3.53) by writing the volumetric source term s_l in terms of the source density function $f(x)$. Similarly, we adapt the reaction coefficient to be scaled by the microcopic volume size L rather than the macroscopic volume Δx. Thus, we obtain

$$\sum_{j \in K_l} q_{lj} + c^* p_l L = s_l L$$

This subtle change radically improved the convergence of our multiscale algorithm for reaction diffusion problems. Utilizing an analogous convergence testing procedure as in the previous sections, we tested our algorithm for various choices of $k(x)$. To observe the effects of the reaction coefficient, we also varied the reaction coefficient to reflect three situations of interest: diffusion dominated flow ($c << k(x)$), a reaction dominated flow ($c >> k(x)$), and a case with reaction and diffusion coefficients of roughly equal magnitude.

Figures 5.31- 5.33 illustrate the convergence results for the multiscale reaction diffusion problem at various reaction coefficients with the modified microscopic model. In all cases,

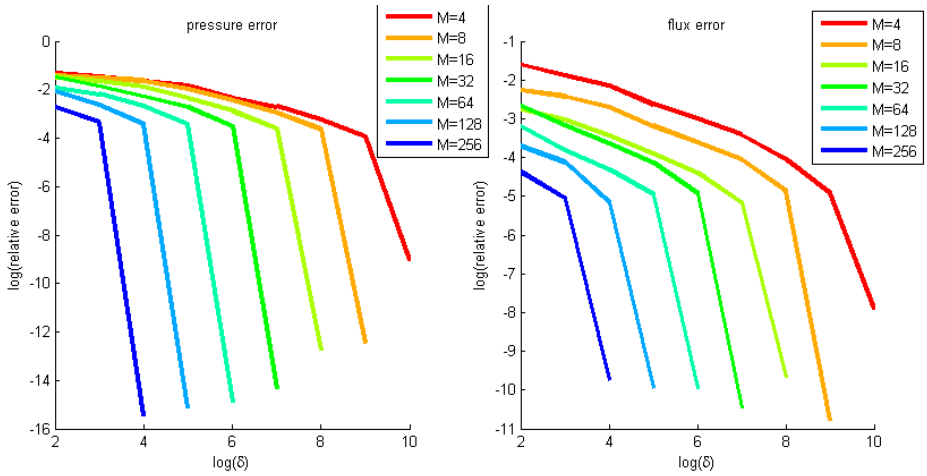

Figure 5.31: Convergence of 1D Reaction Diffusion problem with random $k(x)$ for Diffusion dominated case with coefficient $c = 10$

$k(x) \in 1, 1000$ was chosen to be randomly distributed throughout the domain. Note the stark contrast to the convergence of with the original microscopic model. In this case, we clearly see a monotonically decreasing error as the total sampling area increases for both the diffusion dominated case and the case with reaction and diffusion coefficients of equal magnitude. Convergence was observed in terms of the sampling length δ and the number of sampling subdomains μ in both cases. In the reaction dominated case, we observe that the error decreases monotonically as δ increases, but not necessarily when the number of sampling subdomains μ increases.

However, this observation reflects the presence of a boundary layer where a sharp gradient in the solution values exists. In contrast, our multiscale algorithm is designed to capture gradients in the material coefficient $k(x)$. Thus, the accuracy of our algorithm improves monotonically only after the sampling subdomains capture the flux values within the boundary layer. Adaptive refinement of the control volumes for the reaction diffusion problem may improve the implementation of our multiscale algorithm for this particular problem. However, a complete analysis of adaptive refinement strategies for our multiscale method is beyond the scope of this thesis.

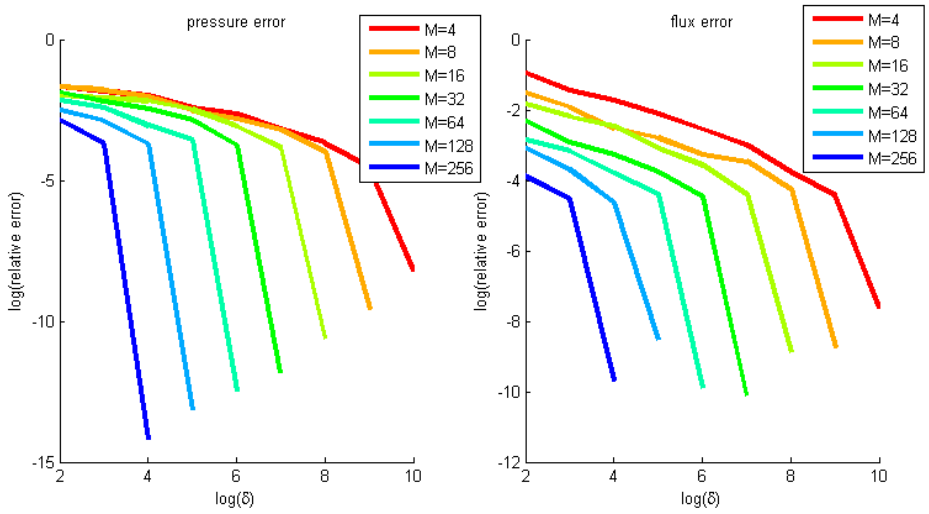

Figure 5.32: Convergence of 1D Reaction Diffusion problem with random $k(x)$ for Equal Magnitude case with coefficient $c = 500$

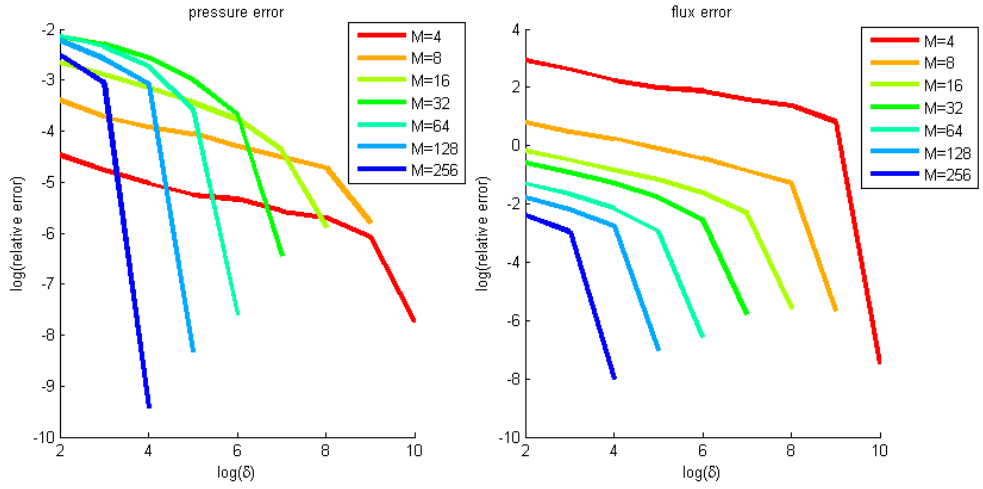

Figure 5.33: Convergence of 1D Reaction Diffusion problem with random $k(x)$ for Reaction Dominated case with coefficient $c = 100,000$

Chapter 6

Hybrid Splitting Method

6.1 Hybrid Method Overview

Based on our observation of the fixed stress splitting strategy, we propose a simple method to accelerate our iterative splitting strategy. First, we recall our semi-discrete equations (3.34) and consider a sequence of approximations n within the timestep $t+1$ by replacing the unknown variables σ_v^{t+1} and p^{t+1} with $\sigma_v^{t+1,n+1}$ and $p^{t+1,n+1}$, respectively. This applies to both the fluid and solid equations, but we shall modify the fluid equation using a slightly different method. Substituting the $n+1$ iterates into 3.34, we obtain

$$\left(c_0 + \frac{K_{dr}(x)}{\alpha}\right)\frac{p^{t+1,n+1}-p^t}{\Delta t} + \left(\frac{\alpha}{K_{dr}(x)}\right)\frac{\epsilon_v^{t+1,n+1}-\epsilon_v^t}{\Delta t} - \frac{d}{dx}\left(k(x)\frac{dp^{t+1,n+1}}{dx}\right) = g \quad (6.1)$$

Note that the iterations occur only over the unknowns p^{t+1} and ϵ_v^{t+1} and that dependence of (6.1) on $\epsilon_v^{t+1,n+1}$ implies dependence on $\nabla \cdot u^{t+1,n+1}$ as well. To remove this dependence, we impose a slightly different constraint from the traditional fixed stress splitting. Instead of constraining the variation in the rate of volumetric stress $\delta\dot{\sigma_v} = 0$, we instead constrain the variation in volumetric stress at the time level $t+1$ over the iterations n and $n+1$. This constraint is written as

$$\delta\sigma_v^{t,n} = 0$$

or equivalently

$$\sigma_v^{t,n+1} - \sigma_v^{t,n} = 0 \quad (6.2)$$

Again, we exploit the relation between volumetric stress, volumetric strain, and pore pressure in (3.37). By reformulating this relation in terms of the iterates n and $n+1$ and

substituting into both terms of (6.2), we obtain

$$\epsilon_v^{t+1,n+1} = \epsilon_v^{t+1,n} + \frac{\alpha}{K_{dr}(x)} \left(p^{t+1,n+1} - p^{t+1,n} \right) \tag{6.3}$$

Substituting (6.3) into (6.1), we eliminate the flow equation's dependence on $u^{t+1,n+1}$ and enable a solution in terms of pressure terms $p^{t+1,n+1}$ only.

Note that this new approach differs from both the traditional fixed-stress splitting and the fixed-point iteration described eariler, and is a hybrid of both approaches. This approach is also similar to the undrained splitting method, as described by Wheeler in [55]. The primary difference here is that our method removes the dependence on ϵ_v from the flow equation, instead of removing dependence on p from the solid equation.

We utilize the fixed point iteration to setup a fully implicit sequence of approximations within the timestep t. We also utlize the volumetric stress equation to remove the dependencies on the volumetric strain in the current iteration ϵ_v. Unlike the traditional fixed-stress splitting, we hold the volumetric stress constant between iterations instead of its time derivative. In doing so, the new approximation $p^{t+1,n+1}$ in our hybrid approach does not require the information from two previous timesteps p^t and p^{t-1} as seen in the traditional fixed-stress splitting approach. Instead, it only utilizes information from the previous timestep p^t and the previous iteration $p^{t+1,n}$ to determine the next iteration $p^{t+1,n+1}$.

6.2 Convergence

In our previous work, we established the convergence properties of the fixed point iteration based operator splitting method. One primary drawback of the fixed point iteration is that the spectral radius of the iteration matrix must be less than unity in magnitude to ensure convergence. Since the spectral radius depended greatly on the spatiotemporal discretization sizes and material parameters, this severely limits the range of problems that can be solved by this method.

In this section, we explore the use of the hybrid Fixed Point-Fixed Stress splitting method. First, we establish the stability of this method in the case of constant coefficients.

Then, we will illustrate convergence in the exact same cases tested for the pure fixed point splitting approach. We will conclude this section with a comparison between the two splitting methods.

6.2.1 Stability Analysis

Instead of analyzing the eigenvalues of stationary matrix as we saw previously, we shall establish stability by von neumann analysis in the case of constant coefficients $k_{dr}(x) \equiv k_{dr}$ and $k(x) \equiv k$. To acheive this, we must first reinterpret the hybrid fixed point iteration method as a single-pass splitting method. Consider the fixed point iteration equations with no source terms given by

$$-k_{dr}\frac{d}{dx}\left(\frac{du^{t+1,n+1}}{dx}\right) + \alpha\frac{dp^{t+1,n+1}}{dx} = 0 \tag{6.4}$$

$$\left(c_0 + \frac{K_{dr}}{\alpha}\right)\frac{p^{t+1,n+1} - p^t}{\Delta t} + \left(\frac{\alpha}{K_{dr}}\right)\frac{\epsilon_v^{t+1,n+1} - \epsilon_v^t}{\Delta t} - k\frac{d}{dx}\left(\frac{dp^{t+1,n+1}}{dx}\right) = 0 \tag{6.5}$$

By fixing the variation in stress, we obtain an expression for $\epsilon_v^{t+1,n+1}$ given by

$$\epsilon_v^{t+1,n+1} = \epsilon_v^{t+1,n} + \frac{\alpha}{K_{dr}}\left(p^{t+1,n+1} - p^{t+1,n}\right) \tag{6.6}$$

Substituting (6.6) into (6.4), the flow equation yields

$$\frac{c_0 + \frac{1}{\tau} + \tau^2}{\Delta t}p^{t+1,n+1} + \frac{c_0 + \tau}{\Delta t}p^t - \frac{\tau^2}{\Delta t}p^{t+1,n} + \frac{\tau}{\Delta t}\epsilon_v^{t+1,n} - \frac{\tau}{\Delta t}\epsilon_v^t - k\frac{d}{dx}\left(\frac{dp^{t+1,n+1}}{dx}\right) = 0 \tag{6.7}$$

where $\tau \equiv \frac{alpha}{k_dr}$. If we invoke only a single iteration in (6.4), then the notation in (6.7) can be simplified as

$$\frac{c_0 + \frac{1}{\tau} + \tau^2}{\Delta t}p^{t+1} + \frac{c_0 + \tau}{\Delta t}p^t - \frac{\tau^2}{\Delta t}p^* + \frac{\tau}{\Delta t}\epsilon_v^* - \frac{\tau}{\Delta t}\epsilon_v^t - k\frac{d}{dx}\left(\frac{dp^{t+1}}{dx}\right) = 0 \tag{6.8}$$

where ϵ_v^* and p^* are some predicted field value at the timestep $t+1$. Naturally, if Δt is sufficiently small, then we expect the field values at $t+1$ to be close to their values at the previous timestep t. Thus, we choose $p^* = p^t$ and $\epsilon_v^* = \epsilon_v^t$. Substituting these predictors

into (6.8), we completely decouple the flow equation from its dependence on displacement u by canceling the ϵ_v terms. Hence, (6.8) becomes

$$\frac{c_0 + \frac{1}{\tau} + \tau^2}{\Delta t}\left(p^{t+1} - p^t\right) - k\frac{d}{dx}\left(\frac{dp^{t+1}}{dx}\right) = 0 \tag{6.9}$$

Together with the solid equation (4.7), we obtain the system

$$-k_{dr}\frac{d}{dx}\left(\frac{du^{t+1}}{dx}\right) + \alpha\frac{dp^{t+1}}{dx} = 0 \tag{6.10}$$

$$\frac{c_0 + \frac{1}{\tau} + \tau^2}{\Delta t}\left(p^{t+1} - p^t\right) + -k\frac{d}{dx}\left(\frac{dp^{t+1}}{dx}\right) = 0 \tag{6.11}$$

Now, we discretize this system of equations on an equispaced, staggered finite volume cell grid and obtain

$$-\frac{k_{dr}}{\Delta x}\left(u^{t+1}_{j-\frac{3}{2}} - 2u^{t+1}_{j-\frac{1}{2}} + u^{t+1}_{j+\frac{1}{2}}\right) + \alpha\left(p^{t+1}_j - p^{t+1}_{j-1}\right) = 0 \tag{6.12}$$

$$\frac{\Delta x\left(c_0 + \frac{1}{\tau} + \tau^2\right)}{\Delta t}\left(p^{t+1}_j - p^t_j\right) - \frac{k}{\Delta x}\left(p^{t+1}_{j-1} - 2p^{t+1}_j + p^{t+1}_{j+1}\right) = 0 \tag{6.13}$$

In a similar manner to [49], we assess the stability of this time stepping scheme in the context of Von Neumann Analysis by considering a characteristic solution of the form $p^t_j = \gamma^n e^{ij\theta}\hat{P}$ and $u^t_j = \gamma^n e^{ij\theta}\hat{U}$, with with $\theta \in [-\pi, \pi]$ and amplification factor γ. Substituting these expressions in (6.12) and utilizing half angle and complex expoential identities, we obtain

$$\begin{bmatrix} \frac{1}{\tau\Delta x}\left(1 - cos\theta\right) & \alpha isin\left(\frac{\theta}{2}\right) \\ 0 & \left(b_1\left(\gamma - 1\right) + b_2\gamma\right) \end{bmatrix} \begin{bmatrix} \hat{U} \\ \hat{P} \end{bmatrix} = \begin{bmatrix} 0 \\ 0 \end{bmatrix} \tag{6.14}$$

where $b_1 = \Delta x\left(c_0 + \frac{1}{\tau} + \tau^2\right)$ and $b_2 = \frac{2k\Delta t}{\Delta x}\left(1 - cos\theta\right)$. As in [49], we require that the determinant of the matrix in (6.14) be zero and obtain the characteristic polynomial in terms of the amplification factor γ as

$$\frac{1}{\Delta x}\left(1 - cos\theta\right) \cdot \left((b_1 + b_2)\gamma - b_1\right) = 0 \tag{6.15}$$

Note that (6.15) is automaticaly satisfied in the case when $(1 - cos\theta) = 0$. Thus, to show stability we need only demonstrate that the roots of (6.15) have magnitude less than 1 in the case when $(1 - cos\theta) \neq 0$. If we assume $(1 - cos\theta) \neq 0$, we can divide $\frac{1}{\tau\Delta x}(1 - cos\theta)$ from both sides of the equation. Then, the root is trivially recovered as

$$\gamma = \frac{b_1}{b_1 + b_2} = \frac{\left(c_0 + \frac{1}{\tau} + \tau^2\right)}{\left(c_0 + \frac{1}{\tau} + \tau^2\right) + \frac{2k\Delta t}{\Delta x^2}(1 - cos\theta)} \tag{6.16}$$

Since all ther terms $c_0, \tau, \Delta t$, and Δx are positive and $(1 - cos\theta) > 0$ for all θ, the numerator is clearly smaller than the denominator in magnitude. Thus, $|\gamma| < 1$ and our method is **stable**.

Stability alone does not necessarily result in convergence. By Lax Equivalence Theorem, we also need to show **consisitency**; that is, the local truncation error $L(\Delta t, \Delta x) \to 0$ as $(\Delta t, \Delta x) \to (0, 0)$ must hold true. By standard taylor expansions of the finite difference scheme, it is clear that the (6.9) has local truncation error $O(\Delta t + \Delta x^2)$. If we consider the pressure term in (6.12) as a source term, the displacement terms clearly retain a local truncation error $O(\Delta x)$. Since the local truncation errors in both equations are linear combinations of Δt and Δx, their limits converge to 0 in the limit as $(\Delta t, \Delta x) \to (0, 0)$

6.3 Numerical Experiments

Clearly, we have demonstrated the convergence of the hybrid splitting method in the case of constant material parameters with a single iteration. However, this analysis does not necessarily hold true for the general case of variable coefficient parameters. In this section, we shall demonstrate that the method does, indeed, converge over a wide range of cases when multiple iterations are allowed. This is particularly useful in the case of heterogeneous material parameters.

In all cases, we chose a staggered spatial discretization consisting of $N = 1000$ intervals in both u and v, yielding a total of $2N + 2$ nodes on the unit interval $\Omega = [0, 1]$. We applied the standard boundary conditions for the Terzaghi problem, with left pressure $P_L = 0$,

left traction $T_L = -1$, right displacement $U_R = 0$ and right flux $F_R = 0$. We used a time stepsize $\Delta t = 0.001$ for all simulations as well.

In Case I, we verify the convergence of the single iteration hybrid splitting method for constant unit bulk modulus K_{dr} and constant unit mobility k. Case II explores the convergence of the hybrid splitting method with bulk modulus and mobility parameters expressed as linear functions of the form $f(x) = mx + b$. The third and final case illustrates the application of the hybrid method for randomly distributed K_dr and k in the range $[1, 1000]$ for both parameters.

To verify convergence, we compare the hybrid splitting solution to the numerical solution of the fully coupled poroelasticity equations. For both the hybrid splitting and fully coupled solutions, the initial condition is obtained by imposing the increment in fluid content as zero.

6.4 Case I Results

As figures 6.1- 6.2 illustrate, the fully coupled and hybrid splitting solutions are virtually indistinguishable from each other when only a single iteration is applied to the constant coefficient case. The relative L^∞ norm error illustrated in figure 6.3 shows good agreement in both pressures and displacements between the two solutions across all time steps. Despite the small initial relative error, we observe the error increasing at the beginning of the solution and decreasing as $t \to \infty$. It is anticipate that any initial error should be monotonically amplified with successive timesteps. We attribute the decrease in error to the convergence of both the hybrid and fully coupled solutions to an asymptotic state for the given Terzaghi problem with no source terms.

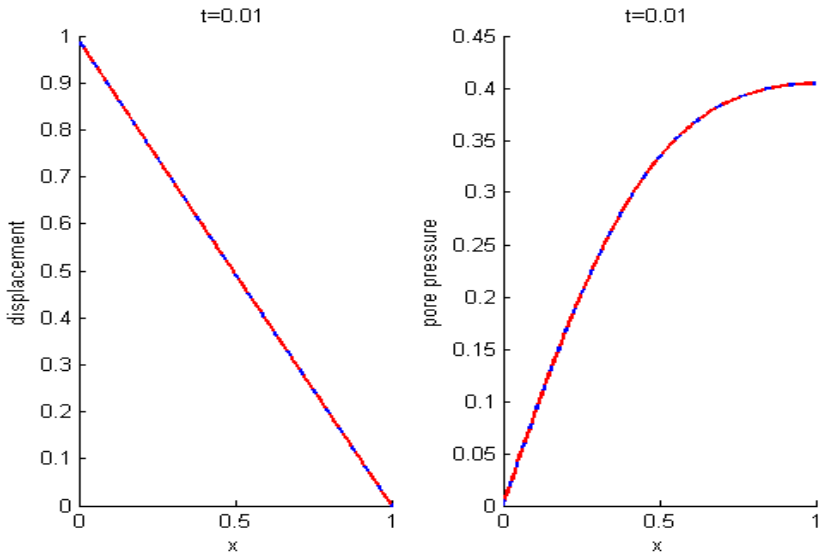

Figure 6.1: Hybrid Splitting & Fully Coupled Solutions at t=0.01 for constant material coefficients

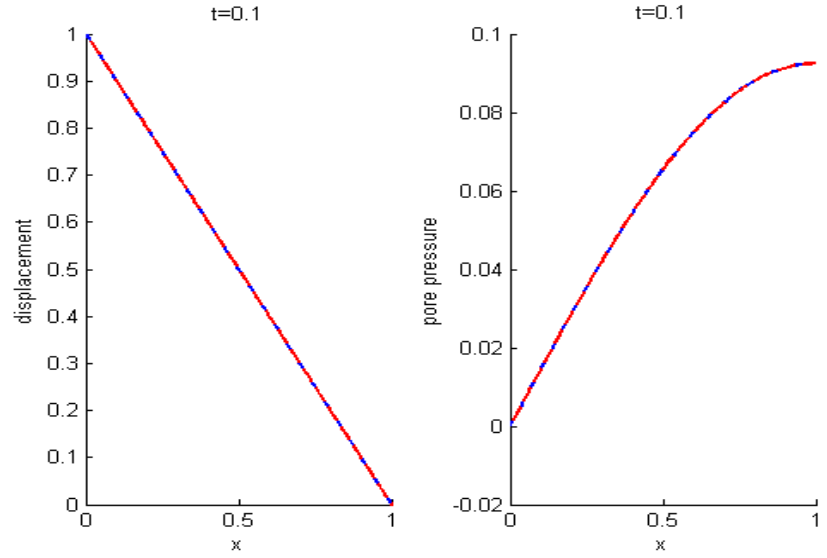

Figure 6.2: Hybrid Splitting & Fully Coupled Solutions at t=0.1 for constant material coefficients

6.5 Case II Results

In Case II, we chose $f(x) = 1000x + 1$ as the variable material coefficient for K_{dr} and k for all simulations. To capture the salient behavior of the PDE's, we chose a smaller

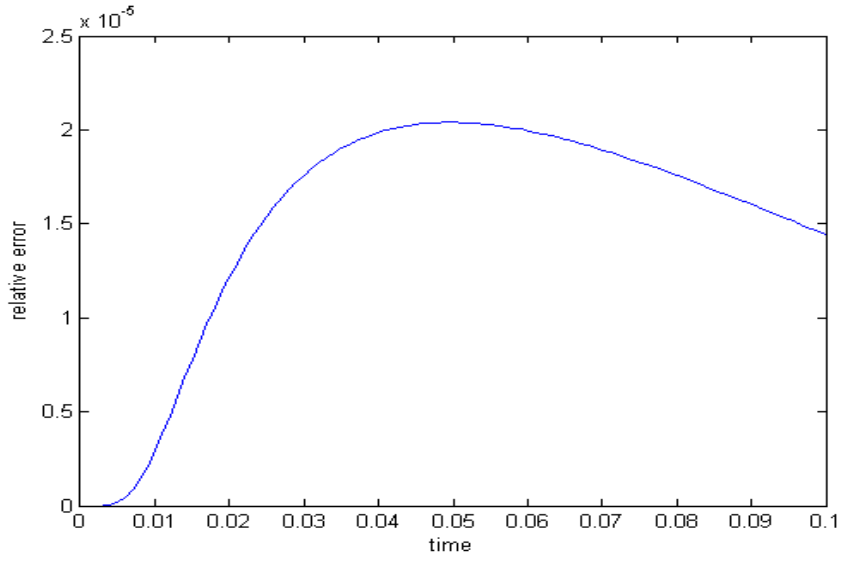

Figure 6.3: Maximum Relative Error in Hybrid Splitting Method for constant material coefficients

timestep $\Delta t = 0.0001$ than that of Case I. Figures 6.4 and 6.5 illustrate a stark contrast in the case of variable material coefficients. Clearly, the error between the hybrid and fully coupled solutions is significantly large in magnitude to observe a visible difference between the solutions. With multiple timesteps[1], the solution converges with sufficiently small error to render the solutions visually indistinguishable.

The error plots 6.6 and 6.7 confirm the stark difference in relative error between a single and multiple iterations of the hybrid method. In the single iteration approach, the error grows significantly to 40% relative error before decaying rapidly to zero. Again, this is an artifact of the approximate solutions approaching the asymptotic solution, rather than convergence between the hybrid and fully coupled solutions. The error in the multiple iteration oscillates within $10^{-}6$ error before decaying to the asymptotic solution. Clearly, both approaches appear to converge to the asymptotic solution, but the evolution in time is clearly more easily captured by using multiple iterations in the case of linear material

[1]In this case, nine iterations were sufficient to converge to within relative error near 10^{-7} in all timesteps.

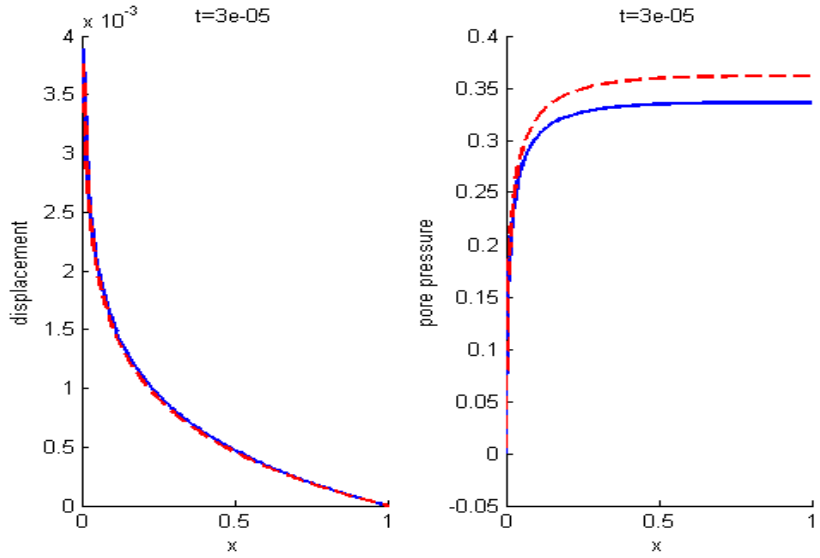

Figure 6.4: Hybrid Splitting (blue) and Fully Coupled (red) Solutions at t=0.0003 with only one iteration for Linear Material Coefficients

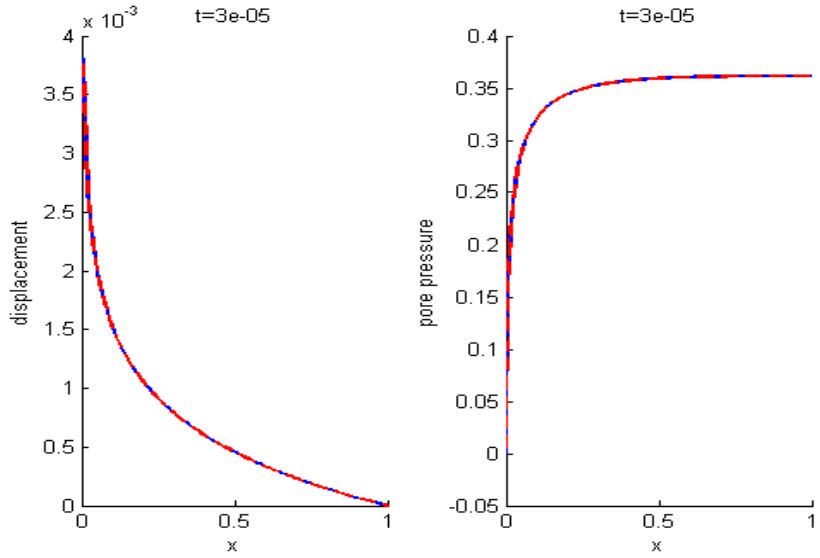

Figure 6.5: Hybrid Splitting (blue) and Fully Coupled (red) Solutions at t=0.0003 with nine iterations for Linear Material Coefficients

coefficients.

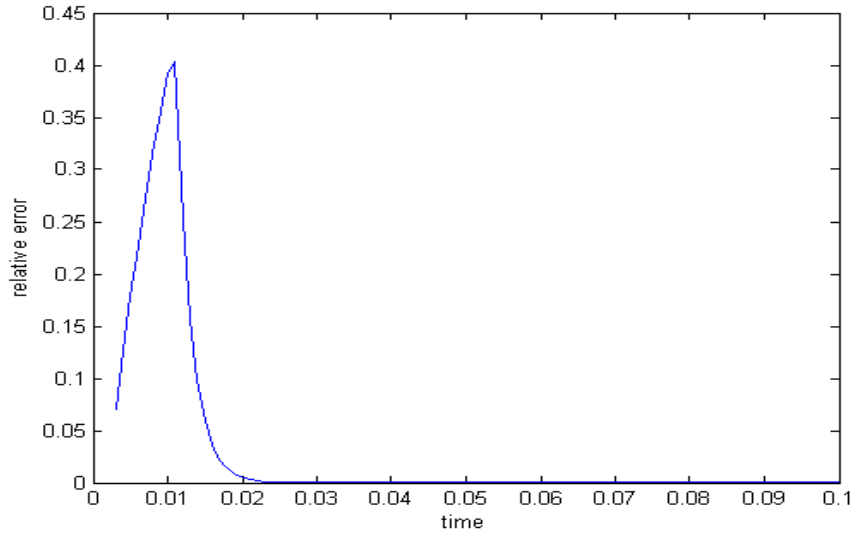

Figure 6.6: Error Propagation of Hybrid Splitting Method with only one iteration for **Linear** Material Coefficients

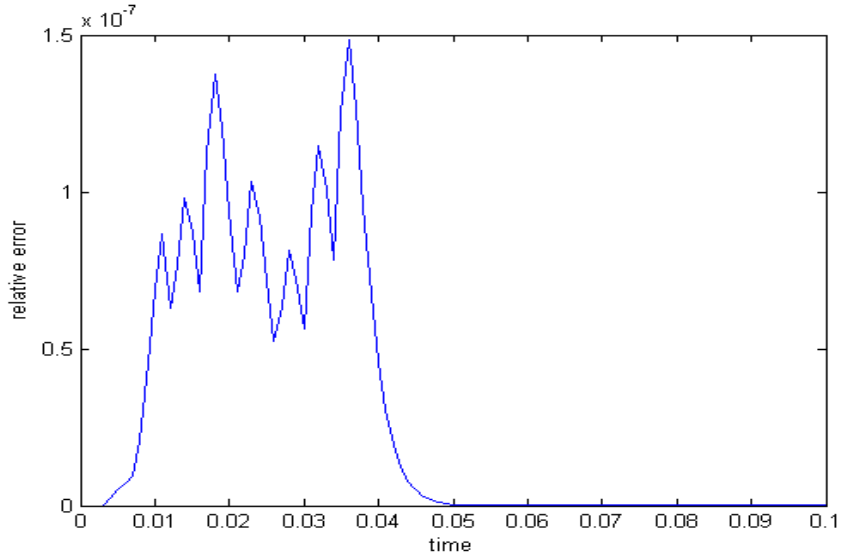

Figure 6.7: Error Propagation of Hybrid Splitting Method with many iterations for Linear Material Coefficients

6.6 Case III results

Based on our previous observation in the linear case, we observe that convergence is not guaranteed for a single iteration when the material coefficients K_{dr} and k vary in space.

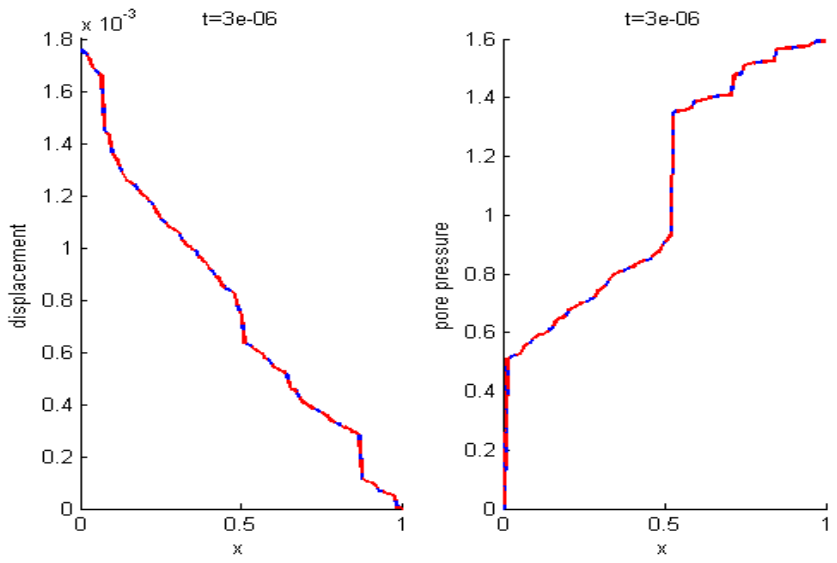

Figure 6.8: Hybrid Splitting (blue) and Fully Coupled (red) Solutions at t=0.0003 with nine iterations for **Random** Material Coefficients

Thus for case III, we only consider the hybrid method with multiple iterations. We note that for this case, approximately sixteen iterations were required to converge to within a tolerance of $5e-6$ relative error.

Figure 6.8 again illustrates that the hybrid method again converges to the desired accuracy when multiple iterations are utilized. The error is well controlled over all timesteps. Again, we observe that the error initially increases, but then stabilizes and decreases beyond this point. Though not illustrated in figure 6.9, further analysis of the error reveals a steady decay of the error to zero as $t \to \infty$. Again, this phenomenon is a result of the rapid convergence of the numerical solution to its asymptotic state, rather than a property of the hybrid splitting method itself.

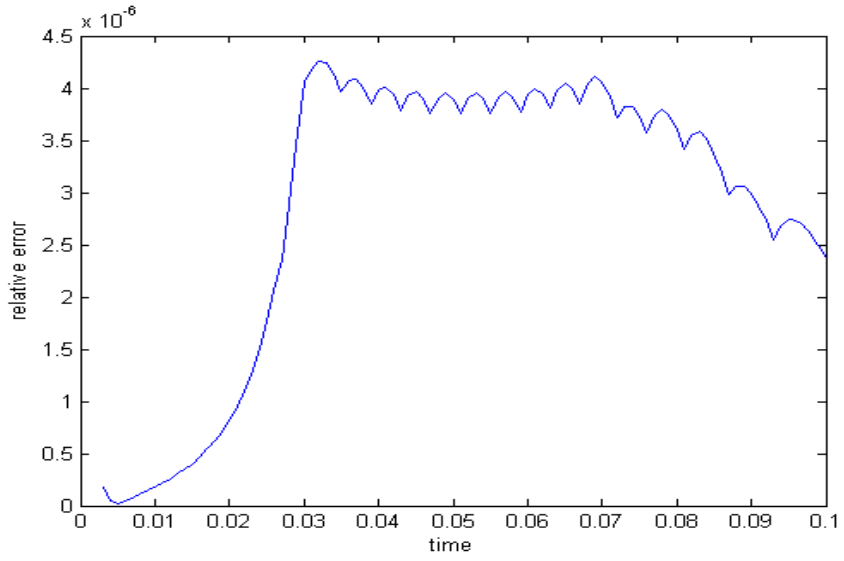

Figure 6.9: Error Propagation of Hybrid Splitting Method with only one iteration for Linear Material Coefficients

Chapter 7

Source Terms

The proposed splitting method in chapter 3 transforms the system of PDE's into a sequence of decoupled PDE's with information passing through source terms. In order to make use of the proposed multiscale algorithm, the macroscopic source terms must be incorporated adequately.

The primary complication in our multiscale method is the presence of source terms in global micromodels which project onto boundary conditions of local micromodels. In this section, we propose an interpolation scheme to account for the presence of these terms.

7.1 One Dimensional Case

For simplicity and without loss of generality, we consider the one dimensional problem

$$\frac{dF}{dx} = S, x \in \Omega,$$
$$F = -k(x)\frac{dP}{dx}$$

where S is a source term and F denotes a linear constitutive relation. We divide the domain Ω into $\mu + 1$ control volumes of size $\Delta x = \frac{|\Omega|}{\mu}$. For pure dirichlet conditions in dimension, the underlying microscopic model must be sampled locally at μ control volume boundaries in total.

7.1.1 Microscopic Model

Under appropriate restrictions on the connectivity between pores, the full microscopic model can be interpreted as having the structure a one dimensional poisson equation with

variable coefficient $k(x)$. The **global microscopic model** is obtained by solving the system

$$\frac{k_{i-\frac{1}{2}}}{L}P_{i-1} + \frac{k_{i-\frac{1}{2}} + k_{i+\frac{1}{2}}}{L}P_i + \frac{k_{i+\frac{1}{2}}}{L}P_{i+1} = S_i L \tag{7.1}$$

where L denotes a uniform spatial stepsize and P_i is the macroscopic pressure. The global microscopic model is used as the reference solution for convergence analysis.

Within the scope of our multiscale method, the **local microscopic model** exhibits a similar form to 7.2, and is given by

$$g_{i-\frac{1}{2}}p_{i-1} + \left(g_{i-\frac{1}{2}} + g_{i+\frac{1}{2}}\right)p_i + g_{i+\frac{1}{2}}p_{i+1} = \tilde{s}_i \tag{7.2}$$

What distinguishes the local and global microscopic models is the size of the domain and the location of imposed boundary conditions. The global microscopic model encompasses the entire computational domain Ω where as the local models are defined on sampled subdomains of size $\delta \leq \Delta x$ centered at each of the control volume boundaries.

7.1.2 Multiscale Macro Model Source Terms

Our multiscale scheme's macroscopic model is based on the finite volume method, which enforces conservation locally around control volumes by

$$\int_{\partial CV} F \cdot n = \int_{CV} S(x).$$

The integral on the right hand side term can be discretized in a number of ways. Among the simplest implementations is the midpoint rule, which in one dimension yields

$$\int_{\Omega} S(x) \approx S(k)\Delta x$$

, where S_i is the value of $S(x)$ at the center of the ith control volume. For sufficiently well behaved source terms $S(x)$, a midpoint integral approximation is sufficient. For general $S(x)$, a more sophisticated quadrature scheme is required to capture local oscillations present in S. In our scheme, we define Q_i as an approximation of the integral of $S(x)$ within

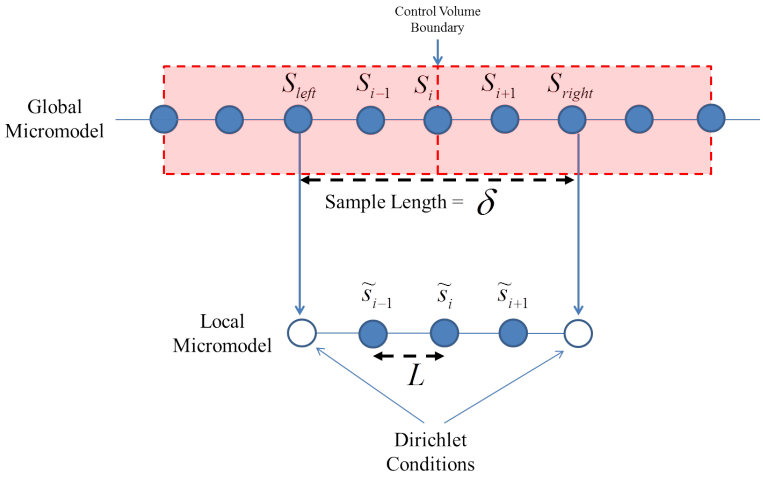

Figure 7.1: Dirichlet Conditions on local micromodels forbid the presence of source terms directly projected from left (S_R) and right (S_L) nodes of the global microscopic model

the ith control volume. If the points of the global micromodel are equispaced, we may exploit composite newton-cotes quadrature to obtain Q_i. Though higer order quadrature is possible, we utilize a trapezoid rule in the current implementation.

7.1.3 Local Micromodel Source Terms

The global microscopic model may contain non-zero source terms throughout the domain Ω except at the boundary nodes. However, some of these source terms project directly onto boundary nodes of local microscopic models within our multiscale method as seen in figure 7.1. Note that global model souce terms S_{i-1}, S_i, and S_{i+1} can be directly projected onto interior source terms of the local micro model $\tilde{s_{i-1}}$, $\tilde{s}_i$, and $\tilde{s_{i+1}}$, respectively. However, the source terms on the left (S_L) and right S_R boundaries of the sample cannot be projected directly.

Our sampling scheme [34] requires imposing dirichlet conditions along boundary nodes in the local subsample models where source terms would otherwise be required in the reference solution. The multiscale scheme proposed by Chu et al.[27, 26] does not account for source terms existing along boundaries of subsampled micromodels. As we will demon-

strate later in this chapter, **failure to account for boundary source terms results in erroneous simulation results**.

To properly account for source terms defined at boundary nodes, we must incorporate the contributions of the boundary source terms S_L and S_R onto interior source term nodes of the micro model. We adopt a generalized partition of unity approach which interpolates boundary values onto interior nodes based on a given weight function $w(x)$. The details of this approach are described next.

7.1.4 Modified Source Terms

Let B_δ^j denote the jth micro sample of size δ corresponding to the interval $\left[X_{left}^j, X_{right}^j\right] \subset \Omega$ of the original domain. We define the sample length $\delta \equiv N_{sample} \cdot L$, where L is the equispaced subinterval stepsize (between consecutive nodes) in both the local and global macro models and N_{sample} is the number of subintervals. Denote the nodes of the global micromodel located in the region $\left[X_{left}^j, X_{right}^j\right]$ as $X_{global,i}^j$ such that $X_{global,0}^j = X_{left}^j$ and $X_{global,N_{sample}}^j = X_{right}^j$. We also denote the corresponding nodes of the local micro sample as $X_{local,i}^j$ such that $X_{local,0}^j$ and $X_{local,N_{sample}}^j$ are the left and right local boundary nodes, respectively.

We impose the constraint

$$\int_{B_\delta^j} \tilde{s}(x)dx = \int_{\left[X_{left}^j, X_{right}^j\right]} S(x)dx$$

Discretizing the left hand side of the above equation by trapezoid rule, we obtain

$$\int_{B_\delta^j} \tilde{s}(x)dx \approx \frac{L}{2}\left[S(X_{global,0}^j) + 2\sum_{i=1}^{N_{sample-1}} S(X_{global,i}^j) + S(X_{global,N_{sample}}^j)\right]$$

Clearly, the trapezoid rule exploits the existence of source terms on the boundaries of B_δ^j. Consequently, the local micro models must distribute the contributions $\frac{S\left(X_{global,0}^j\right)}{2}$ and $\frac{S\left(X_{global,N_{sample}}^j\right)}{2}$ onto the interior nodes $X_{local,i}^j\big|_{i=1}^{i=N_{sample}-1}$. The distribution depends upon

the choice of a discrete weight function w defined on the local interior discrete nodes. We can interpret w as a function defined over the discrete position in the local micro model and not in the global model.

Given w, we obtain the total sum over interior nodes $T^{N_{sample}-1} \equiv \sum_{i=1}^{N_{sample}-1} w(X^j_{local,i})$. Then, the left boundary source term $\frac{S(X^j_{global,0})}{2}$ may be distributed as

$$\tilde{s}\left(X^j_{local,i}\right) = S\left(X^j_{global,i}\right) + \frac{S(X^j_{global,0})}{2T_{N_{sample}-1}} w\left(X^j_{local,i}\right)$$

Since the terms we wish to distribute originate from the boundaries, it is natural to consider separate weight functions $w_L(x)$ and $w_R(x)$ for each of the contributions on the left and right boundaries, respectively. For the left boundary source term, we seek to distribute heavier weights closer to the left boundary and lighter on the right boundary. The choice of weight function $w(x)$ with these properties is not unique and different choices may result in different accuracies.

In this work, we explore the monomial weight function of the form $w(x) = x^p$ for some $p > 0$ and determine their effects on the accuracy of the multiscale simulation. This choice of weight function provides a natural setting for analysis as encompasses the two extreme limiting cases and provides a continuous homotopic transition between the limiting cases via the parameter p. At one extreme, the parameter $p = 0$ leads to a constant weight function $w(x) = \frac{1}{N_{sample}-1}$ which enforces uniform distribution of boundary source contributions onto all interior source terms. At the other extreme, as the parameter $p \to \infty$, the weight function $w(x)$ transforms into a kronecker delta function $w(x) = \delta_{X^j_{local,boundary}}$ which aggregates the entire contribution from the one boundary onto the next closest interior source term at $X^j_{local,boundary}$.

For all other $0 < p < \infty$, the weight function adds a fraction of a boundary source term proportional to a power of the distance from the given boundary as seen in figures 7.2-7.3. Note that the left and right weight functions are mirror reflections of each other and thus the right weight function has the explicit form $w_R(x) = (1 - x)^p$. We obtain the values of $w(x_i)$ at equidistant intervals as dictated by the number of intervals in the local

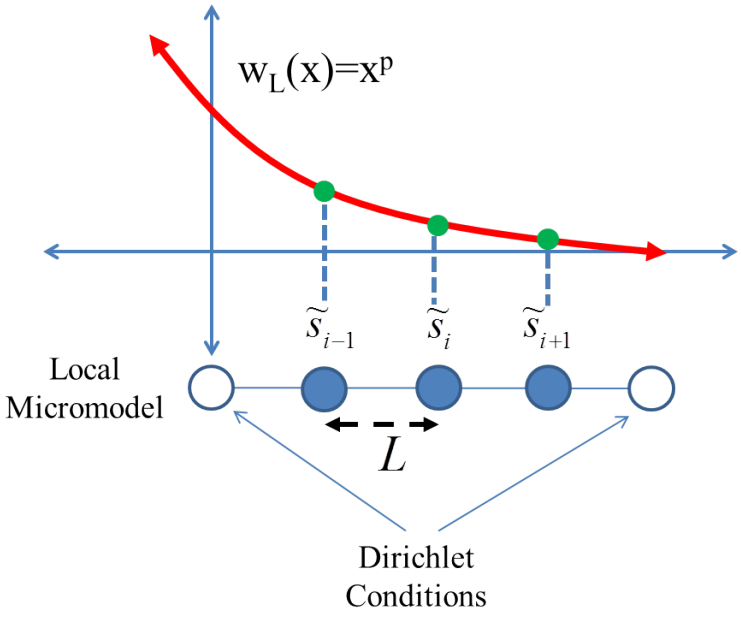

Figure 7.2: Left Weight function $w(x) = x^p$

micro model. To ensure proper weighting, the values are then normalized by the total sum of weights $\sum_i w(x_i)$. Each interior source term s_i receives the portion $S_L \frac{w(x_i)}{\sum_i w_L(x_i)}$ and $S_R \frac{w(x_i)}{\sum_i w_R(x_i)}$ from the left and right boundary source terms, respectively.

7.2 Numerical Experiments

It is unclear which weight function yields the best approximation within the scope of our multiscale scheme. To discern the optimal strategy, we employ numerical experimentation. We consider three particular cases with constant and linear source terms. In all cases, we conduct a numerical convergence study over the sample sizes δ and number of samples μ analogous to those in chapter 6. We only consider the case of randomly distributed material coefficients $E \in [1, 1000]$ for the 1D deformation problem. To ensure that the source term $s(x)$ contributes significantly to the behavior of the PDE, we must choose the source term to have values of roughly equivalent magnitude as the material coefficient.

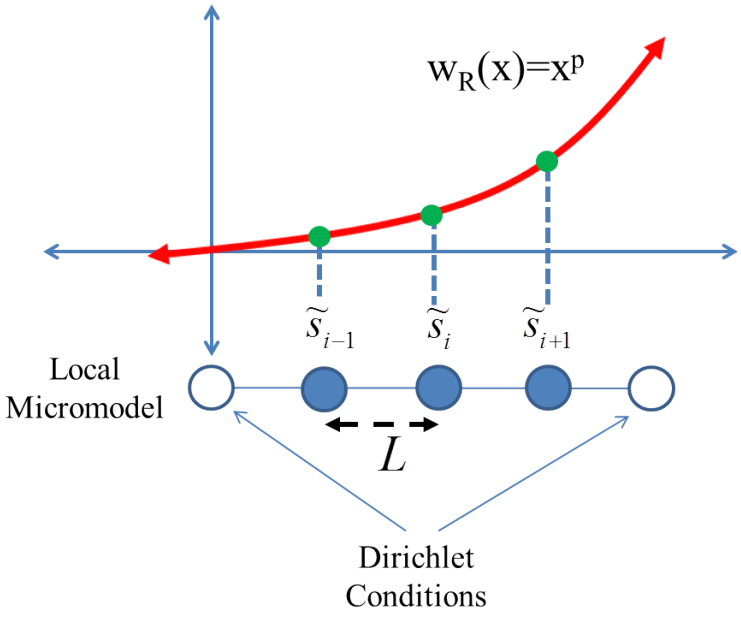

Figure 7.3: Right Weight function $w_R(x) = x^p$

Hence, we choose $s(x) = 500$ in the constant case and $s(x) = 1 + 1000x$ in the linear source term case. We choose a domain $\Omega = [0, 1]$ and utilze the reference solution obtained from $N = 2^12$ intervals over Ω. As before, we average the relative errors in displacement and flux over 100 random simulation runs. Additionally, we vary the weight function power $p = 0, 1, 10, 100$, and ∞ and obtain the maximum error over all simulation runs for each source term case.

7.3 Results

Figures 7.4- 7.6 illustrate the convergence tendencies for the various weight functions tested in the case of a constant source term. As we saw in the zero source term cases tested in the previous chapter, the relative error decays roughly linearly when $\mu\delta < |\Omega|$. When full sampling is utilized ($\mu\delta = |\Omega|$), we observe displacement convergence to within floating point accuracy with total force relative error roughly one order of magnitude higher.

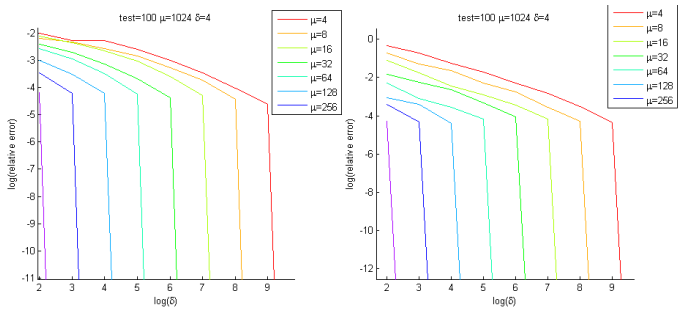

Figure 7.4: Convergence analysis for displacement (left) and total force (right) with uniform weight distribution function $w(x) = x^0$ and constant source term

The case with linear source terms yields nearly analogous results as the constant case, with similar relative error and general convergence tendencies. Figures 7.7- 7.9 illustrate the convergence for various weight functions. As before, there was no significant difference between the relative accuracy or convergence tendencies.

Other weight function powers and source term functions were also tested, but all other variable coefficient cases yielded equivalent results. Only one case tested did not yield equivalent results. When boundary source term distribution was absent in the model, we do not observe convergence any convergence in our method. Specifically, when the normalized weight function is chosen identically as zero (i.e. $\frac{w(x_i)}{\sum_i w(x_i)} \equiv 0$), all numerical simulations yielded significant relative errors even in the case with full sampling $\mu\delta = |\Omega|$.

These results underscores the importance of accounting for boundary source term values and give evidence to the hypothesis that any distribution function $w(x) = x^p$ may be utilized as long as the weights are normalized. It still remains unclear whether any arbitrary choice of weight function $w(x)$ may be utilized with convergent results within the scope of our method. Full analysis of the effects of arbitrary distribution functions is beyond the scope of this thesis. However, it is clear that for weight functions $w(x)^p$, any choice of p appears to lead to convergence. All other things being equal, simplicity of implementation suggests that uniform distribution $w(x) = x^0$ is the best choice for all future cases, including higher dimensional cases.

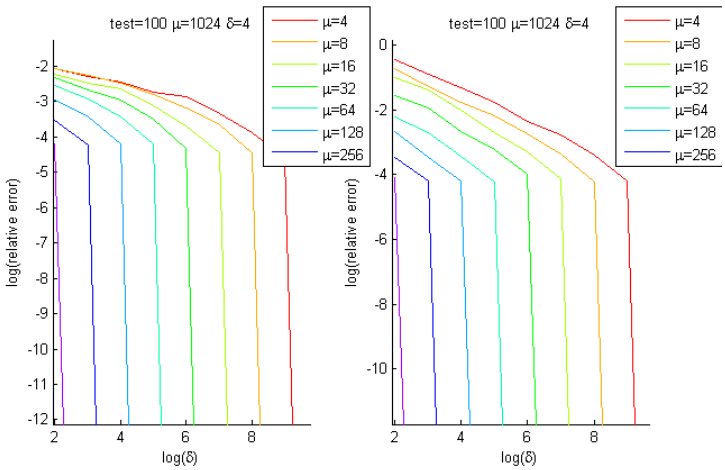

Figure 7.5: Convergence analysis for displacement (left) and total force (right) with linear weight distribution function $w(x) = x^1$ and constant source term

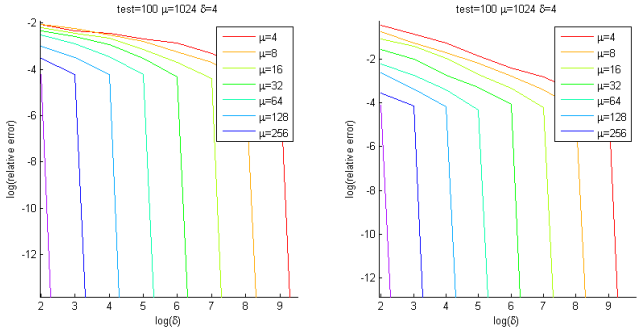

Figure 7.6: Convergence analysis for displacement (left) and total force (right) with dirac delta weight distribution function $w(x) = x^\infty$ and constant source term

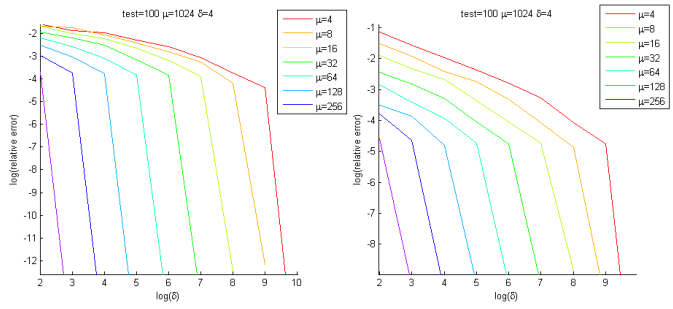

Figure 7.7: Convergence analysis for displacement (left) and total force (right) with uniform weight distribution function $w(x) = x^0$ and Linear source term

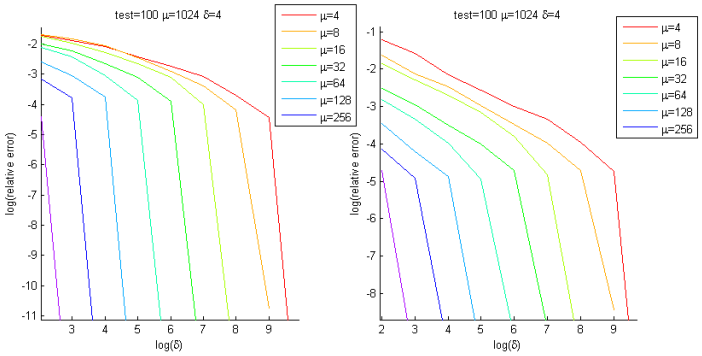

Figure 7.8: Convergence analysis for displacement (left) and total force (right) with dirac delta weight distribution function $w(x) = x^1$ and Linear source term

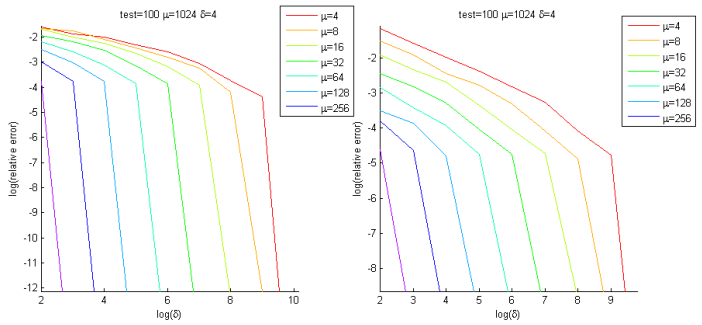

Figure 7.9: Convergence analysis for displacement (left) and total force (right) with dirac delta weight distribution function $w(x) = x^\infty$ and Linear source term

Chapter 8

Boundary Conditions

Many problems of interest in poroelasticity involve a mixture of dirichlet and neumann conditions for both the flow and deformation equations. Note that Chu et al.[27] and our previous multiscale simulations[34, 33] focused only on problems with pure dirichlet conditions via a staggered cell construction which aligns the centers of boundary cells with the boundary conditions. In this chapter, we present an alternative formulation for pure dirichlet boundary conditions and alternative formulations for neumann and mixed conditions as well.

8.1 One Dimension

The different approaches to implement the boundary conditions are intimately connected to the ways in which the domain is discretized into finitely many control volume cells. For simplicity, we shall only consider equispaced grid cell discretizations whose construction depends on how the boundary cells align with respect to the remainder of the domain. Either the cell centers or the cell faces must align perfect with each of the domain boundaries. This results in three possible discretization strategies in 1D, each of which is illustrated[1] in Figure 8.1. The Dirichlet Center approach assumes that the centers of both boundary cells align perfectly with the domain boundary points. The Neumann Center approach utilizes the opposite assumption; that is, the faces of both boundary cells align with the domain boundaries. The Hybrid approach aligns the center of one boundary cell with a domain

[1]Technically, there exists a fourth possibility with the right boundary being cell-center aligned and the left boundary being cell-face aligned. However, it still falls under the category of the Hybrid approach.

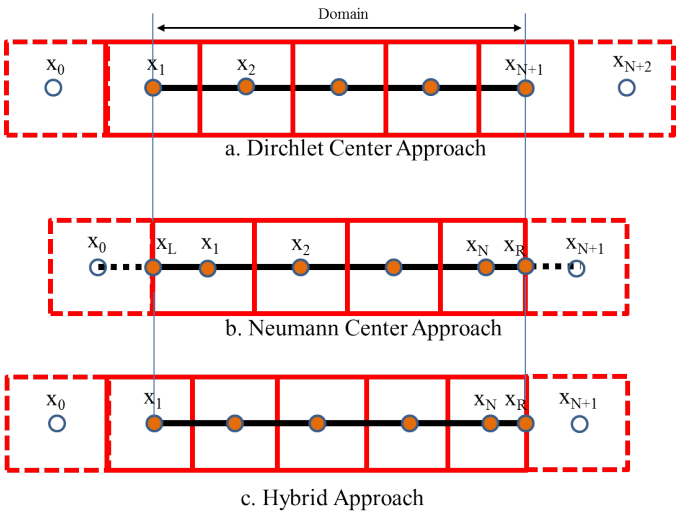

Figure 8.1: Three Approaches to Grid Cell Construction with Halo Nodes

boundary while the other boundary cell aligns its face with a domain boundary.

We note that all three approaches yield equivalent second order accuracy, but certain approaches streamline the implementation of certain types of boundary conditions more efficiently than others. We shall analyze their implementation for three common cases.

8.1.1 Dirichlet Conditions

When the macroscopic problem has pure dirichlet boundary conditions, it is natural to prescribe the **Dirichlet Center** approach since it yields the simplest implementation. Suppose x_1 and x_{N+1} denote the points at the left and right boundaries (respectively). Assume further U_L and U_R denote the dirichlet conditions at the left and right boundaries, respectively. The boundary conditions for the unknown field variable u under the Dirichlet Center approach are trivially implemented as

$$u_1 = U_L \text{ and } u_{N+1} = U_R.$$

Note that this approach is equivalent to the implementation of dirichlet boundary conditions in the classical finite difference method and was utilized in our previous work and in [27].

Alternatively, implementation of dirichlet conditions in the **Neumann Center** approach requires a constitutive relation for the flux/stress halo (ghost) nodes and an interpolation scheme. To understand this approach, one must first recognize that the finite volume discretization of the PDE results in equations balancing the flux through the boundaries of each control volume. This equation can be expressed as

$$F_R^{i+\frac{1}{2}} - F_L^{i-\frac{1}{2}} = S_i \Delta x \tag{8.1}$$

where F_R^i, F_L^i are the flux through the right and left boundaries of control volume i. At this point, we must make an assumption on the form of the constitutive relation in flux[2]. For simplicity, we shall only consider the linear flux assumption given by

$$F = k(x)\frac{du}{dx}$$

whose discrete form at face $i - \frac{1}{2}$ is expressed as

$$F_L^i = k(x_{i+\frac{1}{2}})\frac{u_i - u_{i-1}}{\Delta x}.$$

Applying this equation to the left face of the left-most control volume (i.e. the one containing the left boundary condition), we obtain

$$F = k(x_L)\frac{u_1 - u_0}{\Delta x} \tag{8.2}$$

where x_L is the left-boundary point of the domain. Note that for the Neumann Center approach, u_1 is the unknown at the center of the first (left-most) cell and u_0 is the halo node which lies outside the domain at a distance Δx to the left of u_1.

Since u_0 lies outside the domain, no value can be directly imposed as we saw in the Dirichlet Center case. Instead, we impose a constraint on u_0 in terms of u_1 and the boundary condition at the point x_L which we denoted as u_L. If we assume a linear flux, then the value u_L can be linearly interpolated from the values at u_1 and u_0. This interpolation yields

$$u_L = \frac{u_1 + u_0}{2}.$$

[2]Note that for many multiscale problems, a constitutive relation is unavailable throughout the domain. However, it is plausible to assume a particular relation is valid near the boundaries of the domain.

By solving this equation for u_0 and substituting into (8.2), we eliminate its dependence on the halo node and obtain

$$F = k(x_L)\frac{2u_1 - 2u_L}{\Delta x} \tag{8.3}$$

Since the term $\frac{-2u_L}{\Delta x}$ is a known quantity, it can be moved to the right hand side of the cell equation (8.1). The dirichlet boundary condition on the right boundary x_{n+1} can also be implemented by analogous proceedure.

Clearly, the **Hybrid** approach exploits both aforementioned implementation strategies as dictated by the alignment of the boundary cells to their respective domain boundaries.

8.1.2 Neumann Conditions

Flux/Traction conditions require 1st order derivatives to be approximated on the boundaries. Clearly, the most easiest approach to implement pure neumann conditions is the **Neumann Center** since the finite volume method naturally defines the equations in terms of cell boundary fluxes. Suppose the neumann conditions at the left and right domain boundaries are given by q_L and q_R, respectively. Recall grid b. in Figure 8.1 and the cell equation

$$F_R^{i+\frac{1}{2}} - F_L^{i-\frac{1}{2}} = S_i \Delta x.$$

For the flux terms defined at the domain boundaries, we simply substitute

$$F_L^1 = q_L \text{ and } F_R^{n+1} = q_R$$

at the left and right boundaries, respectively.

To implement neumann boundary conditions with the **Dirichlet Center** grid cell construction, we also require ghost nodes and an interpolation scheme. Consider the left boundary of grid a. in Figure 8.1. Suppose that the flux values at the left and right boundaries are again given by q_L,q_R, respectively. We define a ghost node x_0 at a distance Δx to the left of x_1. The cell equation is given by

$$F_R^{i+\frac{1}{2}} - F_L^{i-\frac{1}{2}} = S_i \Delta x$$

with $i = 1$. Note that the flux at the left domain boundary can be given in terms of a centered finite difference

$$q_R = k(x_L)\frac{u_2 - u_0}{\Delta x}. \tag{8.4}$$

By interpolating u_1 with the average

$$u_1 = \frac{u_2 + u_0}{2},$$

and solving for u_0, we can substitute for u_0 into into (8.4) and eliminate the cell equation's dependence on the halo node. The boundary condition on the remaining boundary can be implemented by analogous proceedure. Again, the Hybrid approach exploits the above two implementations at each respective boundary.

8.1.3 Mixed Conditions

Mixed boundary conditions in 1D require different boundary conditions (dirichlet/neumann) on opposite sides. The Hybrid approach is the simplest implementation since one can perfectly align boundary cells to match the given boundary condition type. However, both the Dirichlet Center and Neumann Center approaches are ameanable to to mixed boundary conditions, utilizing the halo/interpolation method wherever the boundary condition and cell do not naturally match. Note that the hybrid approach is ideal for the one dimensional Terzhaghi problem, since the pressure and displacement cells can be defined in a staggered manner so that the mixed boundaries in each equation align perfectly. However, this approach is considerably more difficult to implement in higher dimensions for arbitrary assignments of the neumann and dirichlet conditions, much less for arbitrary domain geometries. In contrast, the Dirchlet/Neumann Center strategies are easily ameanable to higher dimensions. More importantly, both strategies are needed to enable coupling between the flow and deformation problems.

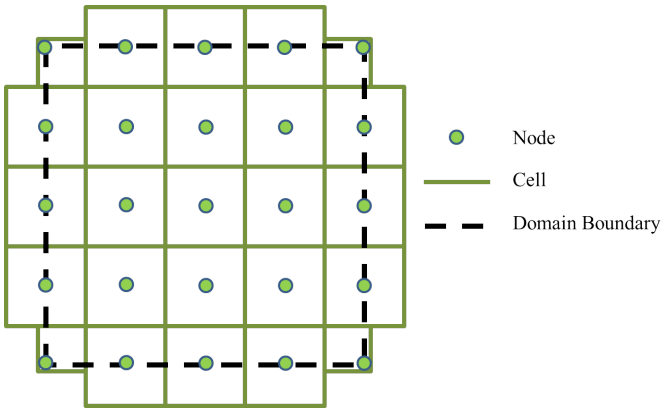

Figure 8.2: Dirichlet Center Approach to Equispaced Control Volume Cell Construction in 2D

8.2 Higher Dimensions

In this section, we focus on extrapolations of the Dirichlet Center and Neumann Center approaches to higher dimensions. Figures 8.2- 8.3 illustrate the grid construction of both approaches in 2D. As we saw for the 1D case, each approach is most easily ameanble to its respective boundary type and does not require explanation. Wherever the boundary condition and the boundary cell do not match naturally, halo nodes and interpolation schemes are needed. Thus, we shall restrict our discussion to the cases of implementing a neumann condition in the Dirchlet Center Approach and the dirichlet condition in the Neumann Center Approach

To simplify the discussion of boundary conditions, we shall only illustrate the proceedure for the north boundary. All other boundaries can be implemented analogously.

8.2.1 Neumann Conditions with the Dirichlet Center Approach

Consider the boundary node P_C lying on the north boundary as shown in figure 8.4. Note that P_C is a **not** a corner node and thus neither of the neighboring boundary nodes P_W and P_E are halo nodes. Only the node $\tilde{P}_N$ is a halo node outside the domain at a distance Δx north of P_C. Given this construction, the flux boundary condition $F_N = q_N$ must be

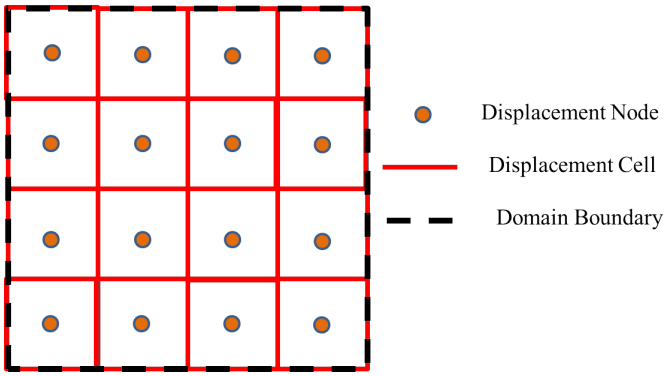

Figure 8.3: Neumann Center Approach to Equispaced Control Volume Cell Construction in 2D

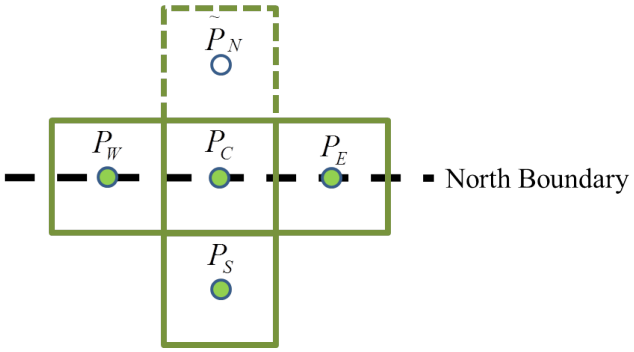

Figure 8.4: Non-Corner Boundary Cell

imposed across the midline of the control volume containing P_C. We assume the neumann condition can be modeled at this boundary by the discrete centered difference

$$q_N = k(x_C)\frac{\tilde{P}^N - P_S}{2\Delta y} \tag{8.5}$$

Note that Δy and Δx are interchangeable due to the underlying equispaced grid assumption. Since $\tilde{P}^N$ lies outside the domain, we must redefine it in terms of the nodes on the boundary/interior of the domain. To accomplish this, we simply approximate the center point P_C by the average of its four neighboring points given by

$$P_C \approx \frac{\tilde{P}_N + P_S + P_E + P_W}{4}.$$

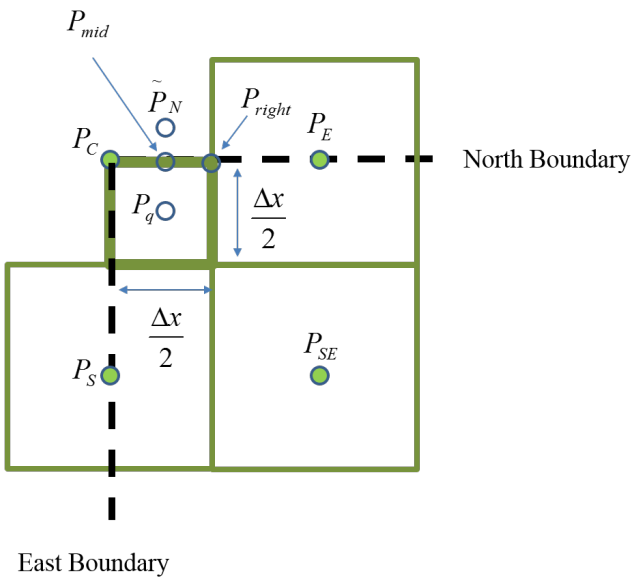

Figure 8.5: Corner Boundary Cell

Solving this equation for $\tilde{P}_N$ and substituting into (8.5), we eliminate the neumann boundary condition's dependence on the halo node. An analogous proceedure can be imposed on all non-corner neumann boundary conditions.

For **corner boundaries**, we consider a slighlty different formulation. As illustrated in Figure 8.2, we redefine the control volumes at the boundaries with a half width $\frac{\Delta x}{2}$. Figure 8.5 shows a close up of the northeast corner control volume with center value P_q and halo node $\tilde{P}^N$ which lies at a distance of $\frac{\Delta x}{4}$ north of the boundary and $\frac{\Delta x}{2}$ north of P_q. In this construction, we approximate the flux q_N across the north boundary of the corner control volume instead of the midline. The discrete approximation of this flux can be approximated by

$$k_{mid}\frac{\tilde{P}_N - P_q}{\frac{\Delta x}{2}} = q_N \tag{8.6}$$

where k_{mid} is the material coefficient at the mid point of the north face of the corner control volume.

Note that the value P_q is not a natural point in the structured grid and must be interpolated from the four nearest neighboring values $P_C, P_E, P_S, and P_{SE}$. We choose a

bilinear interpolant of the form

$$B(x, y) = a + bx + cy + dxy$$

where a, b, c, d are constants. Choosing the point P_C as the center of this interpolation, we assign a local coordinate $(0, 0)$ to P_C. Similarly, the remaining gridpoints P_E, P_S, P_{SE} are at the local coordinates $(\Delta x, 0)$, $(0, -\Delta y)$, and $(\Delta x, -\Delta y)$, respectively. Substituting local coordinates and gridpoints into the bilinear interpolant as

$$B(0, 0) = P_C \tag{8.7}$$

$$B(\Delta x, 0) = P_E \tag{8.8}$$

$$B(0, -\Delta y) = P_S \tag{8.9}$$

$$B(\Delta x, -\Delta y) = P_{SE}, \tag{8.10}$$

We obtain a system of equations for the coefficients a, b, c, d. These coefficients are obtained as

$$a = P_C \tag{8.11}$$

$$b = \frac{P_E - P_C}{\Delta x} \tag{8.12}$$

$$c = \frac{P_C - P_S}{\Delta y} \tag{8.13}$$

$$d = \frac{P_E - P_C + P_S - P_{SE}}{\Delta x \Delta y} \tag{8.14}$$

Substituting $(\frac{\Delta x}{4}, \frac{\Delta x}{4})$ into the interpolant, we obtain the approximation for P_q as

$$P_q \approx \frac{15P_C + 5P_E + 3P_S - P_{SE}}{16}$$

To remove the neumann condition's dependence on the halo node $\tilde{P}_N$, we again exploit the bilinear interpolant relations

$$P_{mid} = P_C + \frac{P_E - P_C}{4}$$

and

$$P_{right} = \frac{P_E + P_C}{2}$$

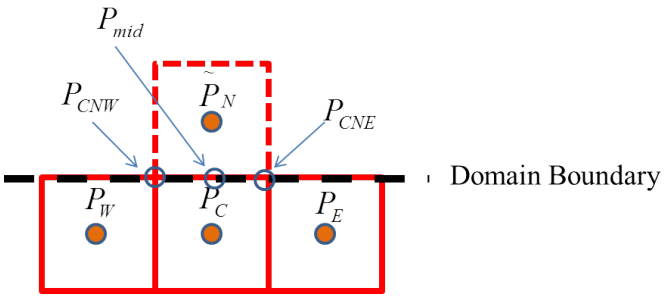

Figure 8.6: North Boundary Cell

with the approximation

$$P_{mid} \approx \frac{\tilde{P}_N + P_q + P_{right} + P_C}{4}$$

we obtain

$$\tilde{P}_N = 2P_C + P_E - P_q - P_{right}.$$

Substituting the expression into (8.6), we eliminate the dependence on the halo node and express the corner boundary condition solely in terms of the cour nearest neighbor nodes P_C, P_E, P_S, and P_{SE}. All other corner neumann conditions in the Dirichlet Center approach can be implemented by analogous proceedure.

8.2.2 Dirichlet Conditions with Neumann Center Approach

Unlike the implementation of Neumann conditions with the Dirichlet Center approach, the Dirichlet conditions with the Neumann Center approach does not require special treatment of corner cells since the grid construction is a true partition of the domain. Consider the an arbitrary boundary cell as shown in Figure 8.6. The flux through the north boundary of cell C is not given explicitly and must be approximated at the point x_{mid}. Assuming the linear flux relation at this boundary, we can approximate the normal flux by

$$k(x_{mid})\frac{\tilde{P}_N - P_C}{\Delta y} \tag{8.15}$$

where $\tilde{P}_N$ is a halo node lying at a distance of $\frac{\Delta y}{2}$ north of P_{mid}. The cell corner nodes P_{CNE} and P_{CNW} both lie on the north boundary and thus are known quantities. Furthermore

both corner points lie at a distance $\frac{\Delta y}{2}$ from P_{mid}. Exploiting the four point average approximation

$$P_{mid} = \frac{\tilde{P}^N + P_C + P_{CNE} + P_{CNW}}{4}$$

we can easily solve for $\tilde{P}^N$ and substitute into the north flux term of this cell.

8.3 Initial Guesses

Recall that our multiscale method is iterative and requires an initial guess of the macroscopic field values. As reported in [27, 26, 35] and our previous results in this thesis, the case of dirichlet boundary conditions provides a natural choice for an initial distribution of macroscopic field values; namely, interpolation between the boundary conditions. For 1D simulation, we can simply choose the linear interpolation between the left and right boundary conditions. For higher dimensional simulation, we can choose a macroscopic field value distribution which satisfies the PDE with homogeneous unit coefficients. In our simulation results, we observed that all simulations with pure dirichlet boundary conditions converged independently of how the values were interpolated between the boundaries. We note that in all these cases, the initial guess of the macroscopic field variable distribution retained the property that boundary conditions were satisfied to within numerical precision.

In the case of mixed boundary conditions, the choice is nontrivial since flux boundary conditions do not necessarily provide a specific, fixed field value from which to interpolate. Nonetheless, a distribution must be chosen to initialize the multiscale iterations. From our observations of the pure dirichlet, we suspect that the initial guess can be chosen arbitrarily, provided that all boundary conditions are satisfied. We explore the effect of satisfying the neumann boundary condition by numerical simulation as described in the following section.

8.4 Numerical Experimentation

In our numerical experiments, we test whether satisfaction of the neumann boundary condition is a necessary condition to ensure convergence of our multiscale method in the context of mixed boundary conditions. We conduct a series of convergence studies on the 1D multiscale reaction diffusion problem both with and without satisfaction of the neumann boundary condition and observe whether the resulting solution converges or diverges as the total sampling area $\mu\delta \rightarrow |\Omega|$. We utilize the same convergence sampling pattern as described in chapter 6. We only consider the reaction-diffusion problem because the problem naturally encompasses deformation problem in the case with $c = 0$. In all tests, we assume the case where the left boundary condition is dirichlet with a value P_R and the right boundary condition is neumann with a value F_R.

To obtain an initial guess which enforces the neumann boundary condition, we assume the linear flux constitutive relation with a harmonically averaged material coefficient

$$-k_{harmonic}\frac{P_R - P_L}{x_R - x_L} = F_R$$

where $k_{harmonic} = \frac{n}{\sum_{i=1}^{n}\frac{1}{k_i}}$ is the harmonic mean of the material coefficients k_i of the reference problem; i.e. the material coefficient values of original PDE solved entirely at the fine scale. From this assumption, we simply solve the above equation for P_R and use its value to interpolate all other intermediary field values.

By using the harmonic mean, we impose the condition that the initial guess has (on average) a constant flux given by the neumann condition F_R. The use of the harmonic average, as opposed to the arithmetic average, follows from its wide-spread use in discrete homogenization of porous media[47].

To test initial guesses which do not satisfy the neumann boundary condition, we simply choose arbitrary values P_R and interpolate accordingly. We chose P_R randomly with a uniform distribution between [-20,20] to discern the effects of non-compliance with respect to the neumann condition. We are specifically interested in cases where the initial

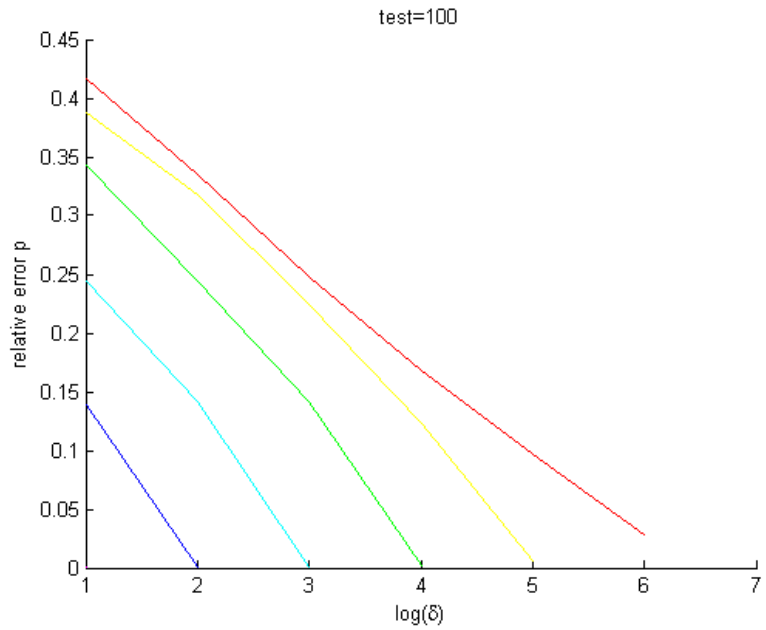

Figure 8.7: Convergence of reaction diffusion problem with initial guess satisfying the neumann boundary condition

homogenized flux is close to F_R, has the same sign as F_R and has the opposite sign as F_R.

In all simulations, we tested the case with material and reaction coefficients of roughly equal magnitude. We imposed the dirichlet boundary condition as $P_L = 0$ and the neumann condition as $F_R = 1$. We chose material coefficients randomly distributed $k \in [1, 1000]$ and a reaction coefficient $c = 500$. As before, we averaged the maximum relative errors over a series of 100 random tests for each choice of P_R.

8.5 Results

Figure 8.7 shows the convergence results of solving the mixed boundary condition problem such that the initial guess satisfies the neumann boundary condition. As expected, all simulations converged with similar accuracy as the case of pure dirichlet conditions.

To our surprise, all simulations of mixed boundary conditions with initial guess not

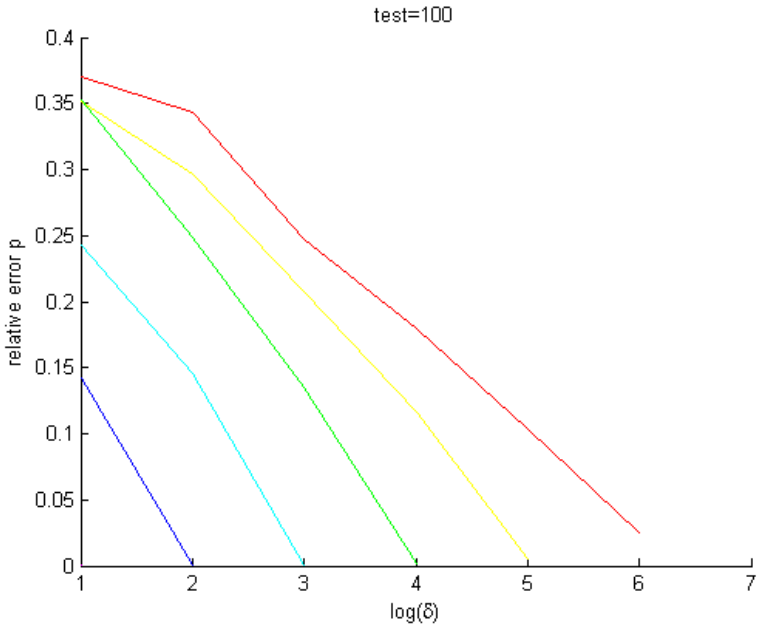

Figure 8.8: Convergence of reaction diffusion problem with initial guess interpolated from $P_R = 17.38$

satisfying the neumann boundary condition also converged as well. Figures 8.8- 8.9 are exemplary of this counterintuitive convergence behavior. It is apparent that the initial guess need not have a neumann condition close to nor even the same sign as the given flux condition. It is apparent that convergence is guaranteed in all situations. Clearly, this is not the case for dirichlet conditions. When the initial guess contains boundary values which do not match the given conditions, the iteration converges to the incorrect solution. Our simulation results also revealed that when we use an initial guess which does not satisfy the dirichlet condition for the mixed boundary problem, the multiscale iterations also converge to the incorrect solution.

From our tests, we can assert that for the case of mixed boundary conditions in the multiscale problem, our algorithm need only satisfy the dirichlet boundary conditions. The distribution of macroscopic field values can otherwise be chosen arbitrarily and yield equivalent convergence tendencies and equivalent accuracy.

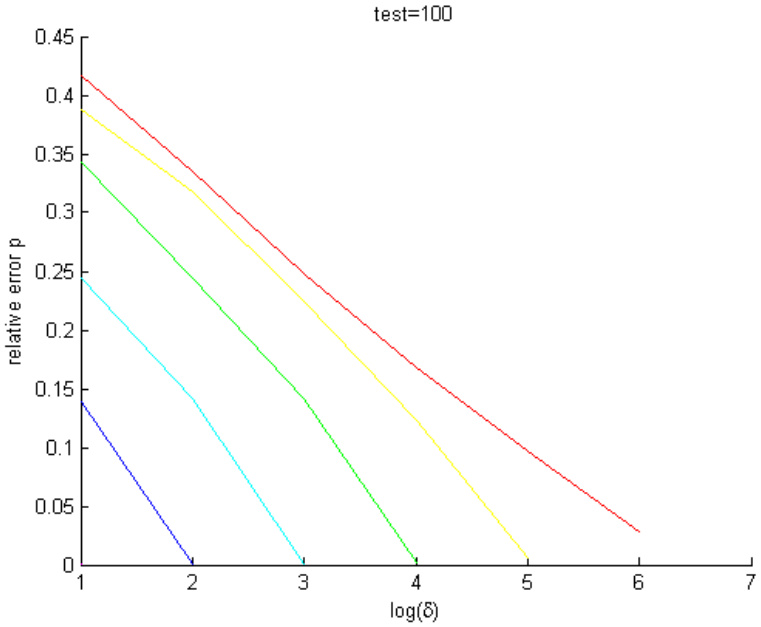

Figure 8.9: Convergence of reaction diffusion problem with initial guess interpolated from $P_R = -10$

Chapter 9

Higher Dimensional Models

The work we established in previous chapters is valid for single dimensional simulation. In this section, we extend our method to two dimensions for both flow and deformation models. Three dimensional approaches can be easily extrapolated from the 2D approach as well.

The primary complication to extending our 1D multiscale method to multiple dimensions is the existence of multiple partial derivatives and/or multiple primary variables. As we did with the 1D model, we shall treat the partial derivatives of the primary variables (pressure, displacement) as independent variables and refer to them as **subgradients**. Thus, we can expand a first order taylor series of each flux/stress component in terms of these independent variables to obtain the coupling coefficients. By applying the finite volume discretization at the macroscopic scale, the coupling coefficients are naturally defined in terms of fluxes/stresses along each control volume boundary.

9.1 Flow

Whether we choose the iterative splitting or the fixed-stress splitting approach, the decoupled flow model becomes a reaction-diffusion equation of the form

$$\nabla \cdot v + C^* P = S \text{ in } \Omega$$

where v denotes the discharge velocity, C^* is a positive constant, and Ω is a square domain with pure dirichlet boundary conditions given by

$$u = g(x) \text{ on } \partial\Omega.$$

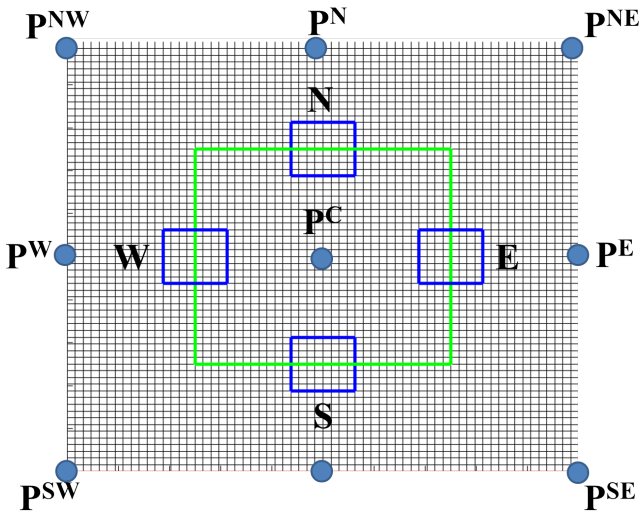

Figure 9.1: Control Volume (green) with samples of size $\delta \times \delta$ on each boundary and local nodal pressure values P in each of the neighboring control volumes.

We follow our 1D approach and formulate an incomplete finite volume discretization. This discretization enforces conservation locally in each control volume CV and results in the expression

$$\int_{\partial CV} v \cdot n + C^* \int_{CV} P = \int_{CV} S \tag{9.1}$$

We do not assume that a constitutive relation for v is given explicitly. Instead, we assume that it is a vector valued function $v = [v_1, v_2]^T$ such that each component is a function of space x, pressure P, and pressure gradient $\nabla P = [P_x, P_y]^T$ given by $v_i = v_i(x, P, P_x, P_y)$.

Assume that the domain Ω is tesselated into square control volumes. Then, the boundary ∂CV can be divided into its north, south, east, and west components as seen in figure 9.1. Note that the normal vectors to each boundary enable us to simplify the surface integrals along each boundary as

$$\int_{\partial CV^E} v \cdot n = \int_{\partial CV^E} v_1$$

$$\int_{\partial CV^N} v \cdot n = \int_{\partial CV^N} v_2$$

$$\int_{\partial CV^W} v \cdot n = -\int_{\partial CV^W} v_1$$
$$\int_{\partial CV^S} v \cdot n = -\int_{\partial CV^S} v_2.$$

We discretize the surface integrals by evaluating each integrand at the midpoint of each boundary (i.e. the quadrature point), yielding

$$\int_{\partial CV^E} v_1 = v_1^E \Delta y$$
$$\int_{\partial CV^N} v_2 = v_2^N \Delta x$$
$$-\int_{\partial CV^W} v_1 = v_1^W \Delta y$$
$$-\int_{\partial CV^S} v_2 = v_2^S \Delta x$$

where v_i^D is the velocity component i evaluated at the midpoint of control volume boundary CV^D for $D = E, N, W, S$. Note that this quantity is not evaluated directly from the macroscopic equation. Instead, we infer the information v_i^D from simulations of an underlying microscopic model witin a small square subdomain B_δ^D centered at the midpoint of control volume boundary CV^D.

9.1.1 Microscale Model

Note that the underlying microscale model is the same as for the 1D case: a modified form of the pore-network model with an additional reaction term. Recall this model as

$$\sum q_{ij} + c^* p_i L = s_i L$$
$$q_{ij} = c_{ij}(p_i - p_j)$$

In our 2D model, we assume the microscopic model is defined on an equispaced rectangular lattice of stepsize L with connectivity 4. The flux through a cross-sectional plane of the subdomain is also approximated by the total sum of fluxes in the normal direction as in the 1D case.

9.1.2 Iterative Coupling

In the pure diffusion flow model, we make the assumption that $\nabla \cdot v = 0$ when $\nabla P = 0$ based upon the *physical* assumption that a zero pressure gradient induces no flow. For the reaction-diffusion process, this assumption may not be interpreted as a direct extension of the physics of the underlying problem. Instead, we interpret this assumption as a linearization of the velocity model v under sufficiently small pressure gradients. Thus, we also make use of the this assumption and incorporate it into the construction of our method for the reaction-diffusion equations.

Thus, we can construct the taylor series expansion of the velocity components v_1 and v_2. Treating the components of the gradient P_x and P_y as independent variables, we write

$$\begin{aligned} v_i(x, P, P_x, P_y) &= v_1(x, P, 0, 0) + \frac{\partial v_i(x, P, \xi_1, \xi_2)}{\partial P_x} P_x + \frac{\partial v_i(x, P, \xi_1, \xi_2)}{\partial P_y} P_y \qquad (9.2) \\ &= \frac{\partial v_i(x, P, \xi_1, \xi_2)}{\partial P_x} P_x + \frac{\partial v_i(x, P, \xi_1, \xi_2)}{\partial P_y} P_y. \qquad (9.3) \end{aligned}$$

Since ξ_1, ξ_2 are intermediate values[1], we can approximate the partial derivatives in (9.3) by

$$\frac{\partial v_i(x, P, \xi_1, \xi_2)}{\partial P_x} \approx \frac{v_i(x, P, P_x, 0) - v_i(x, P, 0, 0)}{P_x} = \frac{v_i(x, P, P_x, 0)}{P_x}$$

and

$$\frac{\partial v_i(x, P, \xi_1, \xi_2)}{\partial P_y} \approx \frac{v_i(x, P, 0, P_y) - v_i(x, P, 0, 0)}{P_y} = \frac{v_i(x, P, 0, P_y)}{P_y}$$

Note that this decomposition expresses the velocities v_i as functions of incomplete or partial gradients $[P_x, 0]^T$ and $[0, P_y]^T$.

Since the velocity can be interpreted as the flux per cross-sectional area, we can rewrite v_i in terms of the flux induced by each subgradient $[P_x, 0]^T$ or $[0, P_y]^T$. We shall utilize the flux f obtained from the numerical solution of the micromodel on local subdomain B_δ. The reference cross-sectional area in 2D is precisely the length δ of the micro models. Thus, we can express

$$v_i(x, P, P_x, 0) \approx \frac{f^{P_x}}{\delta}$$

[1] By extension of the multivariate mean value theorem.

and

$$v_i(x, P, 0, P_y) \approx \frac{f^{P_y}}{\delta}$$

Hence, each micromodel requires the flux in the normal direction i induced by partial derivatives of the pressure in both the normal and tangential directions. Note that for isotropic constitutive models, the flux in direction i induced by an subgradient in the orthogonal direction is identically zero. For anisotropic tensors, a tangential subgradient can induce flow in the normal direction as well. Thus, our model has the potential to account for anisotropy.

Recall that the quantity v_1 is only evaluated at quadrature points in the x-direction (E & W) and v_2 in the y-direction quadrature points (N & S). Hence, we shall denote v_i^D as the velocity in direction i at the required quadrature point D. Using this notation, we shall define the coefficients

$$\left(K_D^{x_i,P_{x_j}}\right)^n \equiv \frac{v_i^{D,P_{x_j}^n}}{P_{x_j}^n} = \frac{f_D^{x_i,P_{x_j}^n}}{\delta P_{x_j}^n}$$

where the index n denotes the current iteration of our multiscale algorithm with the micro models all receiving boundary conditions interpolated from the macroscopic pressure field P^n.

Substituting these coefficients into our macroscopic finite volume discretization, we obtain the system of equations

$$(F^N)^n + (F^S)^n + (F^E)^n + (F^W)^n + C^* P^n \Delta x \Delta y = S_{i,j} \Delta x \Delta y$$

with

$$(F^D)^n = \left(\left(K_D^{x_i,P_x}\right)^n \partial_x^D P^{n+1} + \left(K_D^{x_i,P_y}\right)^n \partial_y^D P^{n+1}\right) H$$

where $H = \Delta x$ or Δy as needed and ∂_x, ∂_y are the discrete approximations of the gradient at the required quadrature point D.

9.2 Deformation

The operator-splitting schemes employed in this thesis result in the standard linear elasticity equations given by

$$\begin{aligned} \nabla \cdot \sigma + \vec{F} &= 0 \\ \sigma \equiv &= 2\mu\epsilon + \lambda tr(\epsilon) I \\ \epsilon &= \frac{1}{2}\left(\nabla \vec{u} + \nabla \vec{u}^T\right) \\ u &= d(x) \text{ in } \partial\Omega_d \\ (2\mu\epsilon + \lambda tr(\epsilon) I) \cdot n &= t(x) \text{ in } \partial\Omega_t \end{aligned}$$

Though the linear constitutive relation forms a part of our derived equations, our multiscale method is sufficiently generalized to the case where the constitutive model is unknown and must be inferred from the microscopic models defined on local subdomains B_δ.

9.2.1 Microscopic Model

Unlike the case of fluid flow, solid deformation requires two separate parameters to characterize the effects of applied normal and shear stresses to the surface of the object. Likewise, we require a microscale model with two-parameter field characterizing these stresses. Many potential options exist for microscale models, depending on the scale of the heterogeneity being modelled. In our particular case, we assume that the continuum model of linear elasticity is still applicable in our micro models. We further assume that at this scale, a linear constitutive relation is feasible. Thus, the micromodels are governed by the equations

$$\begin{aligned} \nabla \cdot \sigma &= \vec{F} \\ \sigma &= \mu\epsilon + \mu tr(\epsilon) \\ \epsilon &= \frac{1}{2}\left(\nabla \vec{u} + (\nabla \vec{u})^T\right) \end{aligned}$$

These equations are identical to those of the original problem, except that they are defined locally on square subdomains B_δ centered at the midpoints of each control volume as illustrated in figure 9.4. The boundary conditions of each model is obtained from linear interpolation of the neighboring macroscopic displacement grid.

Once a numerical solution of each model is obtained, the total normal and shear force in each subdomain can be obtained by approximating the integral of the constitutive relation

$$\int_{B_\delta} \sigma_x, \int_{B_\delta} \sigma_y, \text{ and } \int_{B_\delta} \tau_{xy}$$

as needed.

9.2.2 Macroscopic Model

We apply a finite volume discretization of the momentum balance equation

$$-\nabla \cdot \sigma = \vec{F}$$

Integrating over a given control volume CV, and applying divergence theorem, we obtain a the conservation equation

$$-\int_{\partial CV} \sigma \cdot n = \int_{CV} \vec{F} \tag{9.4}$$

Without loss of generality, we a domain $\Omega \in \mathbb{R}^2$ that can be partitioned into a finite number of rectangular cells with boundaries ∂CV^N, ∂CV^S, ∂CV^E, ∂CV^W as depicted in Figure 9.2. We define the unknown displacement field variables u and v at each of the cell centers. Exploiting this notation, equation 9.4 becomes

$$-\int_{\partial CV^N} \sigma \cdot n - \int_{\partial CV^S} \sigma \cdot n - \int_{\partial CV^E} \sigma \cdot n - \int_{\partial CV^W} \sigma \cdot n = \int_{CV} \vec{F} \tag{9.5}$$

Denoting the body force density vector in component form $\vec{F} = [f, g]^T$, we transform equation 9.5 into the system

$$-\int_{CV^E} \sigma_x + \int_{CV^W} \sigma_x - \int_{CV^N} \tau_{xy} + \int_{CV^S} \tau_{xy} = \int_{CV} f \tag{9.6}$$

$$-\int_{CV^N} \sigma_y + \int_{CV^S} \sigma_y - \int_{CV^E} \tau_{xy} + \int_{CV^W} \tau_{xy} = \int_{CV} g \tag{9.7}$$

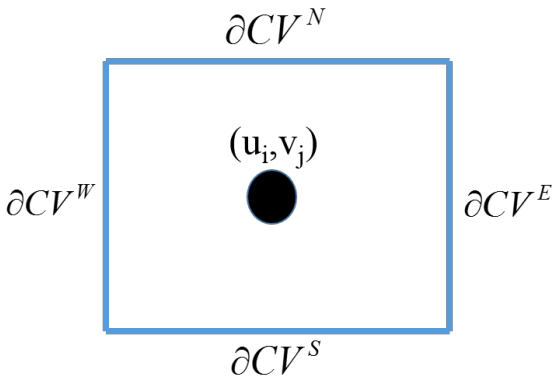

Figure 9.2: Representative Control Volume Cell with North, South, East, and West boundaries.

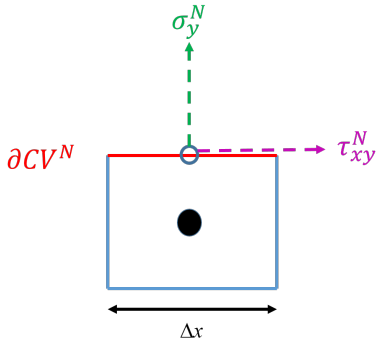

Figure 9.3: North Control Volume with normal and shear stress components.

We note that equations 9.6- 9.7 are expressed in terms of total normal and shear forces along each boundary.

For our multiscale model, we need not assume a linear stress-strain relation or any explicit constitutive relation for the macroscopic model. Instead, we approximate the macroscopic stresses from microscale simulations on small sample subdomains centered at the midpoints of each control volume boundary. The details of this coupling are described as follows.

9.2.3 Iterative Coupling

We make a fundamental assumption that no stress is induced when the displacement gradient $\nabla\vec{u} = 0$. This assumption can written in component form as

$$\sigma \equiv \begin{bmatrix} \sigma_x & \tau_{xy} \\ \tau_{xy} & \sigma_y \end{bmatrix} = \begin{bmatrix} 0 & 0 \\ 0 & 0 \end{bmatrix} \text{ when } \nabla\vec{u} \equiv \begin{bmatrix} u_x & u_y \\ v_x & v_y \end{bmatrix} = \begin{bmatrix} 0 & 0 \\ 0 & 0 \end{bmatrix}$$

We further assume that the stress components can be written as functions of the position $\vec{x} = [x, y]^T$, displacement $\vec{u} \equiv [u, v]^T$, and displacement gradient $\nabla\vec{u}$, with

$$\begin{aligned} \sigma_x &= \sigma_x(\vec{x}, \vec{u}, \nabla\vec{u}) \\ \sigma_y &= \sigma_y(\vec{x}, \vec{u}, \nabla\vec{u}) \\ \tau_{xy} &= \tau_{xy}(\vec{x}, \vec{u}, \nabla\vec{u}) \end{aligned}$$

For simplicity of notation, we shall omit the explicit dependence on $\vec{x}, \vec{u}$, and emphasize the dependence on the displacement gradient $\nabla\vec{u}$ and the vector $\vec{\xi}$. Thus, we write the above three equations simply as

$$\sigma_x = \sigma_x(\nabla\vec{u}) \tag{9.8}$$

$$\sigma_y = \sigma_y(\nabla\vec{u}) \tag{9.9}$$

$$\tau_{xy} = \tau_{xy}(\nabla\vec{u}) \tag{9.10}$$

Expanding the taylor series of the stress components centered at $\nabla\vec{u} = 0$ and applying the mean value theorem, we obtain

$$\sigma_x(\nabla\vec{u}) = \sigma_x(\vec{0}) + \frac{\partial\sigma_x(\vec{\xi})}{\partial u_x}u_x + \frac{\partial\sigma_x(\vec{\xi})}{\partial u_y}u_y + \frac{\partial\sigma_x(\vec{\xi})}{\partial v_x}v_x + \frac{\partial\sigma_x(\vec{\xi})}{\partial v_y}v_y$$

$$\sigma_y(\nabla\vec{u}) = \sigma_y(\vec{0}) + \frac{\partial\sigma_y(\vec{\xi})}{\partial u_x}u_x + \frac{\partial\sigma_y(\vec{\xi})}{\partial u_y}u_y + \frac{\partial\sigma_y(\vec{\xi})}{\partial v_x}v_x + \frac{\partial\sigma_y(\vec{\xi})}{\partial v_y}v_y$$

$$\tau_{xy}(\nabla\vec{u}) = \tau_{xy}(\vec{0}) + \frac{\partial\tau_{xy}(\vec{\xi})}{\partial u_x}u_x + \frac{\partial\tau_{xy}(\vec{\xi})}{\partial u_y}u_y + \frac{\partial\tau_{xy}(\vec{\xi})}{\partial v_x}v_x + \frac{\partial\tau_{xy}(\vec{\xi})}{\partial v_y}v_y$$

with $\vec{\xi}, \vec{0} \in \mathbb{R}^4$ and $\vec{\xi} \equiv (\xi_1, \xi_2, \xi_3, \xi_4)$ is a vector of intermediate values lying in the hypercube $[0, u_x] \times [0, u_y] \times [0, v_x] \times [0, v_y]$, respectively.

Substituting our assumption that $\sigma = 0$ when the displacement gradient $\nabla \vec{u} = 0$, we eliminate the first term in each of the above three equations, yielding

$$\sigma_x(\nabla \vec{u}) = \frac{\partial \sigma_x(\vec{\xi})}{\partial u_x} u_x + \frac{\partial \sigma_x(\vec{\xi})}{\partial u_y} u_y + \frac{\partial \sigma_x(\vec{\xi})}{\partial v_x} v_x + \frac{\partial \sigma_x(\vec{\xi})}{\partial v_y} v_y \tag{9.11}$$

$$\sigma_y(\nabla \vec{u}) = \frac{\partial \sigma_y(\vec{\xi})}{\partial u_x} u_x + \frac{\partial \sigma_y(\vec{\xi})}{\partial u_y} u_y + \frac{\partial \sigma_y(\vec{\xi})}{\partial v_x} v_x + \frac{\partial \sigma_y(\vec{\xi})}{\partial v_y} v_y \tag{9.12}$$

$$\tau_{xy}(\nabla \vec{u}) = \frac{\partial \tau_{xy}(\vec{\xi})}{\partial u_x} u_x + \frac{\partial \tau_{xy}(\vec{\xi})}{\partial u_y} u_y + \frac{\partial \tau_{xy}(\vec{\xi})}{\partial v_x} v_x + \frac{\partial \tau_{xy}(\vec{\xi})}{\partial v_y} v_y \tag{9.13}$$

For each of the stress functions $\nu = \sigma_y, \sigma_x$ and τ_{xy}, we denote its Jacobian matrix by

$$J_\nu(\vec{\xi}) \equiv \begin{bmatrix} \frac{\partial \nu(\vec{\xi})}{\partial u_x} & \frac{\partial \nu(\vec{\xi})}{\partial u_y} \\ \frac{\partial \nu(\vec{\xi})}{\partial v_x} & \frac{\partial \nu(\vec{\xi})}{\partial v_y} \end{bmatrix}, \tag{9.14}$$

and rewrite equations 9.11- 9.13 as

$$\nu_x(\nabla \vec{u}) = J_\nu(\vec{\xi}) : \nabla \vec{u}$$

where the colon (:) the Frobenius matrix inner product.

The quantities of interest are the entries comprising the Jacobian matrices $J_{\sigma_x}(\vec{\xi})$ for all $\nu = \sigma_y, \sigma_x$ and τ_{xy}. These entries are the partial derivatives of the normal and shear stresses with respect to each component of $\nabla \vec{u}$ evaluated at the intermediate vector $\vec{\xi}$. We shall refer to these as the **functional coefficients**.

When the stress components $\nu = \sigma_x$,σ_y, and τ_{xy} are linear functions of the stress gradients, the Jacobians J_ν are constant matrices and the Frobenius inner products above result in linear equations. For general elasticity problems, these Jacobians are non constant and the inner products result in in a non-linear normal and shear stress functions. To eliminate these potential non-linearities, we construct a sequence of approximations to the

stress components σ_x, σ_y and τ_{xy}. Applying a fixed point iteration over iterates K, we obtain

$$\nu^{K+1}(\nabla\vec{u}) = J_\nu^K(\vec{\xi}) : \nabla\vec{u}^{K+1} \tag{9.15}$$

where $J_\nu^K(\vec{\xi})$ are approximation of Jacobians of the stress functions $\nu = \sigma_y, \sigma_x$ and τ_{xy} over the previous iterate K.

The dependence of the jacobians on the intermediate vector $\vec{\xi}$ can be eliminated by replacing the partial derivatives with finite difference approximations over the respective subgradients. We define the ***subgradient*** G_i as vector of all zeros except in the ith element, where it retains the ith component of the vectorized displacement gradient $vec(\nabla\vec{u})$. The explicit formula for the subgradient is given by

$$G_i \equiv vec\,(\nabla\vec{u}) \circ e_i.$$

where

$$vec\,(\nabla\vec{u}) \equiv \begin{bmatrix} u_x \\ u_y \\ v_x \\ -v_y \end{bmatrix}$$

and e_i is the standard basis vector in $\mathbb{R}^4$ for $i = 1, ..., 4$. Here, the open circle notation $(\circ)$ denotes the *Hadamard* product.

Replacing the partial derivatives in the Jacobian matrices by finite differences in the respective unidimensional intervals $[0, u_x], [0, u_y], [0, v_x], [0, v_y]$ and again exploiting our initial assumption that $\sigma = 0$ when $\nabla\vec{u} = 0$, we approximate the Jacobian matrices $J_\nu^K(\vec{\xi})$ as

$$J_\nu^K(\vec{\xi}) \approx \begin{bmatrix} \frac{\nu(G_1^K)}{u_x^K} & \frac{\nu(G_2^K)}{u_y^K} \\ \frac{\nu(G_3^K)}{v_x^K} & \frac{\nu(G_4^K)}{v_y^K} \end{bmatrix} \tag{9.16}$$

To simplify notation further, we denote the numerators of each entry of the approximate Jacobian matrix in equation 9.16 as $\nu_{G_i}^K$, for all $\nu = \sigma_y, \sigma_x, \tau_{xy}$ and $i = 1, ..., 4$. Substituting 9.16 into equation 9.15, we obtain:

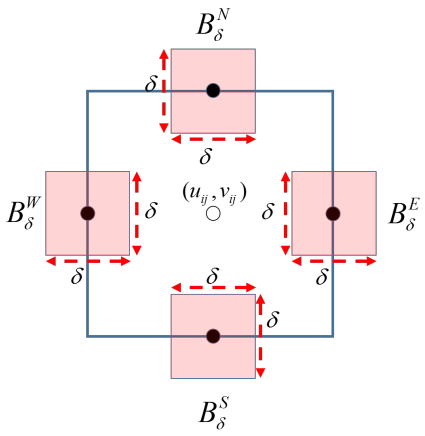

Figure 9.4: Boundary samples centered at midpoints of control volume boundaries

$$\int_{\partial CV} \nu \;=\; \sum_{i=1}^{4} \frac{\int_{\partial CV} \nu_{G_i}^K}{G_i^K \cdot e_i} \left(G_i^{K+1} \cdot e_i\right) \tag{9.17}$$

Observe that each of the quantities $\int_{\partial CV} \nu_{G_i}^K$ needs to be estimated for every control volume boundary and every subgradient G_i for $i = 1, ..., 4$, with ν varying over the normal and shear stress components of each boundary as seen in 9.6- 9.7. We utilize our microscopic model to estimate these values as described in the next section.

9.2.4 Data Estimation

For each control volume centered at the macroscopic grid point $\vec{x}^C$, we denote the sample subdomains B_δ^D of size $\delta \times \delta$ for $D = N, S, E$, and W centered at the midpoint of each corresponding control volume boundary as seen in Figure 9.4. We also denote $\nu_{G_i^D}^{D,K}$ as the functional coefficients corresponding to each boundary $D = N, S, E$, and W, each subgradient G_i^D, and each normal and shear stress component ν.

To estimate $\nu_{G_i^D}^{D,K}$, we first construct a local microscale model from the material parameters overlapping the region B_δ^D. For each subgradient G_i^D, we linearly interpolate pure dirichlet conditions onto the boundary of B_δ^D using only the subgradient G_i^D of the local macroscopic values (U,V) of the previous iteration K. Since the interpolation occurs over a

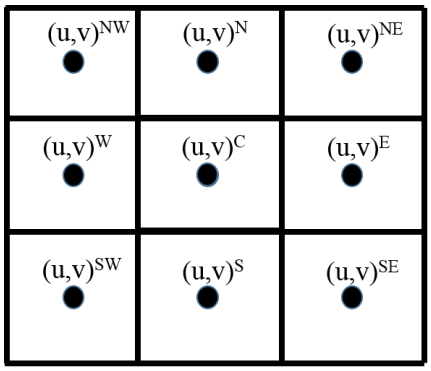

Figure 9.5: Local macroscopic grid notation with superscript C denoting the center control volume cell.

discrete rectangular grid, it is natural to estimate each subgradient using its corresponding finite differences approximation at the midpoint of the control volume boundary. Table 9.1 enumerates the finite difference stencils for each boundary D and subgradient G_i^D with local macroscopic displacement values as notated in Figure 9.5.

Once a solution to the microscopic model is obtained for a specific boundary sample D and its corresponding subgradient G_i^D, we calculate the total normal and shear force $\tilde{\nu}_{G_i^D}^{D,K}$ along the center cross-section of the micromodel intersecting the macroscopic control volume boundary. To assemble the macroscopic equations, we approximate each of the integrals in equation 9.17 with

$$\int_{\partial CV^D} \nu_{G_i}^{D,K} \approx \frac{\tilde{\nu}_{G_i^D}^{D,K}}{\delta} H.$$

where $H = \Delta x$ or Δy, depending on the length of the control volume boundary D. Let $C_{\nu,G_i}^{D,K} = \frac{\tilde{\nu}_{G_i^D}^{D,K} H}{\delta\left(G_i^{D,K} \cdot e_i\right)}$ for all $D = N, S, E$ and W, $i = 1, ..., 4$, and for all normal and shear stress components ν of each boundary D and

$$C_{\nu,y}^{D,K} = \begin{bmatrix} C_{\nu,G_1}^{D,K} & C_{G_4}^{D,K} \\ C_{\nu,G_2}^{D,K} & C_{G_3}^{D,K} \end{bmatrix}.$$

Then, each of the integrals in equations 9.6- 9.7 can be evaluated by the expression

$$\tilde{\nu}^{D,K+1} = C_{\nu,y}^{D,K} : \nabla \vec{u}^{D,K+1} \tag{9.18}$$

Boundary	Subgradient	Discrete Approximation
North	$G_1^N = [u_x, 0, 0, 0]^T$	$u_x \frac{u^{NE}+u^E-u^{NW}-u^W}{4\Delta x}$
North	$G_2^N = [0, u_y, 0, 0]^T$	$\frac{u^N-u^C}{\Delta y}$
North	$G_3^N = [0, 0, v_x, 0]^T$	$\frac{v^{NE}+v^E-v^{NW}-v^W}{4\Delta x}$
North	$G_4^N = [0, 0, 0, v_y]^T$	$\frac{v^N-v^C}{\Delta y}$
East	$G_1^E = [u_x, 0, 0, 0]^T$	$\frac{u^E-u^C}{\Delta x}$
East	$G_2^E = [0, u_y, 0, 0]^T$	$\frac{u^{NE}+u^N-u^{SE}-u^S}{4\Delta y}$
East	$G_3^E = [0, 0, v_x, 0]^T$	$\frac{v^N-v^C}{\Delta x}$
East	$G_4^E = [0, 0, 0, v_y]^T$	$\frac{v^{NE}+v^N-v^{SE}-v^S}{4\Delta y}$
South	$G_1^S = [u_x, 0, 0, 0]^T$	$\frac{u^{SE}+u^E-u^{SW}+u^W}{4\Delta x}$
South	$G_2^S = [0, u_y, 0, 0]^T$	$\frac{u^C-u^S}{\Delta y}$
South	$G_3^S = [0, 0, v_x, 0]^T$	$\frac{v^{SE}+v^E-v^{SW}+v^W}{4\Delta x}$
South	$G_4^S = [0, 0, 0, v_y]^T$	$\frac{v^C-v^S}{\Delta y}$
West	$G_1^W = [u_x, 0, 0, 0]^T$	$\frac{u^C-u^W}{\Delta x}$
West	$G_2^W = [0, u_y, 0, 0]^T$	$\frac{u^{NW}+u^N-u^{SW}-u^S}{4\Delta y}$
West	$G_3^W = [0, 0, v_x, 0]^T$	$\frac{v^C-v^W}{\Delta x}$
West	$G_4^W = [0, 0, 0, v_y]^T$	$\frac{v^{NW}+v^N-v^{SW}-v^S}{4\Delta y}$

Table 9.1: Discrete Gradient approximations at the midpoints of each of the control volume boundaries.

where $\nabla \vec{u}^{D,K+1}$ is also approximated by local finite difference approximations along boundary D as in Table 9.1. Explicitly, we write

$$(\tilde{\sigma_y})^{D,K+1} = C^{D,K}_{\sigma_y,y} : \nabla \vec{u}^{D,K+1} \tag{9.19}$$

By similar argument and analogous notation, the total normal force along the south boundary and total shear force along the east and west boundaries become

$$\tilde{\sigma}^{S,K+1}_y = C^{S,K}_y : \nabla \vec{u}^{S,K+1}, \tag{9.20}$$

$$\tilde{\tau}^{E,K+1}_{xy} = C^{E,K}_y : \nabla \vec{u}^{E,K+1}, \tag{9.21}$$

$$\tilde{\tau}^{W,K+1}_{xy} = C^{W,K}_y : \nabla \vec{u}^{W,K+1}, \tag{9.22}$$

with

$$C^{S,K}_y = \begin{bmatrix} C^{S,K}_{u_x} & C^{S,K}_{u_y} \\ C^{S,K}_{v_y} & C^{S,K}_{v_y} \end{bmatrix} = \begin{bmatrix} \frac{\tilde{\sigma}^{S,K}_{y,u_x}\Delta x}{\delta \cdot u^{S,K}_x} & \frac{\tilde{\sigma}^{S,K}_{y,u_y}\Delta x}{\delta \cdot u^{S,K}_y} \\ \frac{\tilde{\sigma}^{S,K}_{y,v_x}\Delta x}{\delta \cdot v^{S,K}_x} & \frac{\tilde{\sigma}^{S,K}_{y,v_y}\Delta x}{\delta \cdot v^{S,K}_y} \end{bmatrix},$$

$$C^{E,K}_y = \begin{bmatrix} C^{E,K}_{u_x} & C^{E,K}_{u_y} \\ C^{E,K}_{v_y} & C^{E,K}_{v_y} \end{bmatrix} = \begin{bmatrix} \frac{\tilde{\tau}^{E,K}_{xy,u_x}\Delta x}{\delta \cdot u^{E,K}_x} & \frac{\tilde{\tau}^{E,K}_{xy,u_y}\Delta x}{\delta \cdot u^{E,K}_y} \\ \frac{\tilde{\tau}^{E,K}_{xy,v_x}\Delta x}{\delta \cdot v^{E,K}_x} & \frac{\tilde{\tau}^{E,K}_{xy,v_y}\Delta x}{\delta \cdot v^{E,K}_y} \end{bmatrix},$$

and

$$C^{W,K}_y = \begin{bmatrix} C^{W,K}_{u_x} & C^{W,K}_{u_y} \\ C^{W,K}_{v_y} & C^{W,K}_{v_y} \end{bmatrix} = \begin{bmatrix} \frac{\tilde{\tau}^{W,K}_{y,u_x}\Delta x}{\delta \cdot u^{W,K}_x} & \frac{\tilde{\tau}^{W,K}_{xy,u_y}\Delta x}{\delta \cdot u^{W,K}_y} \\ \frac{\tilde{\tau}^{W,K}_{y,v_x}\Delta x}{\delta \cdot v^{W,K}_x} & \frac{\tilde{\tau}^{W,K}_{xy,v_y}\Delta x}{\delta \cdot v^{W,K}_y} \end{bmatrix}.$$

Then, the y-momentum equation becomes:

$$-C^{N,K}_y : \vec{u}^{N,K+1} + C^{S,K}_y : \vec{u}^{S,K+1} - C^{E,K}_y : \vec{u}^{E,K+1} + C^{W,K}_y : \vec{u}^{W,K+1} = \int_{CV} g \tag{9.23}$$

Likewise, the x-momentum equation becomes

$$-C^{E,K}_y : \vec{u}^{E,K+1} + C^{W,K}_y : \vec{u}^{W,K+1} - C^{N,K}_x : \vec{u}^{N,K+1} + C^{S,K}_y : \vec{u}^{S,K+1} = \int_{CV} f \tag{9.24}$$

with

$$C^{E,K}_x = \begin{bmatrix} C^{E,K}_{u_x} & C^{E,K}_{u_y} \\ C^{E,K}_{v_y} & C^{E,K}_{v_y} \end{bmatrix} = \begin{bmatrix} \frac{\tilde{\sigma}^{E,K}_{x,u_x}\Delta x}{\delta \cdot u^{E,K}_x} & \frac{\tilde{\sigma}^{E,K}_{x,u_y}\Delta x}{\delta \cdot u^{E,K}_y} \\ \frac{\tilde{\sigma}^{E,K}_{x,v_x}\Delta x}{\delta \cdot v^{E,K}_x} & \frac{\tilde{\sigma}^{E,K}_{x,v_y}\Delta x}{\delta \cdot v^{E,K}_y} \end{bmatrix},$$

$$C_x^{W,K} = \begin{bmatrix} C_{u_x}^{W,K} & C_{u_y}^{W,K} \\ C_{v_y}^{W,K} & C_{v_y}^{W,K} \end{bmatrix} = \begin{bmatrix} \frac{\tilde{\sigma}_{x,u_x}^{W,K}\Delta x}{\delta \cdot u_x^{W,K}} & \frac{\tilde{\sigma}_{x,u_y}^{W,K}\Delta x}{\delta \cdot u_y^{W,K}} \\ \frac{\tilde{\sigma}_{x,v_x}^{W,K}\Delta x}{\delta \cdot v_x^{W,K}} & \frac{\tilde{\sigma}_{x,v_y}^{W,K}\Delta x}{\delta \cdot v_y^{W,K}} \end{bmatrix},$$

$$C_x^{N,K} = \begin{bmatrix} C_{u_x}^{N,K} & C_{u_y}^{N,K} \\ C_{v_y}^{N,K} & C_{v_y}^{N,K} \end{bmatrix} = \begin{bmatrix} \frac{\tilde{\tau}_{xy,u_x}^{N,K}\Delta x}{\delta \cdot u_x^{N,K}} & \frac{\tilde{\tau}_{xy,u_y}^{N,K}\Delta x}{\delta \cdot u_y^{N,K}} \\ \frac{\tilde{\tau}_{xy,v_x}^{N,K}\Delta x}{\delta \cdot v_x^{N,K}} & \frac{\tilde{\tau}_{xy,v_y}^{N,K}\Delta x}{\delta \cdot v_y^{N,K}} \end{bmatrix},$$

Equations 9.23- 9.24 complete the macroscopic equations for our multiscale model for solid deformation in two dimensions.

9.3 Summary

The two-dimensional multiscale methods for flow and deformation are easily seen as extensions of the 1D multiscale models developed in earlier chapters. The key difference is that the taylor expansion of the velocity and stress terms yield multiple sets of boundary conditions that need to be imposed and solved on the local sample microscale models; that is, one set of boundary conditions for each subgradient for each sample. We can summarize our multiscale method in dimesion-agnostic and macroscopic field variable-agnostic form in pseudo-code as follows:

Algorithm 1 Finite Volume-Based Heterogeneous Multiscale Algorithm

1: Given an initial guess of macroscopic field Q^0
2: **for** $K = 0$,... until convergence **do**
3: **for** Each sample B_δ **do**
4: **for** Each Subgradient G **do**
5: Project boundary conditions from subgradient G of Q^K in B_δ.
6: Assemble and solve micro model in B_δ
7: Compute Coupling parameters $C_G^{B_\delta,K}$
8: Assemble and solve macro model for Q^{K+1} from coupling parameter $C_G^{B_\delta,K}$
9: Return Q^{K+1}

9.4 Numerical Experiments

To assess the convergence of our multiscale method in higher dimensions, we conducted numerical experiments in two dimensions. First, we verified the numerical convergence of our multiscale method applied to the steady state flow (pure diffusion) problem as in [27, 26]. Then, we tested the convergence of the solid deformation and reaction diffusion problems.

We applied a similar sampling/testing scheme as in 1D. Namely, we chose a unit square computational domain $\Omega = [0, 1]^2$ and chose equispaced macroscopic control volume cells of size $\Delta x = \frac{1}{2^{p_1}}$ such that all the centers of all cells that intersect the boundary aligned perfectly on the boundary. For each control control μ volume lying entirely on the interior of the computational domain, we sample the underlying material parameters on a subdomain B_δ of length $\delta = 2^{p_2} L$ centered at each face of control volume μ. Here, p_1 and p_2 are positive integer powers such that μ and δ satisfy $\mu\delta \leq |\Omega|$.

We only consider problems with pure dirichlet boundary conditions. Unlike the 1D case, there is greater freedom to choose dirichlet conditions a function of the spatial variables x and y. More over, due to our 2D multiscale scheme's dependence on values lying in 9-point stencil surrounding each macroscopic gridpoint, it is imperative to ensure that the boundary conditions are chosen as continuous functions of the spatial variables. Unlike the traditional 5 point stencil utilized in solving the fine scale problem, piecewise constant boundary conditions cannot be utilized.

To alleviate continuity issues, we employ the method of manufactured solutions for all simulations except in the case of randomly distributed material parameters. In all cases where a source term is necessary (for the manufactured solution), we utilize its nodal values in the local microscale model and a numerical integration approximation in the macroscopic model. For the random case, we simply utilize the numerical solution of the PDE on a fine scale as our reference solution.

As we saw in the 1D case, we compare calculate the relative L^∞ norm error of our

Case	Manufactured Solution $p(x, y)$	Material Coefficient $k(x, y)$
1	$x + y$	1
2	$x + y$	$1 + 100(x^3 + y^3)$
3	$sin\left(\frac{\pi x}{2}\right) sin\left(\frac{\pi y}{2}\right)$	$101 + sin(10\pi x)sin(10\pi y)$
4	Boundary Condition $x + y$	Random $k(x, y) \in [1, 1000]$

Table 9.2: Manufactured solutions and Material Coefficients tested for the 2D Flow (pure diffusion) problem.

multiscale method to a reference solution (manufactured or fine scale) for each sample size δ and for each number of sampling subdomains μ.

9.5 2D Pure Diffusion

9.5.1 Cases

We first tested the convergence of our multiscale method for the Pure diffusion problem (reaction coefficient $c = 0$) using the manufactured solutions and material coefficients as illustrated in table 9.2. Case 1 is equivalent to testing the case of constant material parameters as seen in previous chapters. Case 2 involves a variable coefficient which is a cubic function of the spatial variables. Case 3 involves a highly oscillatory material coefficient.

To ensure that our method captured two dimensional flow and was not simply a special extension of the 1D model, we further imposed constraints on the form of the manufactured solutions. We chose them such that the average solution gradients contained non-zero components in both the x and y directions. This ensures that the average flux across the medium is neither purely along the x or y axes, but is diagonal across the domain.

Case 4 consists of testing our algorithm on a heterogeneous media with a randomly distributed material coefficient. As before, we 100 tests of our algorithm on a material

coefficient distributed in the range [1,1000] and computed the average relative L^∞ norm error.

9.5.2 Results

The convergence results for Pure Diffusion Cases 1-4 are illustrated in figures 9.7- 9.9, respectively. In Case 1 with constant coefficients, we observe that our multiscale method produces a solution near machine precision in pressure, with flux error approximately one order of magnitude higher, as expected.

Cases 2 and 3 illustrate the effects of variable coefficients without scale separation on the solutions produced by our multiscale algorithm. Clearly, in both cases, we observe a monotonically decreasing error as the sample size δ and number of sampling subdomains μ increase. However, these cases also illustrate that when the variable coefficient contains no scale separation, the multiscale scheme provides little enhancement to the solution. In fact, the error is controlled primarily by the number of sampling subdomains, which is correlated to the macroscopic spatial discretization size $\Delta x = \Delta y \equiv H$.

In case 4, we observe much more clear convergence trend. As both μ and δ increase, the error decreases roughly linearly on the log-log plot shown in figure 9.9. This trend is consistent with our previous observations in the 1D case. However, we observe that the flux error is significantly larger than a single order of magnitude in difference compared to the pressure. This is clearly consistent with our observations in 1D, since our multiscale method treats the flux variable implicitly through its relation to the primary variable (pressure).

9.6 2D Reaction Diffusion

9.6.1 Cases

The performance of the multiscale algorithm in the pure diffusion case indicated that the best performance of the algorithm occurs when scale separation is present in the medium;

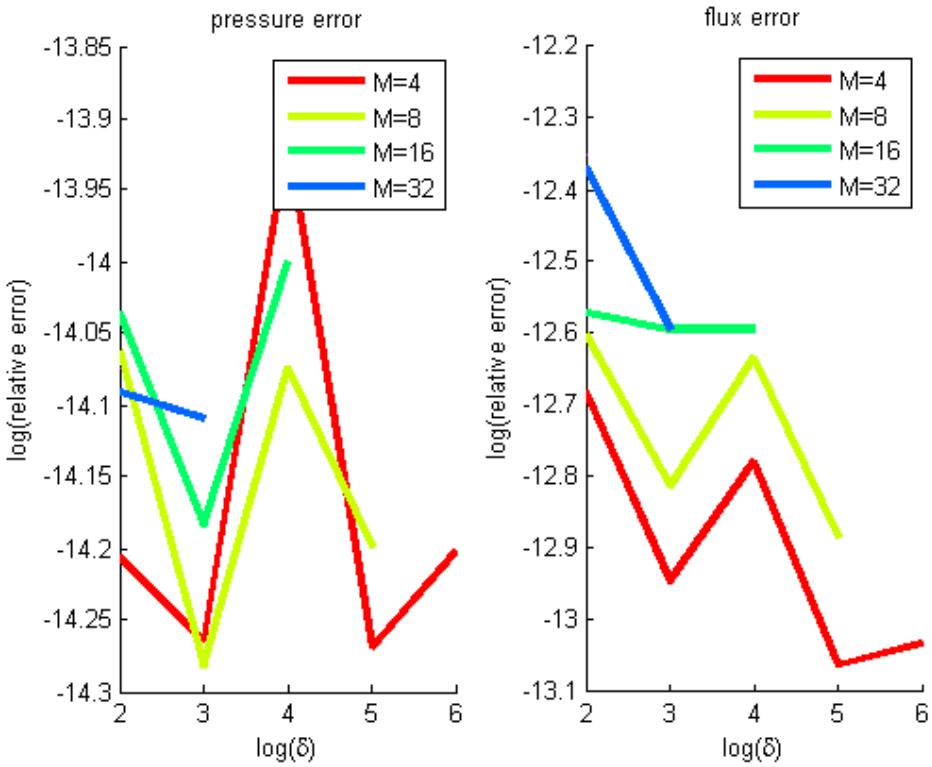

Figure 9.6: Case 1 Convergence for Diffusion Flow Problem

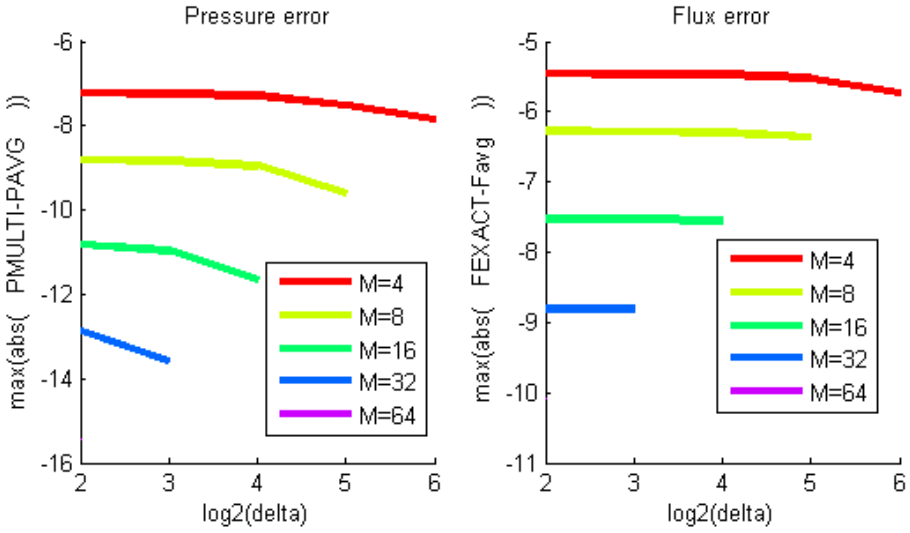

Figure 9.7: Case 2 Convergence for Diffusion Flow Problem

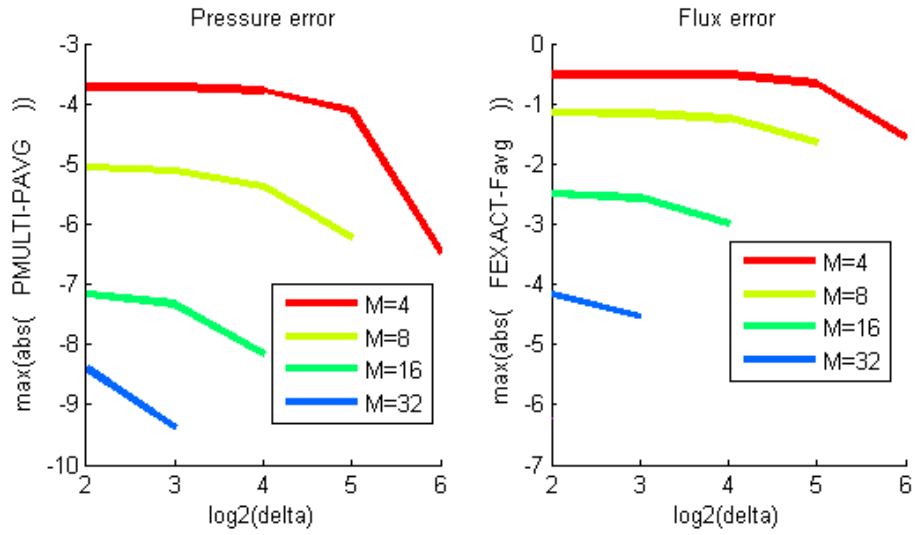

Figure 9.8: Case 3 Convergence for Diffusion Flow Problem

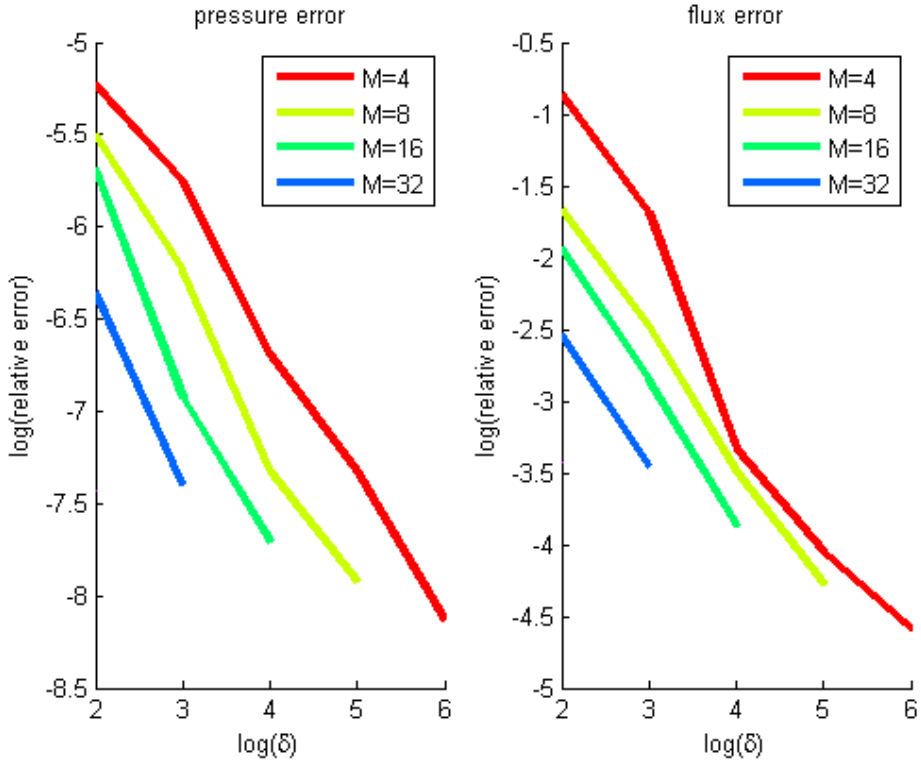

Figure 9.9: Case 4 Convergence for Diffusion Flow Problem

particularly when the material parameters are randomly distributed. For the Reaction Diffusion problem, we limit our analysis to the case of randomly distributed mobility parameters $k(x, y)$ throughout the domain.

Based on our observations of the 1D multiscale reaction diffusion problem, the relative magnitude of the linear reaction coefficient c with respect to the diffusion coefficient $k(x, y)$ plays a vital role in the expected behavior of the algorithm. When the diffusion coefficient dominated ($k(x) >> c$), the 1D multiscale algorithm yielded comparable results to the pure diffusion case. A similar trend was observed when the diffusion and reaction coefficients were of roughly equal magnitude. When the reaction coefficient dominated ($c >> k(x)$), the random variations of $k(x)$ in 1D played little role in the accuracy of the simulation. Rather, the error was primarily controlled by the macroscopic spatial stepsize H and decreased insignificantly with respect to the size of the sampling subdomains δ.

Consistent with the 1D trends, we also tested our algorithm for the 2D multiscale reaction diffusion problem under the three scenarios $c << k(x, y)$, $c \approx k(x, y)$ and $c >> k(x, y)$. We used an analogous convergence analysis as described for the 2D pure diffusion problem. Our reference solution was obtained from the numerical solution of the original PDE on a fine scale grid and the macroscopic grid and sampling subdomains were chosen as integer powers of two as before. Due to computer memory limitations, we were only able to test with a reference solution obtained on an 2D equispaced grid of size 1024×1024 on a unit square domain.

9.6.2 Results

Figures 9.10- 9.12 illustrate the convergence of our multiscale algorithm as applied to the reaction diffusion problem for the three cases tested. In each case, we chose the diffusion coefficient $k(x, y) \in [1, 1000]$ randomly and set the reaction coefficient c constant. Cases 1 & 2 illustrate that our multiscale algorithm has similar convergence trends as observed in the 1D reaction diffusion case. The error in pressure and flux both decrease monotonically as the sample size δ and number of sampling subdomains μ increase. The convergence

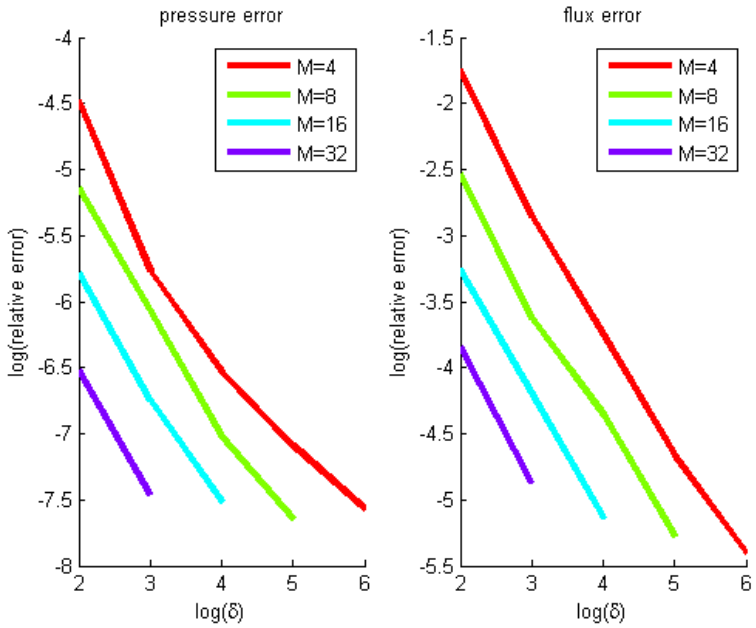

Figure 9.10: Convergence of Diffusion Dominated Reaction-Diffusion Problem with $c = 10$ and $k \in [1, 1000]$.

trends are roughly linear on the log-log scale plots in both cases. Also, the flux is observed to be more than one order of magnitude higher than the pressure. This is consistent with our previous observations in the 2D pure diffusion case.

In case III, where the reaction term $c = 100,000 >> k(x, y)$, we observe that increasing the sample size monotonically decreases the error. However, the error does not monotonically decrease as the number of sampling subdomains increases. For the 2D reaction diffusion problem, there exists a boundary layer in which the solution naturally undergoes a large gradient. When the sampling subdomains μ begin to capture data within this region, the error begins to decrease as μ increases. This is consistent with our previous results in 1D.

Our results show that our method may not be particularly effective for reaction-dominated processes. However, when the reaction term $c \leq k(x, y)$ for all $(x, y) \in \Omega$, our method is convergent in the random heterogeneity case. We note that other cases with $c \leq k(x, y)$

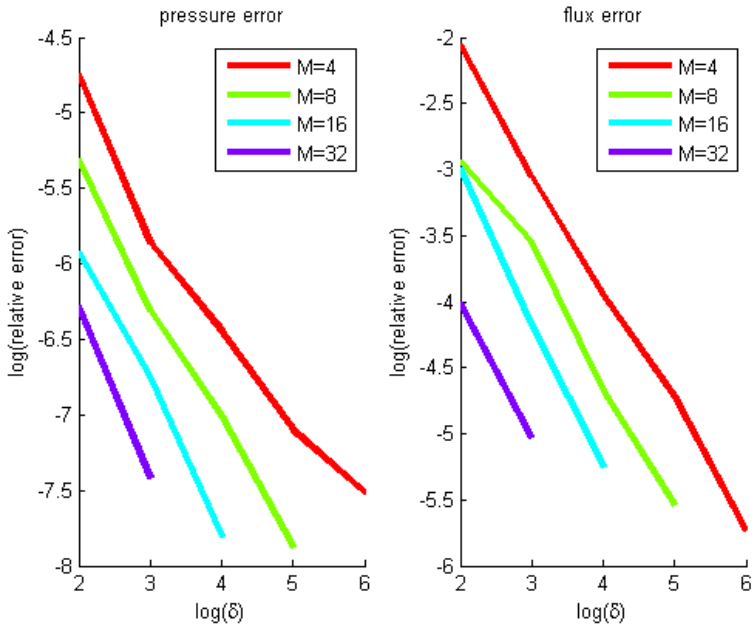

Figure 9.11: Convergence of Reaction-Diffusion Problem with $c = 500$ and $k \in [1, 1000]$.

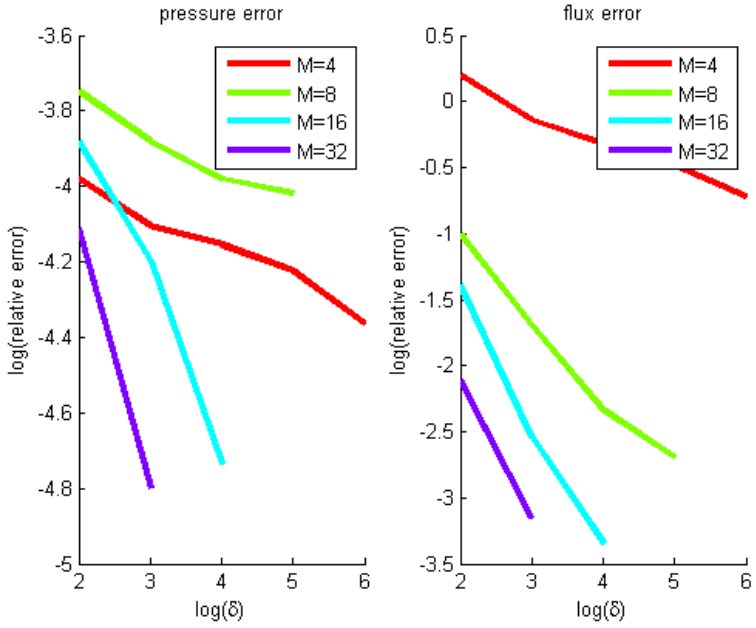

Figure 9.12: Convergence of Reaction Dominated Reaction-Diffusion Problem with $c = 100,000$ and $k \in [1, 1000]$.

involving smooth functions $k(x, y)$ did not necessarily lead to convergence. Under most circumstances, the error increased slightly as δ increased and the error decreased slightly as μ increased. We attribute this to the fact that for smooth, non-oscillatory material coefficients, there is no scale separation. Clearly, our method for the reaction-diffusion problem in 2D works best in the cases with clear scale separation, as is consistent with multiscale methods in general[73].

9.7 2D Deformation

9.7.1 Cases

For our final series of convergence tests, we chose an analogous test set to that of the 2D flow (pure diffusion) problem. Since there are two material parameters involved with elasticity, we chose to test $\lambda(x) = \mu(x)$ in all tested cases. In case I, we verified convergence with constant Lame parameters $\lambda(x) = \mu(x) = 1$ throughout the computational domain. Case II involves sinusoidal variable coefficients of the form $\lambda(x, y) = \mu(x, y) = 1 + asin(2\pi\omega x)sin(2\pi\omega y)$, with $a = 10$ and $\omega = 5$. In Case III, we chose $\lambda(x, y), \mu(x, y) \in [1, 1000]$ with uniformly random distribution.

As before, we chose a computational domain $\Omega = [0, 1]^2$ with pure dirichlet boundary conditions. To illustrate the ability of our algorithm to capture gradients not aligned with the coordinate axes, we chose the condition $u = v = x + y$ on $\partial\Omega$ in all tests. We chose the number of sampling subdomains μ and sample sizes δ as integer powers of two such that $\mu\delta \leq |\Omega|$. Since the deformation problem involves multiple field variables (u, v) and conserved variables $\sigma_x, \sigma_y, \tau_{xy}$, we measure the relative L^∞ norm displacement and stress error by extracting the maximum absolute error of (u, v) and $(\sigma_x, \sigma_y, \tau_{xy})$.

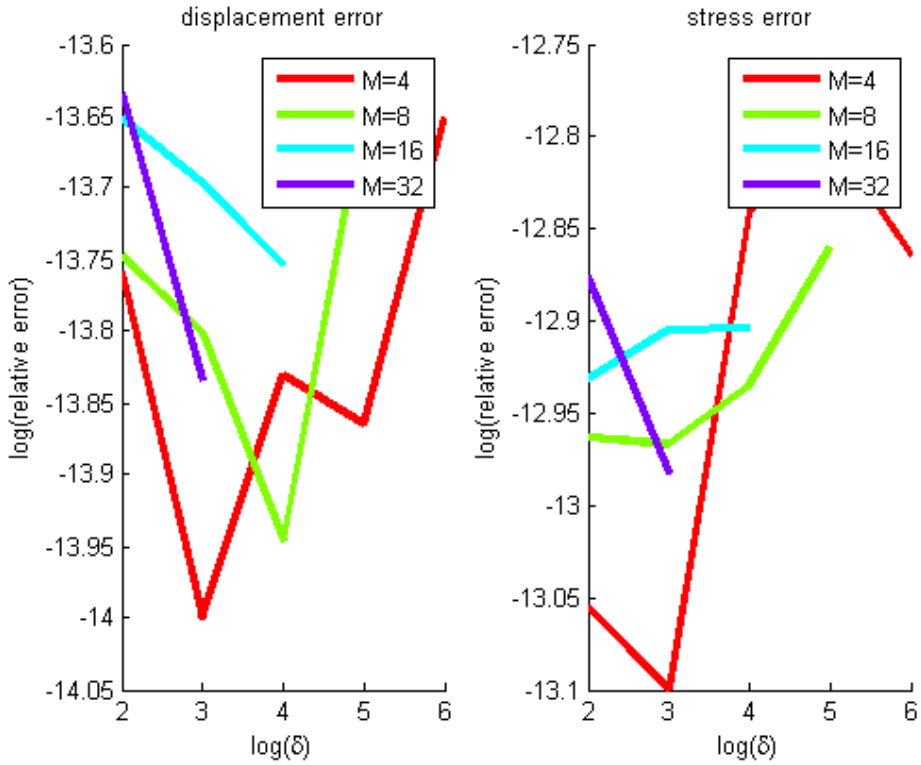

Figure 9.13: Convergence of 2D Deformation Problem, Case I.

9.7.2 Results

Figures 9.13- 9.15 illustrate the converges results for the 2D Deformation problem. As expected, we observe similar convergence results to those of the 2D Pure Diffusion and Reaction Diffusion problems for the constant case. As shown in figure 9.13, the constant case leads to error near floating point precision. This tendency is an artifact of the linear nature of the solution and does not capture the effectiveness of our multiscale algorithm. Case I merely verifies that our solution algorithm is consistent with the solution of the PDE in the simplest case.

The convergence of our algorithm in Case II shown in figure 9.14 is similar cases II and III of the Pure Diffusion problem. The error is primarily controlled by increasing the number of sampling subdomains μ. Note that for the particular problem tested, we

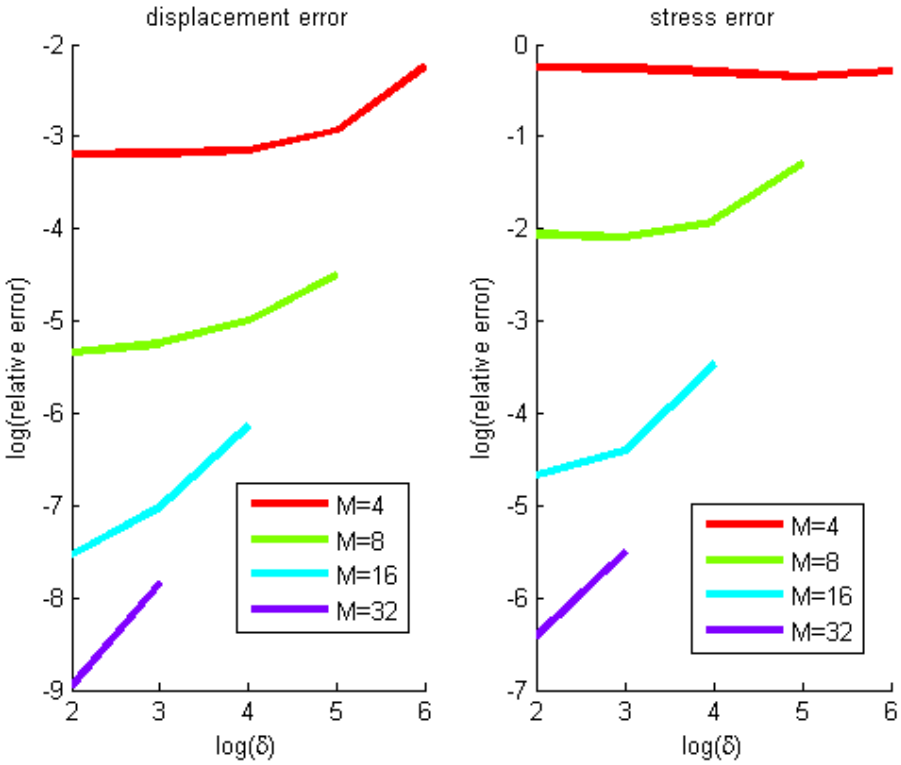

Figure 9.14: Convergence of 2D Deformation Problem, Case II.

observed a slightly increasing relative error as δ increases. That is, increasing the sample size did not prove to be an effective strategy for decreasing the error. Despite the fact that the material coefficients $\lambda(x, y), \mu(x, y)$ are have oscillatory behavior, they did not provide sufficient scale separation to enable our multiscale algorithm to capture the overall behavior of the system by sampling small subregions.

In contrast, the random heterogeneity in Case III provides sufficient scale separation to enable a clear convergence. As shown in Figure 9.15, the relative error in both displacement and stress decrease monotonically with increasing δ and μ.

The clear difference between the convergence of the 1D and 2D multiscale models for reaction-diffusion and deformation is that scale separation appears to play a bigger role in the method's accuracy. The stress error again is greater than an order of magnitude higher than the displacement error, as was observed in the reaction diffusion case.

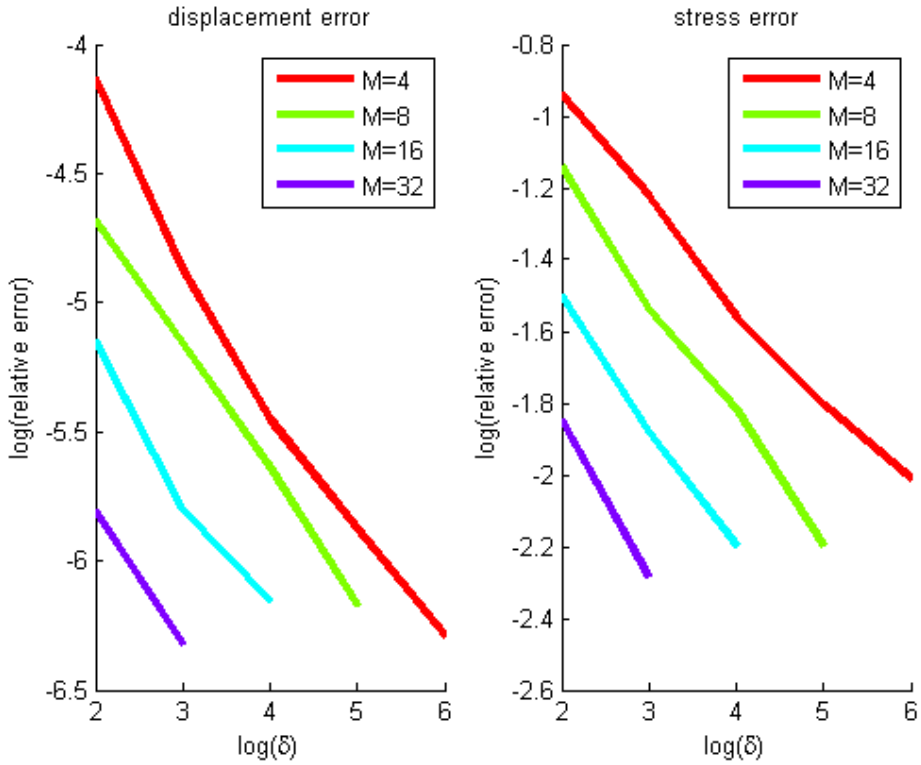

Figure 9.15: Convergence of the 2D Deformation Problem, Case III

9.8 Overlapping Sample Cases

In the case of 1D multiscale problems as in chapter 6, each sampling subdomain $B_\delta(x_{i+\frac{1}{2}})$ can be chosen with sampling length $\delta \leq \Delta x$ without overlapping other sampling subdomains. In the extreme case with $\delta = \Delta x$, sampling subdomains only overlap at their boundaries where the dirichlet condition is imposed. Also, 1D simulations hold the key property that for equispaced macroscopic finite volume cell grid, all available information can be utilized. Furthermore, our 1D simulations indicate that when all microscopic information is utilized, the accuracy of the multiscale simulation increases dramatically.

For higher dimensional simulation, we incur two key differences. Firstly, in the case of equispaced cell grids, it is impossible to cover the entire computational domain with sampling subdomains. Thus, unlike the 1D case, one cannot fully utilize all available infor-

mation when the sample size $\delta > L$, where L is the spatial stepsize of the discrete fine scale problem. If we restrict $\delta < \Delta x$, then material parameters near the four corners of the domain are always omitted by the sampling scheme. As the number of sampling subdomains increases, the amount of information utilized approaches the total information available. However, all available information is only fully utilized when the $\delta = L$. Unfortunately, this is equivalent to solving the (computationally expense) fine scale problem. More importantly, this implies that one cannot realize the highly accurate 'full microscale sampling' as we saw in the 1D case.

Secondly, the sampling subdomains only retain the non-overlapping property only when $\delta \leq \frac{\Delta}{2}$. Beyond this threshold, samples centered on the east/west faces of the control volumes begin to overlap with the samples centered on the north/south faces of the control volumes as illustrated in figures 9.16- 9.18.

One key observation of our multiscale method is the effect of overlapping subdomains on the accuracy of the simulations. Figure 9.19 illustrates that the acccuracy of our multiscale simulations improve as the size of the sampling subdomains increase, up to the point where the subdomains overlap. Beyond this point, we observe a dramatic spike in the relative error. This tendency was observed in all simulations for $\delta > \frac{\Delta x}{2}$. Clearly, a correlation exists between overlapping subdomains and an increase in the relative error. We note that [27, 26] never tested the case of overlapping subdomains for the flow equation, and that this phenomenon exists not only for pure steady state 2D fluid flow, but also the 2D reaction diffusion and deformation problems as well. Our multiscale method is clearly most accurate when the sampling subdomains are non-overlapping.

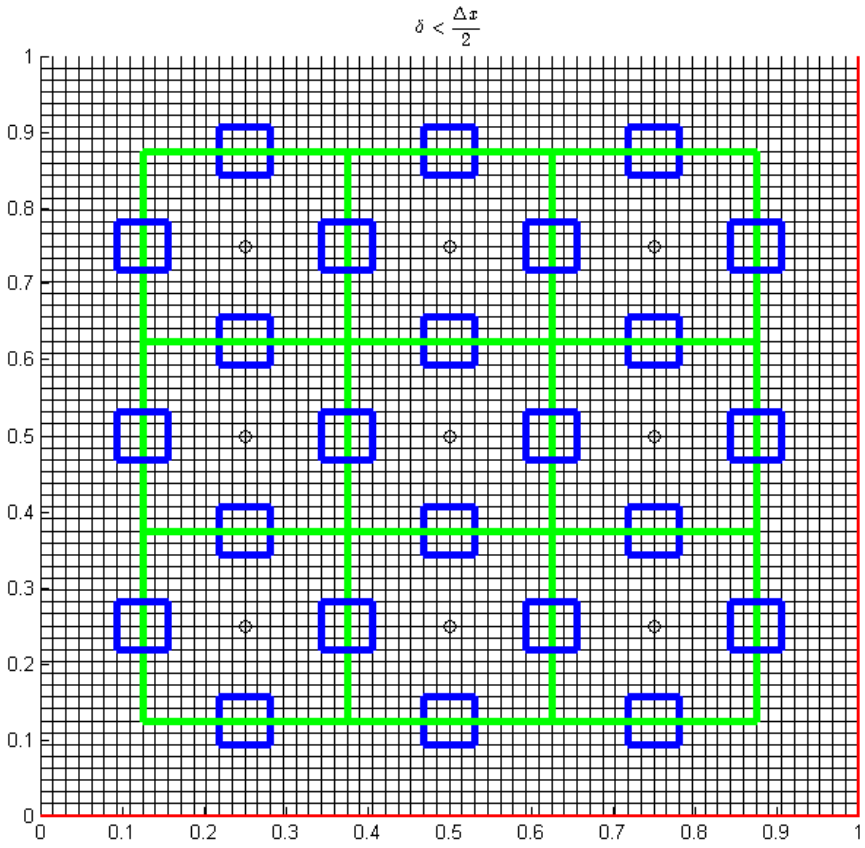

Figure 9.16: 2D sampling with $\delta < \frac{\Delta x}{2}$; Sampling subdomains are indicated in blue, control volumes are marked in green.

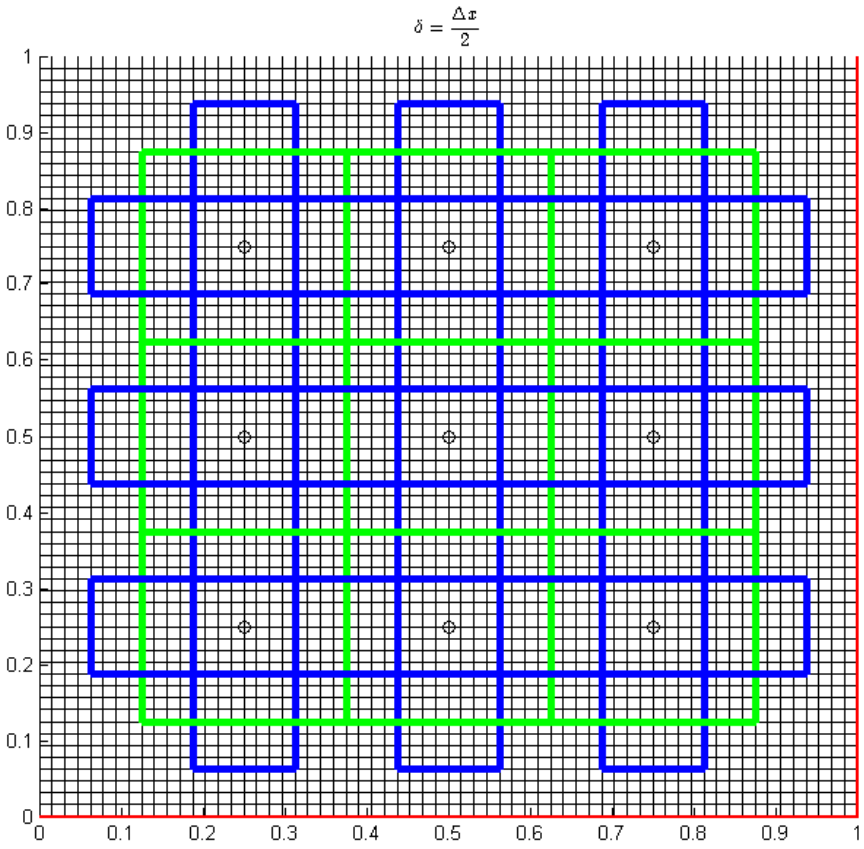

Figure 9.17: 2D sampling with $\delta = \frac{\Delta x}{2}$

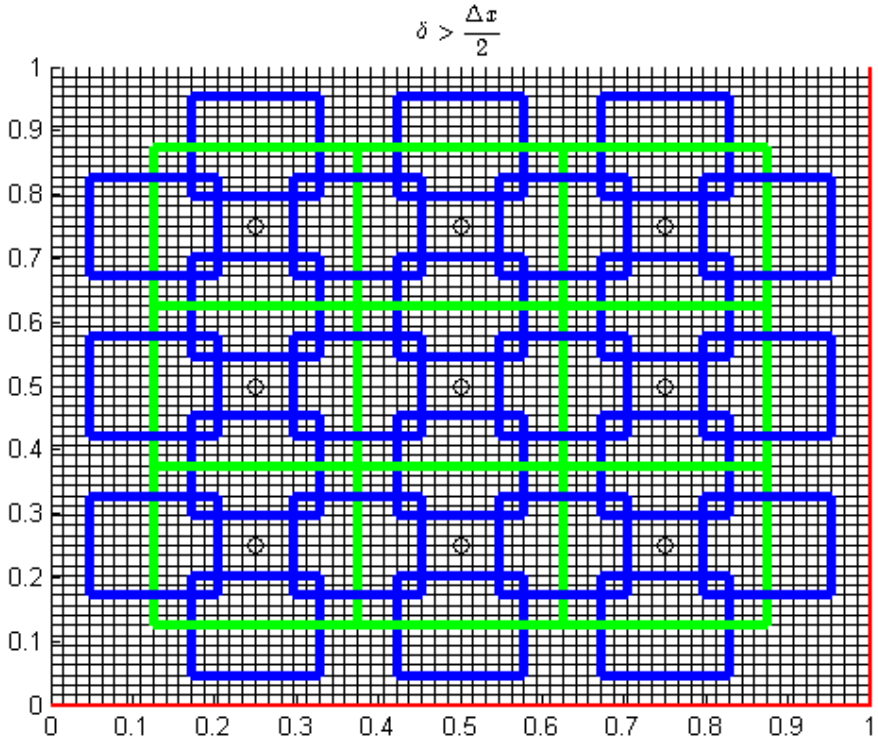

Figure 9.18: 2D sampling with $\delta > \frac{\Delta x}{2}$

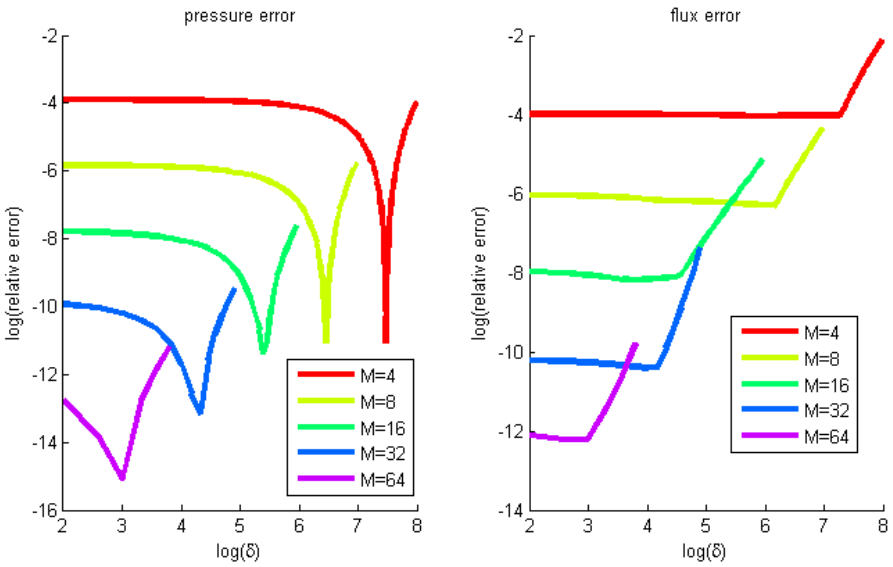

Figure 9.19: Convergence of the 2D reaction-diffusion problem with overlapping sampling subdomains

Chapter 10

Multiscale Error Analysis

In the previous chapters, we have illustrated the computational advantages of our heterogeneous multiscale methods in multiple examples. However, convergence has not yet been quantified rigorously. As noted in [72], various convergence analysis techinques exist for specific methods or problems but a general framework has yet to be established. This is largely due to the wide variety of micro and macro models that can be utilized within the HMM framework.

One popular approach to circumvent the absence of a general analysis framework is to recast the method as a numerical homogenization problem with a material coefficient $a_\epsilon(x)$ which oscillates on a length scale ϵ. We follow the analysis approach for heterogeneous multiscale methods as illustrated in [27] and [73]. As we shall elucidate, the key to this analysis is to observe that **macroscopic equations** of our multiscale schemes and the **discretized homogenization equations** have equivalent forms, but contain very different coefficients. Ultimately, we seek to quantify the difference between the solution to the multiscale model and the numerical solution of the original problem with a spatial stepsize $h < \epsilon$.

In the following section, we shall adapt the analysis approach given in [27] and [73] for the multiscale reaction-diffusion problem in a more intuitive manner. Then, we will derive the error estimate for the multiscale solid deformation problem.

10.1 Reaction-Diffusion Model

To explain our analysis as clearly as possible, we shall first introduce new notation and nomenclature for the analytical and numerical solutions to the reference problem, homogenization problem, and our multiscale problem. Then, we will observe correspondences between the coefficients among these problems and finally derive our error analysis.

10.1.1 Notation and Nomenclature

Consider the multiscale reaction-diffusion problem given by

$$-\nabla \cdot (a_\epsilon(x)\nabla p_\epsilon) + c^* p_\epsilon = 0 \text{ in } \Omega \tag{10.1}$$

$$p_\epsilon = g(x) \text{ on } \partial\Omega \tag{10.2}$$

We shall consider the material coefficient[1] $a_\epsilon \equiv a\,(x, y)$ as a positive, smooth function that is 1-periodic in y with $y \equiv \frac{x}{\epsilon}$. We shall refer to the parameter ϵ as the heterogeneity length scale.

We shall refer to (10.1) as the **reference problem** and consider its analytical and numerical solutions. Assume that there exists an **analytical** solution to (10.1), denoted by $p_\epsilon(x)$. Assume further that there exists a **numerical** solution obtained from a standard finite volume discretization of (10.1) on an equispaced nodal grid $x_{i,j}$ with stepsize h such that $h < \epsilon^2$. We shall refer to $x_{i,j}$ and $p_{i,j}$ as the **reference numerical grid** and the **reference numerical solution** at the corresponding to $x_{i,j}$, respectively.

Applying asymptotic homogenization to (10.1), [3] we obtain the **homogenized prob-**

[1] In this case, a_ϵ represents a locally oscillatory permeability field.

[2] Choosing $h < \epsilon$ enables the numerical solution to capture all the oscillations inherent in a_ϵ as described in Chapter 2

[3] For a full derivation, see [47]

lem

$$-\nabla \cdot (\bar{A}(x)\nabla \bar{P}_\epsilon) + c^* \bar{P}_\epsilon = 0 \text{ in } \Omega \tag{10.3}$$

$$\bar{P}_\epsilon = g(x) \text{ on } \partial\Omega \tag{10.4}$$

As noted in [27] for the 2D case, the homogenized coefficient in (10.3) is a matrix function of the form

$$\bar{A} = \begin{bmatrix} A^{11}(x) & A^{12}(x) \\ A^{21}(x) & A^{22}(x) \end{bmatrix}.$$

As saw for the reference problem, we shall introduce notations for the analytical and numerical solutions to (10.3). Let $\bar{P}(x)$ be the analytical solution of (10.3). Also, let $X_{k,l}$ be an equispaced with spatial stepsize H such $H > \epsilon$ for a given heterogeneity length scale ϵ. We shall $X_{k,l}$ and $\bar{P}_{k,l}$ as the **macroscopic grid** and numerical solution of the homogenization problem on this grid.

Lastly, we shall also consider the solution of our multiscale scheme, which ultimately becomes the solution of the macroscopic model. Let $P_{k,l}$ be the solution of the macroscopic equations of our multiscale method. Note macroscopic solution $P_{k,l}$ lies on the same grid as numerical solution of the homogenization problem $\bar{P}_{k,l}$ and thus has the same spatial stepsize H. Also note that every point in the *macroscopic grid* $X_{k,l}$ overlaps with the *reference numerical grid* point x_{i_k,j_l}. Therefore, there exists a subset of points in the reference numerical solution $p_{i,j}$ which corresponds exactly to the locations where the numerical homogenization $\bar{P}_{k,l}$ and macroscopic multiscale $P_{k,l}$ solutions lie. We shall denote this subset of $p_{i,j}$ as p_{i_k,j_l}.

10.1.2 Error Ansatz

The analytical solution $p_\epsilon(x)$ of the reference problem (10.1) is generally unavailable, but its numerical approximation $p_{i,j}$ can generally be obtained. Thus, our goal is to quantify the difference between the multiscale solution $P_{k,l}$ and numerical approximation p_{i_k,j_l} of the reference problem (10.1); that is,

$$|| \underbrace{P_{k,l}}_{\text{multiscale}} - \underbrace{p_{i_k,j_l}}_{\text{numerical reference}} ||. \tag{10.5}$$

We shall assume that this error can be bounded by considering differences involving the numerical and analytical solutions to the homogenization and reference problems. We shall add and subtract each of these solutions to (10.5), obtaining

$$|| \underbrace{P_{k,l}}_{\text{multiscale}} - \underbrace{p_{i_k,j_l}}_{\substack{\text{numerical}\\ \text{reference}}} || = || \underbrace{P_{k,l}}_{\text{multiscale}} \underbrace{-\bar{P}_{k,l} + \bar{P}_{k,l}}_{\substack{\text{numerical}\\ \text{homogenization}}} \underbrace{-\bar{P}(x_{k,l}) + \bar{P}(x_{k,l})}_{\substack{\text{analytical}\\ \text{homogenization}}} \underbrace{-p_\epsilon(x_{k,l}) + p_\epsilon(x_{k,l})}_{\substack{\text{analytical}\\ \text{reference}}} \underbrace{-p_{i_k,j_l}}_{\substack{\text{numerical}\\ \text{reference}}} ||$$

Using triangle inequality, we obtain

$$\begin{aligned} ||P_{k,l} - p_{i_k,j_l}|| \quad \leq \quad & \underbrace{||P_{k,l} - \bar{P}_{k,l}||}_{E_1} + \underbrace{||\bar{P}_{k,l} - \bar{P}(x_{k,l})||}_{E_2} \\ + \quad & \underbrace{||\bar{P}(x_{k,l}) - p_\epsilon(x_{k,l})||}_{E_3} + \underbrace{||p_\epsilon(x_{k,l}) - p_{i_k,j_l}||}_{E_4} \end{aligned}$$

We will refer to E_1, E_2, E_3, and E_4 as the multiscale, numerical homogenization, analytical homogenization, and numerical reference errors, respectively. Note that E_2 and E_4 can be analyzed using classical numerical analysis techniques. In particular, the standard finite volume discretization of E_4 with stepsize h has equivalent convergence properties to the classic 5-point finite difference stencil on an equispaced grid. Hence,

$$E_4 \leq Ch^2.$$

Similarly, we obtain a bound for E_2 by considering a finite volume discretization of the homogenization problem with stepsize H, with $H > \epsilon > h$. However, due to the tensor nature of the homogenized coefficient, we must a 9-point stencil is required. Nonetheless, the error can be bounded by

$$E_2 \leq CH^2.$$

To bound E_3, we borrow a result from standard homogenization theory; namely that analytical solution of the reference problem with heterogeneity length scale ϵ converges to

the analytical solution of the homogenized problem as $\epsilon \to 0$ at a rate of $O(\epsilon)$. In particular, we can bound the difference between these two solutions by a constant which only depends on the properties of the 1-periodic function $a(x, y)$. We write this bound as

$$E_3 \leq C_2(a)\epsilon.$$

The most crucial and non-trivial error to quantify and bound is the difference between the multiscale solution and the numerical homogenization solution $E_1 = ||P_{k,l} - \bar{P}_{k,l}||$.

In order to quantify this, we must observe two key facts; one regarding the correspondence between the coefficients of our discretized multiscale equations and the numerical homogenization equations; and the other regards the correspondence between the micro and macro coefficients in our multiscale scheme.

10.1.3 Coefficient Correspondence

The finite volume discretization of the homogenization problem (10.3) results in a system of equations of the form

$$\begin{aligned}
&-\bar{A}_E^{11} D_E^{x_1} \bar{P}_{k,l} - \bar{A}_E^{12} D_E^{x_2} \bar{P}_{k,l} \\
&+\bar{A}_W^{11} D_W^{x_1} \bar{P}_{k,l} + \bar{A}_W^{12} D_W^{x_2} \bar{P}_{k,l} \\
&-\bar{A}_N^{22} D_N^{x_2} \bar{P}_{k,l} - \bar{A}_N^{21} D_N^{x_1} \bar{P}_{k,l} \\
&+\bar{A}_S^{22} D_S^{x_2} \bar{P}_{k,l} + \bar{A}_S^{21} D_S^{x_1} \bar{P}_{k,l} \\
&+C^* \bar{P}_{k,l} = \quad 0
\end{aligned} \tag{10.6}$$

where A_d^{ij} are the entries of the homogenized coefficient $\bar{A}$ evaluated at the midpoint of control volume boundary $d = E, W, N, S$. Here D^{x_n} are the discrete partial derivatives with respect to the variables $x_1 \equiv x$ and $x_2 \equiv y$. Observe that the solution of our multiscale scheme $P_{k,l}$ satisfies the macroscopic equation, which can be expressed almost analogously

as

$$
\begin{aligned}
&-\left(K_E^{x,P_x} D_E^x P_{k,l} + K_E^{x,P_y} D_E^y P_{k,l}\right) \Delta y \\
&+\left(K_W^{x,P_x} D_W^x P_{k,l} + K_W^{x,P_y} D_W^y P_{k,l}\right) \Delta y \\
&-\left(K_N^{y,P_y} D_N^y P_{k,l} + K_N^{y,P_x} D_N^x P_{k,l}\right) \Delta x \\
&+\left(K_S^{y,P_y} D_S^y P_{k,l} + K_S^{y,P_x} D_S^x P_{k,l}\right) \Delta x \\
&\qquad +C^* P_{k,l} \Delta x \Delta y = \quad 0
\end{aligned}
\tag{10.7}
$$

To simplify our forthcoming analysis, we shall relabel the coefficients and partial derivatives in (10.7) as

$$
\begin{aligned}
&-K_E^{11} D_E^{x_1} P_{k,l} - K_E^{12} D_E^{x_2} P_{k,l} \\
&+K_W^{11} D_W^{x_1} P_{k,l} + K_W^{12} D_W^{x_2} P_{k,l} \\
&-K_N^{22} D_N^{x_2} P_{k,l} - K_N^{21} D_N^{x_1} P_{k,l} \\
&+K_S^{22} D_S^{x_2} P_{k,l} + K_S^{21} D_S^{x_1} P_{k,l} \\
&\qquad +\tilde{C} P_{k,l} = \quad 0
\end{aligned}
\tag{10.8}
$$

respectively.

Following the approach in [27], a bound on E_1 can be obtained by difference in the coefficients of (10.8) and (10.6). The addition of the reaction term does not significanly change our approach, since the reaction coefficient is identical in both equations. Thus, we can quantify the error by the bound

$$
||P_{k,l} - \bar{P_{k,l}}|| \leq C |K_d^{m,n} - \bar{A}_d^{m,n}| \tag{10.9}
$$

In general, the coefficients $\bar{A}_d^{m,n}$ are defined implicitly by integrals of the solutions of periodic cell-problems and are not given in an explicit form that this easily computed. Even if the coefficients of $\bar{A}_d^{m,n}$ are known explicitly, the coefficient $K_d^{m,n}$ is not known and thus (10.9) cannot be bounded directly.

To overcome this problem, we introduce a new term A_H whose differences between $K_d^{m,n}$ and $A_d^{m,n}$ are more easily quantified. Thus we can bound (10.9) by

$$
\begin{aligned}
E_1 &\leq C|K_d^{m,n} - A_d^{m,n}| && (10.10)\\
&= C|K_d^{m,n} - A_{H,d}^{m,n} + A_{H,d}^{m,n} - A_d^{m,n}| && (10.11)\\
&\leq C\left(\underbrace{||K_d^{m,n} - A_{H,d}^{m,n}||}_{E_5} + \underbrace{||A_{H,d}^{m,n} - A_d^{m,n}||}_{E_6}\right) && (10.12)
\end{aligned}
$$

We shall now define A_H and obtain bounds for E_5 and E_6.

10.1.4 Effective FE-HMM Coefficient

We shall refer to the coefficient A_H as the **effective coefficient** obtained from implementing the heterogeneous multiscale method within a finite element framework as in [1]. Following the presentation in [56], we assume the reference problem (10.1) and attempt to approximate a solution on a uniform macroscopic grid of stepwise $H > \epsilon$. To do this, we replace the oscillatory coefficient $a_\epsilon(x)$ in (10.1) with the effective coefficient $A_H(x)$. Substituting A_H in (10.1) obtaining the the weak form of the PDE and applying the galerkin projection, the resulting stiffness matrix consists of integrals of the form

$$B(W,V) \equiv \int_\Omega \nabla W \cdot (A_H(x)\nabla V) = 0 \text{ for all } V, W \in X_H$$

for some space X_H. Here, we assume X_H is the space of piecewise linear lagrange functions on the macroscopic grid of size H.

The effective coefficient $A_H(x)$ has no explicit formula, but the quantity $B(W,V)$ can be inferred from solutions of the PDE on small subdomains centered around the quadrature points of each integral. Let x_q, ω_q be the quadrature points and corresponding weights of the integral $B(W,V)$ on a specific element K of area $|A|$. Then,

$$B(W,V) \approx \sum_K |K| \sum_{x_q \in K} \omega_q \left(\nabla W \cdot A_H \nabla V\right)(x_q) \tag{10.13}$$

In the Finite Element Heterogeneous Multiscale Method (FE-HMM), the quantity $\left(\nabla W \cdot A_H \nabla V\right)(x_q)$ is approximated by the solution of the reference problem (10.1) on

a local subdomain $B_\delta(x_q)$ of size $\delta \times \delta$ centered at the quadrature point x_q. This approximation is given by

$$(\nabla W \cdot A_H \nabla V)(x_q) \approx \frac{1}{\delta^d} \int_{B_\delta(x_q)} \nabla w_q^\epsilon(x) \cdot a_\epsilon(x) \nabla v_q^\epsilon(x) \tag{10.14}$$

where $v_q\epsilon$ and w_q^ϵ are solutions of the **local subproblems**

$$-\nabla \cdot (a_\epsilon(x) \nabla p_q^\epsilon) + C^* p_q^\epsilon = 0 \text{ in } B_\delta \tag{10.15}$$

$$p_q^\epsilon = V(x) \text{ on } \partial B_\delta \tag{10.16}$$

where $V(x)$ is a linear the test function V for the macroscopic variational problem, evaluated on the boundary of $B_\delta(x_q)$.

Once an analytical solution to (10.15) is obtained for each test function V, the approximate bilinear function (10.13) can be assembled and solved. In our current method, we use an alternative decomposition of (10.14) which enables it to be evaluated via approximations of the total flux in B_δ.

10.1.5 Flux Factorization

We observe that since (10.14) is evaluated analytically via the values on the boundary of $B_\delta(x_q)$, denoted by $\partial B_\delta(x_q)$. By (10.15), we have that $w_q^\epsilon(x) = W_q(x)$ on $\partial B_\delta(x_q)$. Thus, we obtain

$$\int_{B_\delta(x_q)} \nabla w_q^\epsilon(x) \cdot a_\epsilon(x) \nabla v_q^\epsilon(x) = \int_{B_\delta(x_q)} \nabla W \cdot a_\epsilon(x) \nabla v_q^\epsilon(x) \tag{10.17}$$

If we assume W is a linear function and $B_\delta(x_q)$ does not contain a macroscopic grid point, then ∇W is a constant and can be factored out of the integral. Hence, we obtain

$$\int_{B_\delta(x_q)} \nabla W \cdot a_\epsilon(x) \nabla v_q^\epsilon(x) = \nabla W \int_{B_\delta(x_q)} a_\epsilon(x) \nabla v_q^\epsilon(x) \tag{10.18}$$

Note that the integral

$$F(\nabla V) \equiv \int_{B_\delta(x_q)} a_\epsilon(x) \nabla v_q^\epsilon(x) \tag{10.19}$$

can be interpreted as the average flux over the entire subdomain $B_\delta(x_q)$ from the local solution of (10.15). Thus, we can write

$$\nabla W \int_{B_\delta(x_q)} a_\epsilon(x) \nabla v_q^\epsilon(x) = \nabla W F(\nabla V) \tag{10.20}$$

In this factorized form, we state that the effective stiffness matrix can be subsumed by the flux emanating from local subproblems whose dirichlet boundary conditions are obtained from a linear interpolation of the macroscopic basis functions.

10.1.6 Estimate of E_1

The error term E_5 quantifies the difference between the coefficients of the multiscale solution and the FE-HMM approach. The primary difference between these methods is how the flux is evaluated. For the FE-HMM method, we assume the flux is analytical and thus exact. For our multiscale method, we assume the flux is approximated from the numerical solution of the local subproblems. Using the standard centered difference schemes described earlier, the numerical pressure and flux have order accuracies $O(\frac{h^2}{\epsilon^3})$ and $O(\frac{h}{\epsilon^3})$, respectively. As stated in [27], the term

$$E_5 = ||K_d^{m,n} - A_{H,d}^{m,n}||$$

is bounded by the order of accuracy in the numerical flux approximation in $K_d^{m,n}$. Thus,

$$E_5 = ||K_d^{m,n} - A_{H,d}^{m,n}|| \leq C \cdot \frac{h}{\epsilon^3}$$

The other error term

$$E_6 = ||A_{H,d}^{m,n} - \bar{A}_d^{m,n}||$$

refers to how closely the FE-HMM solution approximates the analytically homogenized coefficient $\bar{A}$. Citing the derivation in [27, 56], this error depends on the size of the subdomains δ and its relative magnitude compared to the heterogeneity length scale ϵ. For the aforementioned macroscopic linear basis functions in the FE-HMM approach, the error can

be quantified by

$$E_6 \leq e(HMM) = \begin{cases} C\epsilon & : \delta = \epsilon \\ C\left(\frac{\epsilon}{\delta} + \delta\right) & : \delta \neq \epsilon \end{cases} \tag{10.21}$$

Combining the bounds for E_5 and E_6, we estimate

$$E_1 \leq C(\frac{h}{\epsilon^3} + e(HMM)).$$

10.1.7 Error Estimate

Combining the results in each of the previous subsections, we can express the error

$$\begin{aligned} ||P_{k,l} - p_{i_k,j_l}|| &\leq ||P_{k,l} - \bar{P}_{k,l}|| + ||\bar{P}_{k,l} - \bar{P}(x_{k,l})|| \\ &+ ||\bar{P}(x_{k,l}) - p_\epsilon(x_{k,l})|| + ||p_\epsilon(x_{k,l}) - p_{i_k,j_l}|| \\ &\leq C(\frac{h}{\epsilon^3} + e(HMM) + H^2 + \epsilon) \end{aligned}$$

Note that this estimate suggests that the error may not approach zero as $h, H \to 0$ for all choices of δ. The error can only reach a minimum of some multiple of ϵ if the sample size $\delta = \epsilon$. On the other hand, if $\delta > \frac{h}{\epsilon^3} + H^2$, then the error may in fact increase as more information is included; that is δ increases. More importantly, this error bound only applies to problems with local periodicity and may not provide accurate bounds otherwise.

10.2 Solid Deformation Model

In contrast to the Reaction Diffusion problem, the solid deformation problem is a pure diffusion problem in 1D and its error analysis can be interpreted as a direct extension of the results reported in [27]. For higher dimensions, the deformation problem is not quite a pure diffusion problem but a similar argument can be made as above. Instead of fluxes, we use the expressions for the normal and shear forces for each subgradient. It is easy to see from [] that the homogenized coefficient has a similar coefficient structure as the coupling parameters of our multiscale scheme. Thus, we can bound the error by the difference in the

coefficients as we have demonstrated above. By similar argument, the error for the solid deformation case can be written as

$$||\vec{u}_{k,l} - \vec{u}_{i_k,j_l}|| \leq C \left(\frac{h}{\epsilon^3} + e(HMM) + H^2 + \epsilon \right)$$

What remains unclear is whether the term $e(HMM)$ retains the same form as seen for the reaction-diffusion case. To the best of the author's ability, this error term has not yet been analyzed under the heterogeneous multiscale method framework. Derivation of this error term is beyond the scope of the current thesis and will be left for future analysis.

10.3 Comparison to Numerical Experimental

We note that this error estimate is only applicable to the case for their respective PDE's with no source terms and with material coefficients of the form $a_\epsilon(x,y) = a(x, \frac{x}{\epsilon}$ when a is 1-perodic in the variable y. The cases that we tested in our numerical experiments do not utilize the assumption of 1-periodicity in the material coefficients and thus do not necessarily obey this error estimate.

If we omit the extreme case with $\mu\delta = |\Omega|$[4] and limit our analysis to the case of problems with pure dirichlet boundary conditions, no source terms, and subject to the constraint $\delta \leq \frac{\Delta x}{2}$, then we can also estimate the order of convergence of our method using our experimental data. For a given constant number of sampling subdomains μ, we can approximate the order of convergence P in δ using the formula

$$P \approx \frac{log(e_\delta) - log(e_{\frac{\delta}{2}})}{log(e_{\frac{\delta}{2}}) - log(e_{\frac{\delta}{4}})},$$

for consecutive choices of δ, $\frac{\delta}{2}$, and $\frac{\delta}{4}$. Using this approximation, we can estimate the order of convergence in the pressure p and displacement (u,v) for the 2D Deformation and

[4]This is the case where we consistently observe strange behavior in our multiscale method. In 1D, we observe a sudden and extreme decrease in the relative error. In the 2D case, we observe that error increases due to overlapping subdomains.

2D Reaction Diffusion problem for the Diffusion dominated and $c \approx k(x, y)$. Since our multiscale method was consistently convergent in δ in the random heterogeneous cases, we only acquired the order of convergence estimate for these cases.

Using the data collected from each set of 100 random simulations, we averaged the estimated order of convergence p for each μ across all 2D simulations reaction diffusion and solid deformation problems. Our estimated order of convergence for a given μ is approximately

$$E_\delta \approx O(\left(\frac{1}{\delta}\right)^1)$$

for the solid deformation problem and for the diffusion dominated reaction-diffusion problem.

We note that this estimate is consistent with our theoretical error estimate term $C\frac{\epsilon}{\delta}$ in $e(HMM)$, which provides the bound for E_6. Our data suggests that, at minimum, this term of $e(HMM)$ may exist in a theoretical error estimate for the case of randomly distributed material coefficients for the 2D reaction-diffusion and solid deformation problems. Further analysis is required to obtain a complete, asymptotically tight bound on the error in the randomly distributed case, which is the only case where our method consistently appears to converge.

When we analyze the order of convergence for the reaction-diffusion problem with $c \approx k(x, y)$, the estimated order of convergence is higher than our theoretical estimate. By averaging the results over 100 random tests, we estimate its order of convergence to

$$E_\delta \approx O(\left(\frac{1}{\delta}\right)^{\frac{1}{2}}$$

This result suggests that our theoretical error estimate does not provide an adequate bound in the case of reaction and diffusion coefficients of roughly equal magnitude. Clearly, the bound is dependent on the strength of the reaction coefficient as we mentioned earlier. The greater the relative magnitude of the reaction coefficient, the less effective our multiscale sampling scheme becomes.

In the case with $\delta > \frac{\Delta x}{2}$, we observe that the error increase is not caused by the overlapping subdomains as previously thought. The root cause of the increase in numerical error is due to the way dirichlet conditions are imposed on the microscale model. As previously mentioned, dirichlet boundary conditions on the microscale models are interpolated from the subgradients of the macroscopic field values at iteration K. For each subgradient, the microscale models' boundary conditions are artificially held constant in one direction. As the microscale models become larger and approach Δx in size, this artificial boundary condition conflicts with the true boundary conditions on the computational domain $\partial\Omega$. Clearly, this is not an issue in 1D because the field variables along a cross-section are naturally formulated in terms of a single, constant value. In higher dimensions, the constant boundary condition assigned to the microscopic model did not match the boundary conditions on the true computational domain. Thus, as the size of the microscale models approaches Δx, the subsamples closest to the boundary may interpolate incorrect values and thus produce a less accurate result.

Chapter 11

Algorithm & Performance Analysis

High resolution simulations of multiphase flow in geological formations are critical for many applications, such as petroleum and natural gas recovery, carbon sequestration, and groundwater management. The inherent multiscale physics governing both fluid flow and solid deformation make direct numerical simulation prohibitively expensive. The multiscale methods described in this thesis alleviate this expense in multiple ways. By employing operator splitting, we reduce the coupled equations into systems involving the individual degrees of freedom: pressure and displacement. By our multi scale method, we remove the need to resolve each system with a stepsize H much larger than the heterogeneity length scale ϵ. The cost of the multi-scale method depends on the degrees of freedom in the local subproblems and the global macroscopic equations. Additionally, since the boundary conditions of the local subproblems depend only on the local subgradients of the macroscopic degrees of freedom, their solutions can be obtained in parallel.

In this chapter, we quantify the asymptotic complexity of the sequential multiscale algorithm in $d \leq 3$ dimensions. We also derive the ideal complexity of the parallel algorithm and analyze two practical implementations of the algorithm in parallel.

11.1 Sequential Analysis

To simplify our analysis, assume that the reference problem has a domain Ω is a d dimensional cube in $\mathbb{R}^d$ and pure dirichlet boundary conditions. Also assume that a reference solution to the PDE is obtained by discretizing the PDE on an equispaced rectangular lattice with n^{ref} intervals in each dimension and spatial stepsize $h = \frac{\sqrt[d]{|\Omega|}}{n^{ref}}$. At each interior

node of the lattice, assume there are n^{dof} degrees of freedom. Thus, the total number of unknowns and equations in the system is approximately N^d, with $N = \left(n^{dof} \cdot n^{ref}\right)$.

The number of operations required to solve this system is highly dependent on the choice of linear solver. Nonetheless, we can quantify the worst-case scenario by considering the sparsity and bandwidth of the discretized reference problem. It's solution in d dimensions is obtained in a maximum of $O\left(L^2 N\right)$ operations, where L is the maximum bandwidth. For the 5-point stencil, this results in $L = N^{d-1}$. Thus, our worst-case analysis yields an asymptotic complexity

$$O(N^{3d-2}).$$

In contrast, the problem size for our multiscale method depends primarily on the degrees of freedom in the micro and macro models, the total number of microscale models that need to be solved, and the number of iterations to converge. To make an effective comparison with the cost of obtaining the reference solution, we assume the microscopic models have a spatial stepsize $h = \frac{\sqrt[d]{|\Omega|}}{n^{ref}}$. Assume further that all nodes of each micro model coincide with nodes of the reference solution. Thus, each local sample B_δ is also a d-dimensional cube in $\mathbb{R}^d$ of unidimensional length δ with $\delta = n^{local} \cdot h$ for some integer n^{local}. Every node of each micro model also contains n^{dof} degrees of freedom as in the reference solution. Assume further that the macroscopic model is also discretized on a square lattice with spatial stepsize $H = \frac{|\Omega|}{n^{macro}}$ for some integer $n^{macro} << n^{ref}$. Note that under this construction, the macro stepsize H is much larger than the micro stepsize h.

The total number of unknowns in each microscale model is of the order $\Theta\left((n^{dof} \cdot n^{local})^d\right)$. For the macroscopic model, the number of unknowns is $\Theta\left((n^{dof} \cdot n^{macro})^d\right)$. Let $N_{micro} = (n^{dof} \cdot n^{local})$ and $N_{macro} = (n^{dof} \cdot n^{macro})$. Then, by our aforementioned worse-case solver analysis, the macroscopic and each microscopic individually can be resolved in $O((N_{macro})^{3d-2})$ and $O((N_{micro})^{3d-2})$, respectively.

Note that $O((N_{micro})^{3d-2})$ quantifies the operations required to solve a single microscale model. The total number of microscale models that need to be solved is $\Theta(N_{macro}^d)$. Hence,

the total asymptotic complexity of each iteration of our multiscale method becomes

$$O\left((N_{micro})^{3d-2} \cdot (N_{macro})^{d} + (N_{macro})^{3d-2}\right) \tag{11.1}$$

Note that when $N_{micro} \approx N_{macro}$, the cost of a multiscale iteration is simplifies to $O((N_{macro})^{4d-2}$, which is more costly than solving a single macroscopic equation alone. When $N_{micro} << N_{macro}$, the asymptotic complexity is dominated by the solution of the macroscopic model and the complexity becomes $O((N_{macro})^{3d-2})$. In the opposite extreme, when $N_{micro} >> N_{macro}$, the multiscale algorithm requires approximately $O(\left((N_{micro})^{3d-2}\right)$. From a practical perspective, it is ideal to have both N_{macro} and N_{micro} as large as possible to obtain better accuracy.

11.2 Parallelization

The complexity bound (11.1) does not account for task independence in our algorithm. At each iteration of our algorithm, boundary conditions are interpolated from the macroscopic equation to each microscopic subdomain B_δ and can be solved independently of each other. On a machine with p processors, we can ideally achieve

$$O\left((N_{micro})^{3d-2} \cdot \frac{(N_{macro})^{d}}{p} + (N_{macro})^{3d-2} + c\right)$$

complexity, where c encompasses the cost of communication in the parallelization strategy. Generally, c depends on message latency λ, the number of messages sent simultaneously m, the size of the messages σ, and the bandwidth β. However, since each microscopic subdomain requires $O\left((N_{dof})^{d}\right)$ values to be sent and generally $(N_{dof})^{d} << N_{micro}$, the cost of communication is negligible in comparison to solving a single micro model for sufficiently large problems.

Note that by ignoring communication costs in the complexity estimate, the 1D case results in our multiscale algorithm having asymptotic complexity of the order

$$O\left(\frac{N_{micro}N_{macro}}{p} + N_{macro}\right) = \left(C_1\frac{N_{micro}}{p} + C_2\right)N_{macro}$$

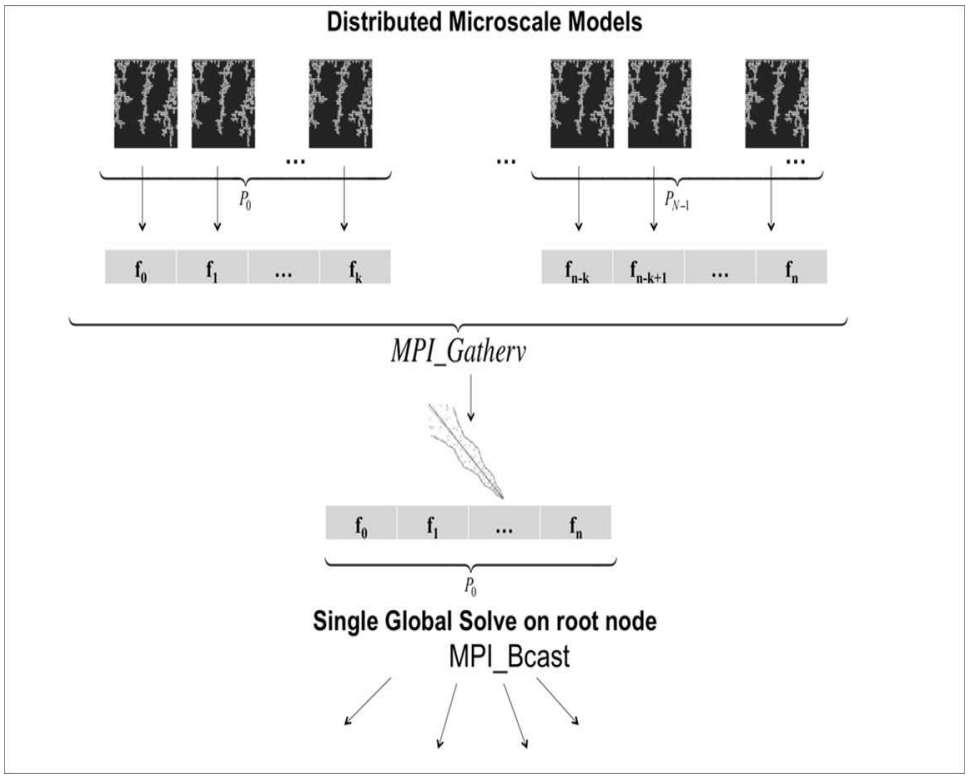

Figure 11.1: The Gather-Broadcast parallelization strategy uses two communication steps to solve the macroscale equations.

Consequently, the computational cost does not necessarily diminish to zero as the number of processors p increases. As $p \to \infty$, the computational cost remains roughly linearly proportional to the number of sampling subdomains denoted by N_{macro}. Since the goal of multiscale methods is to obtain good approximations without an extremely refined grid, the asymptotic limit $N_{macro} \to \infty$ should not be computed in practical applications.

Since microscale models share boundary conditions locally, they are best distributed to each processor contiguously according to their spatial coordinate in the macroscale grid. There are two alternative implementations to acquire the solution of the microscale models at each iteration: 1) the Gather-Broadcast approach and 2) the All-Gather approach. The Gather-Broadcast approach uses a master process that is assigned the tasks of gathering the distributed fluxes values, solving the macroscale equation, and broadcasting the macroscale

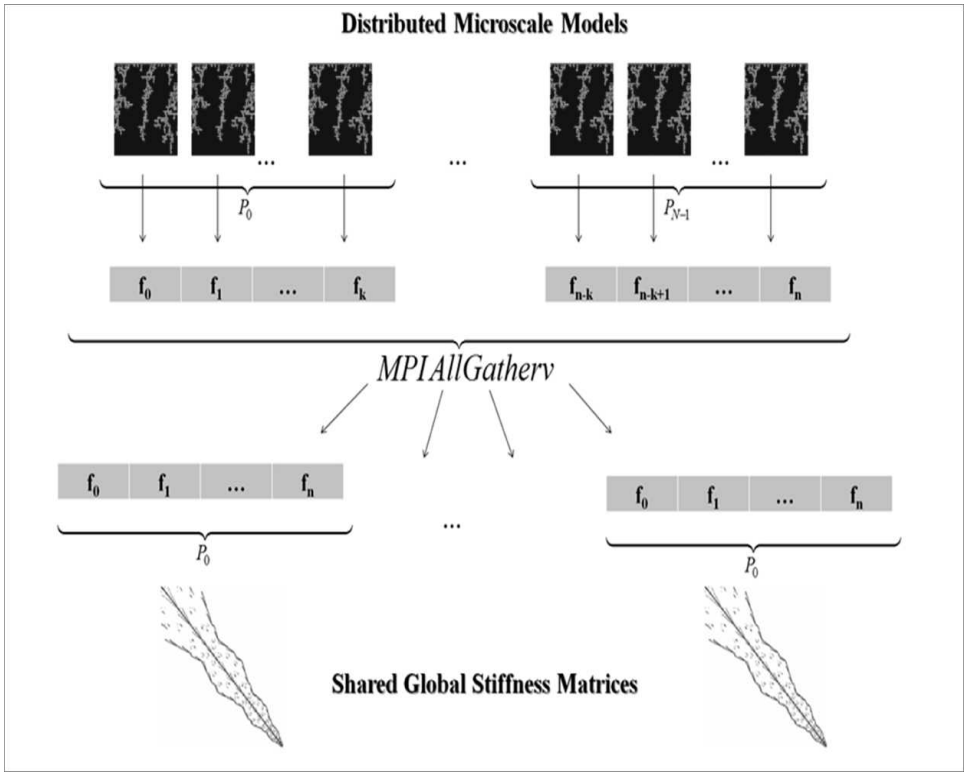

Figure 11.2: The All-Gather approach uses a single global communication step to solve the macroscale equations.

solution at every iteration, as seen in Figure 11.1. In contrast, the All-Gather approach gathers the distributed fluxes to every processes and duplicates the work of solving the macroscale equation as in Figure 11.2.

The common heuristic for improved performance is to duplicate computation on processors to minimize the number of communication phases nested in an iterative loop[65]. Since the All-Gather approach invokes a single asynchronous communication step, while the Gather-Broadcast approach uses two, we hypothesize that the All-Gather implementation should attain better performance at scale than the Gather-Broadcast implementation in the case of sufficiently large multiscale models.

11.3 Experimentation

In order to illustrate the computational advantages of our multiscale algorithm, we conduct numerical experiments quantify how much faster our multiscale algorithm performs compared to the computation of a reference solution. We shall consider both sequential performance as well as parallel performance metrics.

For our sequential tests, we first obtain the time necessary to compute the reference solution on finest scale throughout the entire spatial domain. Then, we obtain the time needed to compute the approximate solution via our multiscale method for a given number of samples μ and a given sample size δ. Without loss of generality, we shall restrict our attention to the 1 dimensional case. In doing so, we shall use the same sampling scheme as we used to illustrate convergence of our method in chapter 5. That is, we take μ & δ to be integer powers of 2 such that $\mu\delta \leq |\Omega|$, where $|\Omega|$ is the size of the domain. For simplicity, we shall assume $|\Omega| \equiv 1$ in all cases.

For our parallelization tests, we also obtain the time necessary to compute the reference solution on the finest scale as we did with the sequential tests. However, we only consider the performance of our multiscale algorithm in the case of full domain sampling with $\mu\delta \equiv |\Omega|$. Clearly, this represents the worst case scenario in which all available information

Table 11.1: Multiscale Simulation Parameters

Parameter	*Symbol*	*Value*
Macroscopic Domain Size	Ω	$1m$
Sample Size	$\frac{\delta}{L}$	256
Throat Radii	r	$10^{-3} - 10^{-6}m$
Pressure Gradient	ΔP	10 Pa

is incorporated into the multiscale model. Since all other cases with $\mu\delta < |\Omega|$ use less information and will clearly perform faster, we do not consider their performance under parallelization. We consider the performance of both All-Gather and Gather-Broadcast implementations of the multiscale algorithm outlined in the previous section.

In all cases, we used the same sparse linear solver method for all microscale and macroscale systems of equations. Speedup and scalability were measured for the execution of the multiscale algorithm on equivalent models for both All-Gather and Gather-Broadcast approaches. Here, scalability is defined as the ratio between sequential and parallel runtime on P processors. Sequential runtime was measured with the parallel implementation on a single processor.

Sequential performance was evaluated using Matlab code on a quad-core processor. Parallel Performance was evaluated at the Texas Advanced Computing Center's Stampede Supercomputer. This cluster uses 64-bit AMD Opteron Quad-Cores, with four processors per node. Each node is connected by a QDR InfiniBand switch fabric through a fat-tree topology, with 40GB/sec unidirectional point-to-point bandwidth. All simulations were implemented in C using MVAPICH2, an MPI-2 implementation optimized for InfiniBand architectures. We used an SGE job scheduler, utilizing the maximum 16 cores per node for all simulations.

Table 11.2: Sequential Multiscale Algorithm Speedup

		δ								
		4L	**8L**	**16L**	**32L**	**64L**	**128L**	**256L**	**512L**	**1024L**
μ	**1**	410.81	196.4900	123.4697	62.8074	60.3338	21.8999	12.2915	8.0296	6.3405
	2	244.4767	370.6935	227.6759	130.1374	61.9550	32.5056	13.0809	3.8405	*
	4	281.8948	144.7355	118.3315	65.4230	30.4724	18.0724	8.4209	*	*
	8	136.4967	93.8171	56.4408	34.5916	17.0344	7.8911	*	*	*
	16	27.2255	13.1294	7.8710	4.2191	3.1698	*	*	*	*
	32	14.5198	11.1439	5.5838	3.1748	*	*	*	*	*
	64	6.2622	4.2592	2.9486	*	*	*	*	*	*
	128	2.8442	2.0400	*	*	*	*	*	*	*
	256	1.0048	*	*	*	*	*	*	*	*

11.4 Results

11.4.1 Sequential Performance

Table 11.2 shows the relative speedup of the sequential multiscale algorithm compared to the solution of the fine scale reference problem without parallelization. Clearly, when δ and μ are small, less information is incorporated into the multiscale algorithm, making it the speed up much higher. Remarkably, even when the multiscale algorithm uses all available information, the reference solution is never acquired faster than the multiscale solution. In most cases of full domain sampling, the multiscale algorithm is at least twice as acquiring the reference solution on a fine scale. Clearly, even in the sequential case, our multiscale algorithm proves to be very competitive in terms of performance time.

11.4.2 Parallel Performance

The average runtimes of each implementation over the test cases described above are summarized in Tables 11.3- 11.4. Results indicate that for relatively small problem sizes ($N_{macro} <= 256$, performance between the two implementations is indistinguishable, with scalability being roughly linear. As N_{macro} increases, the Gather-Broadcast held consistently better performance over the cases tested. However, the improvement from utilizing extra processor power diminished significantly as problem sizes increased. Linear scalability was roughly maintained for smaller macroscale resolutions such as $N = 256$ in both implementations, as is observable in Figures 11.3- 11.4. Simulations with $N < 256$ also retained roughly linear scalability over the number of processors tested.

We maintain that our results are constistent with our asymptotic analysis. As N_{macro} increases beyond the threshold N_{micro}, the solution of the macroscopic problem becomes the dominant factor in the algorithm's complexity. Since the macroscopic solver was designed sequentially, parallelization of the solution to the microscopic problems does not provide significant improvement compared to the sequential algorithm.

While full performance analysis and optimization is beyond the scope of this thesis, we can assert that these results are consistent with our analysis. Specifically, the performance results indicate that in order to acheive significant benefit from parallelization, we must only consider problem sizes such that $N_{macro} < N_{micro}$. Fortunately, these are precisely the cases for which the multiscale algorithm was designed to handle.

Table 11.3: Gather-Broadcast Method Average Runtimes (in seconds)

		N			
		256	**512**	**1024**	**2048**
Π	**1**	38.8	78.1	173.6	669
	2	19.8	44.2	97.4	516
	4	10.4	21.6	58.7	440
	8	5.2	11.0	38.1	393
	16	2.8	6.1	27.1	366
	32	1.9	4.1	22.7	341
	64	0.92	2.4	19.5	340
	128	0.70	1.7	18.5	336
	256	0.56	1.6	17.5	331

Table 11.4: All-Gather Method Average Runtimes (in seconds)

		N			
		256	**512**	**1024**	**2048**
Π	**1**	38.7	89.7	204.6	662
	2	19.8	40.7	99.5	555
	4	10.2	21.8	66.2	485
	8	5.2	11.7	44.2	441
	16	2.7	6.9	37.0	421
	32	1.8	4.3	32.2	429
	64	0.91	3.3	29.8	421
	128	0.56	2.3	28.9	408
	256	0.43	2.2	27.9	405

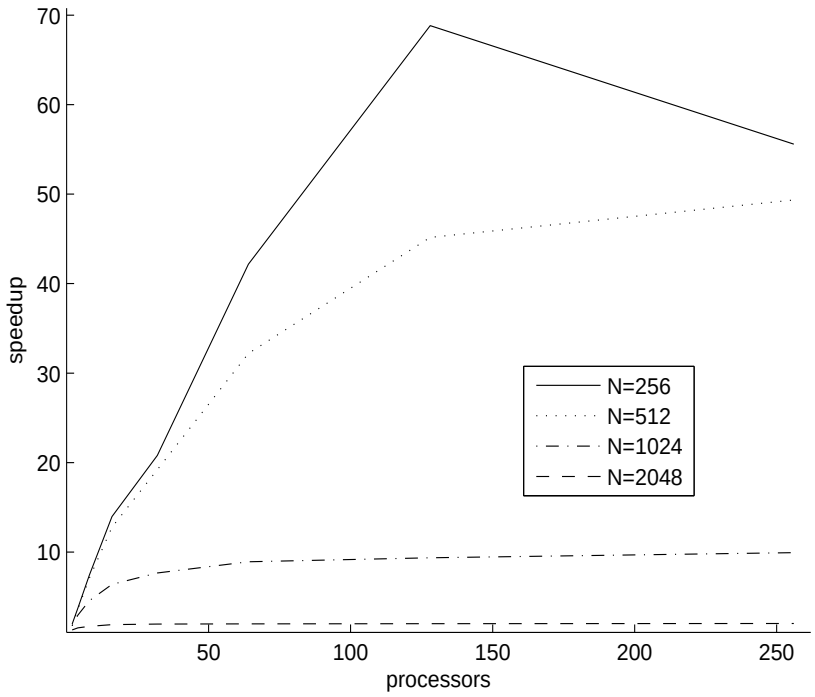

Figure 11.3: Scalability of the Gather-Broadcast Implementation.

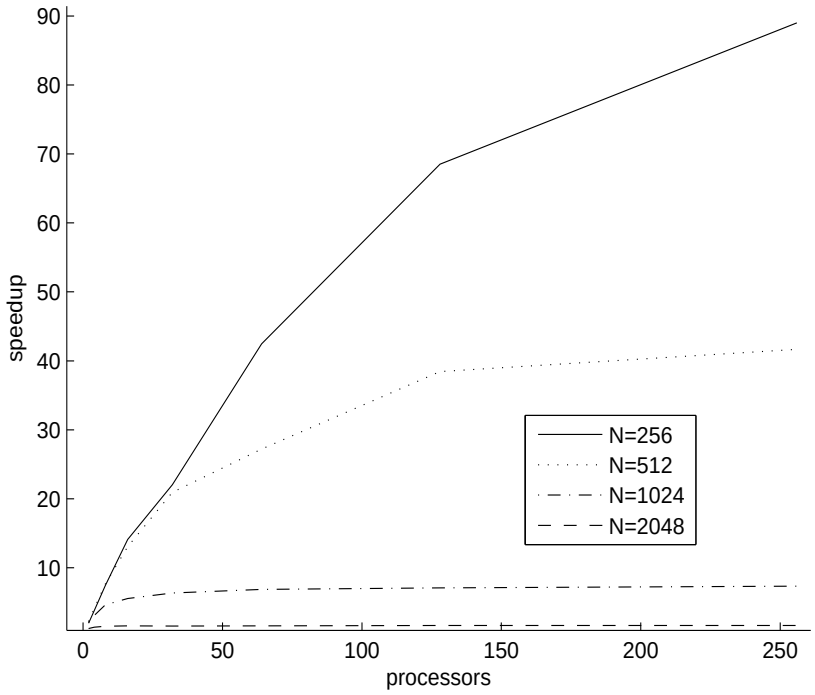

Figure 11.4: Scalability of the All-Gather Implementation.

Chapter 12

Coupled Simulation

The ultimate goal of this thesis is to develop a multiscale method applicable to coupled simulations of fluid flow and solid deformation in porous media. Our approach was to first decouple the problem into two single physics models, each of which can be resolved by our proposed multiscale method. To realize simulations of linear poroelasticity, we must also develop the mechanism by which passes information between the individual flow and deformation models.

The primary concern with coupled simulation is how to utilize the multiscale solution of one equation as a source term in the other equation. In this chapter, we demonstrate the iterative coupling of the multiscale solutions via their respective source terms. We shall then demonstrate the convergence of our method by numerical simulation of the linear steady state multiscale poroelasticity problem with pure dirichlet boundary conditions.

12.1 Coupling via Source Terms

As stipulated in chapter 3, we begin our multiscale solution by decoupling the fluid and solid equations from each other. Without loss of generality, let us consider a one dimensional linear poroelasticity problem on a staggered grid as illustrated in Figure 12.1. Let us also consider an operator splitting approach in which the fluid equation must be resolved first[1] via our multiscale algorithm. The result of the multiscale method is an approximation of the true pressure p on a coarse macroscale grid of stepsize H. Given this approximation, all

[1]The case in which the solid deformation equation is resolved first is analogous, since the fluid equation retains a term involving the divergence of the displacement $\nabla \cdot u$.

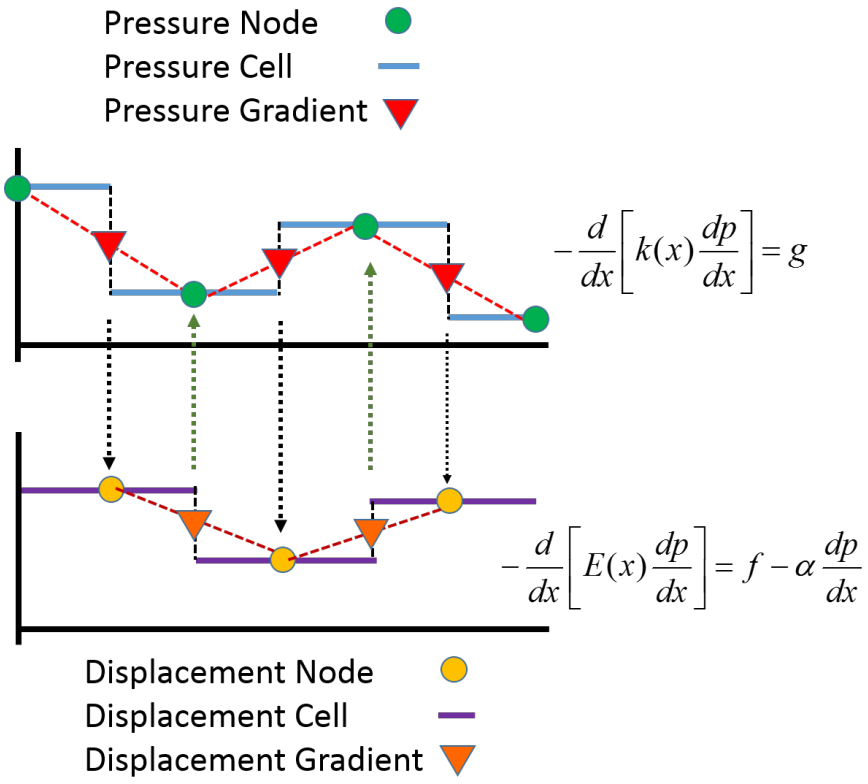

Figure 12.1: Alignment of Pressure Gradient values with Displacment Cell Centers and Displacement Gradient values with Pressure Cell Centers.

instances of the pressure p in the solid deformation equation can be moved to the right hand side of the partial differential equation. Explicitly, the solid equation in 1D is rewritten as

$$-\frac{d}{dx}\left[E(x)\frac{du}{dx}\right]=f-\alpha\frac{dp}{dx}$$

In essence, a scaled gradient of the macroscopic pressure solution becomes an additional source term in the solid equation. At first glance, this fact appears to be trivial to implement. Upon closer inspection of the staggered grid arrangement and its impact on the definition of the pressure gradient (see Figure 12.2, we observe that the pressure gradients obtained from the discrete macroscopic pressure grid are discontinuous at the centers of the sampling subdomains. Clearly, the pressure gradient on the left half of the sampling subdomain corresponds directly with the pressure gradient aligned with the left displacement

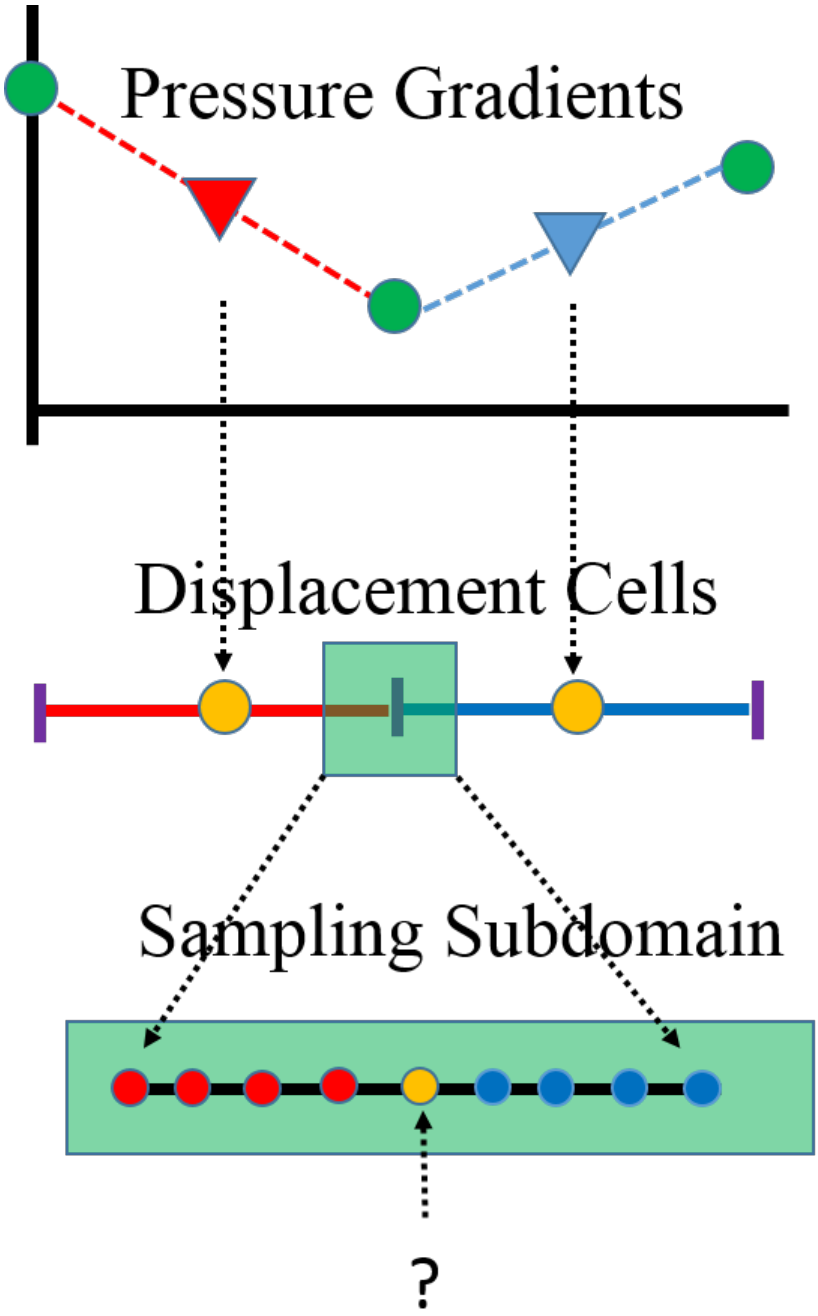

Figure 12.2: Ambiguous Microscopic source term value at the center of a displacement sampling subdomain.

cell and similarly for the right displacement cell. However, since the sampling subdomain intersects both cells continuously, there can exist a point at the center of the sampling subdomain in which the value of the pressure gradient is discontinuous.

Discontinuities of this sort are a common problem in the implementation of finite volume schemes and discontinuous galerkin finite element methods. While there are no unique methods to define the value of the discontinuous flux at the boundaries of cells/elements, some flux approximations are known to yield better approximation than others in special cases. When the underlying problem is strongly advective (as in some hyperbolic PDE's), additional dissipation (artificial viscosity) and other monotone/limiting schemes (e.g. Lax-Friedrichs, Gudonov, TVD, etc..) may be more applicable. Since the decoupled PDE's in our poroelasticity equations are elliptic, there is no preferred direction for the propagation of information. Thus, we can utilize the central difference method for estimating the flux, namely:

$$F = \frac{F_L + F_R}{2}$$

where F_L and F_R denote the fluxes from the intersecting cells to the left and right of the sampling subdomain center, respectively.

12.2 Accuracy

Clearly, if the flux were obtained on a fine scale grid of spatial stepsize h, the flux approximations would have $O(h)$ accuracy. However, since the flux is obtained from the multiscale solution on the macroscopic grid of spatial stepsize $H >> h$, it is clear that the solution of the multiscale solid deformation equation would have lesser accuracy than the solution of the fluid flow equation. In the best case scenario, one can expect that the fluid flux approximation is $O(H)$ accurate. It is unclear if even an $O(H)$ accurate pressure solution, used as a source term in the solid deformation equation, is sufficient to yield a convergent solution for the deformation equation. In cases where the solid deformation equation has

a forcing term f sufficiently larger relative to the pressure gradient, the accuracy of the pressure gradient approximation may not be significant. In other cases, where the forcing term f is zero or otherwise significantly smaller than the pressure gradient, the accuracy of the pressure gradient plays a stronger role in the accuracy of the deformation equation.

12.3 Numerical Experiments

To verify that our multiscale methods work in the context of coupled poroelasticity simulations, we consider the case of one dimensional, steady state, linear poroelasticity with pure dirichlet conditions on all boundaries in both pressure and displacement. The steady state poroelasticity equations are obtained by eliminating the time derivative terms in the fluid flow equation and assuming all source terms f and g are independent of time. Under these assumptions, the system of PDE's becomes

$$-\frac{d}{dx}\left[E(x)\frac{du}{dx}\right] = f - \alpha\frac{dp}{dx} \tag{12.1}$$

$$-\frac{d}{dx}\left[k(x)\frac{dp}{dx}\right] = g \tag{12.2}$$

We follow the same convergence testing procedure for 1D multiscale simulations as in chapter 5. We chose non-homogeneous dirichlet conditions on the left boundary as $u_L = 0.5$, $p_L = 1$, and homogeneous dirichlet conditions on the right boundary as $u_R = 0$,$p_R = 0$. We define the computational domain $\Omega = [0, 1]$ and subdivide it into equally spaced macroscopic control volumes. At each control volume boundary, we define a sampling subdomain B_δ of length δ. We choose the number of sampling subdomains μ and the sample size δ for the flow problem to be integer powers of two such that $\mu\delta \leq |\Omega|$. Due to the staggering of the macroscopic grids and the pure dirichlet boundary conditions, the number of samples in the deformation problem is $\mu - 1$, with μ as previously defined.

We choose a fine scale numerical solution with $N = 2^{12}$ equispaced intervals as our reference solution. We compute the pressure, flux, displacement, and force errors as pre-

viously in our 1D multiscale simulations. As before, we tested three cases associated with constant, linearly variable, and randomly distributed material parameters, with equivalent magnitudes as described in chapter 5. For the coupled simulations, we choose the distribution of the elasticity parameter $E(x)$ to be equivalent to the distribution of mobility parameter $k(x)$. In all cases, we obtain the L^∞ norm relative error. For the random case, we obtained the average error over 100 tests.

12.4 Results

The results of the steady state simulations are summarized in figures 12.3- 12.5. It is clear that there is a significant bias toward the accuracy of the solution to the fluid flow problem over the solution to the solid deformation problem. Clearly, the relative error in the fluid flow problem is well controlled on the order of 10^-12, with fluctuations close to numerical precision. The relative flux errors were within an order of magnitude of the pressure error, as expected. In contrast, the deformation errors are significantly larger and are independent of the size of the sampling subdomain δ. Clearly, in the constant coefficient case, no additional information is gained from increasing the sample size. Convergence in displacement is only attained by increasing the number of sampling subdomains. This trend extends beyond the constant case as illustrated in figures 12.4- 12.5

In the case with linearly varying material coefficients, we chose $E(x) = k(x) = x$. The results in Figure 12.4 are similar to those of the constant case, except for the fact that the displacement error decreases monotonically as δ increases, though only by a small fraction. Errors in both displacement and force are more clearly controlled by the increase in the number of sampling subdomains μ.

In the case of random heterogeneity (figure 12.5), we observe a different trend in the convergence. The errors in both displacement and force both decrease monotonically as μ and δ increase. When all available microscopic material properties are sampled ($E(x)$), we do not observe a drastic reduction of the error to near floating point precision as we see in

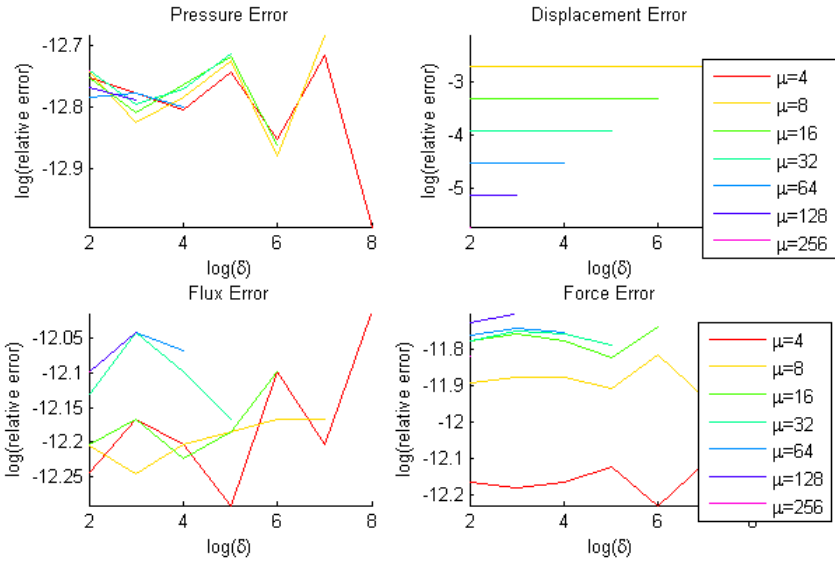

Figure 12.3: Convergence of the multiscale method for the steady state problem with **constant** material coefficients

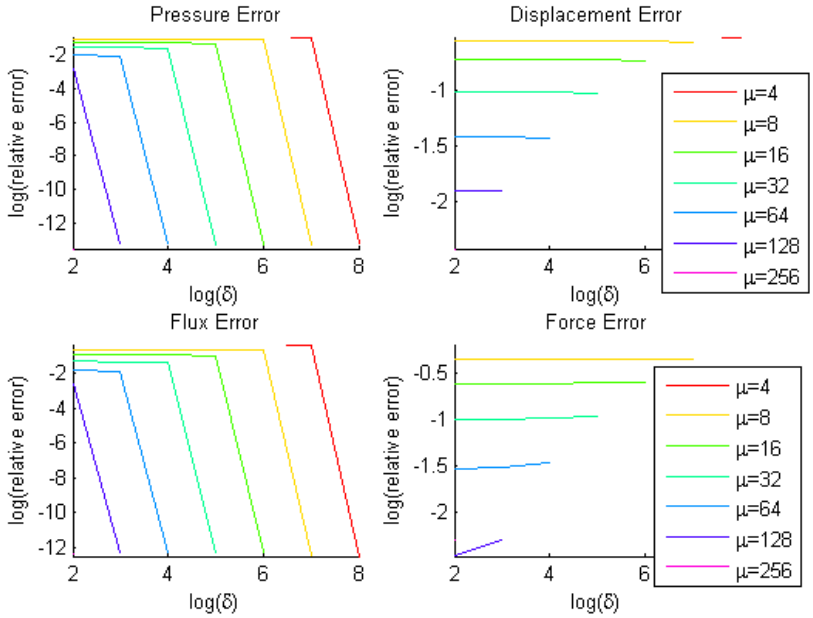

Figure 12.4: Convergence of the multiscale method for the steady state problem with **linearly varying** material coefficients

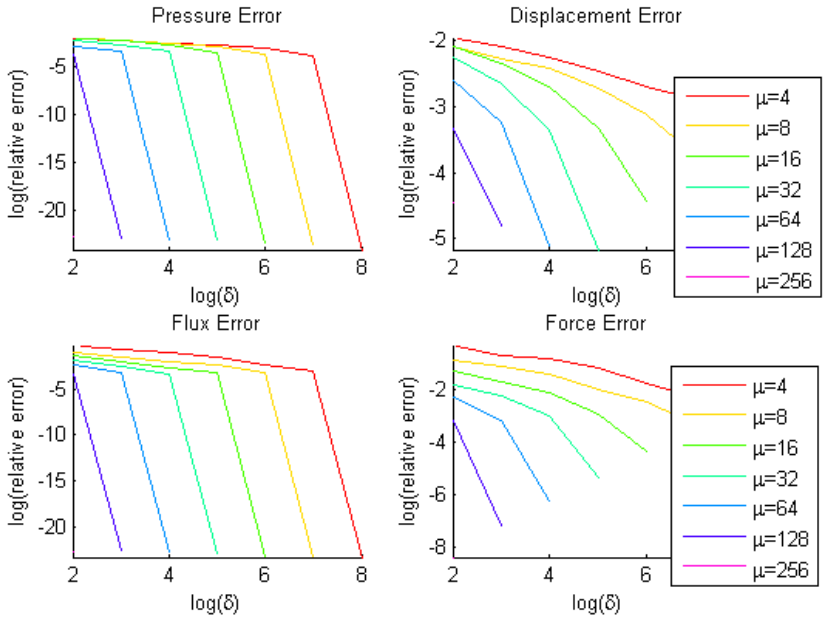

Figure 12.5: Convergence of the multiscale method for the steady state problem with **randomly distributed** material coefficients

the pressure/flux error. Instead, the errors reduce no more than one order of magnitude less the initial error with $\delta = 4L$.

Clearly, our multiscale method applied to the steady state poroelasticity problem performs best in the case of random material coefficients. This is because the random material coefficients provide natural setting for scale separation between microscopic variations and the macroscopic effects.

Chapter 13

Conclusions and Future Work

The current thesis developed a multiscale method applicable to linear poroelasticity problems. Our approach utilizes both operator splitting and the heterogeneous multiscale method. We adapted the finite volume heterogeneous multiscale method of Chu et al[27, 26] to resolve the multiscale heterogeneity in the split fluid flow and solid deformation equation. In the following sections, we summarize the advantages and limitations of our method, and recommend directions for future study.

13.1 Operator Splitting

We developed two approaches to decompose the fully coupled system of multiscale PDE's into a sequence of uncoupled elliptic multiscale problems. Our first approach utilized a fixed point iteration which converges conditionally upon the relative magnitudes of the non-dimensional parameter $\beta \equiv \alpha c_0$. This condition suggested that large time stepsizes were required to ensure convergence for $beta \approx 1$. Unfortunately, this constraint implies that one must sacrifice numerical accuracy significantly to ensure convergence of the operator splitting. In this sense, the applications of the fixed point iteration approach are extremely limited.

In contrast, our hybrid splitting method results in an unconditional convergence independently of the choices of the material parameters or the spatial/time stepsizes. By utilizing holding the stress (and **not the rate of stress**) constant, we obtained an innovative method which combines structure of the fixed point iteration with the advantages of holding conserved quantities constant as in the classical Fixed Stress Splitting method.

Our results indicate that our hybrid method is consistent if only one single iteration is applied for the constant coefficient case. While the advantages of the classical fixed stress splitting method are highly cited in the literature, its application to the heterogeneous poroelasticity case has yet to be demonstrated. On the other hand, we provide evidence that our hybrid splitting method is convergent even for the variable coefficient and randomly distributed material parameter cases. While the results in this thesis only apply to the 1D case, extension to higher dimensional cases may be possible via the use of deviatoric stress decompositions. Further analysis is required to demonstrate its application to these cases.

13.2 Multiscale Methods

Whether we apply our fixed point iteration or our hybrid splitting method, both approaches yield a reaction-diffusion problem for fluid flow and an elliptic linear elasticity problem for solid deformation. To resolve the multiscale nature of these two PDE's, we developed a heterogeneous multiscale method based on finite volume method. Our results indicate that error monotonically decreases in all cases of random material parameter heterogeneity. We further demonstrated that while the 1D case yielded extremely accurate results when all material parameters are sampled, the 2D case cannot be fully sampled under the assumption of equispaced macroscopic cell grids. We also observed that when sampling subdomains overlap in 2D multiscale simulations, the error can increase. This tendency is not reported in previous literature and is not predicted by our error estimate analysis. Further investigation into this phenomenon is required to fully understand its causes and strategies to avert it.

We conducted analysis of our multiscale method and obtained an error estimate for homogenization problems. Our analysis indicates that error does not necessarily decrease as the microscopic (h) and macroscopic (H) discretization stepsizes decrease. The error also depends linearly on the heterogeneity length scale ϵ and the sample subdomain radius

δ. Dependence on δ indicates that even as more information is incorporated into the microscopic model by increasing the sample radius, the error can in fact increase. The linear dependence on ϵ demonstrates that there is a limit to the amount of accuracy that can be achieved by our method. Our method can only be guaranteed to achieve as much accuracy as a constant factor of the heterogeneity length scale.

Though our error estimate analysis is only valid for the homogenization case, we observed similar trends for other cases. For some problems without scale separation, we observe an increase in error as δ increases. For randomly heterogeneous problems, we observed roughly convergence roughly linear in δ on a log-log plot. For a given macroscopic mesh size H, the error decreased by a factor of approximately $\left(\frac{1}{\delta}\right)$ which is consistent with a term appearing in the $e(HMM)$ term of our error estimate.

Our error estimate did not form a suitable bound for the reaction-diffusion problems with $c \approx k(x, y)$, but maintained the form of $O(\left(\frac{1}{\delta}\right)^p)$. For our particular experiments, we estimated $p \approx \frac{1}{2}$. Clearly, as the relative magnitude of the reaction coefficient increases compared to the diffusion coefficient, the order of convergence p decreases, indicating that less accuracy is obtained from the multiscale method we developed.

13.3 Source Terms & Boundary Conditions

We demonstrated the importance of incorporating source terms on the boundary of microscopic sampling subdomains. When an interior node of the fully microscopic model has a non-zero source term that coincides with the boundary of a sampling subdomain and is not distributed into the source terms within the local microscopic model, our multiscale method does not yield a good approximation even when full sampling is used.

We tested various approaches to incorporate these boundary source terms into the model. We observed the best approximations when exactly half the boundary source term densities were accumulated and distributed into the interior nodal source terms of their corresponding local microscopic models. The way in which these boundary source terms

are distributed appears to be arbitrary in 1D, as the accuracy in the remains constant regardless of the shape of the finite interval distribution. Testing in 2D is required to determine if this trend holds in higher dimensions as well.

Additionally, we demonstrated that the convergence of our method for mixed boundary condition problems was independent of how the initial condition was interpolated from the boundary conditions. The only constraints that need be enforced in 1D to ensure convergence are the dirichlet conditions.

13.4 Coupled Simulation

We tested our splitting method for the steady state multiscale poroelasticity problem with pure dirichlet boundary conditions. The primary two difficulties for this problem were setting up the boundary conditions associated with the staggered grids and treatment of the pressure gradient discontinuity at the cell boundaries which coincide with the center of the sampling subdomains. To overcome this difficulty, we used a simple averaging scheme to interpolate the gradient.

We tested our algorithm over three cases involving constant, variable, and random material coefficients in both the solid and fluid equations. We found that expanding the sample size δ did not improve the accuracy of the solid equation in the constant and linearly varying cases. However, we did obtain monotonically decreasing error in the case of random heterogeneity. This further emphasizes that our algorithm performs best under conditions of heterogeneity with scale separation.

Furthermore, we note that the accuracy of the deformation equation is significantly smaller than the accuracy of the flow equation. This severely restricts the applicability of our algorithm from use in the quasi-static case.

13.5 Future Work

Our results of our steady state poroelasticity simulations suggest that splitting the operators before resolving the multiscale nature of the solutions may not be an optimal strategy for the general, time-dependent case. Clearly, the steady state case contained naturally decoupled operators and represented an ideal case study for our multiscale strategy. We observed that when information is passed from the solution of the fluid flow equation to the source term of the solid deformation equation, convergence was achieved as the sample size δ and number of sampling subdomains μ. However, the error in displacement was significantly larger than the pressure error even when the pressure error was extremely small. Clearly, this limitation is a by-product of the use of the macroscopic pressure gradient values as piecewise constant values throughout the medium. In the steady state case, there are no other ways to improve the accuracy of the method since the deformation equation is independent of displacement. Though splitting may be suboptimal in terms of accuracy, we have yet to explore the possibility of resolving the multiscale equations without splitting. A multiscale scheme based on finite volume method which couples both flow and deformation equations on sampling subdomains within a single timestep may provide additional information to overcome the piecewise constant gradient values on macroscopic grid cells.

Recall that the so-called "Fixed Stress Splitting Method" for Poroelasticity actually requires the rate of stress is constant between iterations, not simply the stress itself. In this thesis, we obtain an innovative operator splitting method which imposes constant stress between iterations. We showed that this method works as efficiently as the traditional fixed rate of stress splitting method in the case of pure linear poroelasticity in 1D with constant coefficients, and also converges quickly in the case of variable coefficients. It remains to be seen how well this method extends to higher dimensional cases and non-linear poroelasticity problems.

Clearly, the error estimate we derived is only applicable to homogenization problems for highly oscillatory 1-periodic material coefficients. Currently, there are limited analytical

tools to derive error estimates for multiscale problems. Our estimate required the use of the periodicity assumption so that an analogy between homogenization and the well-studied heterogeneous multiscale finite element method can be exploited in the estimate. Clearly, violation of the periodicity assumption led to an overly-optimistic error estimate since our numerical simulations had an order of convergence lower than expected. In order to generalize the error estimate to other problems such as random heterogeneity and other non-periodic variable material coefficients, alternative techniques must be employed that characterize the behavior of our multiscale method in the case of non-periodic media.

The most surprising result in our simulations is the overlapping sampling subdomain phenomenon. This result was present in all of our simulations in higher dimensions and was not present in the 1D case. In practice, the case with $\frac{\Delta x}{2} < \delta \leq \Delta x$ generally require resolving a larger number of degrees of freedom than solving the original PDE on the fine scale and is thus not of particular interest from an efficiency perspective. The effect observed when $\delta > \frac{\Delta x}{2}$ is consistent with the constant dirichlet condition imposed on the microscale models whose boundaries approach $\partial\Omega$ as $\delta \to \Delta x$. Clearly, there are limitations to the applicability of the artificially constant dirichlet boundary condition to the microscale models. An alternative formulation/interpolation scheme which adheres to the true dirichlet conditions on $\partial\Omega$ as $\delta \to \Delta x$ for all microscale models near the $\partial\Omega$ would improve its convergence properties significantly.

Our multiscale methods are based upon the idea of rewritting the conserved quantities as functions of the primary variables and their subgradients. The approach tried in this thesis assumes the flux to be a function solely of the pressure variable and its subgradients, and the stress to be a function solely of the displacement and its subgradients. Since poroelasticity naturally couples displacement and pressure together, it may be advisable to write the conserved quantitites (stress and flux) in terms of all field variables and their respective subgradients. This alternative formulation which may lead to microscale problems which also couple both displacement and pore pressure, which may be sufficient to overcome the accuracy gap observed in our one-way coupled, steady state linear poroelasticity

simulations.

References

[1] Assyr Abdulle and Achim Nonnenmacher. A short and versatile finite element multiscale code for homogenization problems. *Computer Methods in Applied Mechanics and Engineering*, 198(37):2839–2859, 2009.

[2] G Aguilar, F Gaspar, F Lisbona, and C Rodrigo. Numerical stabilization of biot's consolidation model by a perturbation on the flow equation. *International journal for numerical methods in engineering*, 75(11):1282–1300, 2008.

[3] Ravi Appana. *Aquifer and Shallow San Andreas Fault Permeabilities Inferred from Poroelastic Modeling of InSAR Measurements of Land Surface Deformation in Coachella Valley, California*. PhD thesis, UNIVERSITY OF MINNESOTA, 2009.

[4] Todd Arbogast and Hailong Xiao. A multiscale mortar mixed space based on homogenization for heterogeneous elliptic problems. *SIAM Journal on Numerical Analysis*, 51(1):377–399, 2013.

[5] Christoph H Arns, Mark A Knackstedt, W Val Pinczewski, and Edward J Garboczi. Computation of linear elastic properties from microtomographic images: Methodology and agreement between theory and experiment. *Geophysics*, 67(5):1396–1405, 2002.

[6] Natalie K Axtell, Moongyu Park, and John H Cushman. Micromorphic fluid in an elastic porous body: blood flow in tissues with microcirculation. *Int J Multiscale Comput Eng*, 3(1), 2005.

[7] Juarez S Azevedo, Márcio A Murad, Marcio R Borges, and Saulo P Oliveira. A space–time multiscale method for computing statistical moments in strongly heterogeneous poroelastic media of evolving scales. *International Journal for Numerical Methods in Engineering*, 90(6):671–706, 2012.

[8] Alireza Bahraminasab, S Mehdi Vaez Allaei, Farhad Shahbazi, Muhammad Sahimi, MD Niry, and M Reza Rahimi Tabar. Renormalization group analysis and numerical simulation of propagation and localization of acoustic waves in heterogeneous media. *Physical Review B*, 75(6):064301, 2007.

[9] Miao Bai and Derek Elsworth. *Coupled processes in subsurface deformation, flow, and transport*. ASCE Publications, 2000.

[10] SI Barry and GN Mercer. Flow and deformation in poroelasticityi unusual exact solutions. *Mathematical and computer modelling*, 30(9):23–29, 1999.

[11] J Bear and MY Corapcioglu. Centrifugal filtration in deformable porous media. *A Series of Four Papers on Water Flow in Deformable Porous Media. Technical Report UMR-0284, Department of Civil Engineering, University of Michigan, Ann Arbor, Michigan, Section I*, 1981.

[12] Jacob Bear and M Yavuz Corapcioglu. Mathematical model for regional land subsidence due to pumping: 1. integrated aquifer subsidence equations based on vertical displacement only. *Water Resources Research*, 17(4):937–946, 1981.

[13] Michele Benzi, Gene H Golub, and Jörg Liesen. Numerical solution of saddle point problems. *Acta numerica*, 14(1):1–137, 2005.

[14] James G Berryman. Comparison of upscaling methods in poroelasticity and its generalizations. *Journal of Engineering Mechanics*, 131(9):928–936, 2005.

[15] William Bickford. *A first course in the finite element method*. Irwin, 1990.

[16] M.A. Biot. General theory of three-dimensional consolidation. *Journal of applied physics*, 12(2):155–164, 1941.

[17] MA Biot. Theory of deformation of a porous viscoelastic anisotropic solid. *Journal of Applied Physics*, 27(5):459–467, 1956.

[18] MA Biot. Generalized theory of acoustic propagation in porous dissipative media. *The Journal of the Acoustical Society of America*, 34(9A):1254–1264, 1962.

[19] Maurice A Biot and DG Willis. The elastic coefficients of the theory of consolidation. *J. appl. Mech*, 24(594-601):206, 1957.

[20] John R Booker and John Phillip Carter. Analysis of a point sink embedded in a porous elastic half space. *International Journal for Numerical and Analytical Methods in Geomechanics*, 10(2):137–150, 1986.

[21] JR Booker and JC Small. Finite layer analysis of consolidation. i. *International Journal for Numerical and Analytical Methods in Geomechanics*, 6(2):151–171, 1982.

[22] David F Boutt. Poroelastic loading of an aquifer due to upstream dam releases. *Ground water*, 48(4):580–592, 2010.

[23] Robert Burridge and Joseph B Keller. Poroelasticity equations derived from microstructure. *The Journal of the Acoustical Society of America*, 70:1140, 1981.

[24] Jan Carmeliet, Hannelore Derluyn, Stijn Mertens, Peter Moonen, E Schlangen, and G De Schutter. Multiscale modelling of coupled problems in porous materials. In *International RILEM Symposium on Concrete Modelling-ConMod'08*, pages 325–336. RILEM Publications SARL, 2008.

[25] Chia-Chieh Chu. *Multiscale methods for elliptic partial differential equations and related applications*. PhD thesis, California Institute of Technology, 2010.

[26] Jay Chu, Björn Engquist, Maša Prodanović, and Richard Tsai. A multiscale method coupling network and continuum models in porous media ii-single-and two-phase flows. *Advances in Applied Mathematics, Modeling, and Computational Science*, pages 161–185.

[27] Jay Chu, Björn Engquist, Maša Prodanovic, and Richard Tsai. A multiscale method coupling network and continuum models in porous media i: Steady-state single phase flow. *Multiscale Modeling & Simulation*, 10(2):515–549, 2012.

[28] CRI Clayton, H Müller Steinhagen, and W Powrie. Terzaghi's theory of consolidation, and the discovery of effective stress. In *International Journal of Rock Mechanics and Mining Sciences and Geomechanics Abstracts*, volume 33, pages 162A–162A. Elsevier, 1996.

[29] Massimo Cocco and James R Rice. Pore pressure and poroelasticity effects in coulomb stress analysis of earthquake interactions. *Journal of geophysical research*, 107(B2):2030, 2002.

[30] ME Contadakis and G Asteriadis. Hydrologic changes as possible earthquake precursor in greece. *Natural Hazards*, 23(1):29–47, 2001.

[31] Stephen C Cowin. Bone poroelasticity. *Journal of Biomechanics*, 32(3):217–238, 1999.

[32] H Darcy. Les fontaines publiques de la ville de dijon, 1856. *Dalmont, Paris*, 70.

[33] K. Delgado, P. & Kumar. A heterogeneous multiscale model of solid deformation mechanics using finite volume and direct stiffness methods. In *Proceedings of the 3rd Annual Southwest Energy Science & Engineering Symposium*, 2013.

[34] P. Delgado and K. Kumar. Generalization of a heterogenous multiscale framework coupling discrete microscale and continuous macroscale physics in a porous medium. In *Proceedings of the 2013 ASME Fluid Engineering Division Summer Meeting*, 2013.

[35] Paul M Delgado. A block operator splitting method for heterogeneous multiscale poroelasticity. Master's thesis, THE UNIVERSITY OF TEXAS AT EL PASO, 2013.

[36] Dominique Derome, Ahmad Rafsanjani, Stefan Hering, Martin Dressler, Alessandra Patera, Christian Lanvermann, Marjan Sedighi-Gilani, Falk K Wittel, Peter Niemz,

and Jan Carmeliet. The role of water in the behavior of wood. *Journal of Building Physics*, 2013.

[37] E. Detournay and A.H.D. Cheng. Fundamentals of poroelasticity1. 1993.

[38] I. Fatt. The network model of porous media. i. ii. iii. *Pet. Trans.*, 207(144), 1956.

[39] FJ Gaspar, FJ Lisbona, and CW Oosterlee. On a decoupled algorithm for poroelasticity and its resolution by multigrid. In *Proceedings of the ECCOMAS Computational Fluid Dynamics Conference, Delft*, 2006.

[40] FJ Gaspar, FJ Lisbona, CW Oosterlee, and PN Vabishchevich. An efficient multigrid solver for a reformulated version of the poroelasticity system. *Computer methods in applied mechanics and engineering*, 196(8):1447–1457, 2007.

[41] FJ Gaspar, FJ Lisbona, and PN Vabishchevich. A finite difference analysis of biot's consolidation model. *Applied numerical mathematics*, 44(4):487–506, 2003.

[42] FJ Gaspar, FJ Lisbona, and PN Vabishchevich. Staggered grid discretizations for the quasi-static biot's consolidation problem. *Applied numerical mathematics*, 56(6):888–898, 2006.

[43] Francisco J Gaspar, Francisco J Lisbona, and Petr N Vabishchevich. Finite difference schemes for poro-elastic problems. *Comput. Methods Appl. Math.*, 2(2):132–142, 2002.

[44] Francisco J Gaspar, Francisco J Lisbona, and Petr N Vabishchevich. A numerical model for the radial flow through porous and deformable shells. *Comput. Methods Appl. Math.*, 4(1):34–47, 2004.

[45] Margot G Gerritsen and Louis J Durlofsky. Modeling fluid flow in oil reservoirs. *Annu. Rev. Fluid Mech.*, 37:211–238, 2005.

[46] David J Hart. *Laboratory measurements of poroelastic constants and flow parameters and some associated phenomena*. PhD thesis, UNIVERSITY OF WISCONSIN, 2000.

[47] Ulrich Hornung. *Homogenization and porous media*, volume 6. Springer, 1997.

[48] Wang Jing, Liu Huiqing, and Wang Zenglin. Quantitative models of development laws for heterogeneous sandstone reservoirs by water flooding. *Open Petroleum Engineering Journal*, 5:26–35, 2012.

[49] J. Kim. *Sequential methods for coupled geomechanics and multiphase flow*. PhD thesis, Stanford University, 2010.

[50] V. Kumar. *Advanced computational techniques for incompressible/compressible fluid-structure interactions*. PhD Thesis Rice University, 2005.

[51] Pierre Ladevèze and Anthony Nouy. On a multiscale computational strategy with time and space homogenization for structural mechanics. *Computer Methods in Applied Mechanics and Engineering*, 192(28):3061–3087, 2003.

[52] Daryl L Logan. *A first course in the finite element method*. Thomson Learning, 2007.

[53] J Mandel. Consolidation des sols (étude mathématique)*. *Geotechnique*, 3(7):287–299, 1953.

[54] Günther Meschke, Dirk Leonhart, Jithender J Timothy, and Meng-Meng Zhou. Computational mechanics of multiphase materials–modeling strategies at different scales. *Computer Assisted Mechanics and Engineering Sciences*, 18(1-2):73–89, 2011.

[55] Andro Mikelić and Mary F Wheeler. Convergence of iterative coupling for coupled flow and geomechanics. *Computational Geosciences*, 17(3):455–461, 2013.

[56] Pingbing Ming, Pingwen Zhang, et al. Analysis of the heterogeneous multiscale method for elliptic homogenization problems. *Journal of the American Mathematical Society*, 18(1):121–156, 2005.

[57] TJ Mitchison, GT Charras, and L Mahadevan. Implications of a poroelastic cytoplasm for the dynamics of animal cell shape. In *Seminars in cell & developmental biology*, volume 19, pages 215–223. Elsevier, 2008.

[58] Anna Naumovich. *Efficient numerical methods for the Biot poroelasticity system in multilayered domains*. PhD thesis, PhD Thesis, Technical University Kaiserslautern, 2007.

[59] Bogdan Orlic. Some geomechanical aspects of geological co2 sequestration. *KSCE Journal of Civil Engineering*, 13(4):225–232, 2009.

[60] Grigorios A Pavliotis and Andrew M Stuart. *Multiscale methods: averaging and homogenization*, volume 53. Springer Science+ Business Media, 2008.

[61] Phillip Joseph Phillips and Mary F Adviser-Wheeler. *Finite element methods in linear poroelasticity: theoretical and computational results*. University of Texas at Austin, 2005.

[62] P.J. Phillips and M.F. Wheeler. A coupling of mixed and continuous galerkin finite element methods for poroelasticity i: the continuous in time case. *Computational Geosciences*, 11(2):131–144, 2007.

[63] P.J. Phillips and M.F. Wheeler. A coupling of mixed and continuous galerkin finite element methods for poroelasticity ii: the discrete-in-time case. *Computational Geosciences*, 11(2):145–158, 2007.

[64] P.J. Phillips and M.F. Wheeler. A coupling of mixed and discontinuous galerkin finite-element methods for poroelasticity. *Computational Geosciences*, 12(4):417–435, 2008.

[65] Michael J Quinn. *Parallel Programming*, volume 526. TMH CSE, 2003.

[66] James R Rice and Michael P Cleary. Some basic stress diffusion solutions for fluid-saturated elastic porous media with compressible constituents. *Rev. Geophys. Space Phys*, 14(2):227–241, 1976.

[67] APS Selvadurai. *Mechanics of poroelastic media*, volume 35. Springer, 1996.

[68] Reza Sepehrinia, M Reza Rahimi Tabar, and Muhammad Sahimi. Numerical simulation of the localization of elastic waves in two-and three-dimensional heterogeneous media. *Physical Review B*, 78(2):024207, 2008.

[69] RE Showalter. Diffusion in poro-elastic media. *Journal of mathematical analysis and applications*, 251(1):310–340, 2000.

[70] Karl Terzaghi and Otto Karl Fröhlich. *Theorie der Setzung von Tonschichten.* Deuticke, 1936.

[71] H.F. Wang. *Theory of linear poroelasticity with applications to geomechanics and hydrogeology.* Princeton University Press, 2000.

[72] E Weinan. *Principles of multiscale modeling.* Cambridge University Press, 2011.

[73] E Weinan, Bjorn Engquist, et al. The heterognous multiscale methods. *Communications in Mathematical Sciences*, 1(1):87–132, 2003.

[74] Son-Young Yi. A coupling of nonconforming and mixed finite element methods for biot's consolidation model. *Numerical Methods for Partial Differential Equations*, 2013.

[75] Alexander Ženíšek. The existence and uniqueness theorem in biot's consolidation theory. *Aplikace matematiky*, 29(3):194–211, 1984.

[76] O.C. Zienkiewicz. *Coupled problems and their numerical solution, in Numerical Methods in Coupled Systems, edited by Lewis, Bettes, & Hinton.* John Wiley & Sons Ltd., 1984.

[77] OC Zienkiewicz and T Shiomi. Dynamic behaviour of saturated porous media; the generalized biot formulation and its numerical solution. *International journal for numerical and analytical methods in geomechanics*, 8(1):71–96, 1984.

[78] Olgierd Cecil Zienkiewicz, Robert Leroy Taylor, and Jian Z Zhu. *The finite element method: its basis and fundamentals*, volume 1. Butterworth-Heinemann, 2005.

Curriculum Vitae

Paul Delgado is a Doctoral Candidate in the Computational Science program at UTEP and a Computational Scientist at Leidos Engineering. He is an NSF Fellow (HRD-1139929) and an XSEDE Scholar, and a previous holder of the NASA Training Project Scholarship, New Mexico Lottery Scholarship, and the UNM 3% Scholarship. He holds an M.S. in Computational Science from UTEP, an M.S. in Applied Mathematics from the University of New Mexico, and B.S. degrees in Applied Mathematics and Spanish from the University of New Mexico. He has 16 publications to this date, including articles in the Southwest Energy Science & Engineering Symposium, ASME Fluid Engineering Division, and Photonics West Conference. He presented his research at numerous conferences, including the SIAM Computational Science & Engineering Conference, SIAM Annual Meeting, Emerging Researchers National Conference, XSEDE Conference, Interpore Conference, and Carbon Capture & Utilization Conference. He has worked as a mathematics lecturer at UTEP, and interned at National Energy Technology Labs, Los Alamos National Labs, and NASA Ames Research Center. He is also the author of 5! Calculus Jokes: For the Not-So-Typical Math Nerd. He also is the founder and director of the SIAM Computational Methods & Tools Seminar and SIAM Computational Robotics Seminar at UTEP. He also is the founder and director of the UTEP Graduate Research Elevator Pitch Competition. He was also president of the UTEP SIAM Student Organization, and the UTEP Climate & Energy Science Student Organization. His research interests include Numerical PDE's, Multiscale Modeling & Simulation, Numerical Analysis, Computational Fluid Dynamics, Computational Linear Algebra, Finite Element Methods, Uncertainty Quantification, Polynomial Chaos Methods, Computational Robotics, Mathematical Biology, Non-linear Optics, and Machine Learning.